Nonlinear and Stochastic Dynamics of Compliant Offshore Structures

SOLID MECHANICS AND ITS APPLICATIONS
Volume 98

Series Editor: G.M.L. GLADWELL
Department of Civil Engineering
University of Waterloo
Waterloo, Ontario, Canada N2L 3GI

Aims and Scope of the Series

The fundamental questions arising in mechanics are: *Why?, How?,* and *How much?* The aim of this series is to provide lucid accounts written by authoritative researchers giving vision and insight in answering these questions on the subject of mechanics as it relates to solids.

The scope of the series covers the entire spectrum of solid mechanics. Thus it includes the foundation of mechanics; variational formulations; computational mechanics; statics, kinematics and dynamics of rigid and elastic bodies: vibrations of solids and structures; dynamical systems and chaos; the theories of elasticity, plasticity and viscoelasticity; composite materials; rods, beams, shells and membranes; structural control and stability; soils, rocks and geomechanics; fracture; tribology; experimental mechanics; biomechanics and machine design.

The median level of presentation is the first year graduate student. Some texts are monographs defining the current state of the field; others are accessible to final year undergraduates; but essentially the emphasis is on readability and clarity.

For a list of related mechanics titles, see final pages.

Nonlinear and Stochastic Dynamics of Compliant Offshore Structures

by

SEON MI HAN

Woods Hole Oceanographic Institution,
Department of Applied Ocean Physics and Engineering,
Woods Hole, MA, U.S.A.

and

HAYM BENAROYA

Rutgers, the State University of New Jersey,
Department of Mechanical and Aerospace Engineering,
Piscataway, NJ, U.S.A.

Springer-Science+Business Media, B.V.

A C.I.P. Catalogue record for this book is available from the Library of Congress.

ISBN 978-90-481-5999-4 ISBN 978-94-015-9912-2 (eBook)
DOI 10.1007/978-94-015-9912-2

Printed on acid-free paper

Cover Photo:
The Shell-operated Ursa tension leg platform is located in 3,800 feet of water at Mississippi Canyon Block 809, approximately 130 miles southeast of New Orleans, Louisiana. This is the fourth tension leg platform installed and operated by Shell in the deepwater Gulf of Mexico. Printed by permission of Shell Exploration and Production Company.

Originally published by Kluwer Academic Publishers in 2002.
Softcover reprint of the hardcover 1st edition 2002

Contents

Preface

The purpose of this monograph is to show how a compliant offshore structure in an ocean environment can be modeled in two and three dimensions. The monograph is divided into five parts. Chapter 1 provides the engineering motivation for this work, that is, offshore structures. These are very complex structures used for a variety of applications. It is possible to use beam models to initially study their dynamics. Chapter 2 is a review of variational methods, and thus includes the topics: principle of virtual work, D'Alembert's principle, Lagrange's equation, Hamilton's principle, and the extended Hamilton's principle. These methods are used to derive the equations of motion throughout this monograph. Chapter 3 is a review of existing transverse beam models. They are the Euler-Bernoulli, Rayleigh, shear and Timoshenko models. The equations of motion are derived and solved analytically using the extended Hamilton's principle, as outlined in Chapter 2. For engineering purposes, the natural frequencies of the beam models are presented graphically as functions of normalized wave number and geometrical and physical parameters. Beam models are useful as representations of complex structures. In Chapter 4, a fluid force that is representative of those that act on offshore structures is formulated. The environmental load due to ocean current and random waves is obtained using Morison's equation. The random waves are formulated using the Pierson-Moskowitz spectrum with the Airy linear wave theory.

In Chapter 5, the possibility of beam axial displacement is added to the formulation. The equations of motion are now nonlinear and coupled. The free, damped-free, harmonically forced, and randomly forced responses are considered in this chapter. This model can predict the axial displacement, longitudinal extension, and normal stress in addition to the transverse displacement. However, this is a two-dimensional model, which can only accommodate two-dimensional forcing. The fluid forces

in an ocean environment are inherently three-dimensional. Therefore, a three-dimensional beam model is considered in Chapter 6. Both rigid and elastic models are considered. The elastic model is derived assuming moderate rotation. Free and forced responses are studied. A harmonic force and a constant force are applied in perpendicular directions to simulate possible vortex-induced fluid forcing resulting from the interaction of a constant current with the beam-like structure. Chapter 7 provides a summary and conclusions. Several appendices provide some additional details.

The reader may ask how representative beam models are of the massive offshore structures one finds in the ocean, in applications such as oil drilling, docking facilities and communications junctions. The design of any such complex structure must begin with an understanding of the physical processes of the design environment and how these interact with the potential structure. This understanding is best obtained using reduced-order models that are faithful to the most important underlying physics. Beam models of the type formulated here are ideally suited for the studies at hand. Their analysis signals the analyst and engineer where key issues must be further analyzed in more detail with higher-order models, eventually leading to the full scale model and design. Therefore, the analytical and computational process described in this monograph should be viewed as a first step in a very intricate and complex process. These are valuable exercises.

SEON HAN AND HAYM BENAROYA

The first author dedicates this book to her husband, Andrew Mosedale, for his support. The second author dedicates this book to his parents, Alfred and Esther Benaroya, for all their love and support.

Acknowledgments

We are grateful for the support provided by the Office of Naval Research and by our program manager Dr. Thomas Swean under Grant No. N00014-97-10017. We are also appreciative of the conducive environment of the Mechanical and Aerospace Engineering Department at Rutgers University.

We also thank Professor Graham Gladwell for his thoughtful suggestions on improving this work.

Chapter 1

INTRODUCTION

In this monograph, analytical models of compliant offshore structures in an ocean environment are derived in two and three dimensions, and a spectrum of responses to various environmental loads are computed.

Offshore structures are used in the oil industry as exploratory, production, oil storage, and oil landing facilities. The detailed specifications and descriptions of offshore structures can be found in *Hydrodynamics of Offshore Structures* [17] and *Dynamics of Offshore Structures* [81].

In general, there are two types of stationary offshore structures: fixed and compliant. Fixed structures are designed to withstand environmental forces without any substantial displacement. Compliant structures, on the other hand, are designed to allow small but not negligible deformation and deflection. While the stability of fixed structures is provided by structural rigidity, the stability of compliant structures is provided by tension due to buoyancy chambers and cables anchored to the sea bed. For these compliant structures, the dynamic responses need to be explored fully.

Fixed structures are economically feasible only up to water depths in the range $1,000$ to $1,600$ ft. Fixed platforms are indeed the most popular and prolific structures for water depths of 400 to 500 ft. However, they become impractical for deep water because they must be built stronger and more bulky than the equivalent compliant structures. In recent years, the need to explore for oil in deeper water has made compliant structures more popular. Compliant towers are believed to be economically feasible in water depths exceeding $2,000$ ft. Here, we will consider compliant structures. In particular, we are interested in tension leg platforms (TLP).

S. M. Han et al., *Nonlinear and Stochastic Dynamics of Compliant Offshore Structures*

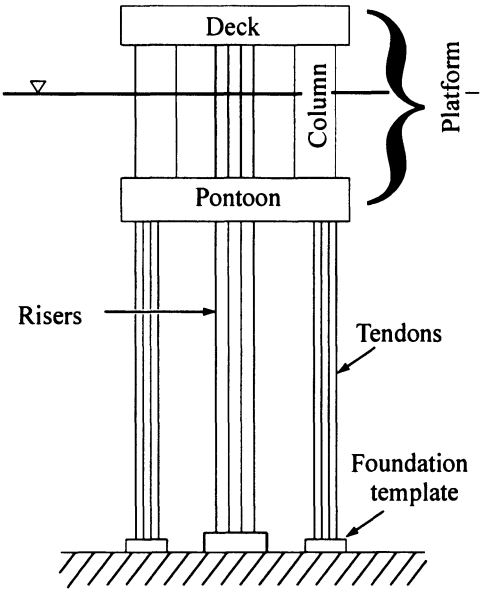

Figure 1.1. A Schematic of a Tension Leg Platform

1. Tension Leg Platforms

A schematic of a TLP is shown in Figure 1.1. A TLP is vertically moored by tendons at each corner of the platform. Buoyancy is provided by the fully submerged pontoons and partially submerged columns. Risers are production-related pipes.

Figure 1.2 shows Shell's Ursa TLP built in the Gulf of Mexico and completed in 1998 at a cost of $1.45 billion. The Ursa TLP stands in 3,800 ft of water, which surpasses the previous water depth record set by the Ram-Powell TLP built in 3,214 ft of water in 1997. The Ursa TLP is the tallest man-made structure in the world. It is more than three times taller than the Empire State Building (1250 ft). The design capacity of the Ursa TLP is 150,000 barrels of oil and 400 million cubic feet of natural gas per day. 400 million cubic feet of natural gas can heat more than six thousand new $2,000\ ft^2$ homes for an entire year.

The hull consists of four circular steel columns, which are 85 ft in diameter and 177 ft high. The ring pontoon is 38 ft wide and 29 ft high with a rectangular cross section. The TLP has 16 tendons, 4 at each corner. Each tendon has a diameter of 32 in and a wall thickness of 1.5 in. The total steel mass of the TLP is 63,000 tons.

The total platform height is 485 ft, which is more than 48 stories. The deck area is over 2.1 acres, and it consists of six modules: wellbay,

Figure 1.2. The Ursa TLP (Courtesy of Shell Exploration and Production Company)

quarters, power, drilling and two process modules. The quarters building is designed for a permanent crew of 156 persons.

Design, construction, and installation of the Ursa TLP were done by various groups. Waldemar S. Nelson and Co. and W. H. Linder and Associates of Metairie, Louisiana were contracted to develop the hull structural design. Deck modules and steel catenary risers were installed by J. Ray McDermott, Inc. The TLP was installed by Heerema of Leiden.

2. Mathematical Models for Dynamic Responses

TLPs are designed to withstand hurricane wind and waves, earthquakes, and virtually any other conceivable environmental hazard, but they can fail due to resonance, fatigue, or extreme tension (both maximum and minimum) in the tendons. In addition, TLPs are also designed to provide a sufficiently stable environment for offshore operations such as drilling and production of oil and comfortable living conditions for a crew.

Customarily, the structure is modeled first and the fluid force is added later. This is because the structure is easier to model than the fluid. The

fluid force is often modeled using empirical or semi-empirical equations, which require experimentally determined coefficients.

A rigid platform can undergo six kinds of motions, as shown in Figure 1.3: three translational and three rotations. The translational motions are surge, sway, and heave. The rotational motions are roll, pitch, and yaw. These terminologies are familiar to ship and aircraft designs. TLPs are designed such that the surge, sway, and yaw frequencies are below the wind and wave frequencies and the heave, pitch, and roll frequencies are above the wind and wave frequencies. Because the surge motion is usually large[1], TLPs are usually surrounded by a safety zone with a diameter of 500 m where other human activities such as fishing are restricted [20].

The equations of motion are nonlinear because the fluid damping force is nonlinear, the interaction between the fluid and the structure is nonlinear, and the geometry of the tendons is nonlinear when the motion is relatively large. The motion is likely to be large since the platform is designed to be compliant and the nonlinear wave forces at the low frequencies. The large surge displacement also affects the buoyancy provided by the hulls such that the tension in the tendons varies with time.

Certain assumptions are made in order to simplify the problem and yet must capture the fundamental characteristics of the dynamics of the TLP. Usually the tension leg platform is modeled either in two or three dimensions. The tendons can be modeled either as a massless spring, flexible cable or beam.

2.1 Single Degree of Freedom Models

The simplest model for a TLP is a single degree of freedom (SDOF) model. The equation of motion takes the form of

$$m\ddot{x}(t) + c\dot{x}(t) + kx(t) = f(x(t), \dot{x}(t), \ddot{x}(t), t), \tag{1.1}$$

where x can be one of the three displacements or three angles[2], m is the mass or mass moment of inertia, c is the structural damping coefficient, k is the stiffness coefficient, and $f(x, \dot{x}, \ddot{x}, t)$ is the fluid-induced forcing function. Such a SDOF a model is shown in Figure 1.4(b), where $x(t)$ represents the surge motion. The mass of the deck and tendons are lumped at the top[3].

[1] The slow oscillation is called the wave draft oscillation, which occurs due to the second order wave forces.

[2] Each degree of freedom can be treated individually and independently.

[3] See Wilson [81], Examples 2.1 and 2.5, for details.

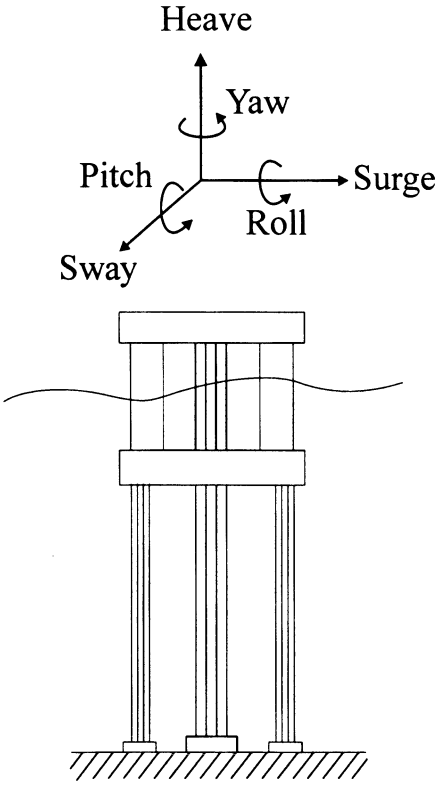

Figure 1.3. Rigid Body Motion of the Deck

The force $f(x, \dot{x}, \ddot{x}, t)$ is most likely random with a power spectral density function obtained from experimental data. The response $x(t)$ can be found in the time domain or in the frequency domain.

The SDOF model for the structure is often used when it is necessary to simplify the structure as much as possible in order to capture the nonlinear interactions between the structure and the fluid. For example, the Dowell model [22] for vortex-induced vibration suggests the motion of a cylinder in a flow is governed by the following equations:

$$\begin{aligned} m\ddot{x} + c\dot{x} + kx &= \tfrac{1}{2}\rho u^2 D C_L \\ \ddot{C}_L + \omega_s^2 C_L &= f(x, \dot{x}), \end{aligned} \tag{1.2}$$

where D is the diameter of the cylinder and C_L is the lift coefficient as shown in Figure 1.5. The motion of the structure is coupled with the time-dependent lift coefficient.

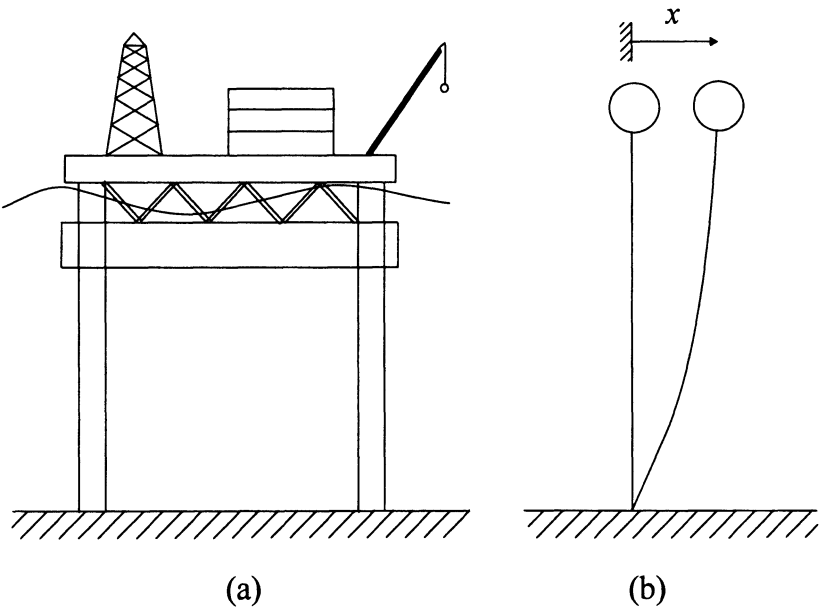

Figure 1.4. Single Degree of Freedom Model

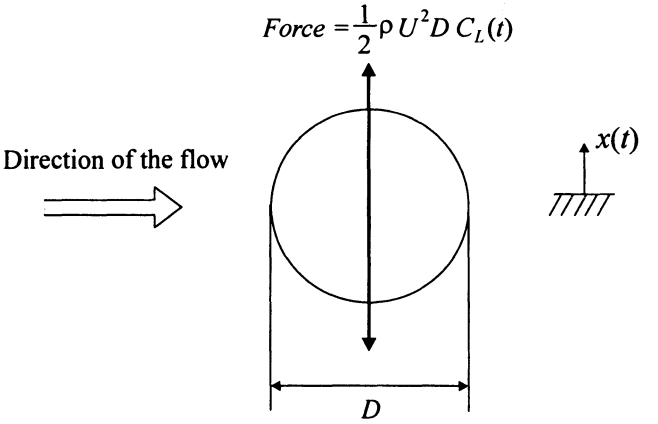

Figure 1.5. Dowell Model

2.2 Six Degree of Freedom Model

The majority of studies of dynamic behavior of the tension leg platform are performed in two dimensions, incorporating three degrees of freedom at the most. The six degree of freedom models are used frequently for floating structures. Mulk and Falzarano [56] investigated

the six degree of freedom model for a ship. The platform of a TLP can also be modeled using a six degree of freedom model. The fundamental difference between the ship and platform dynamics is that a platform is connected to the ocean floor by tendons, which also can deflect and deform. Therefore, the motion of the tendons should also be taken into account. Six degree of freedom models for offshore platforms often treat tendons as a massless spring or springs. Early investigators of six degree of freedom models are Natvig and Pendered [58], Morgan and Malaeb [53], and Kareem and Li [35][36].

Recently, Jain [33] studied the deterministic response of a tension leg platform. The analysis includes varying tension in the tendons due to change in location. The equation of motion takes the form

$$[M]\left\{\ddot{X}\right\} + [C]\left\{\dot{X}\right\} + [K]\{X\} = \left\{F\left(\{X\}, \left\{\dot{X}\right\}, \left\{\ddot{X}\right\}, t\right)\right\}, \quad (1.3)$$

where $\{X\}$ represents the six degrees (surge, sway, heave, roll, pitch, and yaw), $[M]$ is the diagonal mass matrix, $[C]$ is the proportional structural damping matrix, $[K]$ is the stiffness matrix, and $\{F\}$ is the force vector due to regular waves and derived from the Morison equation and Airy wave theory. The effect of tendons is included in the stiffness matrix. The study concludes that surge, sway, and yaw are unlikely to be significant because their natural frequencies are well below the frequencies of waves or wind. They also saw that the tension in the tendons can be large due to resonance in the heave motion since its natural frequencies are close to frequently occurring wave frequencies.

Ahmad et al. [5] studied a similar six degree of freedom model for the platform. Long-crested random wave and wind forces are incorporated in this analysis. The Pierson-Moskowitz spectrum is used for the random wave height and Simiu's spectrum is used for the random wind. They found that the magnitude of the wind force and the location of the aerodynamic center significantly influence the surge and yaw responses. They also found that the coupling between the degrees of freedom substantially enhance the heave response.

A more complicated model may treat the tendons as flexible cables or beams instead of massless springs. The tendons will most likely assume a curved position in static equilibrium due to ocean forces (uniform current) as shown in Figure 1.6. The horizontal displacement of the platform is called 'offset,' and the vertical displacement is called 'setdown.' The presence of offset and setdown affect the dynamics of a TLP since the tendon loads increase due to the increased buoyancy associated with hull setdown.

In order to incorporate this catenary behavior of tendons or risers, Oran [60] modeled each tendon or riser as a three-dimensional cable with

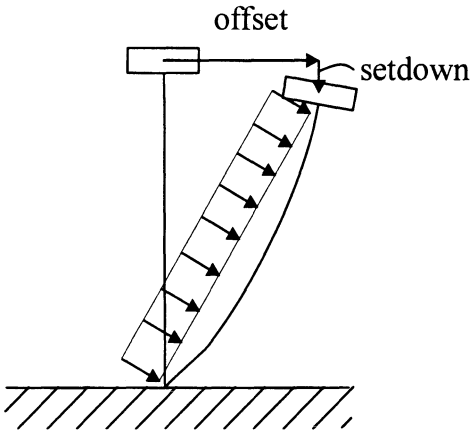

Figure 1.6. Equilibrium Position

small oscillations about a large static offset position. The equations of motion of the platform are given in terms of the six degrees of freedom. The stiffness matrix is obtained by taking the hydrodynamic forces and gravity on the cables into account. It was found that the periods of surge, sway, and yaw motion decrease when compared to other six degree of freedom models with massless springs. It was also found that the coupling between modes increases as the static offset increases.

2.3 Rigid and Elastic Models for Tendons

When the tendons are modeled as cables or beams, most studies are done in two dimensions due to the complexity of three-dimensional modeling of a flexible structure. In these two-dimensional models, only three degrees of freedom for the platform can be monitored. Namely, they are heave, surge, and pitch if the motion is confined in the xy plane in Figure 1.3. Adrezin et al. [2] list works that model the tendons as cables or flexible beams. The studies differ in the degree of nonlinearity, boundary conditions, and fluid forcing models.

Mekha [48] modeled the tendons as elastic springs and flexible beams. The motion is assumed planar. They showed that a simple elastic spring model with constant lateral stiffness is satisfactory for computing the surge amplitude, but not for computing the offset and the hull setdown. They found that the mean surge response (offset) and the hull setdown are significantly affected by the hydrodynamic forces on the tendons.

Adrezin and Benaroya [3][4] examined the nonlinear transverse behavior of a tension leg platform with time dependent tension due to gravity

and buoyancy. They found that the inclusion of hydrodynamic forces on tendons will result in greater surge amplitude and offset position.

So far, most elastic models are planar models so that only forces in one plane can be included. However, the vibration of an offshore structure in an ocean environment is inherently a three-dimensional phenomenon since the fluid load is three-dimensional. When the dynamic response of an offshore compliant tower in an ocean environment is considered in three dimensions, the vertical member of the tower is modeled as either rigid or elastic.

The three-dimensional behavior of the rigid model has been studied by Jain and Kirk [34] and Bar-Avi and Benaroya [9]. The former used two rigid beams in order to model a double articulated offshore structure, and the latter used one rigid beam for a single articulated offshore structure. In their derivations, spherical coordinates are used to describe the motion of the beam. Jain and Kirk showed that if the waves and the current are collinear, the response is two-dimensional, but if the fluid motions are not collinear, the response is a three-dimensional whirling oscillation.

Leonard and Young [40] and Takahashi and Konish [74][75] studied the dynamics of three-dimensional flexible cables. Leonard and Young developed a three-dimensional finite element method for the response of compliant towers such as articulated towers, guyed towers, tension leg platforms, and floating production facilities. The tendons are modeled as three-dimensional cables, and their model includes coupling between the columns and the tendons. They observed behaviors similar to those observed by Jain and Kirk.

Takahashi and Konish studied nonlinear three-dimensional vibration of both horizontal and inclined cables. The cables are hanging between two fixed points. In their study of free vibration, they found that the geometrical nonlinearity may be the stiffening type or the softening type depending on the sag to span ratio. They also monitored out-of-plane vibration when the in-plane sinusoidal load is applied.

3. Outline

In this monograph, a vertical member such as a shaft of an articulated tower or one leg of a tension leg platform is modeled as a beam with a linear-elastic torsional spring at its base and a concentrated mass at its free end as shown in Figure 1.7. The torsional spring simulates the various support conditions from hinged to clamped by varying the spring constant from zero to infinity. The point mass represents the mass of the platform including structures supported by the shaft or tendons.

The vertical member of a compliant tower is modeled in three different ways. The first is the linear transverse model, the second is the coupled

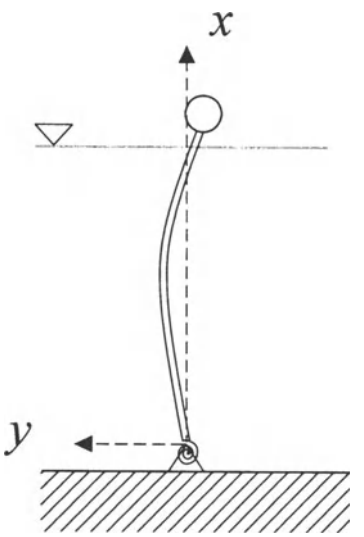

Figure 1.7. A Beam Supported by a Torsional Spring

transverse and axial model, and the third is the three-dimensional model. The first two are two-dimensional models which assume that the beam moves only in the plane of Figure 1.7. The linear transverse model only takes the transverse displacement into account, the coupled transverse and axial model accounts for both the transverse and axial displacements, and the three-dimensional model accounts for two transverse and one axial displacement. The difference between the first two models is shown in Figure 1.8. In the linear transverse model, a beam element can move in the y direction only while the location in the x direction stays fixed. In the coupled transverse and axial model, a beam element can move in both the y and x directions. Similarly, in the three-dimensional model, a beam element can move in all three directions.

Chapter 2 is a review of variational methods, that is, the principle of virtual work, D'Alembert's principle, Lagrange's equation, Hamilton's principle, and the extended Hamilton's principle. These variational methods are essential for the derivation of the equations of motion and boundary conditions for the beam models considered in this monograph. It is recommended that the reader reviews this chapter if he or she is not familiar with these methods.

Chapter 3 is devoted to the development and complete solution of various linear transverse beam models including the Euler-Bernoulli, Rayleigh, shear, and Timoshenko theories. The equation of motion for each model is derived using the extended Hamilton's principle and solved

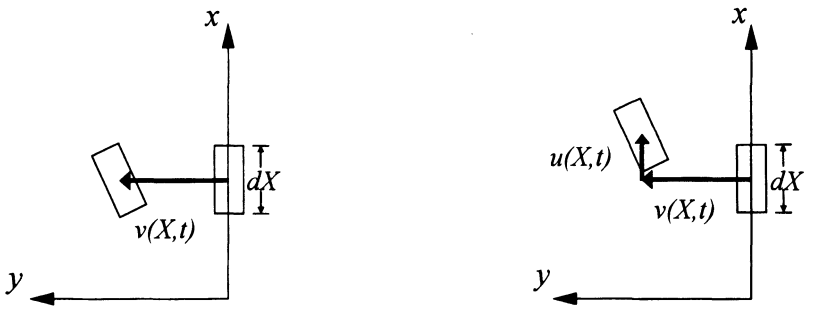

(a) Transverse Model

(b) Coupled Transverse and Axial Model in 2D

Figure 1.8. Two Dimensional Models

analytically. The frequency equations are solved in terms of normalized wave numbers for four sets of boundary conditions. The normalized wave numbers for each set of boundary conditions are tabulated or plotted as a function of a geometric parameter, namely the slenderness ratio (the ratio of length to the radius of gyration of the cross-sectional area). The normalized wave numbers for the remaining six sets of boundary conditions are deduced from the previous four sets using symmetric and antisymmetric mode analysis. The orthogonality conditions that the modes satisfy are given for each beam theory. Sample responses to an external transverse force are obtained for each model using the method of eigenfunction expansion. It is shown that as the slenderness ratio increases, the differences among the theories magnifies.

Since we are considering an offshore structure in an ocean, we need to use a realistic fluid forcing function. Chapter 4 is devoted to the modeling of the current and random wave forces that an offshore structure may encounter in an ocean environment. Fluid flowing in one direction around a structure can exert a three-dimensional force on the structure. Figure 1.9 shows the force on the plane which is defined by the direction of the flow and the structure, and which is in the direction perpendicular to the structure. This *in-plane* force is modeled using the Morison equation, which is composed of three components: inertia, drag, and added mass. The random waves used here are characterized by the Pierson-Moskowitz power spectrum and converted into the time domain using the Borgman method.

The coupled transverse and axial model is derived in Chapter 5. Kirchhoff's hypothesis is used to obtain the displacement field. The equations of motion and boundary conditions are derived assuming that

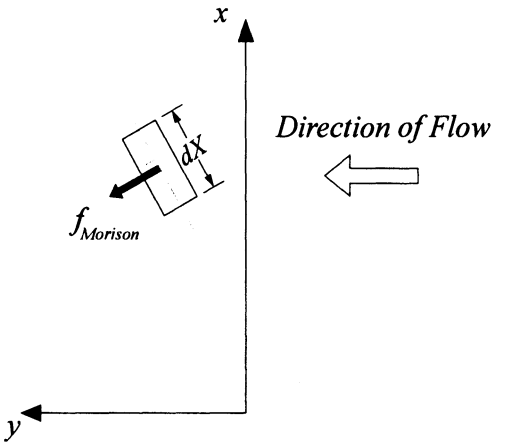

Figure 1.9. In-plane Fluid Force

the strain is small but the rotation can be moderate. Therefore, this model allows a wider range of motion than the linear transverse models in Chapter 3. The equations of motion are nonlinear, so that they can only be solved numerically. Sections 3 and 4 include numerical results for the free response, the damped-free response in still water, the forced response to a deterministic transverse force, and to the random fluid force modeled by the Morison equation in Chapter 4. The deterministic loading is harmonic in time. In obtaining the free and forced responses, a finite difference approach was taken.

The vibration of an offshore structure in an ocean environment is inherently a three-dimensional phenomenon since the force acting on structure is three-dimensional. In Chapter 6, the three-dimensional rigid model is initially investigated. The three-dimensional study is expanded further in this monograph to include a three-dimensional elastic model. Kirchhoff's hypothesis for the displacement field is used, and the equations of motion are derived assuming that the strain is small but the rotation can be moderate. Numerical solutions for free and forced vibrations are obtained using the finite difference method. The solutions are in terms of displacements in the x, y, and z directions. The numerical results for the rigid and elastic models are then compared.

Concluding comments and a summary of this monograph are given in Chapter 7.

Chapter 2

PRINCIPLE OF VIRTUAL WORK, LAGRANGE'S EQUATION AND HAMILTON'S PRINCIPLE

1. Introduction

This chapter presents several of the most important concepts from analytical dynamics. The most important of these concepts to us is Lagrange's equation and how it can be used for the derivation of governing equations of motion. The equation is especially useful for the derivation of the equations of motion for systems, discrete or continuous, with more than one degree of freedom, where the Newtonian free body diagrams become more difficult to apply. We will also derive Hamilton's principle, an integral energy formulation, also applicable to both discrete and continuous systems, and see how it is connected to Lagrange's equation.

The subject of this chapter is based on the principle of virtual work, which is the foundation for the subsequent principles we are about to develop and discuss. There are many advantages to the analytical approach of Lagrange and Hamilton over Newton's force analysis. This is especially true for systems of interacting bodies, where each exerts a force on the other and where constraints, such as boundaries, also exert forces on the system, limiting motion. Such auxiliary conditions can be more easily handled using the analytical approach.

The analytical approaches are based on variational principles, which are the unifying basis of the equations that follow. The term variational is from the calculus of variations, the foundation for such techniques. An important advantage of the analytical method is that the equations of motion are coordinate–independent, which, of course, Newton's second law of motion is not.

The essential ideas of the variational approach are briefly described next before we go on to the details of the math. We will work with a

S. M. Han et al., *Nonlinear and Stochastic Dynamics of Compliant Offshore Structures*

variety of energy functions when we begin to apply the analytical method to specific physical problems. To motivate and explain the procedure, let us first look at a very simple function: $y = f(x)$. This could represent a displacement that is a function of position on a body. Our purpose in the variational approach is to demonstrate that a stationary (maximum or, most likely, minimum) value exists for $f(x)$. This is accomplished by comparing the function $f(x)$ with a slightly modified function $f_\epsilon(x) = f(x) + \epsilon\phi(x)$, where ϵ can be as small as necessary, including zero, and ϕ must be continuous and differentiable. Then, for any particular value of the independent variable x, we can compare the difference or variation,

$$\delta y \equiv f_\epsilon(x) - f(x) = \epsilon\phi(x). \tag{2.1}$$

There are two fundamental points to be emphasized here: (i) the variation is arbitrary or virtual, and (ii) it is an infinitesimal change since ϵ can be made arbitrarily small. Note that while both δy and dy represent infinitesimal changes in the function $f(x)$, dy refers to a change in $f(x)$ caused by an infinitesimal change of the independent variable dx, while δy is an infinitesimal change of y that results in a new function $y + \delta y$.

This process of variation is for each fixed value of x. Thus, x is not varied, meaning that $\delta x = 0$, and the two end points of this function are prescribed and therefore also not varied. The variation is between definite limits. When we work with time as the independent variable, the beginning and ending times are prescribed and therefore not varied.

As we will discover below, in applying the variational procedures to a particular system, in addition to finding the governing the equation of motion, we will also automatically find the necessary number of boundary conditions. The stationary value conditions imposed by the variational principles result in both the differential equations and the boundary conditions.

Before proceeding with the details of the analytical techniques, it is useful to summarize the key topics to be examined in this chapter:

- We will learn about the principle of virtual work and its relation to the equilibrium of a body.

- We will then extend the principle of virtual work, with d'Alembert's principle, to include dynamic systems.

- Lagrange's equation and Hamilton's variational principle will be derived from d'Alembert's principle, and will be applied to a beam dynamic problem.

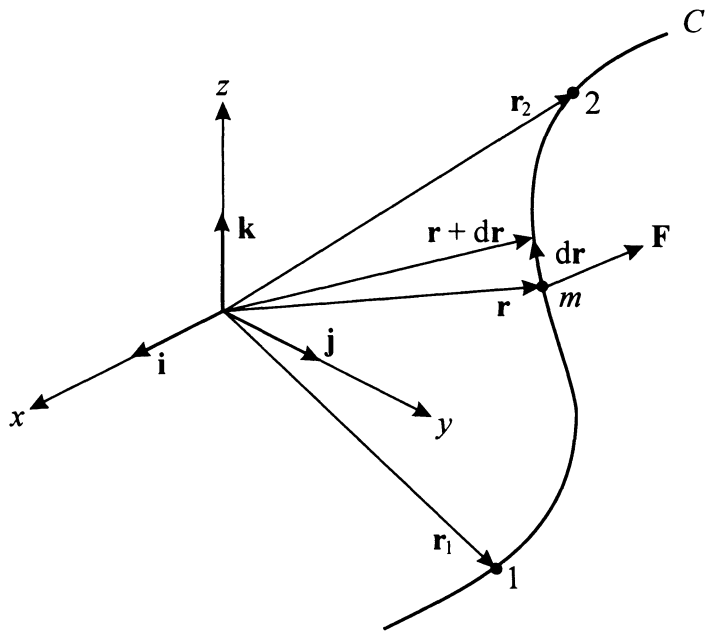

Figure 2.1. Path of Mass m Due to Force $\mathbf{F}$

2. Virtual Work

The principle of virtual work is the basis for the remainder of this chapter and also forms the foundation for the variational principles of mechanics. Some of the most powerful computational models are based on a variational approach. Let us review the concepts of work and energy before proceeding to virtual work. Consider a particle of mass m moving along a curve C under the action of a force $\mathbf{F}$ as shown in Figure 2.1. In this chapter, we follow the custom in dynamics of showing vectors as **bold face** variables.

The position of the particle with respect to an origin O is given by the vector $\mathbf{r}$, which is a function of time. The work necessary to move the mass a distance $d\mathbf{r}$ *is* $dW = \mathbf{F} \cdot d\mathbf{r}$. The dot product physically indicates the product of the projection of the force in the direction of $d\mathbf{r}$. The work done to move the particle from position $\mathbf{r}_1$ to position $\mathbf{r}_2$ is

$$W_{12} = \int_{\mathbf{r}_1}^{\mathbf{r}_2} \mathbf{F} \cdot d\mathbf{r}. \tag{2.2}$$

Assuming the mass of the particle to be constant, Newton's second law of motion relates force $\mathbf{F}$ to the acceleration of the particle,

$$F = m\frac{d\dot{\mathbf{r}}}{dt} = m\frac{d}{dt}\left(\frac{d\mathbf{r}}{dt}\right). \tag{2.3}$$

Our purpose here is to connect force, work, and energy. Using $d\mathbf{r} = \dot{\mathbf{r}}dt$, and the above equations, we have

$$\begin{aligned} W_{12} &= \int_{t_1}^{t_2} m\frac{d\dot{\mathbf{r}}}{dt}\cdot\dot{\mathbf{r}}\,dt \\ &= \frac{1}{2}\int_{t_1}^{t_2} m\frac{d}{dt}\left(\dot{\mathbf{r}}\cdot\dot{\mathbf{r}}\right)dt \\ &= \frac{1}{2}m\left[(\dot{\mathbf{r}}_2\cdot\dot{\mathbf{r}}_2) - (\dot{\mathbf{r}}_1\cdot\dot{\mathbf{r}}_1)\right] \\ &= \frac{1}{2}m\left(\dot{\mathbf{r}}_2^2 - \dot{\mathbf{r}}_1^2\right) \\ &= T_2 - T_1, \end{aligned} \tag{2.4}$$

where the limits of integration have been transformed from $\mathbf{r}$ to t, and T is the kinetic energy of the mass, $T = m\dot{\mathbf{r}}\cdot\dot{\mathbf{r}}/2$. As expected, we started with a scalar, the work, and ended with a scalar, the change in kinetic energy.

Next, we need to relate the work done by the external force and the respective change in position of a mass. To do this, define a conservative force field as one where the work done depends only on the initial and the final positions of the particle and is independent of the (integration) path connecting these positions. (Non-conservative forces, such as friction and external forces, are energy–dissipating, and for these the work done is path–dependent.) An example of a conservative force field is gravity.

From Figure 2.2, we can select any path within the conservative force field which connects points 1 and 2, and the work done bringing the particle from 1 to 2 will be the same, and is denoted by

$$W_{12c} = \int_{\mathbf{r}_1}^{\mathbf{r}_2} \mathbf{F}\cdot d\mathbf{r}_{Path\ I} = \int_{\mathbf{r}_1}^{\mathbf{r}_2} \mathbf{F}\cdot d\mathbf{r}_{Path\ II}. \tag{2.5}$$

The potential energy $V(\mathbf{r}_1)$ is associated with position $\mathbf{r}_1$ and is defined as the work done in a conservative force field by moving a particle from position $\mathbf{r}_1$ to a reference position $\mathbf{r}_p$,

$$V(\mathbf{r}_1) = \int_{\mathbf{r}_1}^{\mathbf{r}_p} \mathbf{F}\cdot d\mathbf{r}. \tag{2.6}$$

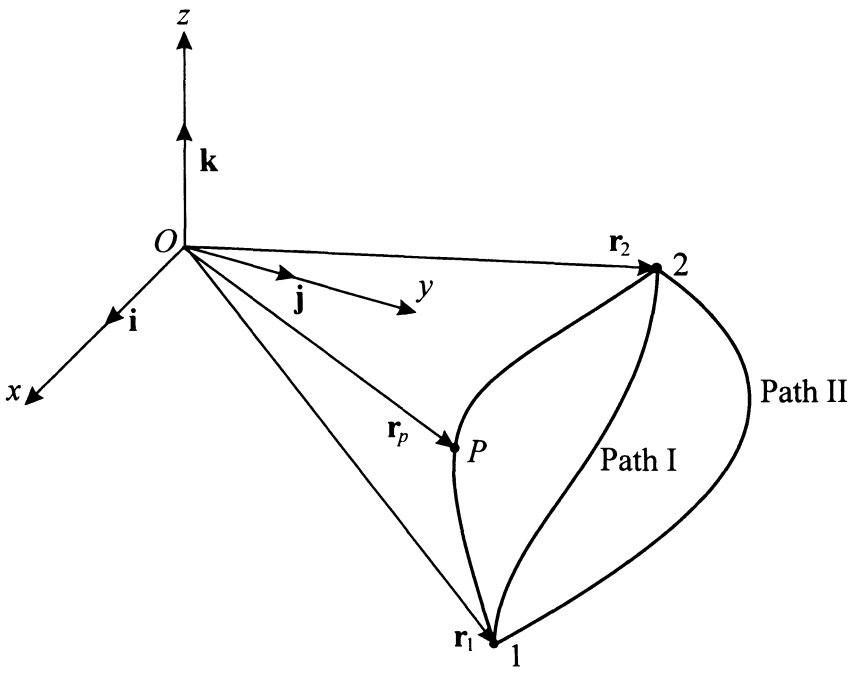

Figure 2.2. Path in a Conservative Force Field

We would like to relate the work done moving a particle in a conservative force field to the potential energy of the particle. To do this, consider again W_{12c} but choose the arbitrary path through reference position, then

$$W_{12c} = \int_{\mathbf{r}_1}^{\mathbf{r}_p} \mathbf{F}\cdot d\mathbf{r} + \int_{\mathbf{r}_p}^{\mathbf{r}_2} \mathbf{F}\cdot d\mathbf{r} = -\left(V_2 - V_1\right). \tag{2.7}$$

This equation tells us that work done in a conservative force field is the negative of the change in potential energy. Finally, if we denote W_{12nc} as the non-conservative work, then $W_{12nc} = E_2 - E_1$, where E denotes the total energy. Therefore, W_{12nc} is a measure of the change in particle energy, and if $W_{12nc} = 0$, then $E_2 = E_1$, that is, energy has been conserved.

2.1 The Principle of Virtual Work

The Principle of Virtual Work states that the work performed on a body in static equilibrium by the applied forces undergoing infinitesimal

virtual displacements compatible with the system constraints is zero,

$$\delta W = \sum_{i=1}^{N} \mathbf{F}_i \cdot d\mathbf{r}_i = 0. \tag{2.8}$$

A constraint is a physical barrier to free motion, for example, a wall, a string connecting two bodies, or a magnetic field. Equation 2.8 applies to static systems, or quasi–static systems where inertia effects can be ignored. The dynamic version of the principle of virtual work, known as d'Alembert's principle, is developed in the next section. These principles form the basis for the variational principles that follow.

Our formulation will be for a system of N particles moving in three dimensions. The results are applicable for discrete as well as continuous systems. We define virtual displacements in each of the three dimensions for each particle,

$$\delta x_i, \ \delta y_i, \ \delta z_i, \tag{2.9}$$

where $1 \leq i \leq N$. Virtual displacements may be interpreted as possible alternate configurations of the system of particles. These alternate configurations must be consistent with the system constraints. We consider the system at its initial configuration and at its alternate configuration due to the virtual displacement. Time is not a variable here since we are only examining the system in two possible configurations. Time will be soon considered with d'Alembert's principle.

Next, assume that the N particles are subject to resultant force $\mathcal{F}_i = \mathbf{F}_i + \mathbf{f}_i$, where $\mathbf{F}_i$ is an applied force, and $\mathbf{f}_i$ is a constraint force. For the system to be in static equilibrium, every particle is at rest, and $\mathcal{F}_i = 0$ in any possible configuration. For the alternate virtual displacement configuration, static equilibrium requires that $\mathcal{F}_i \cdot \delta\mathbf{r}_i = 0$.

Given virtual displacements, one can proceed to define virtual work as the product of a force and its corresponding virtual displacement. For the system in equilibrium, the virtual work for the entire system vanishes according to the relation

$$\begin{aligned} \delta W &= \sum_{i=1}^{N} \mathcal{F}_i \cdot \delta\mathbf{r}_i \ = \ 0 \\ &= \sum_{i=1}^{N} (\mathbf{F}_i + \mathbf{f}_i) \cdot \delta\mathbf{r}_i \ = \ 0. \end{aligned} \tag{2.10}$$

Before proceeding, consider the types of constraints to which a structure may be exposed. Likely examples include physical boundaries, in which case the boundary force is perpendicular to the motion of the body

and there is no work performed. It is possible that contact friction will do work in resisting a motion. Dissipative forces such as friction will be introduced later in this chapter when dynamic motion is added. Therefore, $\sum_{i=1}^{N} \mathbf{f}_i \cdot \delta \mathbf{r}_i = 0$. The remaining equation is given the name Principle of Virtual Work for a static system,

$$\delta W = \sum_{i=1}^{N} \mathbf{F}_i \cdot \delta \mathbf{r}_i = 0, \tag{2.11}$$

where $\mathbf{F}_i$ represents the external forces on the system. We next proceed with d'Alembert's Principle.

2.2 D'Alembert's Principle

D'Alembert's Principle extended the applicability of the principle of virtual work to dynamic problems. Newton's law of motion can be rewritten as d'Alembert's principle in the following form for N particles,

$$\mathbf{F}_i + \mathbf{f}_i - m_i \ddot{\mathbf{r}}_i = 0, \quad i = 1, 2, \ldots, N. \tag{2.12}$$

The term $-m_i \ddot{\mathbf{r}}_i$ may be considered to be an inertia force. Each force in Equation 2.12 may be a constant or a function of time. The virtual work for the i^{th} particle is

$$(\mathbf{F}_i + \mathbf{f}_i - m_i \ddot{\mathbf{r}}_i) \cdot \delta \mathbf{r}_i = 0, \tag{2.13}$$

where the virtual displacements δr_i are compatible with the constraints. Assuming virtual work due to constraint forces is zero, the virtual work for the system is

$$\sum_{i=1}^{N} (\mathbf{F}_i - m_i \ddot{\mathbf{r}}_i) \cdot \delta \mathbf{r}_i = 0, \tag{2.14}$$

where this is called the generalized principle of d'Alembert. $(F_i - m_i \ddot{\mathbf{r}}_i)$ is sometimes called the effective force. D'Alembert's principle will be used in the next section to derive Lagrange's equation.

> "The importance of d'Alembert's principle lies in the fact that it is more than a reformulation of Newton's equation. It is the expression of a principle. We know that the vanishing of a force in Newtonian mechanics means equilibrium. Hence, Equation 2.12 says that the addition of the force of inertia to the other forces produces equilibrium. But this means that if we have any criterion for the equilibrium of a mechanical system, we can immediately extend that criterion to a system which is in motion. All we have to do is add the new 'force of inertia' to the previous forces. By this device dynamics is reduced to statics [39]."

The linking of Newton's second law of motion with the principle of virtual work clarifies that the principle is equally applicable to masses at rest and to masses in motion. The virtual displacement involves a possible but purely mathematical experiment that can be applied at any specific time. At that instant, the actual motion of the body does not enter into account and the dynamic problem is reduced to a static one.

3. Lagrange's Equation

Lagrange's equation provides a general formulation for the equations of motion of a dynamical system. The behavior of the system may be linear or nonlinear, and the advantage of the method becomes evident for multi–degree of freedom systems. In addition, this approach is based on the energies of the system, the kinetic, potential, and strain energies. Therefore, it is not necessary to invoke the vectorial approach in applying Lagrange's equation as one must with Newton's second law of motion.

The equations derived below are written in terms of the generalized coordinates q_k. The physical coordinates, r_i, of an n degree of freedom system for N particles can be related to the generalized coordinates by an appropriate set of equations,

$$\mathbf{r}_i = \mathbf{r}_i(q_1, q_2, \ldots, q_n), \quad i = 1, 2, \ldots, N. \tag{2.15}$$

The purpose of these transformations from physical coordinates, which are vectorial, to generalized coordinates, which are not, is to recast the vectorial d'Alembert's principle into the energy-based expression known as Lagrange's equation.

In the following derivations, d'Alembert's generalized principle is expanded and rewritten in terms of potential and kinetic energies, all in terms of the generalized coordinates. First, we derive the relations between physical and generalized coordinates.

The total derivative of Equation 2.15 is

$$\dot{\mathbf{r}}_i = \sum_{k=1}^{n} \frac{\partial \mathbf{r}_i}{\partial q_k} \dot{q}_k, \qquad i = 1, 2, ..., N. \tag{2.16}$$

Note that variations $\delta \mathbf{r}_i$ follow the same rules as differentials $d\mathbf{r}_i$ such that

$$\delta \mathbf{r}_i = \sum_{k=1}^{n} \frac{\partial \mathbf{r}_i}{\partial q_k} \delta q_k. \tag{2.17}$$

We can then differentiate these equations with respect to $\dot{q}_k$

Then, considering the second term from d'Alembert's principle in Equation 2.14, we have

$$\begin{aligned}
\sum_{i=1}^{N} m_i \ddot{\mathbf{r}}_i \cdot \delta \mathbf{r}_i &= \sum_{i=1}^{N} m_i \ddot{\mathbf{r}}_i \cdot \left(\frac{\partial \mathbf{r}_i}{\partial q_k} \delta q_k \right) \\
&= \sum_{k=1}^{n} \left(\sum_{i=1}^{N} m_i \ddot{\mathbf{r}}_i \cdot \frac{\partial \mathbf{r}_i}{\partial q_k} \right) \delta q_k \\
&= \sum_{k=1}^{n} \left(\frac{d}{dt} \left(m_i \dot{\mathbf{r}}_i \cdot \frac{\partial \mathbf{r}_i}{\partial q_k} \right) - m_i \dot{\mathbf{r}}_i \cdot \frac{\partial \dot{\mathbf{r}}_i}{\partial q_k} \right) \delta q_k \\
&= \sum_{k=1}^{n} \left[\frac{d}{dt} \left(\frac{\partial}{\partial \dot{q}_k} \right) - \frac{\partial}{\partial q_k} \right] \left(\frac{1}{2} m_i \dot{\mathbf{r}}_i \cdot \dot{\mathbf{r}}_i \right) \delta q_k \\
&= \sum_{k=1}^{n} \left[\frac{d}{dt} \left(\frac{\partial T}{\partial \dot{q}_k} \right) - \frac{\partial T}{\partial q_k} \right] \delta q_k. \qquad (2.18)
\end{aligned}$$

The other term in d'Alembert's principle is the virtual work $\delta W = \sum_{i=1}^{N} \mathbf{F}_i \cdot \delta \mathbf{r}_i$, and so d'Alembert's equation can be written as

$$\sum_{k=1}^{n} \left[\frac{d}{dt} \left(\frac{\partial T}{\partial \dot{q}_k} \right) - \frac{\partial T}{\partial q_k} \right] \delta q_k = \delta W. \qquad (2.19)$$

The virtual work can be written in terms of the generalized coordinates by using generalized forces Q_k,

$$\delta W = \sum_{k=1}^{n} Q_k \delta q_k. \qquad (2.20)$$

We can further specialize d'Alembert's equation on our way to Lagrange's equation by separately considering the conservative and nonconservative forces acting on the system. From Equation 2.20, $\delta W = \delta W_c + \delta W_{nc}$. We know that work in a conservative vector field equals the negative of the change in potential, δV. The virtual work of nonconservative generalized forces Q_{knc} undergoing virtual displacements δq_k is given by $\sum_{k=1}^{n} Q_{knc} \delta q_k$. Therefore,

$$\delta W = -\sum_{i=1}^{n} \frac{\partial V}{\partial q_i} \delta q_i + \sum_{k=1}^{n} Q_{knc} \delta q_k. \qquad (2.21)$$

D'Alembert's generalized principle 2.19 becomes

$$\sum_{k=1}^{n} \left[\frac{d}{dt} \left(\frac{\partial T}{\partial \dot{q}_k} \right) - \frac{\partial T}{\partial q_k} + \frac{\partial V}{\partial q_k} - Q_{knc} \right] \delta q_k = 0. \qquad (2.22)$$

Since the virtual displacements δq_k are arbitrary, the sum of the terms in the square brackets must be equal to zero for each index. Therefore,

$$\frac{d}{dt}\left(\frac{\partial T}{\partial \dot{q}_k}\right) - \frac{\partial T}{\partial q_k} + \frac{\partial V}{\partial q_k} = Q_k, \qquad k = 1, 2, ..., n. \tag{2.23}$$

Q_k includes dissipative forces such as damping and external forces. These are Lagrange's equations of motion, one equation for each of the generalized degrees of freedom. It is customary to define the Lagrangian function as $L = T - V$. Since potential energy V is a function of position only, it cannot vary with velocity, and thus, Equation 2.23 becomes

$$\frac{d}{dt}\left(\frac{\partial L}{\partial \dot{q}_k}\right) - \frac{\partial L}{\partial q_k} = Q_k, \qquad k = 1, 2, ..., n. \tag{2.24}$$

There are several key advantages to Lagrange's equation:

- Lagrange's equation contains only scalar quantities, eliminating the force and acceleration vectors inherent in Newton's second law of motion.
- There is one Lagrange's equation for each degree of freedom, whereas the use of free body diagrams in Newton's formulation leads to extraneous equations resulting from the internal forces between bodies that are attached to each other. Via Newton's approach, such internal forces have to be eliminated after the equations of motion are derived. Of course, in some applications, we need to find these internal forces.
- Lagrange's equation is independent of the coordinate system since the scalar energy functions T and V do not depend on coordinates.

3.1 Lagrange's Equation for Small Oscillations

We have learned that Lagrange's equation can be utilized to derive the fully nonlinear equations of motion for a dynamic system. But in many applications, vibrations are essentially linear. Therefore, it is of interest to examine how Lagrange's equation simplifies for small amplitude oscillations.

Expand the expression for the potential energy $V(q_1, q_2, \ldots, q_n)$ in an n-variable Taylor series about an arbitrary equilibrium reference position $V(0, 0, \ldots, 0)$,

$$V(q_1, q_2, \ldots, q_n) = \frac{1}{2}\left(\frac{\partial^2 V}{\partial q_1^2} q_1^2 + \frac{\partial^2 V}{\partial q_2^2} q_2^2 + \cdots + 2\frac{\partial^2 V}{\partial q_1 \partial q_2} q_1 q_2 + \cdots\right) + \cdots . \tag{2.25}$$

We have made use of the fact that $V(0,0,\ldots,0) = 0$ and $\partial V/\partial q_i = 0$ in the equilibrium position. For small amplitudes, q_i to powers two and higher can be ignored, leaving

$$V \approx \frac{1}{2}\sum_{i=1}^{n}\sum_{j=1}^{n}\frac{\partial^2 V}{\partial q_i \partial q_j}q_i q_j = \frac{1}{2}\sum_{i=1}^{n}\sum_{j=1}^{n}k_{ij}q_i q_j, \tag{2.26}$$

where k_{ij} are known as the stiffness coefficients. The kinetic energy is given by

$$T = \frac{1}{2}\sum_{i=1}^{n}\sum_{j=1}^{n}m_{ij}\dot{q}_i\dot{q}_j. \tag{2.27}$$

Substituting the above expressions into Lagrange's equation leads to the following n coupled equations of motion,

$$[m]\{\ddot{q}\} + [k]\{q\} = \{0\}. \tag{2.28}$$

This is a matrix equation of motion, to be solved using matrix numerical techniques.

4. Hamilton's Principle

We now offer an alternate approach to the derivation of Lagrange's equation. Along the way we derive Hamilton's principle, a very powerful integral variational statement. Begin with the left hand side of Equation 2.18, and rewrite this term as follows,

$$\begin{aligned}\sum_{i=1}^{N}m_i\ddot{\mathbf{r}}_i\cdot\delta r_i &= \sum_{i=1}^{N}m_i\frac{d}{dt}\left(\dot{\mathbf{r}}_i\cdot\delta\mathbf{r}_i\right) - \delta\sum_{i=1}^{N}\frac{1}{2}m_i\left(\dot{\mathbf{r}}_i\cdot\dot{\mathbf{r}}_i\right)\\ &= \sum_{i=1}^{N}m_i\frac{d}{dt}\left(\dot{\mathbf{r}}_i\cdot\delta\mathbf{r}_i\right) - \delta T.\end{aligned} \tag{2.29}$$

Substitute this equation and the principle of virtual work into d'Alembert's principle to find

$$\delta T + \delta W = \sum_{i=1}^{N}m_i\frac{d}{dt}\left(\dot{\mathbf{r}}_i\cdot\delta\mathbf{r}_i\right). \tag{2.30}$$

Consider a varied path, as shown in Figure 2.3, where the paths coincide at the initial and final times, and integrate between t_1 and t_2,

$$\begin{aligned}\int_{t_1}^{t_2} (\delta T + \delta W)\, dt &= \int_{t_1}^{t_2} \sum_{i=1}^{N} m_i \frac{d}{dt} (\dot{\mathbf{r}}_i \cdot \delta \mathbf{r}_i)\, dt \\ &= \sum_{i=1}^{N} \int_{t_1}^{t_2} m_i \frac{d}{dt} (\dot{\mathbf{r}}_i \cdot \delta \mathbf{r}_i)\, dt \\ &= \sum_{i=1}^{N} m_i \dot{\mathbf{r}}_i \cdot \delta \mathbf{r}_i \Big|_{t_t}^{t_2} = 0, \end{aligned} \tag{2.31}$$

where by our previous discussion the variations at the end times equals zero. Therefore,

$$\int_{t_1}^{t_2} (\delta T + \delta W)\, dt = 0, \tag{2.32}$$

is called the extended Hamilton's principle. If the forces are only conservative, $\delta W = -\delta V$, and then

$$\delta \int_{t_1}^{t_2} (T - V)\, dt = 0. \tag{2.33}$$

This equation may be physically interpreted as nature trying to equalize the kinetic and potential energies of a system, in absence of nonconservative forces. It is also possible to derive Lagrange's equation from Hamilton's principle.

5. Lagrange's Equation with Damping

Prior to this section, damping was not formally considered in the variational formulation. Here, the inclusion of damping is examined. There are many types of damping, and the particular application will determine which is most suitable. For example, viscous damping is proportional to the first power of the speed and opposite in direction to its motion. This form of damping is adequate if the speed is "not too great". At higher speed, the damping may be proportional to the speed taken to a power greater than one.

For viscous drag, there is a special form for the generalized force,

$$Q_D = -\frac{\partial R}{\partial \dot{q}} \tag{2.34}$$

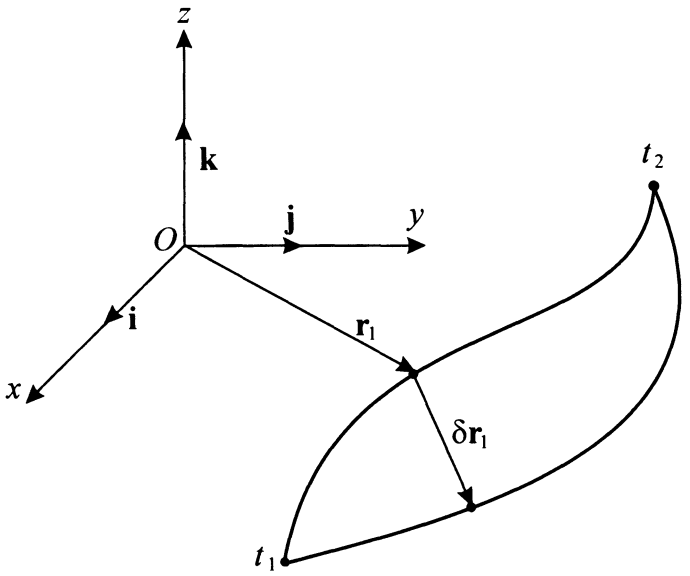

Figure 2.3. Path and Varied Path for Hamilton's Principle

for each generalized coordinate, where R is known as the Rayleigh dissipation function and is given by

$$R = \frac{1}{2}\sum_k \sum_l c_{kl}\dot{q}_k\dot{q}_l, \tag{2.35}$$

where the c_{kl} are damping coefficients. For the k^{th} generalized coordinate then,

$$Q_{D_k} = -\frac{\partial R}{\partial \dot{q}_k} = -\sum_l c_{kl}\dot{q}_l, \tag{2.36}$$

with the resulting Lagrange's equation,

$$\frac{d}{dt}\left(\frac{\partial T}{\partial \dot{q}_k}\right) - \frac{\partial T}{\partial q_k} + \frac{\partial V}{\partial q_k} + \frac{\partial R}{\partial \dot{q}_k} = Q_k \qquad k = 1, 2, \ldots, n. \tag{2.37}$$

6. Application to Longitudinally Vibrating Beams

We will derive the equation of motion first using a free body diagram and Newton's second law of motion. Then we will do the same using Hamilton's principle.

Consider the schematic of the beam in Figure 2.4 (a). Displacements, strains, and stresses are assumed uniform at a given cross section. Newton's second law of motion is a statement of the force balance for any

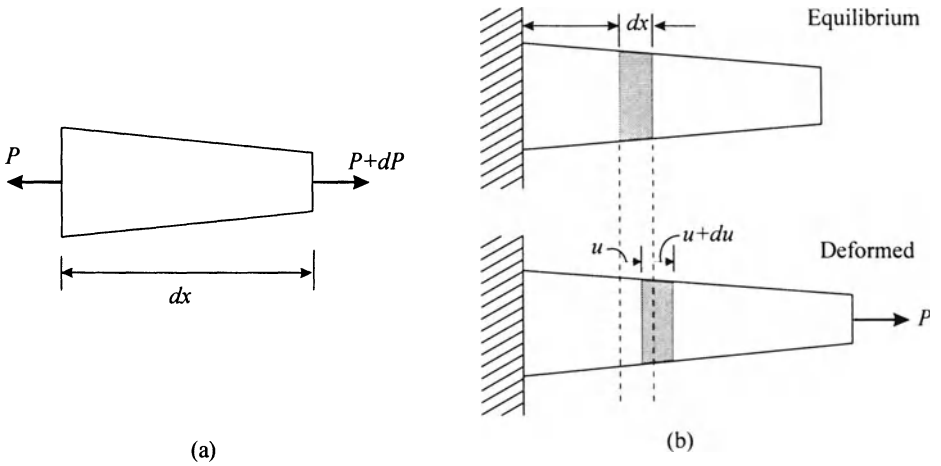

Figure 2.4. Schematic for the Longitudinal Vibration of a Beam

free body element of the beam. From the figure, force P acts to the left and this force plus an undetermined increment dP acts to the right. Had this been a static problem, $dP = 0$ for static equilibrium. For the dynamic problem, the sum of the forces equals the product of mass and acceleration. Let the element have a mass per unit length of $m(x)$ (or alternatively $m(x) = \rho(x)A(x)$, where $\rho(x)$ is the density and $A(x)$ is the area of the cross section at x). Then, by Newton's second law of motion for an element of length dx,

$$(P + dP)(x,t) - P(x,t) = m(x)dx\frac{\partial^2 u(x,t)}{\partial t^2}. \tag{2.38}$$

Using relations from strength of materials,

$$\begin{aligned} dP(x,t) &= \frac{\partial P(x,t)}{\partial x}dx \\ &= \frac{\partial}{\partial x}\left(A(x)E\frac{\partial u(x,t)}{\partial x}\right)dx, \end{aligned} \tag{2.39}$$

and

$$\frac{\partial}{\partial x}\left(A(x)E\frac{\partial u(x,t)}{\partial x}\right) = m(x)\frac{\partial^2 u(x,t)}{\partial t^2}. \tag{2.40}$$

If the beam is uniform, then $m(x) = m = \rho A$ and the area A can be canceled from both sides of the equation, leading to the wave equation,

$$c^2\frac{\partial^2 u(x,t)}{\partial x^2} = \frac{\partial^2 u(x,t)}{\partial t^2}, \tag{2.41}$$

where $c^2 = E/\rho$ has units of speed squared.

We next use Hamilton's principle to derive the governing equation of motion for the longitudinal vibration of a beam where x is the direction of motion. Considering the deformed beam of Figure 2.4 (b), we see that in response to load $P(t)$, the change in length dx is

$$\Delta(dx) = \frac{\partial u}{\partial x} dx = \varepsilon dx, \tag{2.42}$$

where $u(x,t)$ is the axial displacement, and ε is the strain. We require expressions for the potential and kinetic energies.

The strain energy associated with this deformation is

$$dV(t) = \frac{1}{2} P(t) \Delta(dx) = \frac{1}{2} P(t) \varepsilon dx. \tag{2.43}$$

The axial stress at a particular location x is given by $\sigma(x,t) = P(t)/A(x)$ and by $\sigma(x,t) = E\varepsilon(x,t)$. The potential energy of deformation for the element is then

$$dV = \frac{1}{2} \frac{P^2}{EA} dx = \frac{1}{2} EA\varepsilon^2 dx. \tag{2.44}$$

For the whole beam, the potential energy is

$$\begin{aligned} V(t) &= \frac{1}{2} \int_0^L \frac{P(t)^2}{EA(x)} dx = \frac{1}{2} \int_0^L EA(x) \varepsilon^2(x,t) dx \\ &= \frac{1}{2} \int_0^L EA(x) \left(\frac{\partial u}{\partial x} \right)^2 dx, \end{aligned} \tag{2.45}$$

where $EA(x)$ is the longitudinal stiffness.

The kinetic energy is given by

$$T(t) = \frac{1}{2} \int_0^L m(x) \left(\frac{\partial u}{\partial t} \right)^2 dx. \tag{2.46}$$

Now we are prepared to apply and work with Hamilton's principle. Substitute $V(t)$ and $T(t)$ into Hamilton's principle,

$$\begin{aligned} &\delta \int_{t_1}^{t_2} (T - V)\, dt \\ &= \delta \int_{t_1}^{t_2} \left(\frac{1}{2} \int_0^L m(x) \left(\frac{\partial u}{\partial t} \right)^2 dx - \frac{1}{2} \int_0^L EA(x) \left(\frac{\partial u}{\partial x} \right)^2 dx \right) dt \\ &= \delta \int_{t_1}^{t_2} \left(\int_0^L m(x) \delta \left(\frac{\partial u}{\partial t} \right) dx - \int_0^L EA(x) \delta \left(\frac{\partial u}{\partial x} \right) dx \right) dt = 0. \end{aligned} \tag{2.47}$$

Perform the usual interchanges and integration by parts. Recall that δu is taken to vanish at t_1 and t_2, and find the resulting expression to be

$$\int_{t_1}^{t_2}\int_0^L \left[\frac{\partial}{\partial x}\left(EA(x)\frac{\partial u}{\partial x}\right) - m(x)\frac{\partial^2 u}{\partial t^2}\right]\delta u dx dt - \int_{t_1}^{t_2}\left(EA(x)\frac{\partial u}{\partial x}\right)\delta u\Big|_0^L dt = 0. \tag{2.48}$$

Since δu is arbitrary in $0 < x < L$, the factor in the square braces must equal zero,

$$\frac{\partial}{\partial x}\left(EA(x)\frac{\partial u}{\partial x}\right) - m(x)\frac{\partial^2 u}{\partial t^2} = 0. \tag{2.49}$$

This is the equation of motion. In addition, we have the statement of the possible boundary conditions in the relation

$$\left(EA(x)\frac{\partial u}{\partial x}\right)\delta u\Big|_0^L = 0. \tag{2.50}$$

For example, a clamped end at $x = 0$ results in a known displacement so that $\delta u = 0$ over all time t. In this case, $u(0,t) = 0$. A free end at $x = L$ implies that the displacement is not known so that δu does not disappear but rather a moment cannot be resisted or $EA(L)\partial u(L)/\partial x = 0$.

7. Chapter Summary

We have introduced the very fundamental concepts underlying the variational approaches to mechanics and vibration. First among these is the principle of virtual work, from which d'Alembert's principle evolves. From these, Lagrange's equation and Hamilton's principle can be derived. Their importance for us is that they provide a tool for the derivation of governing equations of motion and their boundary conditions. Two particularly important applications from the perspective of this monograph are the derivations of the equations governing the dynamics of beams, here, axially and transversely vibrating beams. The next chapter provides more details about beam models, and subsequent chapters are based on some of these beam models as well as more complex models.

Chapter 3

OVERVIEW OF TRANSVERSE BEAM MODELS

The purpose of this chapter is to provide an overview of the existing linear transverse beam models that can be used to model an offshore structure. The existing beam theories are the Euler-Bernoulli, Rayleigh, shear and Timoshenko. First, a review of the four beam theories are presented. Second, the underlying assumptions used in the beam models are delineated. Third, the equation of motion for each model and the expressions for boundary conditions are obtained using Hamilton's variational principle. Fourth, the frequency equations are obtained for four sets of end conditions: free-free, clamped-clamped, hinged-hinged, and clamped-free. The roots of the frequency equations are presented in terms of normalized wave numbers. The normalized wave numbers for the other six sets of end conditions are obtained using the analysis of symmetric and antisymmetric modes from the wave numbers of the previous four sets of end conditions. For engineering purposes, the normalized wave numbers for each set of end conditions are tabulated or plotted as a function of geometric and physical parameters. Fifth, the orthogonality conditions of the eigenfunctions and the procedure to obtain the forced response using the method of eigenfunction expansion are presented. Finally, a numerical example is shown for a non-slender beam to illustrate the differences among the four beam models. This subject has also been treated by Han et al. [27].

1. Literature Review and Underlying Assumptions

An exact formulation of the beam problem was first investigated in terms of general elasticity equations by Pochhammer (1876) and Chree

S. M. Han et al., *Nonlinear and Stochastic Dynamics of Compliant Offshore Structures*

(1889), and it is reiterated by Love [44]. They derived the equations that describe a vibrating solid cylinder. However, it is not practical to solve the full problem because it yields more information than usually needed in applications. Therefore, approximate solutions for transverse displacement are sufficient. The beam theories under consideration all yield the transverse displacement as a solution.

It was recognized by the early researchers that the bending effect is the single most import factor in a transversely vibrating beam. The Euler-Bernoulli model includes the strain energy due to bending and the kinetic energy due to lateral displacement. The Euler-Bernoulli model dates back to the eighteenth century. Jacob Bernoulli (1654-1705) first discovered that the curvature of an elastic beam at any point is proportional to the bending moment at that point. Daniel Bernoulli (1700-1782), the nephew of Jacob, was the first one who formulated the differential equation of motion of a vibrating beam. Later, Jacob Bernoulli's theory was accepted by Leonhard Euler (1707-1783) in his investigation of the shape of elastic beams under various loading conditions. Many advances on the elastic curves were made by Euler as discussed in Timoshenko [79]. The Euler-Bernoulli beam theory, sometimes called the classical beam theory, Euler beam theory, Bernoulli beam theory, or Bernoulli-Euler beam theory, is the most commonly used because it is simple and provides reasonable engineering approximations for many problems. However, the Euler-Bernoulli model tends to slightly overestimate the natural frequencies. This problem is exacerbated for the natural frequencies of the higher modes. Also, the prediction is better for slender beams than non-slender beams.

The Rayleigh beam theory provides a marginal improvement on the Euler-Bernoulli theory by including the effect of rotation of the cross-section [72]. As a result, it partially corrects the overestimation of natural frequencies in the Euler-Bernoulli model. However, the natural frequencies are still overestimated. Early investigators include Davies who studied the effect of rotary inertia on a fixed-free beam [19].

The shear model adds shear distortion to the Euler-Bernoulli model. It should be noted that this is different from the pure shear model which includes the shear distortion and rotary inertia only or the simple shear beam which includes the shear distortion and lateral displacement only [1]. Neither the pure shear nor the simple shear model fits our purpose of obtaining an improved model to the Euler-Bernoulli model because both exclude the most important factor, the bending effect. By adding shear distortion to the Euler-Bernoulli beam, the estimate of the natural frequencies improves considerably.

Table 3.1. Percentage Deviates from the Experimental Values Obtained by Traill-Nash and Collar [80]

Beam Models	First Natural Frequency	Second Natural Frequency
Euler-Bernoulli	$+14\% \sim +26\%$	$+78\% \sim +133\%$
Shear	$0\% \sim +3\%$	$-1\% \sim +6\%$
Timoshenko	$-1\% \sim +2\%$	$-1\% \sim +6\%$

Timoshenko [77][78] proposed a beam theory which adds the effect of shear as well as the effect of rotation to the Euler-Bernoulli beam. The Timoshenko model is a major improvement for non-slender beams and for high frequency responses where shear or rotary effects are not negligible. Following Timoshenko, several authors have obtained the frequency equations and the mode shapes for various boundary conditions. Some are Kruszewski [37], Traill-Nash and Collar [80], Dolph [21], and Huang [30].

Kruszewski obtained the first three antisymmetric modes of a cantilever beam, and three antisymmetric and symmetric modes of a free-free beam.

Traill-Nash and Collar gave a fairly complete theoretical treatment as well as experimental results for the case of a uniform beam. In the first part of their paper, they obtained the expressions for the frequency equation and mode shapes for six common boundary conditions: fixed-free, free-free, hinged-free, hinged-hinged, fixed-fixed, and fixed-hinged. In the second part of their paper, they reported the experimental results with the numerical results obtained using the Euler-Bernoulli, shear, and Timoshenko models. They used non-slender beams in which the shear and rotary effects were important. They reported that the difference between the first and second natural frequencies predicted by each of the theoretical models and the experimental values. A summary of the results is shown in Table 3.1.

Huang [30] independently obtained the frequency equations and expressions for the mode shapes for all six end conditions. The frequency equations are difficult to solve except for the case of a simply supported beam. Even when the roots of the frequency equations are obtained, it is a challenge to present them in a meaningful way. For example, Traill-Nash and Collar [80], Dolph [21], Huang [30], and Abbas and Thomas [1] presented them in different ways.

Kruszewski, Traill-Nash and Collar, and Huang only gave expressions for the natural frequencies and mode shapes. They did not solve for

the complete response of the beam due to initial conditions and external forces. To do so, knowledge of the orthogonality conditions among the eigenfunctions is required. The orthogonality conditions for the Timoshenko beam were independently noted by Dolph [21] and Herrmann [28]. Dolph solved the initial and boundary value problem for a hinged-hinged beam with no external forces. The methods used to solve for the forced initial-boundary value problem and for the problem with time-dependent boundary conditions are briefly mentioned in his paper. A general method to solve for the response of a Timoshenko beam due to initial conditions and the external forces is given in the book *Elastokinetics* by Reismann and Pawlik [65]. They used the method of *eigenfunction expansion.*

A crucial parameter in Timoshenko beam theory is the shape factor. It is also called the shear coefficient or the area reduction factor. This parameter arises because the shear is not constant over the cross-section. The shape factor is a function of Poisson's ratio and the frequency of vibration as well as the shape of the cross-section. Typically, the functional dependence on frequency is ignored. Davies [19], Mindlin and Deresiewicz [51], Cowper [18], and Spence and Seldin [69] suggested methods to calculate the shape factor as a function of the shape of the cross-section and Poisson's ratio. Stephen [70] showed variation in the shape factor with frequency.

Despite current efforts by Stephen and Levinson [41][42][71] to come up with a new and better beam theory, the Euler-Bernoulli and Timoshenko beam theories are still widely used.

A summary of the four beam theories is tabulated in Table 3.2. The basic assumptions that are made by all models are as follows.

1. One dimension (the dimension in the axial direction) is considerably larger than the other two.

2. The material is linear elastic (Hookean).

3. The Poisson effect is neglected.

4. The cross-sectional area is symmetric so that the neutral and centroidal axes coincide.

5. Planes perpendicular to the neutral axis remain perpendicular after deformation.

6. The angle of rotation is small so that the small angle assumption can be used.

Table 3.2. Four Beam Theories

Beam Models	Bending Moment	Lateral Displacement	Shear Deformation	Rotary Inertia
Euler-Bernoulli	✓	✓	×	×
Rayleigh	✓	✓	×	✓
Shear	✓	✓	✓	×
Timoshenko	✓	✓	✓	✓

2. Nomenclature

Symbol	Description	Units
A^*	the cross-sectional area	m^2
$a^*, b^*, \tilde{b}^*$	the wave numbers	$1/m$
E^*	Young's Modulus	N/m^2
f	transverse force normal to the structure per length	N/m
G^*	the shear modulus	N/m^2
I^*	the mass moment of inertia of the cross-section about the neutral axis	m^4
Q^*	shear	N
L^*	length of the beam	m
M^*	moment	$N \cdot m$
k^*	the radius of gyration I^*/A^*	m
k'	the shape factor	-
KE^*	the kinetic energy	$kg \cdot m^2/s^2$
PE^*	the potential energy	$kg \cdot m^2/s^2$
r_i^*	the ith root of the characteristic equation	$1/m$
t^*	time	s
x^*	axial coordinate of the beam	m
$v^*(x^*, t^*)$	transverse displacement of the beam	m
$\alpha(x^*, t^*)$	angle of rotation due to bending	rad
$\beta(x^*, t^*)$	angle of rotation due to shear	rad
ν	the Poisson's ratio	-
ρ^*	density of the beam	kg/m^3
ω_i^*	ith natural frequency of the beam	rad/s
A	dimensionless area	A^*/L^{*2}
$a, b, \tilde{b}$	dimensionless wave numbers	$a^*L^*, b^*L^*, \tilde{b}^*L^*$
Energy	dimensionless energy	$\text{Energy}^*L^*/(E^*I^*)$
f	dimensionless transverse force per unit length	$f^*L^{*3}/(E^*I^*)$
G	dimensionless shear modulus	$G^*L^{*4}/(E^*I^*)$
I	dimensionless mass moment of inertia of the cross-section about the neutral axis	I^*/L^{*4}
Q	dimensionless shear	$Q^*L^{*2}/(E^*I^*)$
k	dimensionless radius of gyration	$k^*/L^* = \sqrt{I/A}$

M	dimensionless moment	$M^*L^*/(E^*I^*)$
r_i	dimensionless i^{th} root of the characteristic equation	r_i^*L
s	the slenderness ratio	L^*/k^*
t	dimensionless time	$t^*\omega_1^*$
x	dimensionless axial coordinate	x^*/L^*
v	dimensionless transverse displacement	v^*/L^*
ρ	dimensionless density	$\rho^*\left(L^{*6}\omega_1^{*2}\right)/\left(E^*I^*\right)$
ω_n	dimensionless nth natural frequency	ω_n^*/ω_1^*

3. Equation of Motion and Boundary Conditions Via Hamilton's Principle

3.1 Euler-Bernoulli Beam Model

Detailed derivations for the Euler-Bernoulli model can be found in text books by Benaroya [12], Inman [31], Meirovitch [46][45][47], Rao [64], and Thomson [76]. Here, the equation of motion is obtained using Hamilton's variational principle. The potential energy of a uniform beam due to bending is given by

$$PE^*_{bending} = \frac{1}{2}\int_0^{L^*} E^*I^*\left(\frac{\partial^2 v^*(x^*,t^*)}{\partial x^{*2}}\right)^2 dx^*, \tag{3.1}$$

where E^* is the modulus of elasticity, I^* is the area moment of inertia of the cross-section about the neutral axis, $v^*(x^*,t^*)$ is the transverse deflection at the axial location x^* and time t^*, and L^* is the length of the beam. Superscript $*$ symbols are used to signify that they are dimensional quantities. Now, the length scales (L^*, v^*, and x^*) are non-dimensionalized by the length of the beam so that dimensionless quantities (L, v, and x) are given by

$$\begin{aligned} L &= L^*/L^* = 1 \\ v &= v^*/L^* \\ x &= x^*/L^*. \end{aligned} \tag{3.2}$$

In terms of the dimensionless length scales, the potential energy is given by.

$$PE^*_{bending} = \frac{1}{2}\int_0^1 \frac{E^*I^*}{L^*}\left(\frac{\partial^2 v(x,t)}{\partial x^2}\right)^2 dx. \tag{3.3}$$

The potential energy is non-dimensionalized by E^*I^*/L^* so that we can write

$$PE_{bending} = \frac{1}{2}\int_0^1 \left(\frac{\partial^2 v(x,t)}{\partial x^2}\right)^2 dx. \tag{3.4}$$

The kinetic energy is given by

$$KE^*_{trans} = \frac{1}{2}\int_0^{L^*} \rho^* A^* \left(\frac{\partial v^*(x^*,t^*)}{\partial t^*}\right)^2 dx^*, \tag{3.5}$$

where ρ^* is the density of the beam, A^* is the cross-sectional area. The cross-sectional area A^* is non-dimensionalized by L^{*2}, and the time t by $1/\omega_1^*$, where ω_1^* is the first natural frequency yet to be determined. The kinetic energy is non-dimensionalized by E^*I^*/L^* so that we can write

$$KE_{trans} = \frac{1}{2}\int_0^1 \rho^* \frac{L^{*6}\omega_1^{*2}}{E^*I^*} A \left(\frac{\partial v(x,t)}{\partial t}\right)^2 dx \tag{3.6}$$

By non-dimensionalizing the density ρ^* by $E^*I^*/\left(L^{*6}\omega_1^{*2}\right)$, we can write

$$KE_{trans} = \frac{1}{2}\int_0^1 \rho A \left(\frac{\partial v(x,t)}{\partial t}\right)^2 dx. \tag{3.7}$$

The dimensionless Lagrangian, defined by $KE - PE$, is given by

$$L = \frac{1}{2}\int_0^1 \left[\rho A \left(\frac{\partial v(x,t)}{\partial t}\right)^2 - \left(\frac{\partial^2 v(x,t)}{\partial x^2}\right)^2\right] dx, \tag{3.8}$$

The virtual work due to the non-conservative transverse force per unit length $f^*(x^*,t^*)$ is given by

$$\delta W^*_{nc} = \int_0^{L^*} f^*(x^*,t^*)\delta v^*(x^*,t^*)dx^*. \tag{3.9}$$

Non-dimensionalizing the work by E^*I^*/L^* and the transverse external force f^* by L^{*3}/E^*I^*, the dimensionless non-conservative work is given by

$$\delta W_{nc} = \int_0^1 f(x,t)\delta v(x,t)dx. \tag{3.10}$$

Using the extended Hamilton's principle, by including the non conservative forcing, the governing differential equation of motion is given by[1]

$$\rho A\frac{\partial^2 v(x,t)}{\partial t^2} + \frac{\partial^4 v(x,t)}{\partial x^4} = f(x,t), \tag{3.11}$$

[1]For detailed treatments of extended Hamilton's principle, readers are refered to [47].

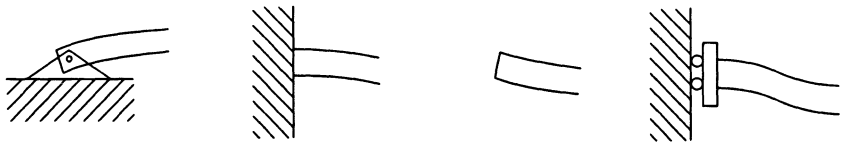

(a) Hinged	(b) Clamped	(c) Free	(d) Sliding
$M(0,t) = 0$ $D(0,t) = 0$	$D(0,t) = 0$ $S(0,t) = 0$	$M(0,t) = 0$ $Q(0,t) = 0$	$S(0,t) = 0$ $Q(0,t) = 0$

Figure 3.1. Four Types of Boundary Conditions

with the boundary conditions to be satisfied

$$\left.\frac{\partial^2 v}{\partial x^2}\delta\left(\frac{\partial v}{\partial x}\right)\right|_0^1 = 0$$

$$\left.\frac{\partial^3 v}{\partial x^3}\delta v\right|_0^1 = 0. \tag{3.12}$$

Before we go on, let us examine the physical meaning of the boundary conditions above. v is the dimensionless displacement, the first derivative $\partial v/\partial x$ is the dimensionless slope, the second derivative $\partial^2 v/\partial x^2$ is the dimensionless moment, and the third derivative $\partial^3 v/\partial x^3$ is the dimensionless shear. Keep in mind that $\delta v = 0$ means that the variation of the displacement is zero. That is, the displacement is known. It does not necessarily mean that the displacement is zero. Here, we do not consider base excited or end forcing problems. Therefore, only in our case, $\delta v = 0$ or $\delta\,(\partial v/\partial x) = 0$ means that the displacement or the slope is zero. In order for Equation 3.12 to be satisfied, four combinations of end conditions are possible,

$$\begin{aligned}
&\frac{\partial^2 v}{\partial x^2} = 0, \quad v = 0 \text{ for hinged end} \\
&\frac{\partial v}{\partial x} = 0, \quad v = 0 \text{ for clamped end} \\
&\frac{\partial^2 v}{\partial x^2} = 0, \quad \frac{\partial^3 v}{\partial x^3} = 0 \text{ for free end} \\
&\frac{\partial v}{\partial x} = 0, \quad \frac{\partial^3 v}{\partial x^3} = 0 \text{ for sliding end.}
\end{aligned} \tag{3.13}$$

These conditions are shown in Figure 3.1 where D, S, M, and Q represent displacement, slope, moment, and shear respectively.

The equation of motion, boundary conditions, and initial conditions form an initial-boundary value problem which can be solved using the methods of *separation of variables* and *eigenfunction expansion.* First, we consider a homogeneous problem by setting $f(x,t) = 0$ in order to obtain the natural frequencies and eigenfunctions. By separating $v(x,t)$ into two functions such that $v(x,t) = W(x)T(t)$, the equation of motion (Equation 3.11) can be separated into two ordinary differential equations,

$$\frac{d^2T(t)}{dt^2} + \omega^2 T(t) = 0 \tag{3.14}$$

$$\frac{d^4W(x)}{dx^4} - a^4 W(x) = 0, \tag{3.15}$$

where a is related to the angular frequency ω by

$$a^4 = \rho A \omega^2. \tag{3.16}$$

The quantity a is $1/2\pi$ times the number of cycles in a beam length, and we call a the dimensionless wave number[2]. Equation 3.16 is called the dispersion relationship. From Equations 3.14 and 3.15, $T(t)$ is sinusoidal in time, and $W(x)$ has both sinusoidal and hyperbolic terms as shown below,

$$T(t) = d_1 \sin \omega t + d_2 \cos \omega t \tag{3.17}$$

$$W(x) = C_1 \sin ax + C_2 \cos ax + C_3 \sinh ax + C_4 \cosh ax, \tag{3.18}$$

where d_i and C_i are constant coefficients.

Note that the boundary conditions can be expressed in terms of the spatial function $W(x)$ only. For instance, Equation 3.12 can be rewritten as

$$\frac{d^2W}{dx^2}\delta\left(\frac{dW}{dx}\right)\Bigg|_0^1 = 0$$

$$\frac{d^3W}{dx^3}\delta W\Bigg|_0^1 = 0, \tag{3.19}$$

[2]We are defining the wave number as

$$a^* = \frac{2\pi}{\text{wave length}^*}$$

so that the dimensionless wave number is given by

$$a = \frac{2\pi}{\text{wave length}}.$$

from which we can obtain four possible end conditions, as in Equation 3.13, in terms of $W(x)$ only. Now we are ready to apply the boundary conditions to the spatial solution to obtain the corresponding frequency equations and eigenfunctions. This is done in Section 4. We proceed next with the Rayleigh beam model.

3.2 Rayleigh Beam Model

As mentioned in the introduction, the Rayleigh beam adds the rotary inertia effects to the Euler-Bernoulli beam. The variables are non-dimensionalized in the same fashion, and they are tabulated in Section 2. The kinetic energy due to the rotation of the cross-section is given by

$$KE_{rot} = \frac{1}{2}\int_0^1 \rho I \left(\frac{\partial^2 v(x,t)}{\partial t \partial x}\right)^2 dx, \tag{3.20}$$

where I^* is non-dimensionalized by L^{*4}. Combining Equation 3.20 with Equations 3.4, 3.7, and 3.10 to form the Lagrangian and using Hamilton's principle, we obtain the equation of motion given by

$$\rho A \frac{\partial^2 v(x,t)}{\partial t^2} + \frac{\partial^4 v(x,t)}{\partial x^4} - \rho I \frac{\partial^4 v(x,t)}{\partial x^2 \partial t^2} = f(x,t), \tag{3.21}$$

with the boundary conditions given by

$$\begin{aligned} \frac{\partial^2 v}{\partial x^2}\delta\left(\frac{\partial v}{\partial x}\right)\Big|_0^1 &= 0 \\ \left(\frac{\partial^3 v}{\partial x^3} - \rho I \frac{\partial^3 v}{\partial x \partial t^2}\right)\delta v\Big|_0^1 &= 0, \end{aligned} \tag{3.22}$$

where v is the dimensionless displacement, $\partial v/\partial x$ is the dimensionless slope, $\partial^2 v/\partial x^2$ is the dimensionless moment, and $\partial^3 v/\partial x^3 - \rho I \cdot \partial^3 v/\partial x \partial t^2$ is the dimensionless shear. Four possible end conditions are

$$\begin{aligned} &\frac{\partial^2 v}{\partial x^2} = 0, \quad v = 0 \text{ for hinged end} \\ &\frac{\partial v}{\partial x} = 0, \quad v = 0 \text{ for clamped end} \\ &\frac{\partial^2 v}{\partial x^2} = 0, \quad \frac{\partial^3 v}{\partial x^3} - \rho I \frac{\partial^3 v}{\partial x \partial t^2} = 0 \text{ for free end} \\ &\frac{\partial v}{\partial x} = 0, \quad \frac{\partial^3 v}{\partial x^3} - \rho I \frac{\partial^3 v}{\partial x \partial t^2} = 0 \text{ for sliding end.} \end{aligned} \tag{3.23}$$

The expression for shear might seem odd. Its validity can be verified by summing the forces and moment on an incremental beam element,

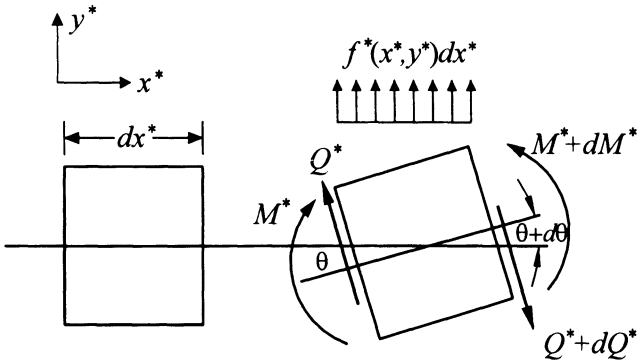

Figure 3.2. An Incremental Beam Element

as shown in Figure 3.2. The sum of the forces on a beam element in the transverse direction is [3]

$$\sum F_y = \rho^* A^* dx^* \frac{\partial^2 v^*}{\partial t^{*2}}$$
$$= -(Q^* + dQ^*)\cos(\theta + d\theta) + Q^* \cos\theta + f^*(x^*, t^*)\, dx^*, \quad (3.24)$$

where θ can be approximated as $\partial v/\partial x$ or $\partial v^*/\partial x^*$, and dQ^* and $d\theta$ represent $(\partial Q^*/\partial x^*)\, dx^*$ and $(\partial\theta/\partial x^*)\, dx^*$, respectively. Expanding $\cos(\theta + d\theta)$ about θ using a Taylor series expansion and using the small angle assumption[4], we obtain

$$-\frac{\partial Q^*}{\partial x^*} = \rho^* A^* \frac{\partial^2 v^*}{\partial t^{*2}} - f^*(x^*, t^*). \quad (3.25)$$

Similarly, taking the sum of the moments about the center of the beam element, we obtain

$$\frac{\partial M^*}{\partial x^*} - Q^* = \rho^* I^* \frac{\partial^3 v^*}{\partial t^{*2} \partial x^*}. \quad (3.26)$$

Taking the first derivative of Equation 3.26 with respect to x^*, and subtracting Equation 3.25 from it, we obtain

$$\frac{\partial^2 M^*}{\partial x^{*2}} = \rho^* I^* \frac{\partial^4 v^*}{\partial t^{*2} \partial x^{*2}} - \rho^* A^* \frac{\partial^2 v^*}{\partial t^{*2}} + f^*(x^*, t^*), \quad (3.27)$$

[3] Symbols with superscript $*$ are dimensional quantities.

[4] The small angle assumption means that

$$\theta^2 \ll 1.$$

whose dimensionless form is given by

$$\frac{\partial^2 M}{\partial x^2} = \rho I \frac{\partial^4 v}{\partial t^2 \partial x^2} - \rho A \frac{\partial^2 v}{\partial t^2} + f(x,t). \tag{3.28}$$

Comparing this with the equation of motion (Equation 3.21), the moment is given by

$$M = \frac{\partial^2 v}{\partial x^2} \text{ or } M^* = E^* I^* \frac{\partial^2 v^*}{\partial x^{*2}}. \tag{3.29}$$

Using Equations 3.29 and 3.26, the shear is given by

$$\begin{aligned} Q^* &= E^* I^* \frac{\partial^3 v^*}{\partial x^{*3}} - \rho^* I^* \frac{\partial^3 v^*}{\partial t^{*2} \partial x^*} \\ \text{or } Q &= \frac{\partial^3 v}{\partial x^3} - \rho I \frac{\partial^3 v}{\partial t^2 \partial x}, \end{aligned} \tag{3.30}$$

which verifies our interpretation.

In order to obtain the homogeneous solution, $f(x,t)$ is set equal to zero in Equation 3.21. Separating $v(x,t)$ into spatial and time functions, $v(x,t) = W(x)T(t)$, Equation 3.21 can also be separated into two ordinary differential equations. The time function $T(t)$ obeys the same differential equation as the one for the Euler-Bernoulli model given in Equation 3.14, and the spatial differential equation is given by

$$\frac{d^4 W(x)}{dx^4} - \omega^2 \left(\rho A W(x) - \rho I \frac{d^2 W(x)}{dx^2} \right) = 0. \tag{3.31}$$

Again, the time solution $T(t)$ is sinusoidal, and the spatial solution $W(x)$ has both sinusoidal and hyperbolic terms,

$$T(t) = d_1 \sin \omega t + d_2 \cos \omega t \tag{3.32}$$

$$W(x) = C_1 \sin ax + C_2 \cos ax + C_3 \sinh bx + C_4 \cosh bx, \tag{3.33}$$

where the dispersion relations are

$$\begin{aligned} a &= \sqrt{\frac{\rho I \omega^2}{2} + \sqrt{\left(\frac{\rho I \omega^2}{2}\right)^2 + \rho A \omega^2}} \\ b &= \sqrt{-\frac{\rho I \omega^2}{2} + \sqrt{\left(\frac{\rho I \omega^2}{2}\right)^2 + \rho A \omega^2}}. \end{aligned} \tag{3.34}$$

Note that there are two wave numbers in this case. It will be shown in Section 4 that these wave numbers are related only by the slenderness ratio.

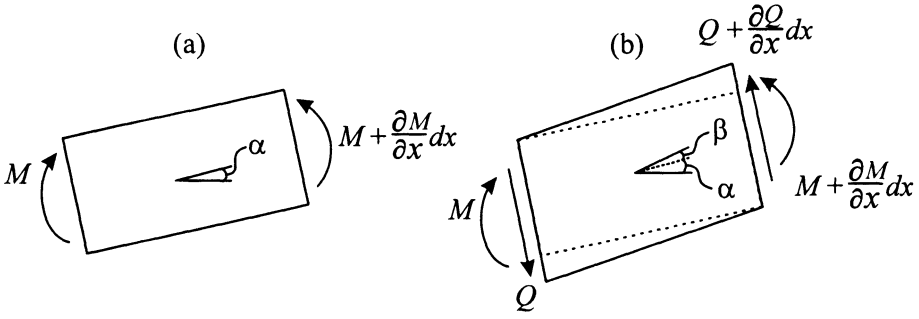

Figure 3.3. Angle of Rotation and Angle of Distorsion

The boundary conditions given in Equation 3.22 can be written in terms of $W(x)$ only,

$$\frac{d^2W}{dx^2}\delta\left(\frac{dW}{dx}\right)\Bigg|_0^1 = 0$$
$$\left(\frac{d^3W}{dx^3} + \rho I\omega^2\frac{dW}{dx}\right)\delta W\Bigg|_0^1 = 0. \tag{3.35}$$

3.3 Shear Beam Model

This model adds the effect of shear distortion (but not rotary inertia) to the Euler-Bernoulli model. We introduce new variables α, the angle of rotation of the cross-section due to the bending moment, and β, the angle of distortion due to shear as shown in Figure 3.3.

The total angle of rotation is the sum of α and β and is approximately the first derivative of the deflection,

$$\alpha(x,t) + \beta(x,t) = \frac{\partial v(x,t)}{\partial x}. \tag{3.36}$$

Therefore, the potential energy due to bending given in Equation 3.4 is slightly modified in this case such that

$$PE_{bending} = \frac{1}{2}\int_0^1 \left(\frac{\partial\alpha(x,t)}{\partial x}\right)^2 dx. \tag{3.37}$$

The potential energy due to shear is given by

$$PE^*_{shear} = \frac{1}{2}\int_0^L k'G^*A^*\left(\frac{\partial v^*(x^*,t^*)}{\partial x^*} - \alpha(x^*,t^*)\right)^2 dx^*. \tag{3.38}$$

Table 3.3. Shear Factors for Various Cross-sections

Cross-Section	k'
Circle	$\frac{6(1+\nu)}{7+6\nu}$
Hollow Circle with $m = \frac{r_{inner}}{r_{outer}}$	$\frac{6(1+\nu)(1+m^2)^2}{(7+6\nu)(1+m^2)^2+(20+12\nu)m^2}$
Rectangle	$\frac{10(1+\nu)}{12+11\nu}$
Thin-Walled Round Tube	$\frac{2(1+\nu)}{4+3\nu}$
Thin-Walled Square Tube	$\frac{20(1+\nu)}{48+39\nu}$

Using the dimensionless length scales and the dimensionless potential energy expressions,

$$PE_{shear} = \frac{1}{2}\int_0^L k' \frac{G^* L^{*4}}{E^* I^*} A \left(\frac{\partial v(x,t)}{\partial x} - \alpha(x,t)\right)^2 dx. \tag{3.39}$$

Non-dimensionalizing G^* by $E^* I^*/L^{*4}$, we can write

$$PE_{shear} = \frac{1}{2}\int_0^1 k' GA \left(\frac{\partial v(x,t)}{\partial x} - \alpha(x,t)\right)^2 dx, \tag{3.40}$$

where k' is the shape factor. Following Cowper's work, some k' values are tabulated in Table 3.3 [18].

Together with the kinetic energy due to lateral displacement given in Equation 3.7, the Lagrangian is given by

$$L = \frac{1}{2}\int_0^1 \left[\rho A \left(\frac{\partial v(x,t)}{\partial t}\right)^2 - \left(\frac{\partial \alpha(x,t)}{\partial x}\right)^2 - k' GA \left(\frac{\partial v(x,t)}{\partial x} - \alpha(x,t)\right)^2\right] dx. \tag{3.41}$$

Unlike in the Euler-Bernoulli and the Rayleigh beam models, there are two dependent variables for the shear beam, namely $v(x,t)$ and $\alpha(x,t)$. The equations of motion, using Hamilton's principle, are given by

$$\begin{aligned} \rho A \frac{\partial^2 v(x,t)}{\partial t^2} - k' GA \left(\frac{\partial^2 v(x,t)}{\partial x^2} - \frac{\partial \alpha(x,t)}{\partial x}\right) &= f(x,t) \\ \frac{\partial^2 \alpha(x,t)}{\partial x^2} + k' GA \left(\frac{\partial v(x,t)}{\partial x} - \alpha(x,t)\right) &= 0, \end{aligned} \tag{3.42}$$

with the boundary conditions given by

$$\left.\frac{\partial \alpha}{\partial x}\delta\alpha\right|_0^1 = 0 \tag{3.43}$$
$$k'GA\left(\frac{\partial v}{\partial x} - \alpha\right)\delta v\Big|_0^1 = 0.$$

v is the dimensionless displacement, α is the angle of rotation due to the bending moment, $\partial\alpha/\partial x$ is the dimensionless moment, and the term $k'GA\,(\partial v/\partial x - \alpha(x,t))$ is the dimensionless shear. Four possible boundary conditions are

$$\begin{aligned}
\frac{\partial \alpha}{\partial x} &= 0, \quad v = 0 \text{ for hinged end} \\
\alpha &= 0, \quad v = 0 \text{ for clamped end} \\
\frac{\partial \alpha}{\partial x} &= 0, \quad k'GA\left(\frac{\partial v}{\partial x} - \alpha\right) = 0 \text{ for free end} \\
\alpha &= 0, \quad \left(\frac{\partial v}{\partial x} - \alpha\right) = 0 \text{ for sliding end.}
\end{aligned} \tag{3.44}$$

Note that the slope due to the bending moment α is zero (instead of the total slope $\partial v/\partial x$) at the clamped or sliding end.

Now, we try to solve the homogeneous problem without the external forcing function. The coupled equations of motion (Equation 3.42) can be decoupled to yield

$$\begin{aligned}
\frac{\partial^4 v(x,t)}{\partial x^4} - \frac{\rho}{k'G}\frac{\partial^4 v(x,t)}{\partial x^2 \partial t^2} + \rho A\frac{\partial^2 v(x,t)}{\partial t^2} &= 0 \\
\frac{\partial^4 \alpha(x,t)}{\partial x^4} - \frac{\rho}{k'G}\frac{\partial^4 \alpha(x,t)}{\partial x^2 \partial t^2} + \rho A\frac{\partial^2 \alpha(x,t)}{\partial t^2} &= 0.
\end{aligned} \tag{3.45}$$

Note that the forms of the differential equations for v and α are identical[5]. Therefore, we can expect that the forms of $v(x,t)$ and $\alpha(x,t)$ are the same.

The next step is to separate the variables. Here, we first assume that they share the same time solution $T(t)$. In other words, $v(x,t)$ and $\alpha(x,t)$ are synchronized in time,

$$\begin{bmatrix} v(x,t) \\ \alpha(x,t) \end{bmatrix} = T(t)\begin{bmatrix} W(x) \\ \Psi(x) \end{bmatrix}. \tag{3.46}$$

[5]The equations can be decoupled in this way only when the cross-sectional area and the density are uniform.

Now, let us substitute the above expression into Equation 3.42 without the term $f(x,t)$ to obtain

$$\begin{aligned} \rho A W(x)\ddot{T}(t) - k'GA\left(W''(x) - \Psi'(x)\right)T(t) &= 0 \\ \Psi''(x)T(t) + k'GA\left(W'(x) - \Psi(x)\right)T(t) &= 0, \end{aligned} \tag{3.47}$$

where the prime and dot notations are used for the derivatives with respect to x and t, respectively. The first expression in Equation 3.47 can be separated into two ordinary differential equations given by

$$\begin{aligned} \ddot{T}(t) + \omega^2 T(t) &= 0 \\ k'GA\left(W''(x) - \Psi'(x)\right) + \omega^2 \rho A W(x) &= 0. \end{aligned} \tag{3.48}$$

Again, $T(t)$ is sinusoidal with angular frequency ω as in Equation 3.17. The spatial equations, the second equation in 3.47 and the second equation in 3.48, are written using matrix notation as

$$\begin{aligned} \mathbf{0} = &\begin{bmatrix} k'GA & 0 \\ 0 & 1 \end{bmatrix}\begin{bmatrix} W''(x) \\ \Psi''(x) \end{bmatrix} + \begin{bmatrix} 0 & -k'GA \\ k'GA & 0 \end{bmatrix}\begin{bmatrix} W'(x) \\ \Psi'(x) \end{bmatrix} \\ &+ \begin{bmatrix} \rho A\omega^2 & 0 \\ 0 & -k'GA \end{bmatrix}\begin{bmatrix} W(x) \\ \Psi(x) \end{bmatrix}. \end{aligned} \tag{3.49}$$

These equations can be decoupled to yield

$$\begin{aligned} W''''(x) + \frac{\rho\omega^2}{k'G}W''(x) - \rho A\omega^2 W(x) &= 0 \\ \Psi''''(x) + \frac{\rho\omega^2}{k'G}\Psi''(x) - \rho A\omega^2 \Psi(x) &= 0. \end{aligned} \tag{3.50}$$

Note that above relations can be obtained from Equation 3.45. The differential equations for $W(x)$ and $\Psi(x)$ have the same form. Therefore, we can further assume that the solutions of $W(x)$ and $\Psi(x)$ have the same form, and they only differ by a constant so that we can write

$$\begin{bmatrix} W(x) \\ \Psi(x) \end{bmatrix} = d\mathbf{u}e^{rx}, \tag{3.51}$$

where d is a constant coefficient, $\mathbf{u}$ is a vector of constant numbers and r is the wave number.

When Equation 3.51 is substituted into 3.49, we obtain

$$\begin{bmatrix} k'GAr^2 + \rho A\omega^2 & -k'GAr \\ k'GAr & r^2 - k'GA \end{bmatrix}\mathbf{u} = \mathbf{0}, \tag{3.52}$$

from which we obtain the eigenvalues r and eigenvectors $\mathbf{u}$. In order to have a non-trivial solution, the determinant of the above matrix has to be zero, that is,

$$r^4 + \frac{\rho\omega^2}{k'G}r^2 - \rho A\omega^2 = 0. \tag{3.53}$$

The eigenvalues are given by

$$r_i = \pm\sqrt{-\frac{\rho\omega^2}{2k'G} \pm \sqrt{\left(\frac{\rho\omega^2}{2k'G}\right)^2 + \rho A\omega^2}} \text{ for } i = 1,2,3,4, \tag{3.54}$$

of which two are real and the other two are imaginary. The corresponding dimensionless eigenvectors $\mathbf{u}_i$ are obtained by substituting r with r_i in Equation 3.52,

$$\begin{bmatrix} k'GAr_i^2 + \rho A\omega^2 & -k'GAr_i \\ k'GAr_i & r_i^2 - k'GA \end{bmatrix} \mathbf{u}_i = \mathbf{0}. \tag{3.55}$$

We find that the eigenvectors are given by

$$\mathbf{u}_i = \begin{bmatrix} k'GAr_i \\ k'GAr_i^2 + \rho A\omega^2 \end{bmatrix} \tag{3.56}$$

or

$$\mathbf{u}_i = \begin{bmatrix} r_i^2 - k'GA \\ -k'GAr_i \end{bmatrix} \text{ for } i = 1,2,3,4. \tag{3.57}$$

The spatial solution is given by

$$\begin{aligned} \begin{bmatrix} W(x) \\ \Psi(x) \end{bmatrix} &= \sum_{i=1}^{4} d_i \mathbf{u}_i e^{r_i x} \\ &= d_1\mathbf{u}_1 e^{bx} + d_2\mathbf{u}_2 e^{-bx} + d_3\mathbf{u}_3 e^{iax} + d_4\mathbf{u}_4 e^{-iax}, \end{aligned} \tag{3.58}$$

where

$$\begin{aligned} a &= \sqrt{\frac{\rho\omega^2}{2k'G} + \sqrt{\left(\frac{\rho\omega^2}{2k'G}\right)^2 + \rho A\omega^2}} \\ b &= \sqrt{-\frac{\rho\omega^2}{2k'G} + \sqrt{\left(\frac{\rho\omega^2}{2k'G}\right)^2 + \rho A\omega^2}}. \end{aligned} \tag{3.59}$$

We can write the spatial solution (Equation 3.58) in terms of the sinusoidal and hyperbolic functions with real arguments,

$$\begin{bmatrix} W(x) \\ \Psi(x) \end{bmatrix} = \begin{bmatrix} C_1 \\ D_1 \end{bmatrix} \sin ax + \begin{bmatrix} C_2 \\ D_2 \end{bmatrix} \cos ax + \begin{bmatrix} C_3 \\ D_3 \end{bmatrix} \sinh bx + \begin{bmatrix} C_4 \\ D_4 \end{bmatrix} \cosh bx. \tag{3.60}$$

It may seem that the spatial solution has eight unknown constant coefficients, C_i and D_i, instead of the four that we started with (d_i in Equation 3.58). By expressing the exponential functions $e^{r_i x}$ in Equation 3.58 in terms of sinusoidal and hyperbolic functions, the expressions for the coefficients C_i and D_i are obtained in terms of eigenvectors,

$$\begin{aligned} \begin{bmatrix} C_1 \\ D_1 \end{bmatrix} &= (d_3\mathbf{u}_3 - d_4\mathbf{u}_4)\, i, \quad \begin{bmatrix} C_2 \\ D_2 \end{bmatrix} = d_3\mathbf{u}_3 + d_4\mathbf{u}_4 \\ \begin{bmatrix} C_3 \\ D_3 \end{bmatrix} &= (d_1\mathbf{u}_1 - d_2\mathbf{u}_2), \quad \begin{bmatrix} C_2 \\ D_2 \end{bmatrix} = d_1\mathbf{u}_1 + d_2\mathbf{u}_2. \end{aligned} \tag{3.61}$$

Keeping in mind that d_3 and d_4 are complex conjugates of each other, we obtain

$$\begin{aligned} D_1 &= -\frac{k'GAa^2 - \rho A\omega^2}{k'GAa} C_2, \; D_2 = \frac{k'GAa^2 - \rho A\omega^2}{k'GAa} C_1 \\ D_3 &= \frac{k'GAb^2 + \rho A\omega^2}{k'GAb} C_4, \; D_4 = \frac{k'GAb^2 + \rho A\omega^2}{k'GAb} C_3. \end{aligned} \tag{3.62}$$

Therefore, there are four unknowns. These relations can be obtained more easily by substituting the assumed solution (Equation 3.60) into the spatial differential equations (Equation 3.49).

The boundary conditions in Equation 3.43 are written in terms of spatial solutions as

$$\begin{aligned} \frac{d\Psi}{dx}\delta\Psi\Big|_0^1 &= 0 \\ k'GA\left(\frac{dW}{dx} - \Psi\right)\delta W\Big|_0^1 &= 0. \end{aligned} \tag{3.63}$$

3.4 Timoshenko Beam Model

Timoshenko [77][78] proposed a beam theory which adds the effects of shear distortion and rotary inertia to the Euler-Bernoulli model[6]. Therefore, the Lagrangian includes the effects of bending moment (Equation 3.37), lateral displacement (Equation 3.7), rotary inertia (Equation 3.20), and shear distortion (Equation 3.40). We assume that there is no rotational kinetic energy associated with shear distortion, but only with the rotation due to bending. Therefore, the kinetic energy term used in the Rayleigh beam (Equation 3.20) is modified to include only the angle of rotation due to bending by replacing $\partial v/\partial x$ with α.

Combining modified Equation 3.20 with Equations 3.7, 3.37, and 3.40, the Lagrangian is given by

$$L = \frac{1}{2}\int_0^1 \left[\rho A\left(\frac{\partial v(x,t)}{\partial t}\right)^2 + \rho I\left(\frac{\partial \alpha(x,t)}{\partial t}\right)^2 - \left(\frac{\partial \alpha(x,t)}{\partial x}\right)^2 - k'GA\left(\frac{\partial v(x,t)}{\partial x} - \alpha(x,t)\right)^2\right] dx. \tag{3.64}$$

The equations of motion are given by

$$\begin{aligned} \rho A\frac{\partial^2 v(x,t)}{\partial t^2} - k'GA\left(\frac{\partial^2 v(x,t)}{\partial x^2} - \frac{\partial \alpha(x,t)}{\partial x}\right) &= f(x,t) \\ \rho I\frac{\partial^2 \alpha(x,t)}{\partial t^2} - \frac{\partial^2 \alpha(x,t)}{\partial x^2} - k'GA\left(\frac{\partial v(x,t)}{\partial x} - \alpha(x,t)\right) &= 0, \end{aligned} \tag{3.65}$$

and the boundary conditions are given by

$$\begin{aligned} \frac{\partial \alpha}{\partial x}\delta\alpha\Big|_0^1 &= 0 \\ k'GA\left(\frac{\partial v}{\partial x} - \alpha\right)\delta v\Big|_0^1 &= 0, \end{aligned} \tag{3.66}$$

which are identical to those of the shear beam.

In order to solve the homogeneous problem, the forcing function is set to zero. The equations of motion (Equation 3.65) can be decoupled into

$$\begin{aligned} \frac{\partial^4 v}{\partial x^4} - \left(\rho I + \frac{\rho}{k'G}\right)\frac{\partial^4 v}{\partial x^2 \partial t^2} + \rho A\frac{\partial^2 v}{\partial t^2} + \frac{\rho^2 I}{k'G}\frac{\partial^4 v}{\partial t^4} &= 0 \\ \frac{\partial^4 \alpha}{\partial x^4} - \left(\rho I + \frac{\rho}{k'G}\right)\frac{\partial^4 \alpha}{\partial x^2 \partial t^2} + \rho A\frac{\partial^2 \alpha}{\partial t^2} + \frac{\rho^2 I}{k'G}\frac{\partial^4 \alpha}{\partial t^4} &= 0, \end{aligned} \tag{3.67}$$

[6]Equivalently, the Timoshenko model adds rotary inertia to the shear model or adds shear distortion to the Rayleigh model.

where it is implied that v and α are functions of x and t. Again, both $v(x,t)$ and $\alpha(x,t)$ are governed by differential equations of the same form, so that we can make the same argument as we did for the shear beam that $v(x,t)$ and $\alpha(x,t)$ themselves are of the same form.

First, we use the method of separation of variables to separate the equations of motion (Equation 3.65) to obtain the time and the spatial ordinary differential equations. The time equation is the same as the ones for the other models given in Equation 3.14, and the spatial equation is given by

$$0 = \begin{bmatrix} k'GA & 0 \\ 0 & 1 \end{bmatrix} \begin{bmatrix} W''(x) \\ \Psi''(x) \end{bmatrix} + \begin{bmatrix} 0 & -k'GA \\ k'GA & 0 \end{bmatrix} \begin{bmatrix} W'(x) \\ \Psi'(x) \end{bmatrix} + \begin{bmatrix} \rho A\omega^2 & 0 \\ 0 & J\omega^2 - k'GA \end{bmatrix} \begin{bmatrix} W(x) \\ \Psi(x) \end{bmatrix}. \tag{3.68}$$

Following the procedure used previously from Equations 3.46 to 3.53, we obtain the characteristic equation

$$r^4 + \left(\rho I + \frac{\rho}{k'G}\right)\omega^2 r^2 - \rho A\omega^2 + \frac{\rho^2 I}{k'G}\omega^4 = 0, \tag{3.69}$$

whose roots are

$$r = \pm\sqrt{-\left(I + \frac{1}{k'G}\right)\frac{\rho\omega^2}{2} \pm \sqrt{\left(I - \frac{1}{k'G}\right)^2 \frac{\rho^2\omega^4}{4} + \rho A\omega^2}}. \tag{3.70}$$

Of the four roots, the two given by

$$r_{1,2} = \pm\sqrt{-\left(I + \frac{1}{k'G}\right)\frac{\rho\omega^2}{2} - \sqrt{\left(I - \frac{1}{k'G}\right)^2 \frac{\rho^2\omega^4}{4} + \rho A\omega^2}} \tag{3.71}$$

are always imaginary, and the other two roots given by

$$r_{3,4} = \pm\sqrt{-\left(I + \frac{1}{k'G}\right)\frac{\rho\omega^2}{2} + \sqrt{\left(I - \frac{1}{k'G}\right)^2 \frac{\rho^2\omega^4}{4} + \rho A\omega^2}} \tag{3.72}$$

are either real or imaginary depending on the frequency ω (for a given material and geometry). They are real when the frequency is less than $\sqrt{k'GA/\rho I}$ and imaginary when the frequency is greater than $\sqrt{k'GA/\rho I}$. We call this cutoff frequency the critical frequency ω_c. Therefore, we must consider two cases when obtaining spatial solutions: $\omega < \omega_c$ and $\omega > \omega_c$.

When $\omega < \omega_c$, the spatial solution is written in terms of both sinusoidal and hyperbolic terms,

$$\begin{bmatrix} W(x) \\ \Psi(x) \end{bmatrix} = \begin{bmatrix} C_1 \\ D_1 \end{bmatrix} \sin ax + \begin{bmatrix} C_2 \\ D_2 \end{bmatrix} \cos ax + \begin{bmatrix} C_3 \\ D_3 \end{bmatrix} \sinh bx + \begin{bmatrix} C_4 \\ D_4 \end{bmatrix} \cosh bx, \tag{3.73}$$

where

$$a = \sqrt{\left(I + \frac{1}{k'G}\right)\frac{\rho\omega^2}{2} + \sqrt{\left(I - \frac{1}{k'G}\right)^2 \frac{\rho^2\omega^4}{4} + \rho A\omega^2}}$$

$$b = \sqrt{-\left(I + \frac{1}{k'G}\right)\frac{\rho\omega^2}{2} + \sqrt{\left(I - \frac{1}{k'G}\right)^2 \frac{\rho^2\omega^4}{4} + \rho A\omega^2}}. \tag{3.74}$$

and C_i and D_i are related by Equation 3.62.

When $\omega > \omega_c$, the spatial solution has sinusoidal terms of two frequencies,

$$\begin{bmatrix} W(x) \\ \Psi(x) \end{bmatrix} = \begin{bmatrix} \tilde{C}_1 \\ \tilde{D}_1 \end{bmatrix} \sin ax + \begin{bmatrix} \tilde{C}_2 \\ \tilde{D}_2 \end{bmatrix} \cos ax + \begin{bmatrix} \tilde{C}_3 \\ \tilde{D}_3 \end{bmatrix} \sin \tilde{b}x + \begin{bmatrix} \tilde{C}_4 \\ \tilde{D}_4 \end{bmatrix} \cos \tilde{b}x \tag{3.75}$$

where

$$a = \sqrt{\left(I + \frac{1}{k'G}\right)\frac{\rho\omega^2}{2} + \sqrt{\left(I - \frac{1}{k'G}\right)^2 \frac{\rho^2\omega^4}{4} + \rho A\omega^2}}$$

$$\tilde{b} = \sqrt{\left(I + \frac{1}{k'G}\right)\frac{\rho\omega^2}{2} - \sqrt{\left(I - \frac{1}{k'G}\right)^2 \frac{\rho^2\omega^4}{4} + \rho A\omega^2}}, \tag{3.76}$$

and $\tilde{C}_i$ and $\tilde{D}_i$ are related by

$$\tilde{D}_1 = -\frac{k'GAa^2 - \rho A\omega^2}{k'GAa}\tilde{C}_2, \quad \tilde{D}_2 = \frac{k'GAa^2 - \rho A\omega^2}{k'GAa}\tilde{C}_1$$

$$\tilde{D}_3 = -\frac{k'GA\tilde{b}^2 - \rho A\omega^2}{k'GA\tilde{b}}\tilde{C}_4, \quad \tilde{D}_4 = \frac{k'GA\tilde{b}^2 - \rho A\omega^2}{k'GA\tilde{b}}\tilde{C}_3. \tag{3.77}$$

Notice that b and $\tilde{b}$ are related by

$$b = i\tilde{b}. \tag{3.78}$$

Let us examine the frequency and the wave number where the transition occurs. This critical frequency can be written as

$$\omega_c = \sqrt{\frac{k'GA}{\rho I}} = \frac{1}{k}\sqrt{\frac{k'G}{\rho}}, \tag{3.79}$$

where k is the dimensionless radius of gyration or the inverse of the slenderness ratio,

$$k = \sqrt{\frac{I^*}{A^*}}\frac{1}{L^*} = \frac{1}{s}. \tag{3.80}$$

By substituting 3.79 into 3.74 and 3.76, the critical wave numbers are

$$\begin{aligned} a_c &= \frac{1}{k}\sqrt{(k'GI+1)} \\ b_c &= \tilde{b}_c = 0. \end{aligned} \tag{3.81}$$

Writing in terms of dimensional variables,

$$\begin{aligned} a_c &= \frac{1}{k}\sqrt{\left(k'\frac{G^*}{E^*}+1\right)} \\ &= \frac{1}{k}\sqrt{\left(\frac{1}{\gamma^2}+1\right)}, \end{aligned} \tag{3.82}$$

where γ is given by[7]

$$\gamma^2 = \frac{E^*}{k'G^*} = \frac{2(1+\nu)}{k'}. \tag{3.84}$$

Recall that k' depends on Poisson's ratio and the shape of the cross-section. Both k' and ν do not vary much so that we can say that the critical wave number essentially depends on the slenderness ratio.

Also, the case when $\omega < \omega_c$ is equivalent to the case when $a < a_c$. This can be verified by taking a derivative of a in the dispersion relationship (Equation 3.74 or 3.76) with respect to ω. We will find that the derivative is always positive implying that a is a monotonically increasing function of ω.

[7] Here, we use

$$G^* = E^*/2(1+\nu). \tag{3.83}$$

4. Natural Frequencies and Mode Shapes

So far, we have obtained the spatial solutions with four unknowns (Equation 3.18 for the Euler-Bernoulli and Rayleigh models, Equation 3.60 with Equation 3.62 for the shear and the Timoshenko models for $\omega < \omega_c$, and Equation 3.75 with Equation 3.77 for the Timoshenko model for $\omega > \omega_c$), and we have identified the possible boundary conditions that the spatial solutions have to satisfy (Equation 3.19 for the Euler-Bernoulli, Equation 3.35 for the Rayleigh and Equation 3.63 for the shear and Timoshenko models). The next step is to apply a set of boundary conditions in order to obtain the four unknown coefficients in the spatial solution. Upon applying the boundary conditions, we obtain four simultaneous equations which can be written as

$$[F]_{4\times4}\{\mathbf{C}\}_{4\times1} = \{\mathbf{0}\}_{4\times1}\,, \tag{3.85}$$

where $\{\mathbf{C}\}$ is the vector of coefficients in the spatial solution, and the matrix $[F]$ typically has sinusoidal and hyperbolic functions evaluated at the end points. The determinant of $[F]$ has to be zero to avoid the trivial solution or $\{\mathbf{C}\} = 0$. At this point, the best we can do is to reduce the number of unknowns from four to one. The equation obtained by setting the determinant to zero is the frequency equation, which has an infinite number of roots. For each root, the coefficients C_i of the corresponding spatial solution are unique only to a constant. The roots are in the form of dimensionless wave numbers, which can be translated into natural frequencies using the dispersion relationships. The corresponding spatial solutions are called the eigenfunctions or the mode shapes. The remaining constant in the eigenfunction is usually determined by *normalizing* the modal equation for convenience. Section 6 describes the normalization process. In this section, for each model, we obtain the frequency equations, their roots, and the mode shapes for four of the ten boundary conditions. Those for the other six cases are obtained using the symmetric and antisymmetric modes.

4.1 Symmetric and Antisymmetric Modes

First, let us identify all ten cases. They are free-free, hinged-hinged, clamped-clamped, clamped-free, sliding-sliding, free-hinged, free-sliding, clamped-hinged, clamped-sliding, and hinged-sliding supports. Using the symmetric and antisymmetric modes, we try to minimize the cases to be considered.

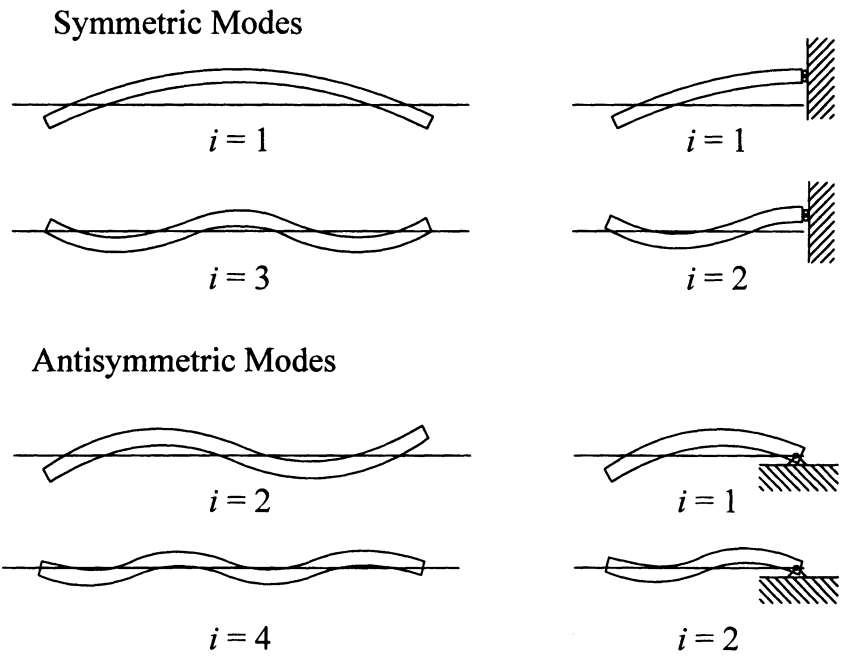

Figure 3.4. Symmetric and Antisymmetric Modes of the Free-Free Beam

Excluding the rigid body mode, the free-sliding is the symmetric mode[8] and the free-hinged is the antisymmetric mode of the free-free case as shown in Figure 3.4.

Similarly, the clamped-sliding is the symmetric mode and the clamped-hinged is the antisymmetric mode of the clamped-clamped case. The hinged-sliding is the symmetric mode of the hinged-hinged case and the antisymmetric mode of the sliding-sliding case.

Once we obtain the dimensionless wave numbers of the free-free, hinged-hinged, clamped-clamped, and clamped-free cases, we can find the dimensionless wave numbers of the remaining cases using the definition of the dimensionless wave number. The dimensionless wave number is $1/2\pi$ times the number of cycles contained in the beam length. As shown in Figure 3.4 for the free-free beam, the symmetric (free-sliding) and the

[8]The symmetric mode of the free-free beam requires that the total slope of the beam $v'(x,t)$ in the middle of the beam is zero. On the other hand, for the shear and Timoshenko models, the free-sliding beam requires that the angle of rotation due to bending α is zero at the sliding end. It seems that the symmetric mode of the free-free beam cannot represent the free-sliding beam. However, if we look more closely, the other condition for the sliding end is that $\beta = 0$ which leads to $v' = 0$. Therefore, the free-sliding beam can be replaced by the symmetric mode of the free-free beam.

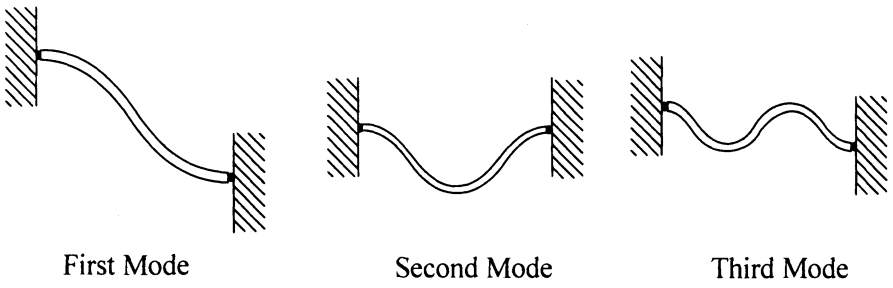

Figure 3.5. First Three Modes of the Sliding-Sliding Beam

Table 3.4. Relationships Between Normalized Wave Numbers of Various Boundary Conditions for $n = 1, 2, 3, ...$

1. $a_n^{free-sliding} = \frac{1}{2} a_{2n-1}^{free-free}$	5. $a_n^{hinged-sliding} = \frac{1}{2} a_{2n-1}^{hinged-hinged}$
2. $a_n^{free-hinged} = \frac{1}{2} a_{2n}^{free-free}$	6. $a_n^{hinged-hinged} = \frac{1}{2} a_{2n}^{hinged-hinged}$
3. $a_n^{clamped-sliding} = \frac{1}{2} a_{2n-1}^{clamped-clamped}$	7. $a_n^{sliding-sliding} = \frac{1}{2} a_{2n}^{sliding-sliding}$
4. $a_n^{clamped-hinged} = \frac{1}{2} a_{2n}^{clamped-clamped}$	8. $a_n^{sliding-hinged} = \frac{1}{2} a_{2n-1}^{sliding-sliding}$

antisymmetric (free-hinged) cases contain half of the cycles contained in the free-free case. Therefore, the dimensionless wave numbers are also half of that of the free-free case. The dimensionless wave numbers are related as shown in Table 3.4. Keep in mind that the rigid body mode ($a_1 = 0$) is omitted for the free-sliding, free-hinged, free-free, sliding-sliding cases. Note that the first mode of the free-free and the clamped-clamped cases are symmetric whereas the first mode of sliding-sliding case is antisymmetric as shown in Figure 3.5.

From the last four relations in Table 3.4, we can further deduce that the sliding-sliding support case is the same as the hinged-hinged case. Therefore, there are only four cases to be considered: free-free, hinged-hinged, clamped-clamped, clamped-free. Similarly, the mode shapes of these four cases can be used to generate the mode shapes of the other six cases. For instance, the first and third mode shapes (symmetric modes) of the free-free case generate the first and second mode shapes of the free-sliding case (excluding the rigid body mode), and the second and fourth mode shapes (antisymmetric modes) generate the first and second mode shapes of the free-hinged case as shown in Figure 3.4. Similarly, mode shapes of the sliding-sliding case can be generated by hinged-hinged case.

Table 3.5. Frequency Equations and the First Five Wave Numbers of the Euler-Bernoulli Model

	Frequency Equation	a_1	a_2	a_3	a_4	a_5
c-c and f-f	$\cos a \cosh a - 1 = 0$	4.730	7.853	10.996	14.137	17.279
h-h or s-s	$\sin a \sinh a = 0$	π	2π	3π	4π	5π
c-f	$\cos a \cosh a + 1 = 0$	1.875	4.694	7.855	10.996	14.137

It is important to note that it is implied in Figure 3.4 that the cross-sectional areas of the beams are the same, and the lengths of the free-sliding or free-hinged beams are half of the free-free beam. In fact, this does not always have to be the case. As long as the slenderness ratio of the free-free beam is twice that of the free-sliding or free-hinged beam, this analysis works. Therefore, more precisely, we can say that the dimensionless wave numbers of the free-free beam with the slenderness ratio of s is twice the dimensionless wave numbers of the free-sliding or free-hinged case with the slenderness ratio of $s/2$.

4.2 Euler-Bernoulli Beam Model

The spatial solution $W(x)$ is given in Equation 3.18, and the expressions for the boundary conditions are given in Equation 3.13. Here the dimensionless wave numbers are obtained by applying the four sets of boundary conditions to the spatial solution.

One special characteristic of this model is that the frequency equations for the free-free and clamped-clamped cases are the same. This is the case only for this model. The frequency equations for four cases and the first five dimensionless wave numbers are tabulated in Table 3.5. The wave numbers for the remaining cases, using Table 3.4, are tabulated in Table 3.6. Note that we were able to obtain the numerical values for the dimensionless wave numbers. It will be shown that for other models, it is not possible to do so.

The actual frequency of vibration can be found using the dispersion relationship in Equation 3.16. That is,

$$\omega^* = \sqrt{\frac{E^* I^*}{\rho^* A^* L^{*4}}} a^2. \tag{3.86}$$

Using the dispersion relationship, we can also write

$$\omega_n^* L^* \sqrt{\rho^*/E^*} = \frac{a_n^2}{s}, \tag{3.87}$$

Table 3.6. First Five Wave Numbers Obtained Using the Symmetric and Antisymmetric Modes

	a_1	a_2	a_3	a_4	a_5
c-s and f-s	2.365	5.498	8.639	11.781	14.923
c-h and f-h	3.927	7.069	10.210	13.352	16.493
h-s	0.5π	1.5π	2.5π	3.5π	4.5π

so that we can plot $\omega_n^* L^* \sqrt{\rho^*/E^*}$ as a function of $1/s$. This will be useful when we compare the natural frequencies predicted by other models.

4.3 Rayleigh Beam Model

The expressions for the boundary conditions are given in Equation 3.23. Unlike in the Euler-Bernoulli beam case, there are two wave numbers in the Rayleigh beam, a and b[9]. The frequency equation will have both a and b. In order to find the solution to the frequency equations, one of the wave numbers has to be expressed in terms of the other so that the frequency equation is a function of one wave number only, let us say a. Following is the procedure used to express b in terms of a.

The dispersion relations given in Equation 3.34 can be written as

$$\begin{aligned} a^2 &= B_1 + \sqrt{B_1^2 + B_2} \\ b^2 &= -B_1 + \sqrt{B_1^2 + B_2}, \end{aligned} \tag{3.88}$$

where B_1 and B_2, in this case, are

$$B_1 = \frac{\rho I \omega^2}{2}, \quad B_2 = \rho A \omega^2. \tag{3.89}$$

Solving for B_1 and B_2 in Equation 3.88, we obtain

$$\begin{aligned} B_1 &= \frac{a^2 - b^2}{2} \\ B_2 &= a^2 b^2. \end{aligned} \tag{3.90}$$

[9]Note that the wave number of a hyperbolic function, b, does not have a physical meaning while the wave number of a sinusoidal function, a, does. Nonetheless, we call b the wave number of the hyperbolic function.

Note that Equations 3.90 are still the dispersion relations. Now, let us examine the ratio of B_1 to B_2. From Equations 3.90 and 3.89,

$$\begin{aligned}\frac{B_1}{B_2} &= \frac{1}{2}\left(\frac{1}{b^2} - \frac{1}{a^2}\right) \\ &= \frac{I}{2A},\end{aligned} \tag{3.91}$$

where the ratio of I to A is k^2 from Equation 3.80. Now, we can write

$$\begin{aligned}\frac{1}{b^2} - \frac{1}{a^2} &= k^2 \\ &= \frac{1}{s^2}.\end{aligned} \tag{3.92}$$

Therefore, the wave numbers of the Rayleigh beam are related by the slenderness ratio. This contrasts with the case of the Euler-Bernoulli beam where the dimensionless wave numbers are independent of the geometry of the beam but dependent solely on the boundary conditions. Expressing b in terms of a and k (or s),

$$\begin{aligned}b &= a\sqrt{\frac{1}{a^2k^2+1}} \\ &= as\sqrt{\frac{1}{a^2+s^2}}.\end{aligned} \tag{3.93}$$

Let us consider the case when $k = 0$. Then, a equals b by Equation 3.92 or 3.93, and B_1 is zero by Equation 3.90. Comparing Equation 3.88 with 3.16, we also find that the wave numbers a and b are equal to the wave number of the Euler-Bernoulli beam. For a slender beam where s is large (k is small), the two wave numbers approach each other so that the result resembles that of the Euler-Bernoulli beam[10].

The frequency equations for four cases are given in Table 3.7. Notice that the frequency equations contain both a and b as predicted earlier. Further, notice that when b is expressed in terms of a using Equation 3.93, the geometrical property, slenderness ratio, enters the frequency equations. Therefore, the roots of the frequency equations depend on the slenderness of the beam and are no longer independent of the geometry of the beam. The significance of the previous statement is that it implies that the mode shapes also vary with the slenderness ratio.

[10] In general, the slenderness ratio of 100 is sufficient so that there is little difference among all four models (Euler-Bernoulli, Rayleigh, shear, and Timoshenko).

Table 3.7. The Frequency Equations of the Rayleigh Model

f-f	$(b^6 - a^6)\sin a \sinh b + 2a^3b^3 \cos a \cosh b - 2a^3b^3 = 0$
c-c	$(b^2 - a^2)\sin a \sinh b - 2ab \cos a \cosh b + 2ab = 0$
h-h or s-s	$\sin a \sinh b = 0$
c-f	$(b^2 - a^2)\, ab \sin a \sinh b + (b^4 + a^4)\cos a \cosh b + 2a^2b^2 = 0$

As mentioned earlier, as s approaches infinity, the frequency equation becomes identical to that of the Euler-Bernoulli beam. The best way to represent the solution of the frequency equation is to plot wave numbers as a continuous function of s or k. Here, we will use k for a reason which will become apparent shortly. The frequency equations in Table 3.7 are transcendental equations that have to be solved numerically. In order to obtain a smooth function, $a(k)$, we use the following analysis. Let one of the frequency equations be $F(a, b)$. For example, for the $free - free$ case, we let

$$\begin{aligned} F(a,b) &= (b^6 - a^6)\sin a \sinh b + 2a^3b^3 \cos a \cosh b - 2a^3b^3 \\ &= 0. \end{aligned} \tag{3.94}$$

From Equation 3.93, b is a function of a and k, $b(a, k)$. dF and db are given by

$$\begin{aligned} dF &= \frac{\partial F}{\partial a}da + \frac{\partial F}{\partial b}db \\ db &= \frac{\partial b}{\partial a}da + \frac{\partial b}{\partial k}dk. \end{aligned} \tag{3.95}$$

Combining two expressions, dF is given by

$$dF = \frac{\partial F}{\partial a}da + \frac{\partial F}{\partial b}\left(\frac{\partial b}{\partial a}da + \frac{\partial b}{\partial k}dk\right) = 0, \tag{3.96}$$

where dF is zero because $F(a, b)$ is zero for all values of a and b. Solving for da/dk, we obtain

$$\frac{da}{dk} = \frac{-\frac{\partial F}{\partial b}\frac{\partial b}{\partial k}}{\frac{\partial F}{\partial a} + \frac{\partial F}{\partial b}\frac{\partial b}{\partial a}}, \tag{3.97}$$

where the right hand side is a function of a, b, and k. After b is expressed in terms of a and k by Equation 3.93, the right hand side is a function of a and k only. Now, this is a first order ordinary differential equation which can be solved once we know the initial value $a(k = 0)$. The initial value is identical to the wave numbers of the Euler-Bernoulli model given

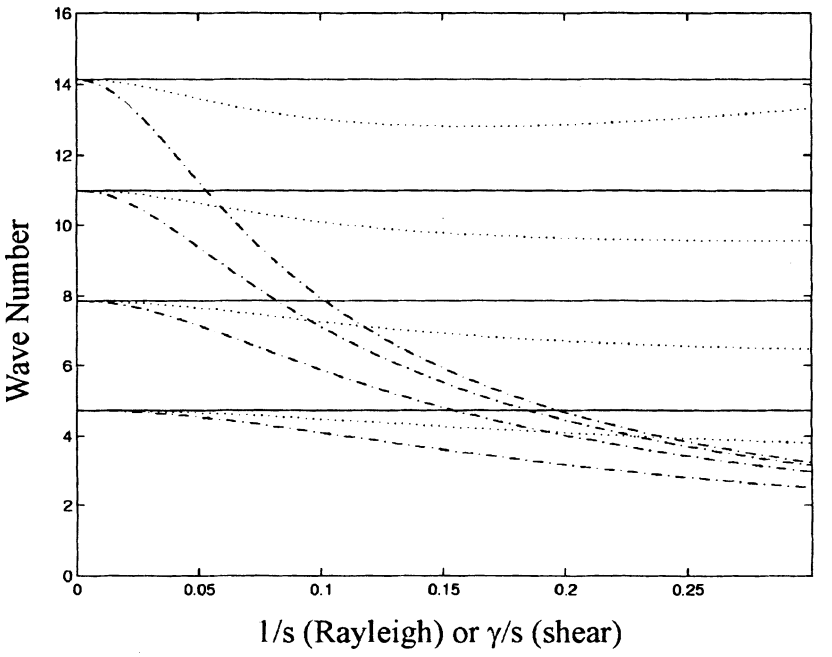

Figure 3.6. First Four Pairs of Wave Numbers of the Free-Free Rayleigh Beam and Clamped-Clamped Shear Beam. – Euler-Bernoulli; —· *b*; ·· *a*

in Table 3.5 and 3.6. Note that depending on which wave number we use as an initial value, $a_1, a_2, \cdots$, we can track that particular wave number as the slenderness ratio varies. The initial value problem is solved using MATLAB, and the results are shown in Figures 3.6, 3.7, 3.8, and 3.9. The four solid lines in each figure are the wave numbers obtained using the Euler-Bernoulli theory. They are not affected by the slenderness ratio. The two lines (dotted and dot-dashed) that emerge from the n^{th} solid line near $1/s = 0$ are the n^{th} waves numbers, a_n and b_n, of the Rayleigh model. Using these plots, we obtain up to four sets of wave numbers for each case.

Having such plots, we can instantly obtain the dimensionless wave numbers once we know the slenderness ratio. These dimensionless wave numbers together with the complete properties of the beam lead to the natural frequencies using the dispersion relations. The natural frequency, solved in terms of the wave numbers and the property of the beam using the dispersion relations (Equations 3.89 and 3.90), is given

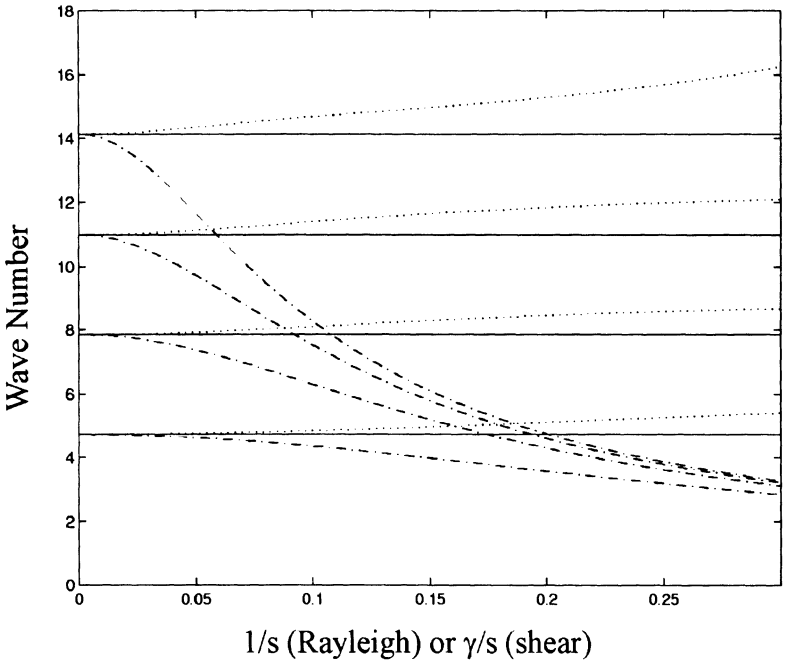

Figure 3.7. First Four Pairs of Wave Numbers of the Clamped-Clamped Rayleigh Beam and Free-Free Shear Beam. – Euler-Bernoulli; –· *b*; ·· *a*

by

$$\omega^2 = \frac{a^2 - b^2}{\rho I} \text{ or } \omega^2 = \frac{a^2 b^2}{\rho A}, \tag{3.98}$$

which is equivalent to

$$\omega^{*2} = \left(a^2 - b^2\right) \frac{E^*}{\rho^* L^{*2}} \text{ or } \omega^{*2} = \frac{a^2 b^2}{s^2} \frac{E^*}{\rho^* L^{*2}}. \tag{3.99}$$

Since we know a and b as discrete functions of $1/s$ from Figures 3.6, 3.7, 3.8, and 3.9, we can plot $\omega^* L^* \sqrt{\rho^*/E^*}$ as a function of $1/s$ using the first relation in Equation 3.99,

$$\omega^* L^* \sqrt{\rho^*/E^*} = \sqrt{a^2 - b^2}. \tag{3.100}$$

The plots of $\omega^* L^* \sqrt{\rho^*/E^*}$ as functions of $1/s$ are shown from Figures 3.10 to 3.13. The benefit of having such plots is that once we know s, L^*, ρ^*, and E^*, we can obtain ω^* instantly. For example, the first four pairs of wave numbers of the clamped-free Rayleigh beam, when $s = 9.1192$ (or $1/s = 0.11$), can be obtained from Figure 3.9 and the

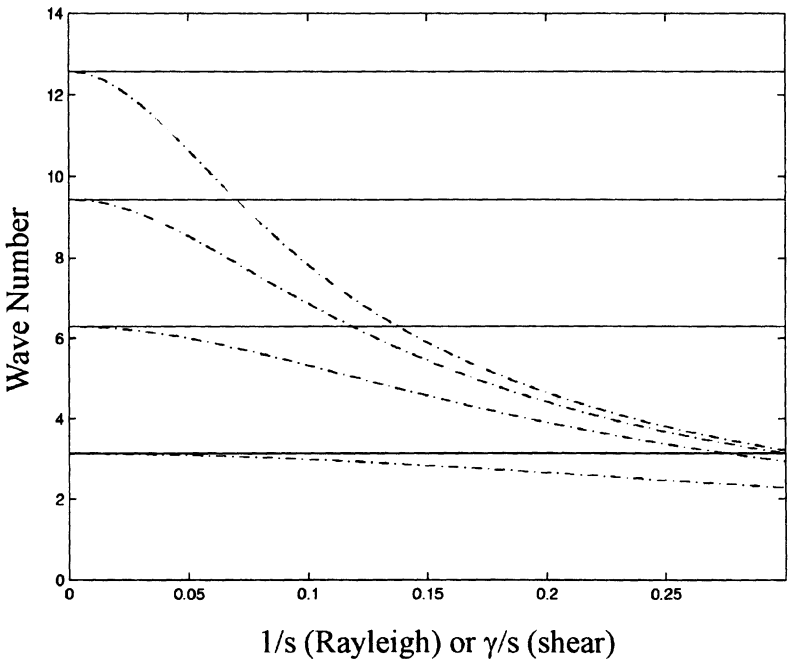

Figure 3.8. First Four Pairs of Wave Numbers of the Hinged-Hinged (or Sliding-Sliding) Rayleigh and Shear Beam. — Euler-Bernoulli or a; $-\cdot$ b

natural frequencies, where $L^* = 1\ m$, $\rho^* = 7830\ kg/m^3$, and $E^* = 200\ GPa$, can be obtained from Figure 3.13. The exact numbers are

$$\begin{aligned}
(a_1, b_1) &= (1.869, 1.831)\,, \quad \omega_1 = 1 \\
(a_2, b_2) &= (4.571, 4.086)\,, \quad \omega_2 = 5.459 \\
(a_3, b_3) &= (7.629, 5.851)\,, \quad \omega_3 = 13.046 \\
(a_4, b_4) &= (10.686, 6.937)\,, \quad \omega_4 = 21.664.
\end{aligned} \tag{3.101}$$

Note that the natural frequencies are non-dimensionalized by the first natural frequency given by $\omega_1^* = 1896\ rad/s$. These numbers will be used in the example problem at the end of this chapter.

One comment is made here regarding the wave numbers and the frequency charts for the other six sets of boundary conditions. It was mentioned earlier that the dimensionless wave numbers of the free-free beam with the slenderness ratio of s are twice the dimensionless wave numbers of the free-sliding or free-hinged case with the slenderness ratio of $s/2$, where the same analogy is applied to the other cases: the clamped-clamped and hinged-hinged beams. For example, the wave numbers of the free-sliding beam are obtained from the wave numbers of the odd

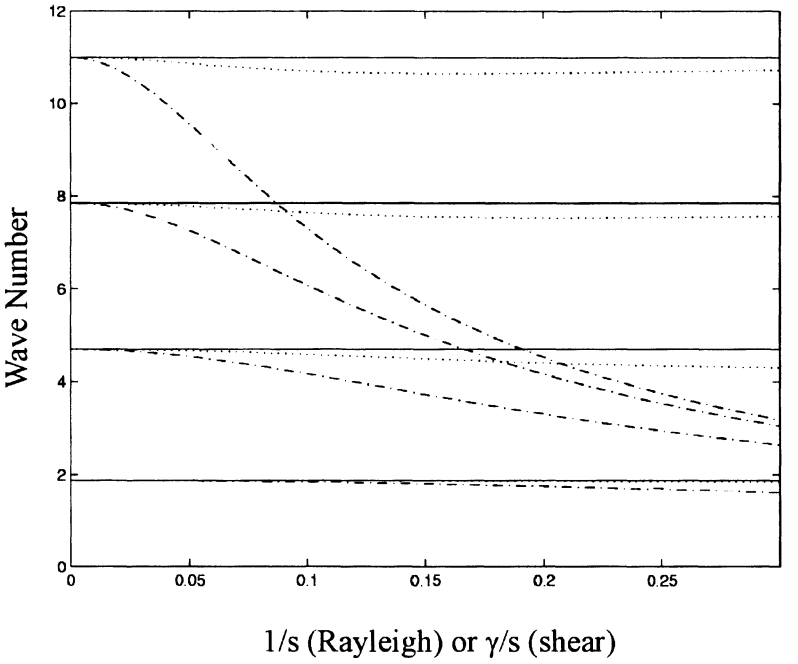

Figure 3.9. First Four Pairs of Wave Numbers of the Clamped-Free Rayleigh and Shear Beam. – Euler-Bernoulli; –· *b*; ·· *a*

modes of free-free beams (a_1, b_1), (a_3, b_3), $\cdots$ by replacing the abscissa label $1/s$ with $1/(2s)$ and ordinate label wave numbers with $2\times$(wave numbers) in Figure 3.6. In this way, a point that correspond to the inverse slenderness ratio of $1/s_o$ and wave numbers of a_o and b_o in Figure 3.6, would correspond to the inverse slenderness ratio of $2/s_o$ and the wave numbers of $a_o/2$ and $b_o/2$ in the new plot. The frequency charts can be modified in the same way so that the abscissa label $1/s$ is replaced by $1/(2s)$ and the wave numbers in ordinate label, $\sqrt{a^2 - b^2}$, are replaced by $2\times$(wave number) so that the new ordinate label is $2\sqrt{a^2 - b^2}$ or $2\omega^* L^* \sqrt{\rho^*/E^*}$. The wave numbers and the frequency charts of the shear and Timoshenko models are obtained in the same way.

4.4 Shear Beam Model

The same analysis as for the Rayleigh beam is applied here. Again, the dispersion relationship given in Equation 3.59 is written in the form of Equation 3.88 where B_1 and B_2 are given by

$$B_1 = \frac{\rho\omega^2}{2k'G}, B_2 = \rho A\omega^2, \tag{3.102}$$

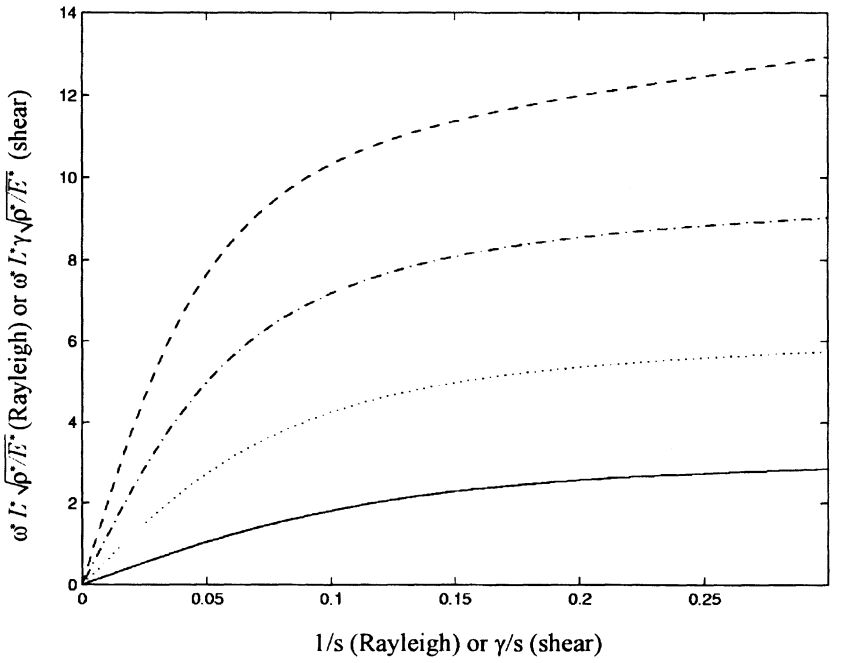

Figure 3.10. Frequency Curves for the Free-Free Rayleigh and Clamped-Clamped Shear Beam. – Ω_1^*; ·· Ω_2^*; –· Ω_3^*; –– Ω_4^*

and

$$B_1 = \frac{a^2 - b^2}{2} \qquad (3.103)$$
$$B_2 = a^2 b^2.$$

The latter relations are identical to those of the Rayleigh beam (Equation 3.90). Using Equation 3.103, the ratio of B_1 to B_2 is reduced to

$$\frac{B_1}{B_2} = \frac{1}{2}\left(\frac{1}{b^2} - \frac{1}{a^2}\right), \qquad (3.104)$$

and using Equation 3.102, the ratio is reduced to

$$\frac{B_1}{B_2} = \frac{1}{2k'GA} = \frac{E^* I^* L^{*2}}{2k'G^* L^{*4} A^*}$$
$$= \frac{(1+\nu)}{k'}\frac{1}{s^2} = \frac{1}{2}\left(\frac{\gamma}{s}\right)^2, \qquad (3.105)$$

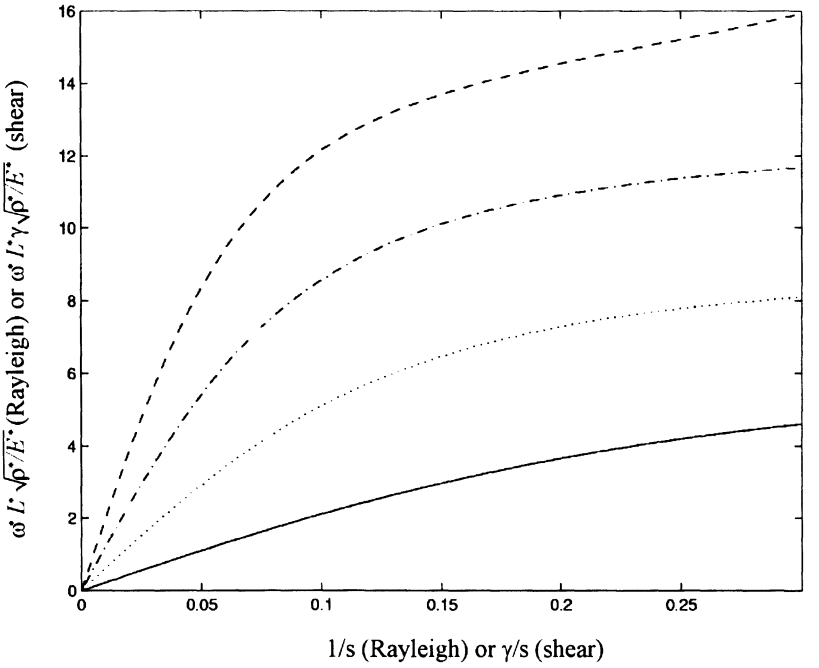

Figure 3.11. Frequency Curves for the Clamped-Clamped Rayleigh and Free-Free Shear Beam. – Ω_1^*; ·· Ω_2^*; –· Ω_3^*; –– Ω_4^*

where γ is given in Equation 3.84 and G^* is related to E^* by Equation 3.83. Therefore, we can write

$$\left(\frac{1}{b^2} - \frac{1}{a^2}\right) = \left(\frac{\gamma}{s}\right)^2 = (\gamma k)^2 . \tag{3.106}$$

Solving for b, we obtain

$$b = a\sqrt{\frac{1}{\gamma^2 k^2 a^2 + 1}} = \frac{as}{\gamma}\sqrt{\frac{1}{a^2 + s^2/\gamma^2}}. \tag{3.107}$$

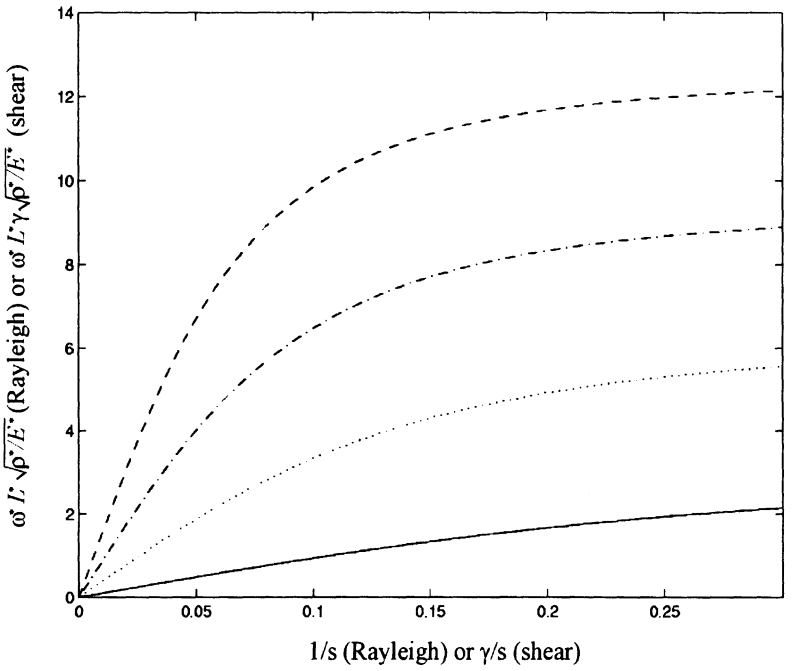

Figure 3.12. Frequency Curves for the Hinged-Hinged (or Sliding-Sliding) Rayleigh and Shear Beam. $-\ \Omega_1^*$; $\cdot\cdot\ \Omega_2^*$; $-\cdot\ \Omega_3^*$; $--\ \Omega_4^*$

Table 3.8. Frequency Equations of the Shear Model

f-f	$(b^2 - a^2)\sin a \sinh b - 2ab\cos a \cosh b + 2ab = 0$
c-c	$(b^6 - a^6)\sin a \sinh b + 2a^3b^3 \cos a \cosh b - 2a^3b^3 = 0$
h-h or s-s	$\sin a \sinh b = 0$
c-f	$(b^2 - a^2)\, ab \sin a \sinh b + (b^4 + a^4)\cos a \cosh b + 2a^2b^2 = 0$

Looking again at Equation 3.62, we find that the coefficients in the spatial solutions are related by

$$D_1 = -\frac{b^2}{a}C_2,\ D_2 = \frac{b^2}{a}C_1$$
$$D_3 = \frac{a^2}{b}C_4,\ D_4 = \frac{a^2}{b}C_3, \tag{3.108}$$

so that we can write the spatial solution in terms of the wave numbers only.

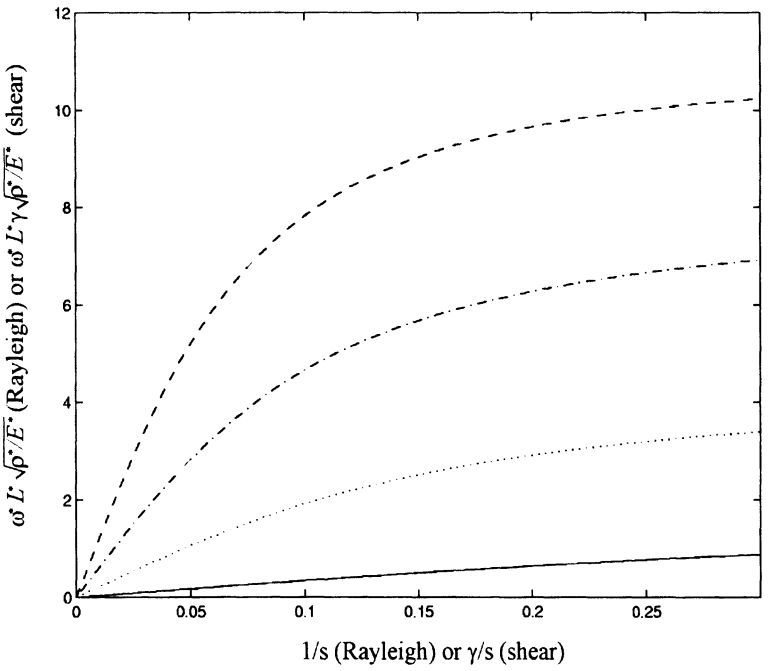

Figure 3.13. Frequency Curves for the Clamped-Free Rayleigh and Shear Beam. – Ω_1^*; ·· Ω_2^*; –· Ω_3^*; –– Ω_4^*

The frequency equations for the shear beam are given in Table 3.8. Note that the frequency equation for the free-free shear beam is identical to the clamped-clamped Rayleigh beam. Also, the frequency equation for the clamped-clamped shear beam is identical to that of the free-free Rayleigh beam. The frequency equations for the other two cases are the same as the ones for the Rayleigh beam. Also note that the relationship between wave numbers (Equation 3.106) is similar to that of the Rayleigh beam (Equation 3.92). In fact, $1/s$ is modified by the factor γ. We can use the plots for the Rayleigh beam here by just replacing the label for the abscissa $1/s$ with γ/s and switching the free-free case with the clamped-clamped case. The clamped-clamped case is shown in Figure 3.6, free-free in Figure 3.7, hinged-hinged (or sliding-sliding) in Figure 3.8, and clamped-free in Figure 3.9.

From Equations 3.102 and 3.103, the natural frequency is given by

$$\sqrt{\frac{\rho^* L^{*2}}{E^*}}\sqrt{\frac{2(1+\nu)}{k'}}\omega^* = \sqrt{a^2 - b^2}, \tag{3.109}$$

where $\sqrt{2(1+\nu)/k'}$ is denoted as γ throughout this chapter (Equation 3.84). Notice the similarity between Equations 3.100 and 3.109. Therefore, we can use the plots used in the Rayleigh beam (Figures 3.10 to 3.13) by simply replacing the ordinate with $\omega^* L^* \gamma \sqrt{\rho^*/E^*}$. The notation Ω_n^* in the figures are representative of $\omega_n^* L^* \sqrt{\rho^*/E^*}$ for the Rayleigh and $\omega_n^* L^* \gamma \sqrt{\rho^*/E^*}$ for the shear model.

Again, these plots are convenient for easily obtaining the natural frequencies for a given s and γ. From Figures 3.9 and 3.13, for $1/s = 0.11$, $L^* = 1\ m$, $\gamma = 2.205$, $\rho^* = 7830\ kg/m^3$, and $E^* = 200\ GPa$, the pairs of wave numbers and the natural frequencies are

$$\begin{aligned}
(a_1, b_1) &= (1.846, 1.686)\,, \quad \omega_1 = 1 \\
(a_2, b_2) &= (4.352, 2.998)\,, \quad \omega_2 = 4.1923 \\
(a_3, b_3) &= (7.539, 3.626)\,, \quad \omega_3 = 8.7823 \\
(a_4, b_4) &= (10.686, 3.857)\,, \quad \omega_4 = 13.241,
\end{aligned} \tag{3.110}$$

where the natural frequencies are non-dimensionalized by the first natural frequency $\omega_1^* = 1725\ rad/s$.

4.5 Timoshenko Beam Model

Here, we follow the same procedure used for the Rayleigh and the shear beams by letting

$$\begin{aligned}
B_1 &= \frac{\rho I \omega^2}{2} \\
B_2 &= \frac{\rho \omega^2}{2k'G} = B_1 \gamma^2 \\
B_3 &= \rho A \omega^2,
\end{aligned} \tag{3.111}$$

so that the dispersion relations in Equations 3.74 and 3.76 can be written as

$$\begin{aligned}
a &= \sqrt{(B_1 + B_2) + \sqrt{(B_1 - B_2)^2 + B_3}} \\
b &= \sqrt{-(B_1 + B_2) + \sqrt{(B_1 - B_2)^2 + B_3}} \\
&= i\tilde{b}.
\end{aligned} \tag{3.112}$$

Solving for B_1, B_2, and B_3, we obtain

$$B_1 = \frac{a^2 - b^2}{2(1+\gamma^2)}$$
$$B_2 = \frac{\gamma^2 (a^2 - b^2)}{2(1+\gamma^2)}$$
$$B_3 = \frac{1}{4}\left\{ (a^2+b^2)^2 - \frac{(1-\gamma^2)^2}{(1+\gamma^2)^2}(a^2-b^2)^2 \right\}, \tag{3.113}$$

where γ is a constant given in Equation 3.84. Note that B_1, B_2, and B_3 can be obtained in terms of a and $\tilde{b}$ by replacing b^2 with $\tilde{b}^2$ in Equation 3.113. By equating the ratio of B_3 to B_1 obtained using Equations 3.111 and 3.113, we obtain the relationship between the wave numbers given by

$$\frac{(\gamma^2 b^2 + a^2)(a^2\gamma^2 + b^2)}{(a^2 - b^2)(1+\gamma^2)} = s^2. \tag{3.114}$$

Again, the relationship between a and $\tilde{b}$ can be obtained by replacing b with $i\tilde{b}$ in Equation 3.114 as

$$\frac{\left(-\gamma^2\tilde{b}^2 + a^2\right)\left(\gamma^2 a^2 - \tilde{b}^2\right)}{\left(a^2 + \tilde{b}^2\right)(1+\gamma^2)} = s^2. \tag{3.115}$$

Note that the wave numbers are related by s and γ.

Using Equations 3.111 and 3.113, we can write Equation 3.62 as

$$D_1 = -\frac{a^2 + \gamma^2 b^2}{(1+\gamma^2)\,a} C_2, \quad D_2 = \frac{a^2 + \gamma^2 b^2}{(1+\gamma^2)\,a} C_1$$
$$D_3 = \frac{b^2 + \gamma^2 a^2}{(1+\gamma^2)\,b} C_4, \quad D_4 = \frac{b^2 + \gamma^2 a^2}{(1+\gamma^2)\,b} C_3, \tag{3.116}$$

so that the spatial solution for $\omega < \omega_c$ can be written in terms of wave numbers only. Using Equations 3.111 and 3.113 with b replaced by $i\tilde{b}$, the coefficients $\tilde{C}_i$ and $\tilde{D}_i$ in Equation 3.77 are then related by

$$\tilde{D}_1 = -\frac{a^2 - \gamma^2\tilde{b}^2}{(1+\gamma^2)\,a} \tilde{C}_2, \quad \tilde{D}_2 = \frac{a^2 - \gamma^2\tilde{b}^2}{(1+\gamma^2)\,a} \tilde{C}_1$$
$$\tilde{D}_3 = -\frac{\tilde{b}^2 - \gamma^2 a^2}{(1+\gamma^2)\,\tilde{b}} \tilde{C}_4, \quad \tilde{D}_4 = \frac{\tilde{b}^2 - \gamma^2 a^2}{(1+\gamma^2)\,\tilde{b}} \tilde{C}_3, \tag{3.117}$$

which we can use to express the spatial solution for $\omega > \omega_c$ in terms of the wave numbers only.

Table 3.9. Frequency Equations of the Timoshenko Model When $a < a_c$

f-f	$\frac{(a^2-b^2)(a^2+b^2+\gamma^2ab-ab)(a^2+b^2-\gamma^2ab+ab)}{2ab(b^2+\gamma^2a^2)(a^2+\gamma^2b^2)}\sin a\sinh b-\cos a\cosh b+1=0$
c-c	$\frac{(a^2-b^2)(\gamma^2a^2+\gamma^2b^2+\gamma^2ab-ab)(\gamma^2a^2+\gamma^2b^2-\gamma^2ab+ab)}{2ab(b^2+\gamma^2a^2)(a^2+\gamma^2b^2)}\sin a\sinh b-\cos a\cosh b+1=0$
h-h	$\sin a\sinh b=0$
c-f	$(a^2-b^2)\sin a\sinh b-ab\frac{(a^4+a^4\gamma^4+4\gamma^2a^2b^2+b^4\gamma^4+b^4)}{(b^2+\gamma^2a^2)(a^2+\gamma^2b^2)}\cos a\cosh b-2ab=0$

Table 3.10. Frequency Equations of the Timoshenko Model When $a > a_c$

f-f	$\frac{(a^2+\tilde{b}^2)\left[(a^2-\tilde{b}^2)^2+(a\tilde{b}\gamma^2-a\tilde{b})^2\right]}{2a\tilde{b}(-\tilde{b}^2+\gamma^2a^2)(a^2-\gamma^2\tilde{b}^2)}\sin a\sin\tilde{b}-\cos a\cos\tilde{b}+1=0$
c-c	$\frac{(a^2+\tilde{b}^2)\left[(\gamma^2a^2-\gamma^2\tilde{b}^2)^2+(\gamma^2a\tilde{b}-a\tilde{b})^2\right]}{2a\tilde{b}(-\tilde{b}^2+\gamma^2a^2)(a^2-\gamma^2\tilde{b}^2)}\sin a\sin\tilde{b}-\cos a\cos\tilde{b}+1=0$
h-h	$\sin a\sin\tilde{b}=0$
c-f	$\left(a^2+\tilde{b}^2\right)\sin a\sin\tilde{b}-a\tilde{b}\frac{(a^4+a^4\gamma^4-4\gamma^2a^2\tilde{b}^2+\tilde{b}^4\gamma^4+\tilde{b}^4)}{(-\tilde{b}^2+\gamma^2a^2)(a^2-\gamma^2\tilde{b}^2)}\cos a\cos\tilde{b}-2a\tilde{b}=0$

Note that we only need to obtain one frequency equation for each boundary condition. Once the frequency equation for the case $a < a_c$ is obtained, the other frequency equation for $a > a_c$ can be obtained by replacing b with $i\tilde{b}$. The frequency equations for the case $a < a_c$ are tabulated in Table 3.9 and for the case $a > a_c$ in Table 3.10.

The frequency equations depend on a, b (or $\tilde{b}$) and γ. From Equations 3.114 (or 3.115), b (or $\tilde{b}$) can be written as a function of a, s and γ so that the frequency equation can be written in terms of a, s, and γ only. Therefore, the roots of the frequency equations, a, depend on both s and γ. After obtaining the roots of the frequency equations in terms of a for a given s and γ, b (or $\tilde{b}$) can be found using the relationship in Equation 3.114 (or 3.115). Similarly, a can be written as a function of b (or $\tilde{b}$) using Equations 3.114 (or 3.115) so that the frequency equation can be written in terms of b (or $\tilde{b}$), s, and γ. The roots of the frequency equation b (or $\tilde{b}$) are found for a given s and γ. Then, the corresponding a can be found using Equations 3.114 or 3.115.

The proper way to represent the roots is to make a three-dimensional plot of wave numbers as functions of s and γ. Note that the roots of the frequency equations (a and b) in the shear beam case also depend on both s and γ. However, in that case, s and γ always appear as γ/s

so that we can treat γ/s as one variable. Therefore, we only needed two-dimensional plots of wave numbers as functions of γ/s. In the case of the Timoshenko beam, such a simplification cannot be made because s and γ do not always appear together. Therefore, the wave numbers are plotted for $\gamma = 2.205$ which is a reasonable value for a thin steel hollow section[11].

In order to obtain the pairs of wave numbers a_n and b_n for $a_n < a_c$ that satisfy the frequency equations, we would solve the initial value problem given in Equation 3.97 with the n^{th} wave number of the Euler-Bernoulli model as an initial value to obtain a_n first, and then we would obtain b_n using Equation 3.114 as we have done for the Rayleigh and shear models. In order to obtain the pairs of wave numbers a_n and $\tilde{b}_n$ for $a_n > a_c$, we would again solve the same initial value problem with a_n at the transition (a_c) as the initial value instead. The value of the slenderness ratio at the n^{th} transition is denoted as s_n so that $a_n < a_c$ or $\omega_n < \omega_c$ refers to the region where $1/s < 1/s_n$. The pairs of wave numbers are plotted in Figures 3.14 to 3.17. The wave number for the Euler-Bernoulli beam is included for comparison. These plots are obtained by solving an initial value problem for the region $1/s < 1/s_n$ as done in the Rayleigh and shear beam cases. For the region $1/s > 1/s_n$, a root finding program is used because the solution to the initial value problem had difficulties in converging.

Note that four separate plots are shown for the hinged-hinged beam in Figure 3.16. Only in this case, a_n always corresponds to two values of b: a_n corresponds to b_n and $\tilde{b}_n^{(2)}$ for $1/s < 1/s_n$ and to $\tilde{b}_n^{(1)}$ and $\tilde{b}_n^{(2)}$ for $1/s > 1/s_n$. It is important to note that each pair corresponds to a distinct natural frequency. The consequence is that there are twice as many natural frequencies in the hinged-hinged case as in other cases.

In order to explain why this is the case, let us look at the frequency equation of the hinged-hinged beam given in Table 3.9 or 3.10,

$$\begin{aligned} \sin a \sinh b &= 0 \text{ for } a < a_c \\ \sin a \sin \tilde{b} &= 0 \text{ for } a > a_c. \end{aligned} \tag{3.118}$$

Note that the frequency equation is satisfied for any value of b (or $\tilde{b}$) as long as $\sin ax$ is zero (or $a_n = n\pi$ for $n = 1, 2, 3, \cdots$). When we solve for b_n (or $\tilde{b}$) that corresponds to a_n in Equation 3.114 or 3.115, there are two unique expressions. When $1/s < 1/s_n$, one is real and the other is

[11] Poisson's ratio of 0.29, outer radius of 0.16 m, and the inner radius of 0.15 m are used to obtain the shear factor $k' = 0.53066$ using Table 3.3. The value of $\gamma = 2.205$ is then obtained using Equation 3.84.

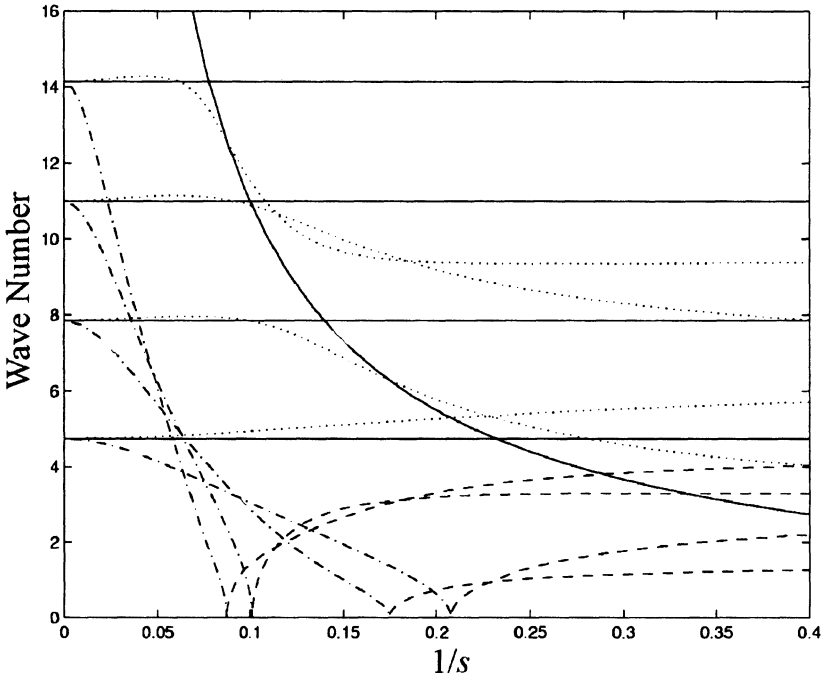

Figure 3.14. First Four Sets of Wave Numbers of the Free-Free Timoshenko Beam. – Euler-Bernoulli; ·· a; –· b; –– $\tilde{b}$

imaginary. We call the real root b_n and the imaginary root $i\tilde{b}_n^{(2)}$. When $1/s > 1/s_n$, both roots are imaginary where one is $i\tilde{b}_n^{(1)}$ and the other is $i\tilde{b}_n^{(2)}$.

The natural frequencies that correspond to each pair can be calculated using the relation for B_1 in Equations 3.111 and 3.113. The natural frequencies for the free-free, clamped-clamped, and clamped-free cases are given by

$$\omega_n^* L^* \sqrt{\rho^*/E^*} = \sqrt{\frac{a_n^2 - b_n^2}{1+\gamma^2}} \text{ for } 1/s < 1/s_n$$

$$= \sqrt{\frac{a_n^2 + \left(\tilde{b}_n\right)^2}{1+\gamma^2}} \text{ for } 1/s > 1/s_n. \qquad (3.119)$$

The quantity $\omega_n^* L^* \sqrt{\rho^*/E^*}$ is plotted as a function of $1/s$ for $\gamma = 2.205$ in Figures 3.18, 3.19, and 3.21 using the values of a_n, b_n, and $\tilde{b}_n$ that we know already from Figures 3.14, 3.15, and 3.17 .

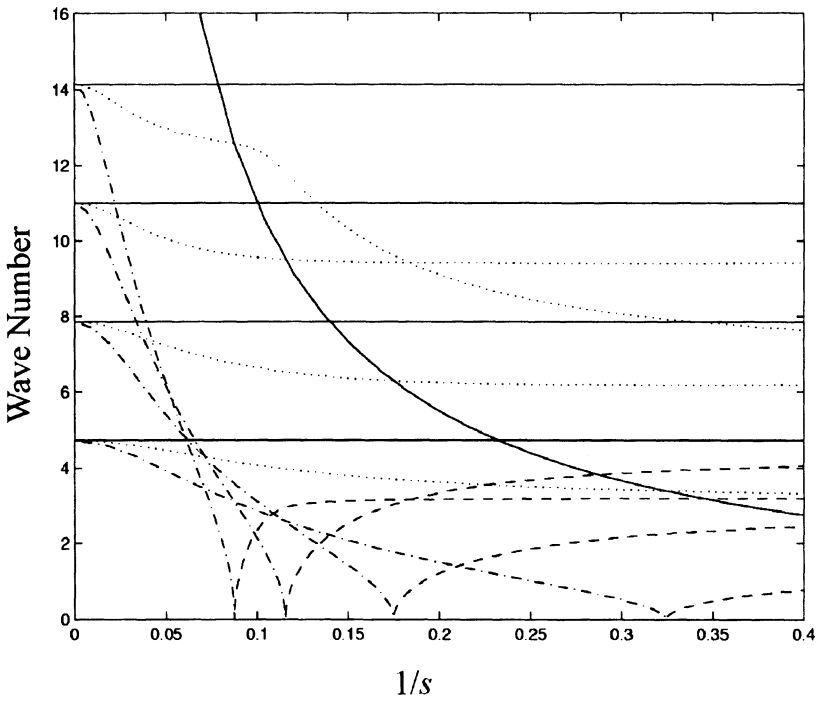

Figure 3.15. First Four Sets of Wave Numbers of the Clamped-Clamped Timoshenko Beam. – Euler-Bernoulli; ·· a; –· b; –– $\tilde{b}$

The natural frequency that corresponds to the wave number pairs (a_n, b_n) and $\left(a_n, \tilde{b}_n^{(1)}\right)$ in the hinged-hinged case is denoted as $\omega_n^{*(1)}$ and is given by

$$\omega_n^{*(1)} L^* \sqrt{\rho^*/E^*} = \sqrt{\frac{a_n^2 - b_n^2}{1+\gamma^2}} \text{ for } 1/s < 1/s_n$$
$$= \sqrt{\frac{a_n^2 + \left(\tilde{b}_n^{(1)}\right)^2}{1+\gamma^2}} \text{ for } 1/s > 1/s_n, \qquad (3.120)$$

and the natural frequency that corresponds to the pairs of wave numbers $\left(a_n, \tilde{b}_n^{(2)}\right)$ for all $1/s$ is denoted as $\omega_n^{*(2)}$ and given by

$$\omega_n^{*(2)} L^* \sqrt{\rho^*/E^*} = \sqrt{\frac{a_n^2 + \left(\tilde{b}_n^{(2)}\right)^2}{1+\gamma^2}} \text{ for all } 1/s. \qquad (3.121)$$

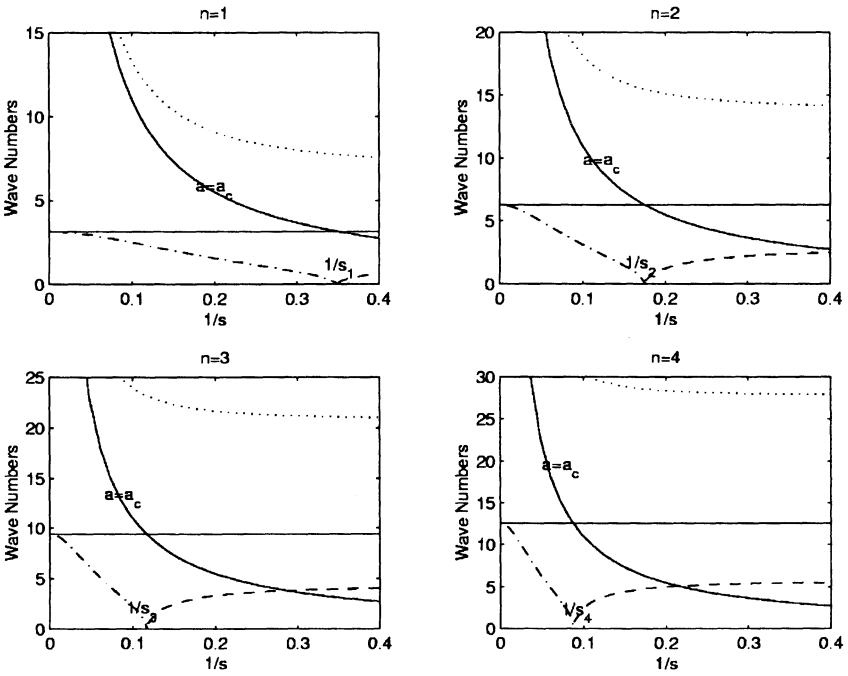

Figure 3.16. First Four Sets of Wave Numbers of the Hinged-Hinged (or Sliding-Sliding) Timoshenko Beam. – Euler-Bernoulli; ·· a_n; –· b_n; –– $\tilde{b}_n$

The quantities $\omega_n^{*(1,2)} L^* \sqrt{\rho^*/E^*}$ are plotted as functions of $1/s$ for $\gamma = 2.205$ in Figure 3.20 using the values of a_n, b_n, $\tilde{b}_n^{(1)}$, and $\tilde{b}_n^{(2)}$ that we know from Figure 3.16. Note that as the slenderness ratio becomes larger ($1/s \to 0$), the natural frequencies $\omega_n^{*(2)}$ disappear by approaching infinity. This is consistent with the other models for which $\omega_n^{*(2)}$ does not exist.

It is interesting to note that in Figures 3.18 and 3.19 curves cross each other. Thus, for a Timoshenko beam with particular sets of boundary conditions, it is possible for a set of wave numbers with a lower index to produce a higher natural frequency. The indices of the wave numbers should not be used to gauge the order of the natural frequencies. In the other cases–the Euler-Bernoulli, Rayleigh, and shear cases–a set of wave numbers with a high index always corresponds to a higher natural frequency.

These figures can be used to obtain the wave numbers and the natural frequencies. Let us consider a clamped-free beam for $1/s = 0.11$ and $\gamma = 2.205$. The critical wave number a_c, obtained using Equation 3.82,

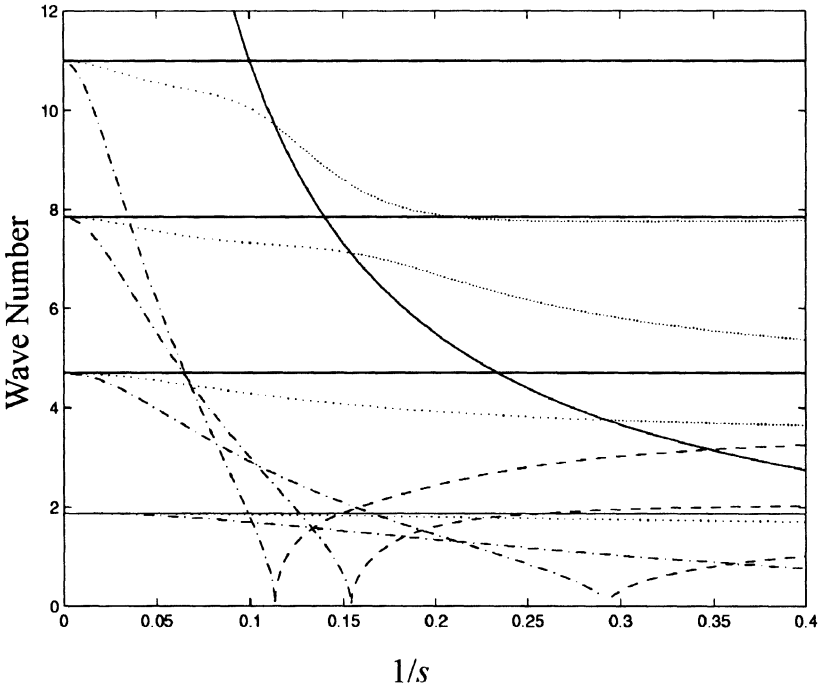

Figure 3.17. First Four Sets of Wave Numbers of the Clamped-Free Timoshenko Beam. – Euler-Bernoulli; ·· a; –· b; –– $\tilde{b}$

at this slenderness ratio is 10.013, which is slightly above a_4. Although a_5 is not plotted, we can guess that a_5 is greater than a_c. Therefore, only first four eigenfunctions will have hyperbolic terms. The sets of the wave numbers can be extracted from Figure 3.17. For example, a_1 in the figure is slightly less than 1.875, which is the wave number of the Euler-Bernoulli problem represented by the first solid line obtained from Table 3.5, and b_1 is slightly below a_1. Note that in order to obtain more accurate readings, the figures should be enlarged. When $\rho^* = 7830$ kg/m^3, $L^* = 1$ m, and $E^* = 200$ GPa, the natural frequencies can be obtained using Figure 3.21. For example, from the figure the quantity $\omega_1^* L^* \sqrt{\rho^*/E^*}$ is approximately 0.32 which corresponds to $\omega_1^* = 1620$ rad/s. The exact wave numbers and the natural frequencies are given by

$$
\begin{aligned}
(a_1, b_1) &= (1.843, 1.655), \ \omega_1 = 1 \\
(a_2, b_2) &= (4.236, 2.727), \ \omega_2 = 3.991 \\
(a_3, b_3) &= (7.305, 2.575), \ \omega_3 = 8.412
\end{aligned}
$$

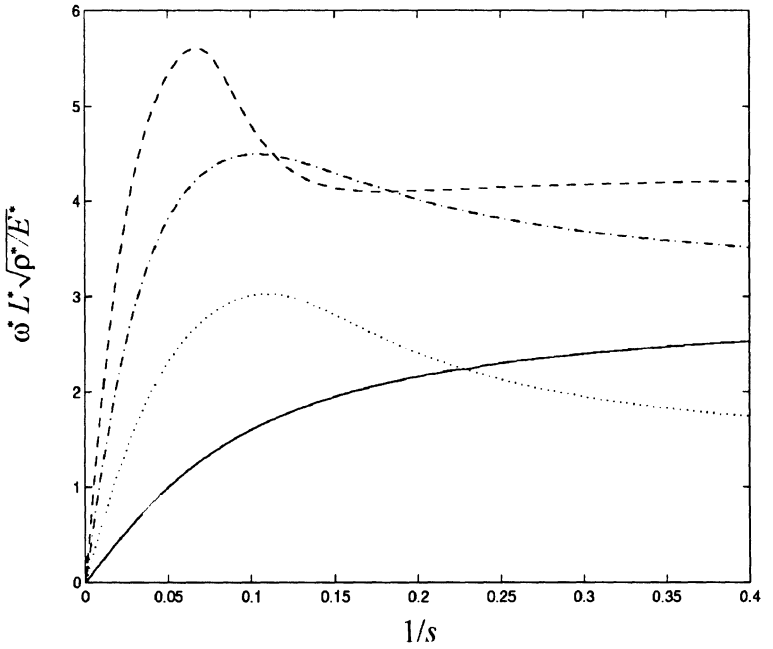

Figure 3.18. Frequency Curves for the Free-Free Timoshenko Beam. – $\omega_1^* L^* \sqrt{\rho^*/E^*}$; ·· $\omega_2^* L^* \sqrt{\rho^*/E^*}$; –· $\omega_3^* L^* \sqrt{\rho^*/E^*}$; –– $\omega_4^* L^* \sqrt{\rho^*/E^*}$

$$
\begin{aligned}
(a_4, b_4) &= (9.813, 0.803)\,, \quad \omega_4 = 12.037 \\
\left(a_5, \tilde{b}_5\right) &= (11.770, 2.581)\,, \quad \omega_5 = 14.829 \\
\left(a_6, \tilde{b}_6\right) &= (13.463, 3.823)\,, \quad \omega_6 = 17.224,
\end{aligned} \tag{3.122}
$$

where the natural frequencies are non-dimensionalized by the first natural frequency $\omega_1^* = 1696\ rad/s$. Note that frequencies can be read from the figure more accurately than the wave numbers.

Figure 3.22 shows the variation of the first pair of wave numbers (a_1, b_1) for $1/s < 1/s_1$ for the free-free Timoshenko beam shown in Figure 3.14. The values of γ used here are 1.7777, 2.2050, and 2.435. $\gamma = 1.7777$ is a reasonable value for a solid circular or rectangular section, and $\gamma = 2.435$ is a reasonable value for a thin square tube[12] with Poisson's ratio of 0.29.

[12] The values of γ are calculated using the Table 3.3 and Equation 3.84.

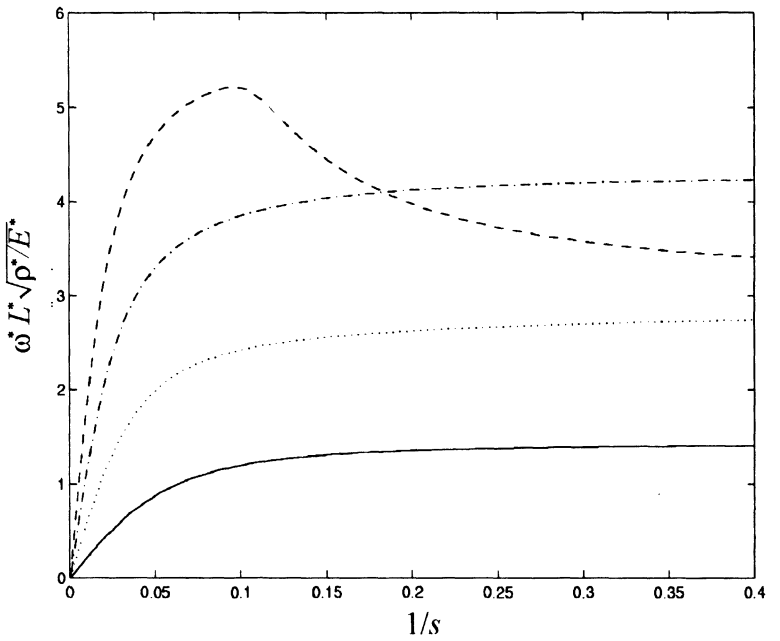

Figure 3.19. Frequency Curves for Clamped-Clamped Timoshenko Beam. $-\omega_1^* L^* \sqrt{\rho^*/E^*}$; $\cdot\cdot\ \omega_2^* L^* \sqrt{\rho^*/E^*}$; $-\cdot\ \omega_3^* L^* \sqrt{\rho^*/E^*}$; $--\ \omega_4^* L^* \sqrt{\rho^*/E^*}$

5. Comparisons of Four Models

So far, we obtained the wave numbers and natural frequencies of four engineering beam theories. The differences among them were the inclusion of different second order terms: rotary and shear terms. The Euler-Bernoulli model included only the first order terms, translation and bending. The Rayleigh model included the rotation, the shear model included the shear, and the Timoshenko model included both rotation and shear in addition to the first order effects. In this section we compare the relative significance of rotary and shear effects and see how it is manifested in the natural frequency and mode shapes.

The rotary effect is represented by the term ρI and the shear by $\rho/k'G$. Note that the shear term is always γ^2 times larger than the rotary term,

$$\begin{aligned} \frac{\rho}{k'G} &= \frac{\rho}{k'} \frac{E^* I^*}{G^* L^{*4}} = \frac{\rho}{k'} \frac{E^* I}{G^*} \\ &= \rho I \frac{2(1+\nu)}{k'} = \rho I \gamma^2. \end{aligned} \tag{3.123}$$

Recall that Poisson's ratio ν is a physical property that depends on the material and the shear factor k' depends on Poisson's ratio and the

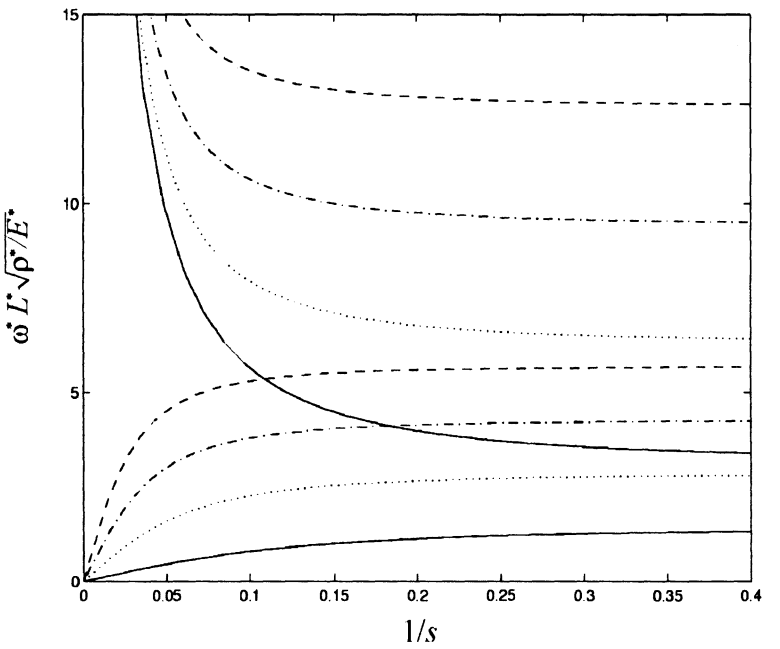

Figure 3.20. Frequency Curves for the Hinged-Hinged Timoshenko Beam. – $\omega_1^* L^* \sqrt{\rho^*/E^*}$; ·· $\omega_2^* L^* \sqrt{\rho^*/E^*}$; –· $\omega_3^* L^* \sqrt{\rho^*/E^*}$; –– $\omega_4^* L^* \sqrt{\rho^*/E^*}$

geometry of the cross-section. Poisson's ratio for a typical metal is about 0.3, and with this value, the shear factor for different cross-sections, using Table 3.3, ranges from 0.436 for the thin-walled square tube to 0.886 for the circular cross-section. Using these values, γ^2 ranges from 2.935 for the circular cross-section to 5.96 for the thin-walled square tube. We have established, for a typical material and cross-section, the shear term is roughly 3 to 6 times larger than the rotary term.

Now we look into circumstances under which those second order effects become important. Consider the frequency equations obtained previously in Tables 3.5, 3.7, 3.8, 3.9, and 3.10. We observe that the frequency equations for the Euler-Bernoulli model depend neither on the geometrical nor the physical properties. Therefore, wave number a is independent of any properties. On the other hand, the frequency equations for the Rayleigh model are functions of a and b which are related by the slenderness ratio s. Therefore, the wave numbers a and b depend on the geometrical property s. The frequency equations for the shear and Timoshenko models depend on both s and γ. Therefore, the wave numbers depend on both geometrical and physical properties. The effects of s and/or γ on the wave numbers are shown in Figures 3.6 to 3.9 for the

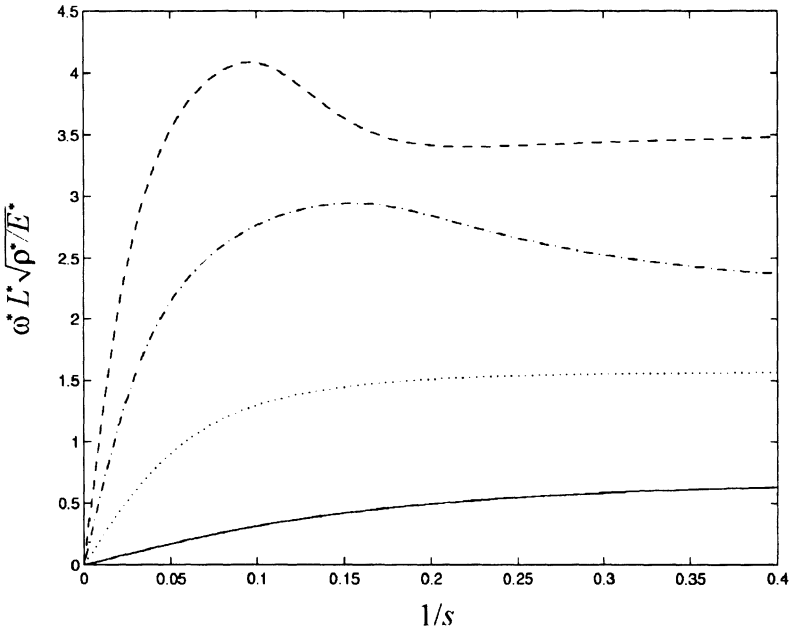

Figure 3.21. Frequency Curves for the Clamped-Free Timoshenko Beam. $\omega_1^* L^* \sqrt{\rho^*/E^*}$; $\cdot\cdot$ $\omega_2^* L^* \sqrt{\rho^*/E^*}$; $-\cdot$ $\omega_3^* L^* \sqrt{\rho^*/E^*}$; $--$ $\omega_4^* L^* \sqrt{\rho^*/E^*}$

Rayleigh and shear model and in Figures 3.14 to 3.17 and Figure 3.22 for the Timoshenko model. Generally, the wave numbers deviate from those of Euler-Bernoulli model as s decreases and γ increases. However, the range of γ^2 is more restricted (between 3 and 6 for a typical metal and cross-section). Therefore, the wave numbers are strong functions of the slenderness ratio.

As a numerical example, the first natural frequencies predicted by each of the four models are plotted in Figure 3.23. The natural frequency is multiplied by $L^* \sqrt{\rho^*/E^*}$ and $\gamma = 2.205$ is used. The straight solid line for the Euler-Bernoulli model is obtained using Equation 3.87. Note that the natural frequency predicted by the Euler-Bernoulli model approaches infinity as the slenderness ratio decreases whereas the natural frequencies predicted by other models level off at some point. In Figure 3.24, the first four mode shapes of a clamped-free beam with $s = 9.1192$ and $\gamma = 2.205$ are plotted. The mode shapes are normalized with respect to each other for easy comparison. Notice that the natural frequencies and mode shapes obtained using the Euler-Bernoulli and Rayleigh models are similar, and those based on the shear and Timoshenko models are

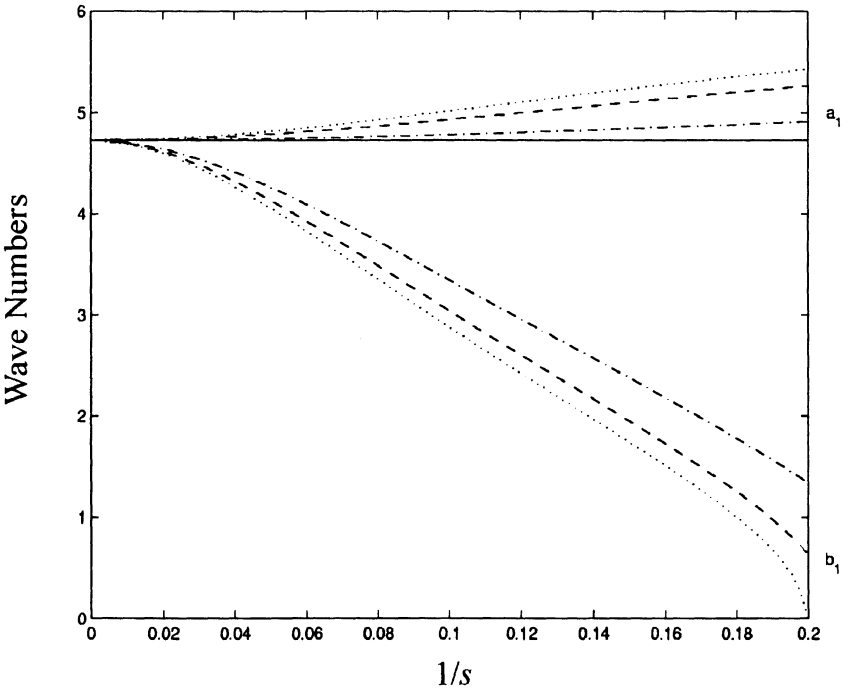

Figure 3.22. First Set of Wave Numbers of the Free-Free Timoshenko Beam When $1/s < 1/s_1$. – Euler-Bernoulli; ·· $\gamma = 2.435$; –– $\gamma = 2.205$; –· $\gamma = 1.777$.

similar. This confirms our result that the shear is more dominant than the rotary effects.

In summary, when the slenderness ratio is large ($s > 100$), the Euler-Bernoulli model should be used. When the slenderness ratio is small, either shear or Timoshenko model can be used.

6. Free and Forced Response

In this section, the free and forces responses will be obtained using the separation of variables and the method of eigenfunction expansion. To do so, we need to establish the orthogonality properties for each model. We will find that the orthogonality of the Rayleigh model slightly differs from the others.

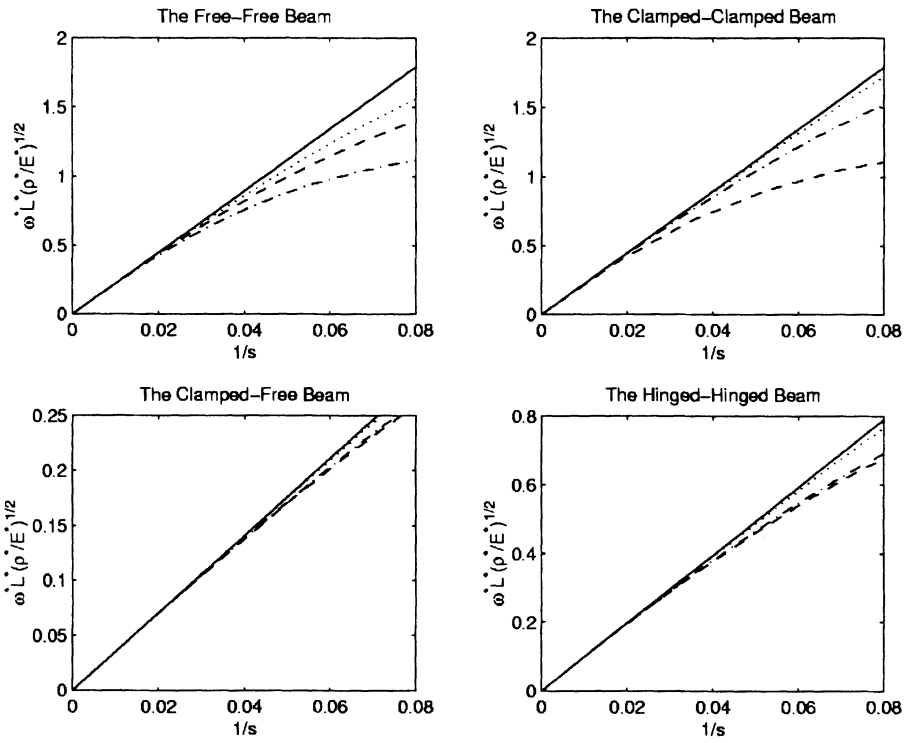

Figure 3.23. Frequency Curves for the First Natural Frequency. — Euler-Bernoulli; –· Shear; ·· Rayleigh; –– Timoshenko

6.1 Orthogonality Conditions for the Euler-Bernoulli, Shear, and Timoshenko Models

In order to obtain the free or forced response of the beam, we use the method of *eigenfunction expansion.* Therefore, the orthogonality conditions of the eigenfunctions have to be established for each beam model. For the models discussed so far, with the exception of the Rayleigh beam[13], the spatial equations of the homogeneous problem, 3.15, 3.49, and 3.68, can be written using the operator formalism

$$L(\mathbf{W}_n) = \omega_n^2 M(\mathbf{W}_n), \tag{3.124}$$

where $\mathbf{W}_n$ can denote the n^{th} eigenfunction W_n for the Euler-Bernoulli model, or the n^{th} vector of eigenfunctions $\left[\begin{array}{cc} W_n & \Psi_n \end{array}\right]^T$ for the shear

[13] The analysis for the Rayleigh beam is slightly different due to the mixed term in the governing differential equation. It will be discussed in detail in the next section.

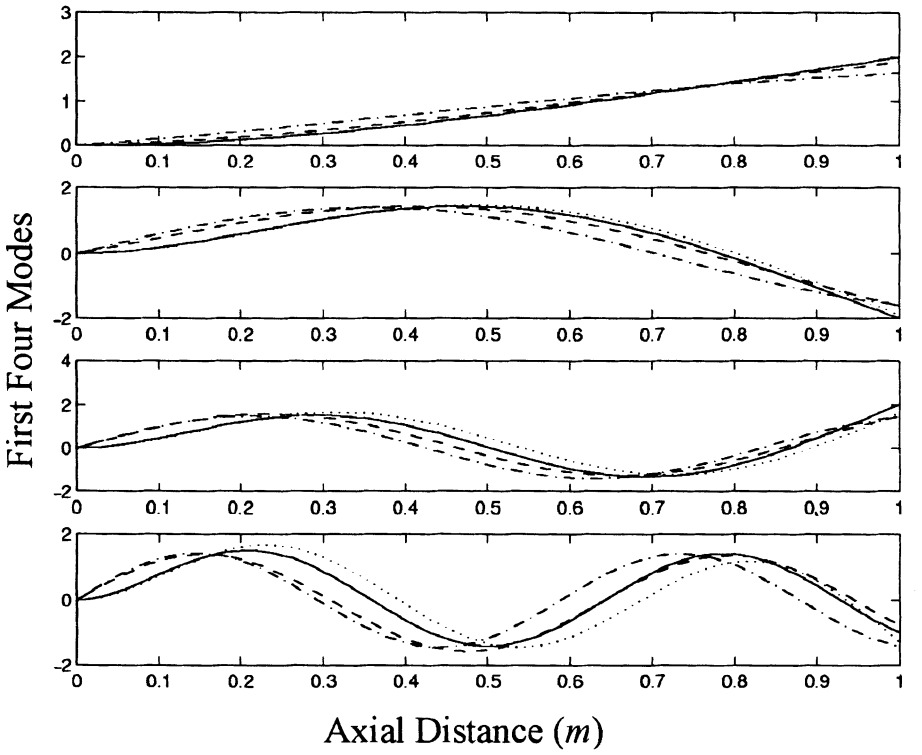

Figure 3.24. First Four Mode Shapes of the Clamped-Free Beam. – Euler-Bernoulli; —· Shear; ·· Rayleigh; –– Timoshenko

and Timoshenko models, and corresponds to the natural frequency ω_n^2 uniquely to within an arbitrary constant [23][14]. The expressions for the operators for each model are given below:

Euler-Bernoulli model

$$L(W_n) = \frac{d^4 W_n}{dx^4}, \quad M(W_n) = \rho A W_n \tag{3.125}$$

Shear model

$$L(\mathbf{W}_n) = \begin{bmatrix} k'GA\frac{d^2}{dx^2} & -k'GA\frac{d}{dx} \\ k'GA\frac{d}{dx} & \frac{d^2}{dx^2} - k'GA \end{bmatrix} \begin{bmatrix} W_n \\ \Psi_n \end{bmatrix}$$

$$M(\mathbf{W}_n) = \begin{bmatrix} \rho A & 0 \\ 0 & 0 \end{bmatrix} \begin{bmatrix} W_n \\ \Psi_n \end{bmatrix} \tag{3.126}$$

[14] See pg. 135.

Timoshenko model

$$L(\mathbf{W}_n) = \begin{bmatrix} k'GA\frac{d^2}{dx^2} & -k'GA\frac{d}{dx} \\ k'GA\frac{d}{dx} & \frac{d^2}{dx^2} - k'GA \end{bmatrix} \begin{bmatrix} W_n \\ \Psi_n \end{bmatrix}$$

$$M(\mathbf{W}_n) = \begin{bmatrix} \rho A & 0 \\ 0 & \rho I \end{bmatrix} \begin{bmatrix} W_n \\ \Psi_n \end{bmatrix}. \tag{3.127}$$

The operators L and M are self-adjoint (with corresponding boundary conditions) if [45]

$$\int_0^1 \left[\mathbf{W}_n^T L(\mathbf{W}_m) - \mathbf{W}_m^T L(\mathbf{W}_n)\right] dx = 0 \tag{3.128}$$

$$\int_0^1 \left[\mathbf{W}_n^T M(\mathbf{W}_m) - \mathbf{W}_m^T M(\mathbf{W}_n)\right] dx = 0. \tag{3.129}$$

Note that the second condition, Equation 3.129, is automatically satisfied for all three models. Using Equation 3.124, we can write Equation 3.128 as

$$(\omega_m^2 - \omega_n^2) \int_0^1 \mathbf{W}_n^T M(\mathbf{W}_m)\, dx = 0. \tag{3.130}$$

Since eigenvalues (squares of natural frequencies) are unique to the eigenfunctions, $\omega_m^2 \neq \omega_n^2$ for $m \neq n$, in order for above equation to be zero, the integral has to be zero,

$$\int_0^1 \mathbf{W}_n^T M(\mathbf{W}_m)\, dx = 0, \text{ for } m \neq n. \tag{3.131}$$

This is the orthogonality condition for the eigenfunctions. When $m = n$, we normalize the eigenfunctions by setting the integral equal to one,

$$\int_0^1 \mathbf{W}_n^T M(\mathbf{W}_n)\, dx = 1, \text{ for } n = 1, 2, 3, \cdots. \tag{3.132}$$

Combining Equation 3.131 and 3.132, we can write

$$\int_0^1 \mathbf{W}_n^T M(\mathbf{W}_m)\, dx = \delta_{nm}, \tag{3.133}$$

where δ_{nm} is the Kronecker delta.

Now we discuss which boundary conditions make the operator L self-adjoint or satisfy Equation 3.128. The conditions can be found by substituting the expression for the operator L into Equation 3.128 and integrating by parts. For example, for the Euler-Bernoulli model, Equation 3.128 becomes, upon substituting Equation 3.125,

$$\int_0^1 \left[\mathbf{W}_n^T \frac{d^4 W_m}{dx^4} - \mathbf{W}_m^T \frac{d^4 W_n}{dx^4}\right] dx = 0. \tag{3.134}$$

Integrating twice by parts, we obtain

$$\left(W_n\frac{d^3W_m}{dx^3} - W_m\frac{d^3W_n}{dx^3}\right)\Big|_0^1 + \left(-\frac{dW_n}{dx}\frac{d^2W_m}{dx^2} + \frac{dW_m}{dx}\frac{d^2W_n}{dx^2}\right)\Big|_0^1 = 0, \tag{3.135}$$

where the remaining integrals cancel each other due to symmetry. These are the conditions that have to be satisfied in order for the system to be self-adjoint and the orthogonality condition to hold. Note that the boundary conditions from the variational problem (Equation 3.19) satisfy this condition.

For the shear and Timoshenko models, the corresponding boundary conditions for the self-adjoint operator L are found to be

$$\begin{aligned} 0 = {} & k'GA\left[W_n\left(\frac{dW_m}{dx} - \Psi_m\right) - W_m\left(\frac{dW_n}{dx} - \Psi_n\right)\right]\Big|_0^1 \\ & + \left[\Psi_n\frac{d\Psi_m}{dx} - \Psi_m\frac{d\Psi_n}{dx}\right]\Big|_0^1, \end{aligned} \tag{3.136}$$

where the boundary conditions obtained from the variational problem (Equation 3.63) also satisfy this condition.

Therefore, for the systems we consider, they are self-adjoint and the eigenfunctions are orthogonal to each other as given in Equation 3.131.

6.2 Orthogonality Conditions for the Rayleigh Model

The spatial equation for the Rayleigh beam (Equation 3.31) can be written in the form given by Equation 3.124 as was done for the other three models with the operators L and M given by

$$L(W_n) = \frac{d^4W_n}{dx^4}, \quad M(W_n) = \left(\rho AW_n - \rho I\frac{d^2W_n}{dx^2}\right). \tag{3.137}$$

However, in this case, the operator M is a differential operator unlike those in the other cases. Equation 3.128, with the operator L substituted with Equation 3.124, is given by

$$\begin{aligned} & \int_0^1 \left[W_nL(W_m) - W_mL(W_n)\right]dx \\ & = \int_0^1 \left[\omega_m^2W_nM(W_m) - \omega_n^2W_mM(W_n)\right]dx. \end{aligned} \tag{3.138}$$

Substituting the expressions for the L and M operators and integrating by parts twice, the left hand side of Equation 3.138 is reduced to

$$\left(W_n \frac{d^3W_m}{dx^3} - W_m \frac{d^3W_n}{dx^3}\right)\Big|_0^1 + \left(-\frac{dW_n}{dx}\frac{d^2W_m}{dx^2} + \frac{dW_m}{dx}\frac{d^2W_n}{dx^2}\right)\Big|_0^1, \tag{3.139}$$

where the remaining integrals cancel each other. The right hand side of Equation 3.138 is reduced to

$$(\omega_m^2 - \omega_n^2)\int_0^1 \left[\rho A W_m W_n + \rho I \frac{dW_m}{dx}\frac{dW_n}{dx}\right] dx - \rho I \left[\omega_m^2 W_n \frac{dW_m}{dx} - \omega_n^2 W_m \frac{dW_n}{dx}\right]\Big|_0^1. \tag{3.140}$$

Combining the left and right hand sides (Equations 3.139 and 3.140), we obtain

$$\left[W_n\left(\frac{d^3W_m}{dx^3} + \rho I\omega_m^2\frac{dW_m}{dx}\right) - W_m\left(\frac{d^3W_n}{dx^3} + \rho I\omega_n^2\frac{dW_n}{dx}\right)\right]\Big|_0^1 + \left(-\frac{dW_n}{dx}\frac{d^2W_m}{dx^2} + \frac{dW_m}{dx}\frac{d^2W_n}{dx^2}\right)\Big|_0^1 = (\omega_m^2 - \omega_n^2)\int_0^1 \left[\rho A W_m W_n + \rho I \frac{dW_m}{dx}\frac{dW_n}{dx}\right] dx. \tag{3.141}$$

Let us examine the left hand side of Equation 3.141. Comparing with the boundary conditions from the variational problem, we find that the left hand side vanishes (see Equations 3.35) so that the orthogonality condition is given by

$$\int_0^1 \left[\rho A W_m W_n + \rho I \frac{dW_m}{dx}\frac{dW_n}{dx}\right] dx = \delta_{nm}. \tag{3.142}$$

There are other orthogonality conditions that we can obtain by manipulating Equation 3.124, where the expressions for the operators are given by Equation 3.137. Multiplying Equation 3.124 by W_m and integrating over the domain $(0 \leq x \leq 1)$, we obtain

$$\int_0^1 W_n \frac{d^4W_m}{dx^4} dx = \int_0^1 \omega_m^2 W_n \left(\rho A W_m - \rho I \frac{d^2W_m}{dx^2}\right) dx, \tag{3.143}$$

which can be rewritten as

$$\int_0^1 W_n \frac{d^4 W_m}{dx^4} dx + \omega_m^2 \rho I \int_0^1 \left[\frac{dW_n}{dx} \frac{dW_m}{dx} + W_n \frac{d^2 W_m}{dx^2} \right] dx$$
$$= \omega_m^2 \int_0^1 \left[\rho A W_n W_m + \rho I \frac{dW_n}{dx} \frac{dW_m}{dx} \right] dx, \tag{3.144}$$

where the right hand side equals $\omega_m^2 \delta_{nm}$ from Equation 3.142. We integrate the left hand side twice by parts to obtain

$$W_n \left(\frac{d^3 W_m}{dx^3} + \omega_m^2 \rho I \frac{dW_m}{dx} \right) \Big|_0^1 - \int_0^1 \frac{dW_n}{dx} \frac{d^3 W_m}{dx^3} dx = \omega_m^2 \delta_{nm}. \tag{3.145}$$

From the boundary conditions (Equation 3.35), the first term vanishes and we are left with

$$- \int_0^1 \frac{dW_n}{dx} \frac{d^3 W_m}{dx^3} dx = \omega_m^2 \delta_{nm}. \tag{3.146}$$

Integrating Equation 3.146 by parts and using the boundary conditions (Equation 3.35) again, we obtain

$$\int_0^1 \frac{d^2 W_n}{dx^2} \frac{d^2 W_m}{dx^2} dx = \omega_m^2 \delta_{nm}. \tag{3.147}$$

Therefore, we now have three orthogonality conditions given by Equations 3.142, 3.146, and 3.147. The orthogonality condition in Equation 3.146 will be used later.

Note that a similar procedure can be applied to the other models to obtain other orthogonality conditions.

6.3 Free and Forced Response via Method of Eigenfunction Expansion of the Euler-Bernoulli, Shear, and Timoshenko Models

The method of *eigenfunction expansion* assumes that the solutions $v(x,t)$ (or solutions $v(x,t)$ and $\alpha(x,t)$) to equations of motion given in Equations 3.11, 3.42, 3.65 and the forcing function $f(x,t)$ can be represented as a summation of eigenfunctions (the spatial solution to the homogeneous problem) multiplied by functions of time that are to

be determined, that is,

$$\mathbf{v}(x,t) = \sum_{n=1}^{\infty} \eta_n(t)\mathbf{W}_n(x) \tag{3.148}$$

$$f(x,t) = \sum_{n=1}^{\infty} F_n(t)M(\mathbf{W}_n(x)). \tag{3.149}$$

Note that $\mathbf{v}(x,t)$ stands for $v(x,t)$ for the Euler-Bernoulli and Rayleigh models and $\begin{bmatrix} v(x,t) & \alpha(x,t) \end{bmatrix}^T$ for shear and Timoshenko models. If we know the time dependent coefficients $\eta_n(t)$, we can solve for the complete solution to the problem as follows.

The expressions for $\eta_n(t)$ can be obtained by applying the operator M to Equation 3.148, multiplying it by $\mathbf{W}_m^T$ and integrating over the domain. Simplifications can be made using the orthonormality conditions given in Equation 3.133,

$$\int_0^1 \mathbf{W}_m^T M(\mathbf{v}(x,t))\,dx = \sum_{n=1}^{\infty} \eta_n(t) \int_0^1 \mathbf{W}_m^T M(\mathbf{W}_n(x))\,dx \tag{3.150}$$

$$\therefore \eta_m(t) = \int_0^1 \mathbf{W}_m^T M(\mathbf{v}(x,t))\,dx. \tag{3.151}$$

Similarly, $F_m(t)$ can be found by multiplying Equation 3.149 by $\mathbf{W}_m^T$ and integrating over the domain,

$$F_m(t) = \int_0^1 \mathbf{W}_m^T f(x,t)dx. \tag{3.152}$$

Substituting the assumed solution (Equation 3.148) and the forcing function (Equation 3.149) into the equations of motion (Equations 3.11, 3.42, and 3.65), respectively, we obtain

$$\sum_{n=1}^{\infty} \frac{d^2\eta_n(t)}{dt^2} M(\mathbf{W}_n(x)) + \sum_{n=1}^{\infty} \eta_n(t) L(\mathbf{W}_n(x)) = \sum_{n=1}^{\infty} F_n(t) M(\mathbf{W}_n(x)), \tag{3.153}$$

where the expressions for the operators M and L are given in Equations 3.125, 3.126, and 3.127, respectively. Using Equation 3.124, the last equation becomes

$$\sum_{n=1}^{\infty} \left[\frac{d^2\eta_n(t)}{dt^2} + \omega_n^2 \eta_n(t) \right] M(\mathbf{W}_n(x)) = \sum_{n=1}^{\infty} F_n(t) M(\mathbf{W}_n(x)). \tag{3.154}$$

Multiplying by $\mathbf{W}_m^T(x)$ and integrating over the domain $(0 \leq x \leq 1)$ results in

$$\frac{d^2\eta_m(t)}{dt^2} + \omega_m^2 \eta_m(t) = F_m(t), \tag{3.155}$$

where the solution is given by

$$\eta_m(t) = \frac{1}{\omega_m} \int_0^t F_m(t) \sin\omega_m (t-\tau)\, d\tau + \eta_m(0) \cos\omega_m t + \frac{1}{\omega_m} \left.\frac{d\eta_m}{dt}\right|_{t=0} \sin\omega_m t. \tag{3.156}$$

$F_m(t)$ is given by Equation 3.152, and $\eta_m(0)$ and $d\eta_m/dt|_{t=0}$ are obtained from the initial conditions, $v(x,0)$ and $\dot{v}(x,0)$, using Equation 3.151,

$$\eta_m(0) = \int_0^1 \mathbf{W}_m^T M(\mathbf{v}(x,0))\, dx$$
$$\dot{\eta}_m(0) = \int_0^1 \mathbf{W}_m^T M(\dot{\mathbf{v}}(x,0))\, dx. \tag{3.157}$$

We now know the time dependent coefficients $\eta_m(t)$ of Equation 3.148 in terms of initial conditions and the forcing function. Finally, the solution is given by

$$\mathbf{v}(x,t) = \sum_{n=1}^{\infty} \eta_n(t) \mathbf{W}_n(x), \tag{3.158}$$

where $\eta_n(t)$ is given by Equation 3.156.

6.4 Free and Forced Response via Method of Eigenfunction Expansion of the Rayleigh Model

We follow a similar procedure to obtain the solution using the method of *eigenfunction expansion.* It is assumed that the solution $v(x,t)$ to the equation of motion given in Equation 3.21 can be expanded in terms of eigenfunctions as in Equation 3.148 or

$$v(x,t) = \sum_{n=1}^{\infty} \eta_n(t) W_n(x). \tag{3.159}$$

We can obtain the time dependent coefficient $\eta_n(t)$ using the orthogonality condition given in Equation 3.142, 3.146, or 3.147. Note that it is awkward to use the first orthogonality condition (Equation 3.142).

Instead, we use Equation 3.146. Taking a spatial derivative of $v(x,t)$ in Equation 3.159, we obtain

$$\frac{\partial v(x,t)}{\partial x} = \sum_{n=1}^{\infty} \eta_n(t) \frac{dW_n(x)}{dx}. \tag{3.160}$$

Multiplying Equation 3.160 by d^3W_m/dx^3 and integrating over the domain, we obtain

$$\eta_m(t) = -\frac{1}{\omega_m^2} \int_0^1 \frac{\partial v(x,t)}{\partial x} \frac{d^3W_m(x)}{dx^3} dx. \tag{3.161}$$

The equation of motion can be written as

$$\sum_{n=1}^{\infty} \eta_n \frac{d^4W_n}{dx^4} + \frac{d^2\eta_n}{dt^2} \left(\rho A W_n - \rho I \frac{d^2W_n}{dx^2} \right) = f(x,t). \tag{3.162}$$

The boundary conditions given in Equations 3.22 can be written as

$$\begin{aligned} \frac{d^2W_n}{dx^2} \left(\delta \frac{dW_m}{dx} \right) \Bigg|_0^1 &= 0 \\ \left(\eta \frac{d^3W}{dx^3} - \rho I \frac{d^2\eta}{dt^2} \frac{dW}{dx} \right) \delta W \Bigg|_0^1 &= 0. \end{aligned} \tag{3.163}$$

Multiplying Equation 3.162 by W_m and integrating over the domain $(0 < x < 1)$, we obtain

$$\begin{aligned} &\sum_{n=1}^{\infty} \int_0^1 \left[\eta_n \frac{d^4W_n}{dx^4} + \frac{d^2\eta_n}{dt^2} \left(\rho A W_n - \rho I \frac{d^2W_n}{dx^2} \right) \right] W_m dx \\ &= \int_0^1 f(x,t) W_m dx. \end{aligned} \tag{3.164}$$

The left hand side of this equation is integrated by parts,

$$\begin{aligned} &\int_0^1 \left[\eta_n \frac{d^4W_n}{dx^4} + \frac{d^2\eta_n}{dt^2} \left(\rho A W_n - \rho I \frac{d^2W_n}{dx^2} \right) \right] W_m dx \\ &= W_m \left(\eta_n \frac{d^3W_n}{dx^3} - \frac{d^2\eta_n}{dt^2} \rho I \frac{dW_n}{dx} \right) \Bigg|_0^1 - \eta_n \frac{dW_m}{dx} \frac{d^2W_n}{dx^2} \Bigg|_0^1 \\ &+ \int_0^1 \eta_n \frac{d^2W_n}{dx^2} \frac{d^2W_m}{dx^2} dx + \frac{d^2\eta_n}{dt^2} \int_0^1 \left[\rho A W_n W_m + \rho I \frac{dW_n}{dx} \frac{dW_m}{dx} \right] dx. \end{aligned} \tag{3.165}$$

Note that the terms evaluated at the boundaries disappear due to boundary conditions given in Equations 3.163. Also, from the orthogonality conditions given in Equations 3.142 and 3.147, we can simplify to

$$\int_0^1 \left[\eta_n \frac{d^4 W_n}{dx^4} + \frac{d^2\eta_n}{dt^2}\left(\rho A W_n - \rho I \frac{d^2 W_n}{dx^2}\right)\right] W_m dx = \left(\eta_n \omega_n^2 + \frac{d^2\eta_n}{dt^2}\right)\delta_{nm}, \tag{3.166}$$

which is substituted into Equation 3.164 so that

$$\frac{d^2\eta_m}{dt^2} + \omega_m^2 \eta_m = \int_0^1 f(x,t) W_m dx. \tag{3.167}$$

By denoting $\int_0^1 f(x,t)W_m dx$ as $F_m(t)$, $\eta_m(t)$ is given as in Equation 3.156. The initial conditions, $\eta_m(0)$ and $\dot{\eta}_m(0)$, can be obtained using Equation 3.161,

$$\begin{aligned} \eta_m(0) &= -\frac{1}{\omega_m^2}\int_0^1 \left.\frac{\partial v}{\partial x}\right|_{(x,0)} \frac{d^3 W_m(x)}{dx^3} dx \\ \dot{\eta}_m(0) &= -\frac{1}{\omega_m^2}\int_0^1 \left.\frac{\partial^2 v}{\partial x \partial t}\right|_{(x,0)} \frac{d^3 W_m(x)}{dx^3} dx. \end{aligned} \tag{3.168}$$

6.5 Sample Responses

In this section, the response of a non-slender clamped-free beam is obtained using all four models. The transverse force is given by

$$f^*(x^*, t^*) = x^* \cos 100 t^*. \tag{3.169}$$

The beam is made of steel whose properties are given in Table 3.11. Using the formula given in Table 3.3 and the Poisson's ratio given in Table 3.11, the shear factor for the thin round tube is $k' = 0.53066$.

Note that the beam is not slender. Therefore, the critical wave number of the Timoshenko beam is relatively low, and the differences among the models are significant. In reality, it is hard to build a beam with such a geometry and obtain reliable experimental results because the end effect will dominate the vibration. In order to avoid such problems Traill-Nash and Collar built box beams supported by diaphragms [80].

For the Euler-Bernoulli and Rayleigh models the initial displacement is given by

$$v^*(x^*, 0) = \left(1.667 x^{*3} - 5 x^{*2}\right) 10^{-3}, \tag{3.170}$$

Table 3.11. Beam Properties

Young's Modulus E^*	200 GPa [63]
Modulus of Rigidity G^*	77.5 GPa
Poisson's Ratio ν	0.29 [68]
Density ρ^*	7830 kg/m^3 [63]
Cross-section	round tube with $r_{inner} = 0.15\ m$, $r_{outer} = 0.16\ m$
Cross-sectional Area A^*	0.0097389 m^2
Area Moment of Inertia I^*	0.0001171 m^2
Length L^*	1 m
Slenderness Ratio $L^*\sqrt{\frac{A^*}{I^*}}$	9.1192
Shear Factor k'	0.53066
γ	2.205

and for the shear and Timoshenko models, the initial displacement and rotation are given by

$$v^*(x^*, 0) = \left(2.021x^{*3} - 6.0635x^{*2} + 0.7094x^*\right) 10^{-3}$$
$$\alpha^*(x^*, 0) = \left(6.0635x^{*2} - 12.127x^*\right) 10^{-3}. \tag{3.171}$$

The initial displacements are chosen so that they satisfy the boundary conditions[15] and the magnitude of the tip displacements are the same.

The natural frequencies are obtained from the frequency charts. The first four natural frequencies of the Rayleigh, shear, and Timoshenko beams were obtained previously in Equations 3.110, 3.101 and 3.122. The natural frequencies of the Euler-Bernoulli model are obtained using the wave numbers tabulated in Table 3.5 and the dispersion relation given in Equation 3.16. The natural frequencies predicted by the four models are given in Table 3.12. The natural frequencies of the Timoshenko beam appear in pairs beyond the critical frequency because each pair of mode shapes has the same number of nodes. It may seem odd that only the Timoshenko model has more than one mode shape with same number of nodes. Experimentally, Barr observed two frequencies corresponding to the same number of nodal points in the study of free-free vibration of a thick beam [11].

The responses are obtained using the method of *eigenfunction expansion* by summing the first eight modes of Equations 3.148 or 3.159 for the Euler-Bernoulli, Rayleigh, and shear models and first twelve modes

[15] In fact, these initial displacements correspond to the shape of the beam when it is statically loaded by a point force at the free end.

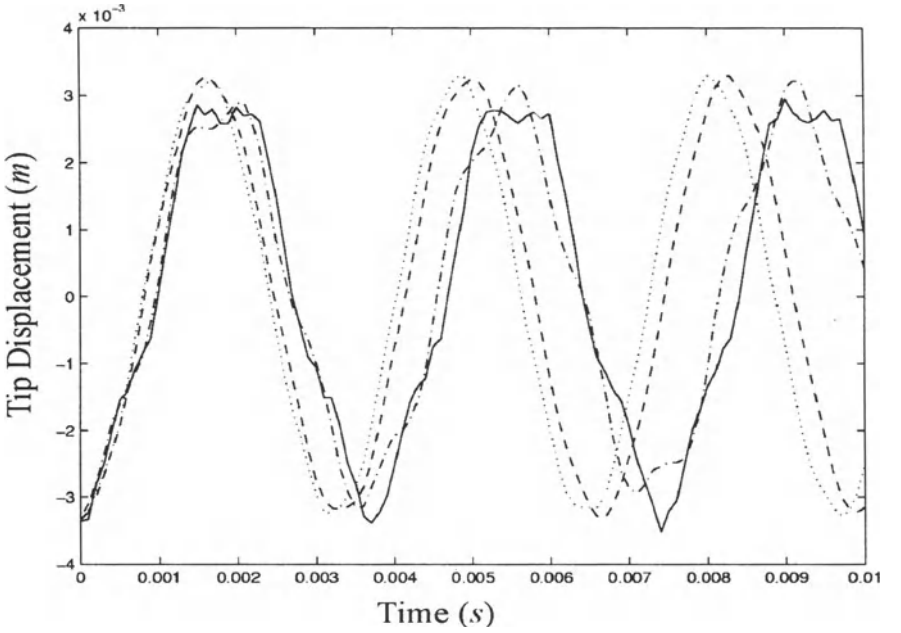

Figure 3.25. Response of the Beam. – Euler-Bernoulli; —· Shear; ·· Rayleigh; –– Timoshenko

of Equation 3.159 for the Timoshenko model. The reason why twelve modes instead of eight are included is that by including eight modes, the Timoshenko model will be missing modes with higher number of nodes. The responses are shown in Figure 3.25.

Notice that there are visible differences in the responses obtained using the four models. Such differences disappear as the slenderness ratio becomes larger. Also, notice that the responses obtained using the Euler-Bernoulli and Rayleigh models are close to each other and that those obtained using the shear and Timoshenko models are close to each other.

6.6 Discussion of the Second Frequency Spectrum of the Timoshenko Beam

Traill-Nash and Collar first claimed the existence of two separate spectra of frequencies beyond the critical frequency $\omega_c = \sqrt{k'GA/\rho I}$ for the free-free and hinged-hinged cases [80]. That is, it is possible that two natural frequencies correspond to a single mode shape.

Both Anderson [6] and Dolph [21] in their studies of the Timoshenko theory confirmed the result of Traill-Nash and Collar for the hinged-hinged case. Since their studies, it was generally accepted that the sec-

Table 3.12. Natural Frequencies (*rad/s*)

No. of nodes	Euler-Bernoulli	Rayleigh	Shear	Timoshenko	
1	1948.62	1896.16	1797.07	-	1696.03
2	12211.80	10351.13	7231.92	-	6768.24
3	34193.39	24737.47	15150.10	-	14267.26
4	67005.41	41078.62	22842.44	-	20415.37
5	110764.74	58187.35	30509.81	25150.52	29211.86
6	165463.34	75396.16	37994.56	33792.23	38003.37
7	231101.69	92504.64	45437.80	44958.47	46401.78
8	307679.76	109447.44	52799.94	53183.33	58849.04

ond spectrum existed for the hinged-hinged case. More recently, Thomas and Abbas showed using their finite element model that "... except for the special case of a hinged-hinged beam there is no separate second spectrum of frequencies." Bhashyam and Prathap [13] also came to the same conclusion using their finite element model.

However, what previous studies neglected is that the mode shape includes both displacement and angle of rotation as a pair. If we see the displacement and the angle of rotation together, the two natural frequencies do not correspond to one mode shape. They correspond to two different mode shapes. For example, let us consider a hinged-hinged beam whose properties are given in Table 3.11. The natural frequencies for $1/s = 0.11$ are shown in Figure 3.20, and the four lowest natural frequencies are $\omega_1^{(1)*}$, $\omega_2^{(1)*}$, $\omega_3^{(1)*}$, and $\omega_1^{(2)*}$. From Figure 3.16, the first natural frequency corresponds to the wave numbers (a_1, b_1) and the fourth natural frequency corresponds to the wave numbers $(a_1, \tilde{b}_1^{(2)})$. Note that the numerical value of a_1 is π. The spatial function in each case is given in Equations 3.73 and 3.75 with coefficients related by Equations 3.116 and 3.117. Upon applying boundary conditions, we find that the spatial functions are reduced to

$$\begin{bmatrix} W_1 \\ \Psi_1 \end{bmatrix} = C_1 \begin{bmatrix} \sin a_1 x \\ \frac{a_1^2+\gamma^2 b_1^2}{(1+\gamma^2)a_1} \cos a_1 x \end{bmatrix} \tag{3.172}$$

$$\begin{bmatrix} W_4 \\ \Psi_4 \end{bmatrix} = \tilde{C}_1 \begin{bmatrix} \sin a_1 x \\ \frac{a_1^2-\gamma^2\left(\tilde{b}_1^{(2)}\right)^2}{(1+\gamma^2)a_1} \cos a_1 x \end{bmatrix}, \tag{3.173}$$

where the coefficients other than C_1 and $\tilde{C}_1$ are zero. The coefficients C_1 and $\tilde{C}_1$ are then set so that the modes are normalized according

to Equation 3.133. The first and the fourth modes with corresponding natural frequencies are given by

$$\begin{bmatrix} W_1 \\ \Psi_1 \end{bmatrix} = \begin{bmatrix} 0.158 \sin \pi x \\ 0.323 \cos \pi x \end{bmatrix}, \omega_1^{(1)*} = 4252.56 \; rad/s \tag{3.174}$$

$$\begin{bmatrix} W_4 \\ \Psi_4 \end{bmatrix} = \begin{bmatrix} 0.035 \sin \pi x \\ -1.443 \cos \pi x \end{bmatrix}, \omega_1^{(2)*} = 26881.97 \; rad/s. \tag{3.175}$$

Note that when the beam is vibrating at the natural frequency belonging to the 'first spectrum,' the amplitudes of the lateral displacement and the angle of rotation could be comparable and the bending moment $(E^*I^*\Psi)$ and the shear $(k'G^*A^*(W' - \Psi))$ are in phase. When the beam is vibrating at the natural frequency belonging to the 'second spectrum', the amplitude of the angle of rotation is considerably larger than that of the lateral displacement and the bending moment and the shear are completely out of phase.

From Figure 3.16, we can establish inequalities given by

$$\begin{aligned} b_n < a_n < \tilde{b}_n^{(2)} \text{ for } 1/s < 1/s_n \text{ and } n = 1, 2, \cdots \\ \tilde{b}_n^{(1)} < a_n < \tilde{b}_n^{(2)} \text{ for } 1/s > 1/s_n \text{ and } n = 1, 2, \cdots . \end{aligned} \tag{3.176}$$

The amplitude of the angle of rotation $\left(\left(a_1^2 - \gamma^2 \left(\tilde{b}_1^{(2)}\right)^2\right) / \left(1 + \gamma^2\right) a_1\right.$ in Equation 3.173) is easily a large negative number. That is, the rotation of the cross-section may be large whereas the lateral deflection is minimal in the 'second spectrum.'

To see whether the bending moment and the shear are in phase or not, the ratios of the bending moment to the shear are obtained in both spectra,

$$\begin{aligned} \frac{\Psi_1}{W_1' - \Psi_1} \frac{E^*I^*}{k'G^*A^*} &= \frac{a_1^2 + \gamma^2 b_1^2}{\left(a_1^2 - b_1^2\right)\gamma^2} \frac{E^*I^*}{k'G^*A^*} \\ \frac{\Psi_4}{W_4' - \Psi_4} \frac{E^*I^*}{k'G^*A^*} &= \frac{a_1^2 - \gamma^2 \left(\tilde{b}_1^{(2)}\right)^2}{\gamma^2 \left(a_1^2 + \left(\tilde{b}_1^{(2)}\right)^2\right)} \frac{E^*I^*}{k'G^*A^*}. \end{aligned} \tag{3.177}$$

Note that the first expression is always positive because a_n is always greater than b_n, and the second expression is always negative because $\tilde{b}_n^{(2)}$ is always greater than a_n. Therefore, we arrive at the conclusion that the bending moment and the shear are in phase in the 'first spectrum' and completely out of phase in the 'second spectrum.'

Now, we can say that the two pairs of mode shapes are indeed distinct and correspond to distinct natural frequencies. There is no need to refer to them as separate frequency spectra. This has been observed by Levinson and Cooke [43] who said "...the two spectra interpretation of the predictions of Timoshenko beam theory is rather a matter of taste and not even a particularly fruitful interpretation at that."

7. Chapter Summary

In this chapter, we examined four approximate models for a transversely vibrating beam: the Euler-Bernoulli, Rayleigh, shear, and Timoshenko models. The equation of motion and the boundary conditions were obtained and the frequency equations for four end conditions were obtained. The solutions of the frequency equations are presented in terms of dimensionless wave numbers. Also frequency charts are plotted so that, for a given material and geometry, the natural frequency can be obtained instantly. For each model, the orthogonality conditions are identified, and the forced response is obtained using the method of eigenfunction expansion. A numerical example is given for a non-slender beam and a brief discussion on the second frequency spectrum is included.

We found that second order effects become more important for small s and large γ. The range of possible γ is small when compared to that of s. Therefore, the slenderness ratio alone can let us determine roughly whether or not the second order effects are important. We also found that shear is always more dominant than the rotary effect for a given geometry and material. Therefore, either the shear or the Timoshenko model should be used for a beam with small s. The shear model may give reasonable results for less complexity.

Chapter 4

ENVIRONMENTAL LOADING -WAVES AND CURRENTS

This chapter is devoted to the formulation of the distributed transverse fluid load $f(X,t)$ in an ocean environment. An offshore structure in an ocean environment is subjected to loadings due to wind, current, and waves. The Morison equation is used to model the *in-plane* fluid force. Random waves are modeled using the Airy linear wave theory and the Pierson-Moskowitz spectrum. A sample time history is generated using Borgman's method. The *out-of-plane* fluid force due to vortex shedding is modeled as a simple sinusoid.

1. Nomenclature

Symbol	Description	Units
A	wave amplitude	m
A_f	cross-sectional area of the displaced volume, πr_o^2	m^2
C_A	added mass coefficient	-
C_D	drag coefficient	-
C_M	inertia coefficient	-
d	water depth	m
D	diameter of the structure	m
$\mathbf{f}$	distributed transverse load	N/m
g	gravitational acceleration	m/s^2
h	height from the still water level	m
H	wave height from trough to peak	m
Hs	significant wave height	m
k	wave number	$1/m$
Kc	Keulegan-Carpenter number	–

S. M. Han et al., *Nonlinear and Stochastic Dynamics of Compliant Offshore Structures*

m_{fl}	displaced fluid mass per length, $\rho_f A_f$	kg/m
$\mathbf{n}$	vector normal to the structure	-
r_o	outer radius of a cylinder	m
$\mathbf{R}$	displacement vector of the structure	m
Re	Reynolds number	-
$\mathbf{t}$	vector tangent to the structure	-
T	period of wave	s
U_c	current velocity	m/s
U_w	wind velocity	m/s
V_{rel}	normal component of the relative velocity of the fluid with respect to the structure	m/s
w_x, w_y	wave velocities	m/s
ρ_f	density of water	kg/m^3
μ	dynamic viscosity of water	$N \cdot s/m^2$
η	surface elevation	m
ω	angular frequency	rad/s

2. Fluid Forces - General

If the diameter of a cylindrical structure is small compared to the wavelength of the incident wave, the Morison equation is used to model the fluid forces [54]. The Morison equation was originally derived for a stationary cylinder under the assumption that the fluid force is composed of drag and inertia forces with the drag force being predominant. The drag force is due to the pressure difference between the downstream and upstream flow region. The drag force is proportional to the square of the relative velocity of the fluid. The inertia force is the force exerted by the fluid while it accelerates and decelerates as the fluid passes the structure. It is also the force required to hold a rigid structure in a uniformly accelerated flow, and it is proportional to the fluid acceleration.

The Morison equation is modified for a moving cylinder by including the added mass term. When a structure accelerates through a fluid medium that would normally be at rest in the absence of the structure, it also accelerates the nearby fluid. Therefore, the force needed to accelerate the structure is

$$F = (m_{\text{structure}} + C_A m_{\text{displaced fluid}})\, \ddot{v},$$

where $m_{\text{displaced fluid}}$ is the mass of the displaced fluid, $\ddot{v}$ is the acceleration of the structure, and C_A is the added mass coefficient that is determined experimentally.

If the structure is not small compared to the wavelength of the incident wave[1] such that the incident wave scatters from the surface of the structure as reflected waves of the order of the incident wave, then diffraction theory must be used instead of Morison's equation. In this case, the inertia force is predominant. A literature review of the fluid force in this flow regime is given by Hogben [29].

If the inertia force still predominates and the drag force is small, but the structure is still small compared to wavelength, the Froude-Krylov theory is applied[2].

In this work, we will assume that the diameter of the structure is small compared to the wavelength of the incidental wave so that the Morison equation is applicable. The Morison force is expressed in terms of the relative acceleration and the square of the relative velocity between the structure and the fluid. The current velocities are usually assumed to be constant with time and to vary with depth. On the other hand, the wave velocities and accelerations are oscillatory. Here, we consider random waves; therefore, a broad band of frequencies are present in the wave.

To model random wave velocities, we first obtain an expression for the random wave height from the Pierson-Moskowitz power spectrum. Then, the horizontal and vertical wave velocities are obtained using the Airy linear wave theory. As well as these *in-plane* fluid forces, the fluid also exerts a lift force in the direction *perpendicular* to the flow and the structure. When the flow passes around a cylinder at a Reynolds number greater than 60 to 100, the vortices attached to the cylinder start to shed alternately. These shedding vortices exert an oscillatory force on the cylinder in the direction perpendicular to both the flow and the structure. For a fixed cylinder, the vortices are shed at the Strouhal frequency, which is proportional to the flow velocity for a wide range of Reynolds number. When the shedding frequency is close to the natural frequencies of the structure, *lock-in* or *synchronization* occurs. The shedding frequency seems to be locked in to the natural frequency of the structure. Structural motion heavily influences the fluid motion and vice versa during lock-in. Therefore, a coupled model (coupled between the structure and the fluid) is needed. A review of the various vortex-induced vibration models, which attempt to capture nonlinear charac-

[1]The structure is considered to be relatively large when

$$D/\lambda > 0.2,$$

where D is the diameter of the cylinder and λ is the wavelength of the incident wave.

[2]The diffraction theory and the Froude-Krylov theory can be found in Chapter 7 of *Hydrodynamics of Offshore Structures* by Chakrabarti [17].

teristics, can be found in Billah [14]. However, we will limit ourselves to a simple harmonic function for the vortex shedding force.

At the free surface of the fluid, the wave slamming force may be important. The wave slamming force is due to a single occasional wave with a particularly high amplitude and energy. Sarpkaya and Isaacson reviewed the research on slamming of water against circular cylinders [67]. Miller found that the peak wave-slamming force on a rigidly held horizontal circular cylinder is proportional to the square of the horizontal water particle velocity [49][50]. For this study, the wave slamming force is not included.

In all cases, the force exerted by the fluid is most likely stochastic since the waves and wind are stochastic and therefore characterized by spectral densities. An excellent review of existing spectral density models is given in [17][3].

3. Fluid Forces I: The Morison Equation

The semi-empirical expression for the fluid force was derived by Morison and his colleagues [54]. Note that the bold faced symbols denote vector quantities, and the superscript n denotes the normal component. The general form of the normal force on an oscillating cylindrical beam element in waves and currents is given by [17]

$$f^n = C_M m_{fl} \dot{w}^n + C_D \rho_f r_o \left|V_{rel}^n\right| V_{rel}^n - C_A m_{fl} \ddot{R}^n, \tag{4.1}$$

where f^n is force per unit length normal to the structure, C_M is the inertia coefficient, C_D is the drag coefficient, C_A is the added mass coefficient which is related to C_M by

$$C_A = C_M - 1, \tag{4.2}$$

r_o is the outer radius of the cylinder, V_{rel}^n is the component of the relative velocity that is normal to the beam element given by

$$V_{rel}^n = w^n + U_c^n - \dot{R}^n, \tag{4.3}$$

w is the wave velocity, and U_c is the current velocity[4], R is the position vector from the base of the beam to a certain location in the beam, and m_{fl} is the displaced mass of the fluid per unit length, which can be

[3] See Chapter 4.

[4] It will be shown in linear wave theory that the wave velocities, w_x and w_y, are functions of time t, vertical coordinate x, and horizontal coordinate y. To be used in Equation 4.1, the normal component of the wave velocity ω^n should be evaluated at the horizontal beam location $y = v(x)$.

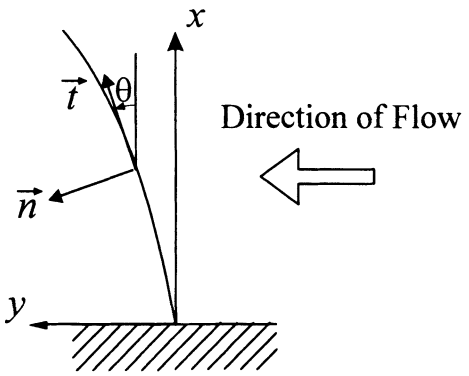

Figure 4.1. Tangential and Normal Vectors

written as

$$m_f = \rho_f \pi r_o^2. \tag{4.4}$$

The normal acceleration and the normal velocity vectors (Figure 4.1) can be written as

$$\begin{aligned} \dot{w}^n &= |\mathbf{t} \times \dot{\mathbf{w}} \times \mathbf{t}| \\ w^n &= |\mathbf{t} \times \mathbf{w} \times \mathbf{t}| \\ U_c^n &= |\mathbf{t} \times \mathbf{U}_c \times \mathbf{t}| \\ \ddot{R}^n &= \left|\mathbf{t} \times \ddot{\mathbf{R}} \times \mathbf{t}\right|, \end{aligned} \tag{4.5}$$

where $\mathbf{t}$ is the vector tangent to the beam. The tangent vector $\mathbf{t}$ is given by

$$\mathbf{t} = \cos\theta \mathbf{i} + \sin\theta \mathbf{j}, \tag{4.6}$$

where $\mathbf{i}$ and $\mathbf{j}$ are the unit vectors of the fixed frame. The wave and current velocities and the position vector can be written in terms of their components,

$$\begin{aligned} \mathbf{w} &= w_x \mathbf{i} + w_y \mathbf{j} \\ \mathbf{U}_c &= U_c \mathbf{j} \\ \mathbf{R} &= u\mathbf{i} + v\mathbf{j}, \end{aligned} \tag{4.7}$$

where we assumed that the current flows only in y direction. Note that in our case where the fluid velocity has no z component, the normal acceleration and the normal velocities can be obtained using a normal vector. The normal vector in this case (Figure 4.1) is given by

$$\mathbf{n} = -\sin\theta \mathbf{i} + \cos\theta \mathbf{j}, \tag{4.8}$$

where

$$\tan\theta = \frac{\partial v}{\partial x}. \tag{4.9}$$

$v(x,t)$ is the displacement in the y direction. When the small angle assumption is used, we can write

$$\begin{aligned} \sin\theta &\approx \theta \\ \tan\theta &\approx \theta \\ \cos\theta &\approx 1, \end{aligned} \tag{4.10}$$

and θ can be approximated by $\partial v/\partial x$. Then, the normal vector can be written as

$$\mathbf{n} = -v'\mathbf{i} + \mathbf{j}. \tag{4.11}$$

Therefore, the normal acceleration and the normal velocities are given by

$$\begin{aligned} \dot{w}^n &= \dot{\mathbf{w}} \cdot \mathbf{n} = -\dot{w}_x v' + \dot{w}_y \\ w^n &= \mathbf{w} \cdot \mathbf{n} = -w_x v' + w_y \\ U_c^n &= \mathbf{U}_c \cdot \mathbf{n} = -U_{cx} v' + U_{cy} \\ \ddot{R}^n &= \ddot{\mathbf{R}} \cdot \mathbf{n} = -uv' + v. \end{aligned} \tag{4.12}$$

Therefore, using Equations 4.3 and 4.12, the relative normal velocity V_{rel} is given by

$$\begin{aligned} V_{rel}^n &= w^n + U_c^n - \dot{R}^n \\ &= -\left(w_x + U_{cx} - \dot{R}_x\right) v' + \left(w_y + U_{cy} - \dot{R}_y\right), \end{aligned} \tag{4.13}$$

so that Equation 4.1 can be rewritten as

$$\begin{aligned} f^n(X,t) = {} & C_D \rho_f r_o \left(-w_x v' + \dot{u}v' + w_y + U_c - \dot{v}\right) \\ & \times \left|-w_x v' + \dot{u}v' + w_y + U_c - \dot{v}\right| \\ & -C_A \rho_f \pi r_o^2 \left(-\ddot{u}v' + \ddot{v}\right) + C_M \rho_f \pi r_o^2 \left(\dot{w}_y - \dot{w}_x v'\right). \end{aligned} \tag{4.14}$$

The drag, inertia and added mass coefficients must be obtained by experiment. However, for a long cylinder, C_M approaches its theoretical limiting value (uniformly accelerated flow) of 2 and C_A approaches unity [38][81]. The inertia and drag coefficients are functions of at least three parameters [81],

$$\begin{aligned} C_M &= C_M(\mathrm{Re}, Kc, \text{ cylinder roughness}) \\ C_D &= C_D(\mathrm{Re}, Kc, \text{ cylinder roughness}), \end{aligned}$$

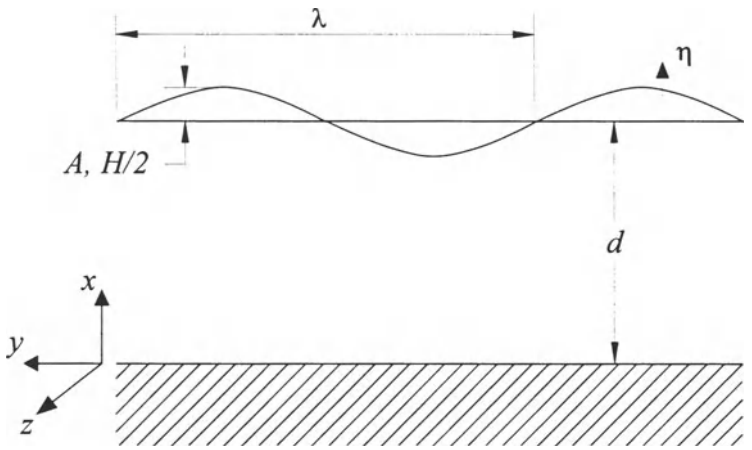

Figure 4.2. Wave Profile

where Re is the Reynolds number and Kc is the Keulegan-Carpenter number, given by

$$\begin{aligned} \mathrm{Re} &= \frac{\rho_f U D}{\mu} \\ Kc &= 2\pi \frac{H}{2D}, \end{aligned} \tag{4.15}$$

where ρ_f is the density of the fluid, U is the free stream velocity, D is the diameter of the structure, μ is the dynamic or absolute viscosity, and $H/2$ is the amplitude of the wave (see Figure 4.2). For water, the dynamic viscosity is $1.12 \times 10^{-3}\ N \cdot s/m^2$ [57].

The drag coefficient can be plotted roughly as a function of Reynolds number for a certain shape of structure. For a cylinder, such a plot can be found in [61][5].

To find the full expression for the fluid force, we need to know how to express the wave and current velocities. The next two sections show how this can be done.

3.1 Wave Velocities

3.1.1 Linear Wave Theory (Plane Waves)

[5]See pg. 387.

Linear wave theory, sometimes called the Airy wave theory, defines the wave profile η as (Figure 4.2)

$$\eta(y,t) = A\cos(ky - \omega t), \tag{4.16}$$

and the velocity components of the gravity wave are given by

$$\begin{aligned} w_y(x,y,t) &= A\omega\frac{\cosh kx}{\sinh kd}\cos(ky-\omega t) \\ w_x(x,y,t) &= A\omega\frac{\sinh kx}{\sinh kd}\sin(ky-\omega t), \end{aligned} \tag{4.17}$$

where k, ω, and A are wave number, angular frequency, and amplitude of a surface wave. The velocities vary with time, horizontal coordinate y, and depth x. The frequency is related to the wave number by the dispersion relationship given by

$$\omega^2 = gk\tanh kd, \tag{4.18}$$

where d is the water depth. For deep water, $\tanh kd$ approaches unity and the frequency is given by

$$\lim_{d\to\infty}\omega^2 = gk. \tag{4.19}$$

3.1.2 Random Waves (Pierson-Moskowitz Spectrum)

The one-sided Pierson-Moskowitz spectrum[6] for the surface elevation or wave profile η is given by

$$S_{\eta\eta}(\omega) = \frac{A_o}{\omega^5}e^{-B/\omega^4}\ \left[m^2 s\right], \tag{4.20}$$

where A_o and B are given by

$$\begin{aligned} A_o &= 0.0081g^2 = 0.7796\ [m^2/s^4] \\ B &= 0.74\left(\frac{g}{U_{w,\,19.5}}\right)^4\ [s^{-4}]. \end{aligned} \tag{4.21}$$

g is the gravitational acceleration, and $U_{w,\,19.5}$ is the wind velocity evaluated 19.5 m above the still water level [81]. Note that the units are specified in square brackets. The only data we need to obtain to evaluate the power spectrum is the wind velocity at $h = 19.5\ m$. However, sometimes

[6]The Pierson-Moskowitz is chosen in this work as a classical spectrum. Without doubt, spectra are chosen for the specific ocean site where the structure will be placed.

the power spectrum is expressed in terms of significant wave height, H_s. The significant wave height is the average height of the highest one-third of all waves [73]. The significant wave height is mathematically defined by [17][7]

$$H_s = 4\sigma \; [m] \,, \tag{4.22}$$

where σ is the standard deviation of the wave profile. For the zero mean case, the variance is the area under the spectral density curve given by

$$\begin{aligned} \sigma^2 &= \int_0^\infty S_{\eta\eta}(\omega)\, d\omega = \frac{A_o}{4B}\, e^{-B/\omega^4}\Big|_0^\infty \\ &= \frac{A_o}{4B} \; [m^2] \,. \end{aligned} \tag{4.23}$$

B, in terms of significant wave height, is given by

$$B = \frac{4A_o}{H_s^2}. \tag{4.24}$$

Therefore, the Pierson-Moskowitz spectrum can be written as

$$S_{\eta\eta}(\omega) = \frac{A_o}{\omega^5} e^{-\frac{4A_o}{H_s^2}\omega^{-4}} \; \left[m^2 s\right] . \tag{4.25}$$

With Equation 4.22 and 4.23, the significant wave height in terms of the wind velocity is given by

$$H_s = 2\sqrt{\frac{A_o}{B}}. \tag{4.26}$$

The peak frequency (frequency at which $S_{\eta\eta}(\omega)$ is maximum) can be obtained by setting the following equal to zero,

$$\frac{dS_{\eta\eta}(\omega)}{d\omega} = 0. \tag{4.27}$$

The peak frequency is given by

$$\omega_{peak} = \left(\frac{4}{5}B\right)^{1/4} . \tag{4.28}$$

The spectra when the significant wave height is 9, 12, and 15 m are plotted in Figure 4.3 for $U_{w,\,19.5m} = 25\ m/s$.

[7] See Equation 4.62.

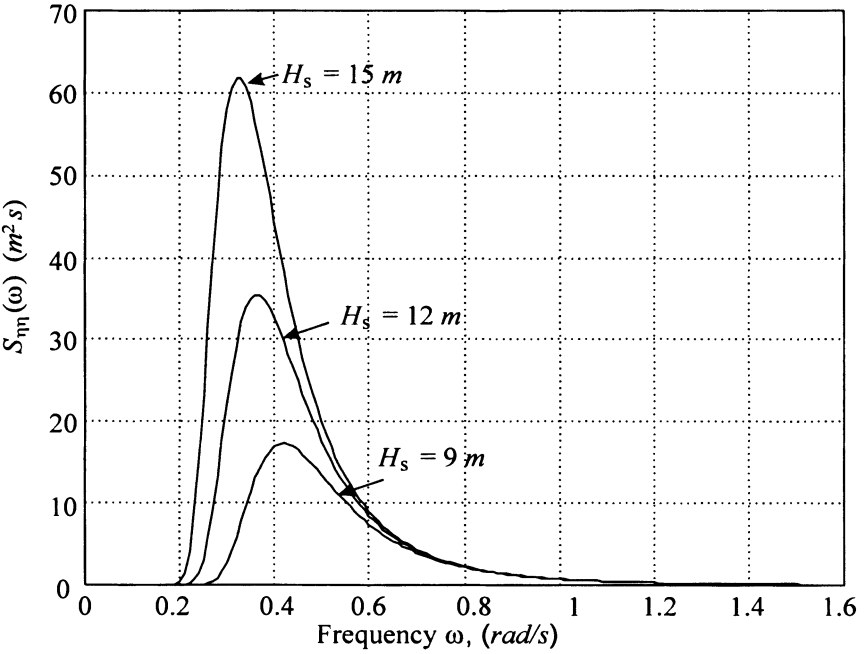

Figure 4.3. Pierson-Moskowiz Spectrum for $H_s = 9, 12, 15\ m$

The next step is to find the surface elevation or wave profile η. In a nonlinear analysis, structural response is found by a numerical integration in time. Therefore, we need to convert the wave elevation spectrum into an equivalent force time-history. To do so, we use the method suggested by Borgman [15]. The surface elevation, as a function of both time and spatial coordinate y, is represented by[8]

$$\eta(y,t) = \int_0^\infty \cos(ky - \omega t)\sqrt{2S_{\eta\eta}(\omega)\, d\omega}, \tag{4.29}$$

where the spectrum is given by Equation 4.20. This integral can be represented in terms of finite sums as

$$\eta(y,t) = \sum_{n=1}^{N} \cos(\bar{k}_n y - \bar{\omega}_n t - \varphi_n)\sqrt{2S_{\eta\eta}(\bar{\omega}_n)\,\Delta\omega_n}, \tag{4.30}$$

[8]The details are provided in Appendix A.

where φ_n is a uniform random number between 0 and 2π and

$$\begin{aligned} \bar{\omega}_n &= \frac{\omega_n + \omega_{n-1}}{2}, \\ \Delta\omega_n &= \omega_n - \omega_{n-1} \\ \bar{k}_n &= k(\bar{\omega}_n) \text{ for } n = 1, \cdots, N. \end{aligned} \tag{4.31}$$

The frequency ω_0 is zero, and ω_N is chosen so that most of the area is contained between ω_0 and ω_N. The frequencies ω_1 to ω_{N-1} are chosen so that the area under the spectrum curve for each interval is equal. The area between the interval $\omega_0 = 0$ to ω_n is $\frac{n}{N}$ of total area under the curve between the interval $\omega_0 = 0$ to ω_N. Therefore, ω_n is given by

$$\begin{aligned} \int_0^{\omega_n} S_{\eta\eta}(\omega)\, d\omega &= \frac{n}{N} \int_0^{\omega_N} S_{\eta\eta}(\omega)\, d\omega \\ \therefore\ \omega_n &= \left(\frac{B}{\ln N/n + B/\omega_N^4} \right)^{1/4} \text{ for } n = 1, \cdots, N-1. \end{aligned} \tag{4.32}$$

Note that the last term in Equation 4.30 is the square root of the incremental area between ω_n and ω_{n-1}. One partitioned area, say a^2, is approximately the total area divided by the number of intervals, N. From Equation 4.23,

$$\begin{aligned} a^2 &= \frac{1}{N} \int_0^{\infty} S_{\eta\eta}(\omega)\, d\omega \\ &= \frac{A_o}{4BN} = \frac{H_s^2}{16N}, \end{aligned} \tag{4.33}$$

and η is written as

$$\eta(y,t) = \frac{H_s}{4} \sqrt{\frac{2}{N}} \sum_{n=1}^{N} \cos(\bar{k}_n y - \bar{\omega}_n t). \tag{4.34}$$

Therefore, the wave velocities are given by

$$\begin{aligned} w_y(x,y,t) &= \frac{H_s}{4} \sqrt{\frac{2}{N}} \sum_{n=1}^{N} \bar{\omega}_n \frac{\cosh \bar{k}_n x}{\sinh \bar{k}_n d} \cos(\bar{k}_n y - \bar{\omega}_n t) \\ w_x(x,y,t) &= \frac{H_s}{4} \sqrt{\frac{2}{N}} \sum_{n=1}^{N} \bar{\omega}_n \frac{\sinh \bar{k}_n x}{\sinh \bar{k}_n d} \sin(\bar{k}_n y - \bar{\omega}_n t). \end{aligned} \tag{4.35}$$

Sample wave profiles are plotted for the case where $H_s = 6.364\ m$, $\omega_N = 1.5\ rad/s$, $d = 480\ m$ and $N = 15$ in Figures 4.4 and for the case

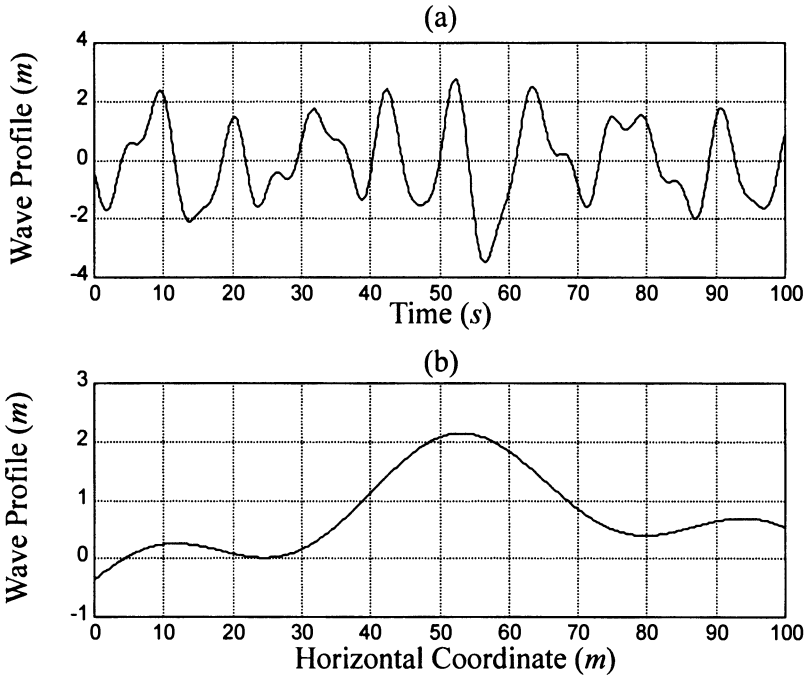

Figure 4.4. Wave Profile $\eta(x,t)$ for $H_s = 6.364\ m$, $d = 480\ m$, $\omega_N = 1.5\ rad/s$, $N = 15$

where and $H_s = 0.06364\ m$, $\omega_N = 10\ rad/s$, $d = 1.05\ m$ and $N = 15$ are plotted in Figure 4.5. Again, the first case is likely to be seen in the ocean, and the second case is likely to be seen in a laboratory setting.

Two components of wave velocities as functions of depth x are also plotted in Figures 4.6 and 4.7.

3.2 Current Velocity in the Ocean, U_c

According to Isaacson, the current velocity consists three components: tidal components U_{tide}, a low frequency component related to long term circulation $U_{circulation}$, and wind-induced drift current U_{drift} [32]. They are measured at the water surface. It is assumed that the current velocity has only a horizontal component. The current velocity is then given by the empirical equation

$$U_c(x) = (U_{tide}(d) + U_{circulation}(d)) \left(\frac{x}{d}\right)^{1/7} + U_{drift}(0) \left(\frac{x - d + d_o}{d_o}\right), \tag{4.36}$$

where d is the water depth, d_o is the smaller of the depth of the thermocline or 50 m. The value of U_{tide} is obtained from tide tables, and U_{drift}

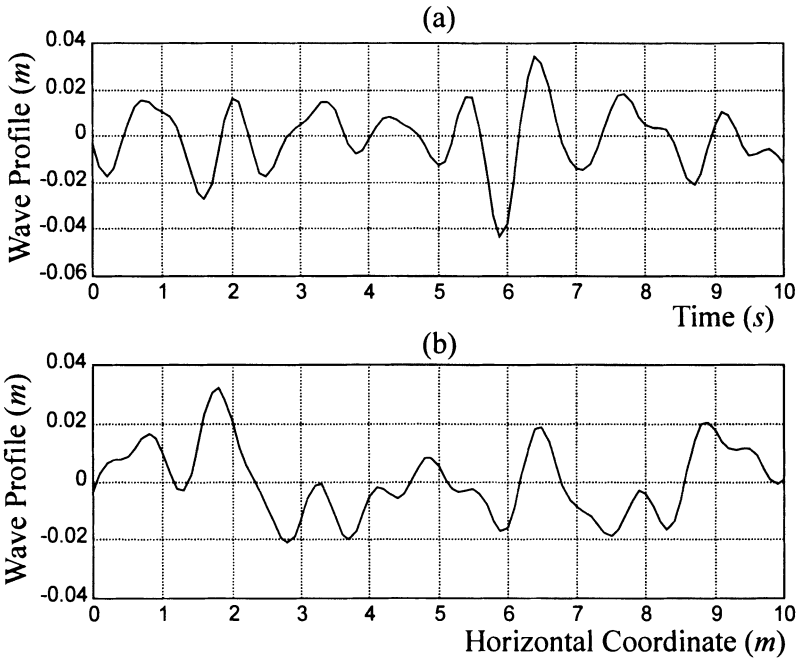

Figure 4.5. Wave Profile $\eta(x,t)$ when $H_s = 0.06364\ m$, $d = 1.05\ m$, $\omega_N = 10\ rad/s$, $N = 15$

is about 3% of the 10 minute mean wind velocity at 10 m above the sea level.

In the laboratory setting the current velocity can be assumed to be constant with depth.

3.3 Wind Velocity, U_w

Wilson gives an expression for the mean wind velocity as follows [81],

$$U_w(h) = \left(\frac{h}{h_{ref}}\right)^{1/n} U_w(h_{ref}), \tag{4.37}$$

where h is the height from the water surface. The reference height, h_{ref}, is usually taken as 10 m. The value of n is taken to be 7 or 8 for an unobstructed sea area and 12 or 13 for gusts.

4. Fluid Force II: Vortex Induced Oscillations

When the flow passes around a fixed cylinder, for a very low Reynolds number ($0 < \mathrm{Re} < 4$), the flow separates and reunites smoothly. When the Reynolds number is between 4 and 40, the eddies are formed and

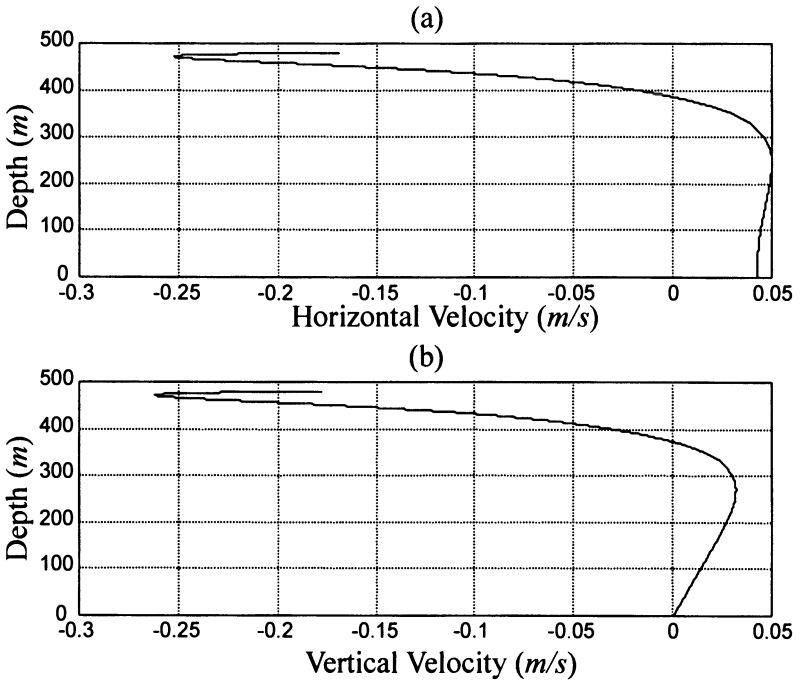

Figure 4.6. Wave Velocities $w_x(x,t,z)$ and $w_y(x,t,z)$ at $y = 0$ and $t = 0$ when $H_s = 6.364\ m$, $d = 480\ m$

are attached to the downstream side of cylinder. They are stable, and there is no oscillation in the flow.

For a flow with a Reynolds number greater than about 40, the fluid near the cylinder starts to oscillate due to the vortices. The frequency of oscillation is related to the non-dimensionalized parameter, the Strouhal number, defined by

$$St = \frac{f_v D}{U}, \tag{4.38}$$

where f_v is the frequency of oscillation, U is the steady velocity of the flow, D is the diameter of the cylinder. For circular cylinders, the Strouhal number roughly stays at 0.2 for $10^3 < \text{Re} < 2 \times 10^5$ [62]. Therefore, the shedding frequency is a function of the flow velocity and the diameter of the cylinder.

When the flow passes by a cylinder which is free to vibrate, the shedding frequency is also controlled by the movement of the beam. When the shedding frequency is close to the first natural frequency of the structure (± 25 to 30% of the natural beam frequency [67]), the beam takes control of the vortex shedding. The vortices will shed at the natural

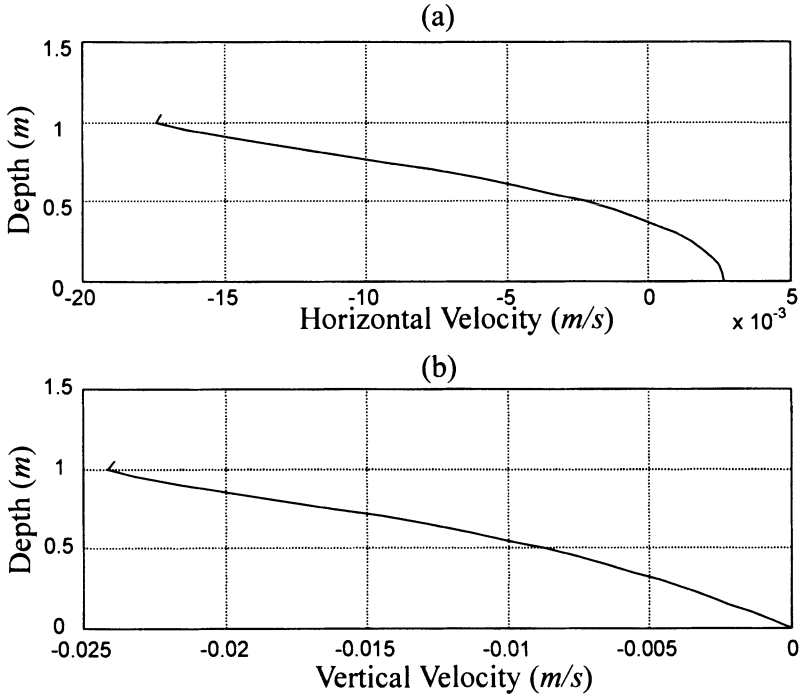

Figure 4.7. Wave Velocities $w_x(x,t,z)$ and $w_y(x,t,z)$ at $y = 0$ and $t = 0$ when $H_s = 0.06364\ m$, $d = 1.05\ m$

frequency of the beam instead of at the frequency determined by the Strouhal number. This is called lock-in or synchronization. Figure 4.8 shows the shedding frequency as a function of flow velocity in the presence of a structure. f_1 and f_2 are the natural frequencies of the structure.

The existing models for vortex induced oscillation include single degree-of-freedom models and coupled models [14]. The SDOF models include the effect of vortex shedding as an external forcing function. The coupled models assume that the equations that govern the motion of the structure and the lift coefficient are coupled.

The synchronization is a result of nonlinear interaction between the oscillation of the body and the action of the fluid. Therefore, a linear model will not predict the synchronization.

In this work, we assume that the force induced by the vortices is a simple sinusoid,

$$f_{shedding}(x,t) = A(x)\cos\omega_v t. \tag{4.39}$$

Because the force is linear and so is the governing equation, this model will not predict the synchronization behavior. Also, when the Strouhal

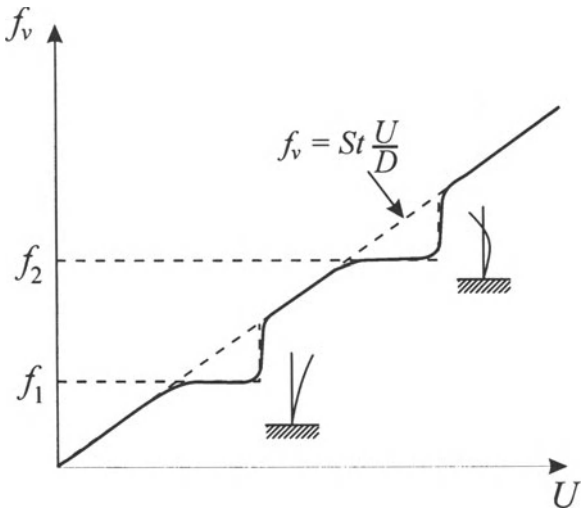

Figure 4.8. An Example of Fluid Dynamic and Fluid Elastic Resonance

frequency, ω_v, approaches the natural frequency of the beam, the response will grow indefinitely. This area of research still has many unanswered questions and is outside the scope of this monograph.

5. Chapter Summary

In this chapter, we formulated the fluid forcing function in the transverse direction using the Morison equation. The fluid force is due to random waves and current. The random waves were characterized by the Pierson-Moskowitz spectrum and the Airy wave theory. The time history is obtained using Borgman's method. The Morison force acts in the plane defined by the structure and the direction of the fluid. The out-of-plane force due to shedding vortices is modeled as a simple sinusoid with the Strouhal frequency.

Chapter 5

COUPLED AXIAL AND TRANSVERSE VIBRATION IN TWO DIMENSIONS

For a vibrating beam, bending and rigid body motion are the primary components of the overall behavior. Therefore, it may be sufficient to use a single degree of freedom model or a linear transverse model such as the Euler-Bernoulli, Rayleigh, shear, or Timoshenko model. A discussion of linear transverse models can be found in Chapter 3. The linear transverse models assume that the coupling between the transverse and the axial motion is negligible. However, the coupling becomes more significant with increasing slenderness ratio (the ratio of length to the radius of gyration of the cross-sectional area). Therefore, the nonlinear coupling effect in long slender members of compliant towers may be important in the overall response. It has also been observed that there are significant high frequency nonlinear effects that appear to be caused by extensional or longitudinal vibration in some cases in an ocean environment. Therefore, it is necessary to investigate the couple transverse and longitudinal response of a beam under realistic environmental forces.

In this chapter, the nonlinear equations of motion and boundary conditions for the coupled transverse and longitudinal vibration are formulated using Hamilton's variational principle. It is assumed that strains are small but the rotation is moderate compared to the strain so that the equations of motion for the axial and transverse motion are nonlinearly coupled. The free response in vacua, the damped-free response in water, and the forced response due to a harmonic transverse load or random wave load are considered in particular. The fluid force, formulated in Chapter 4, is used for the damped response and the forced response due to random waves. The resulting nonlinear coupled partial differential equations are solved numerically using the finite difference approach. This subject has also been treated by Han and Benaroya [24][25].

S. M. Han et al., *Nonlinear and Stochastic Dynamics of Compliant Offshore Structures*

1. Nomenclature

Symbol	Description	Units
A	cross-sectional area of the beam	m^2
A_f	cross-sectional area of the displaced volume, πr_o^2	m^2
C_A	added mass coefficient	-
C_D	drag coefficient	-
C_M	inertia coefficient	-
d	water depth	m
D	diameter of the structure	m
E	Young's modulus	N/m^2
$f(X,t)$	distributed transverse load	N/m
g	gravitational acceleration	m/s^2
h	height from the still water level	m
H	wave height from trough to peak	m
Hs	significant wave height	m
I	area moment of inertia	m^4
k	spring constant	$N \cdot m$
KE	kinetic energy	$N \cdot m$
m_{fl}	displaced fluid mass per length, $\rho_f A_f$	kg/m
M_p	point mass	kg
$p(X,t)$	distributed axial load	N/m
r_i	inner radius of the cylinder	m
r_o	outer radius of the cylinder	m
$\mathbf{R}$	displacement vector of the structure	m
s	slenderness ratio	-
t	time	s
$u(X,t)$	midplane axial displacement	m
$u_1(X,Y,t)$	axial displacement	m
$u_2(X,t)$	transverse displacement in the y direction	m
$u_3(X,t)$	transverse displacement in the z direction	m
U_c	current velocity	m/s
$v(X,t)$	midplane transverse displacement	m
w_x, w_y	wave velocities	m/s
X	Lagrangian coordinate	m
Y	distance from the neutral axis	m
$\mathcal{E}_{if}$	Green's strain	-
δ	damping ratio	-
ρ	density of the structure	kg/m^3
ρ_f	density of the fluid	kg/m^3
ζ	logarithmic decrement	-
ω_{peak}	frequency at which the PSD is maximum	rad/s
ω_f	forcing frequency	rad/s

2. Mathematical Formulation

In linear behavior, transverse and longitudinal motion can be decoupled such that the motions can be described effectively by simple linear partial differential equations: the longitudinal motion by

$$EA\frac{\partial^2 u(x,t)}{\partial x^2} = \rho A\frac{\partial^2 u(x,t)}{\partial t^2}, \tag{5.1}$$

and the transverse motion by one of the four models discussed in Chapter 3. The Euler-Bernoulli model is given by

$$EI\frac{\partial^4 v(x,t)}{\partial x^4} = -\rho A\frac{\partial^2 v(x,t)}{\partial t^2}, \tag{5.2}$$

where $u(x,t)$ is the axial displacement, $v(x,t)$ is the transverse displacement, E is Young's modulus, A is the cross-sectional area, I is the area moment of inertia of the cross-section about the neutral axis, and ρ is the density.

In this chapter, we derive equations of motion that describe the motion of the beam shown in Figure 1.7 assuming that the beam can vibrate both axially and transversely. As in the linear cases, the beam is confined on a plane not allowing the motion in the third direction, that is, out of the page in Figure 1.7.

In addition to the basic beam assumptions listed in Section 1, we make an additional assumption that the displacement is given by Kirchhoff's hypothesis.

2.1 Displacements, Strains, and Stresses

Let us consider a beam with an original length L. Beam elements are labeled by their location in the undeformed configuration, X. The reference and current configurations of the midplane are shown in Figure 5.1. The dotted line is the reference configuration, and the solid line is the current configuration.

Using Kirchhoff's hypothesis, we write the displacements as

$$\begin{aligned} u_1(X,Y,t) &= u(X,t) - Y\frac{\partial v}{dX}(X,t) \\ u_2(X,t) &= v(X,t) \\ u_3(X,t) &= 0, \end{aligned} \tag{5.3}$$

where u is the deflection of the midplane in the x direction and v in the y direction. Y is the transverse distance from the midplane to the point of interest on the cross-section in the reference frame. The Kirchhoff displacement field assumes that the axial displacement in the cross-section

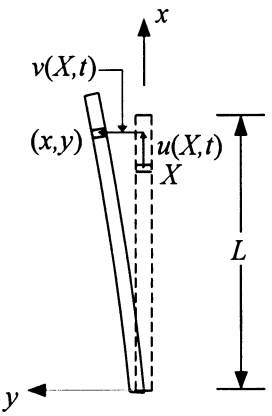

Figure 5.1. Reference and Current Midplane Configurations of the Beam

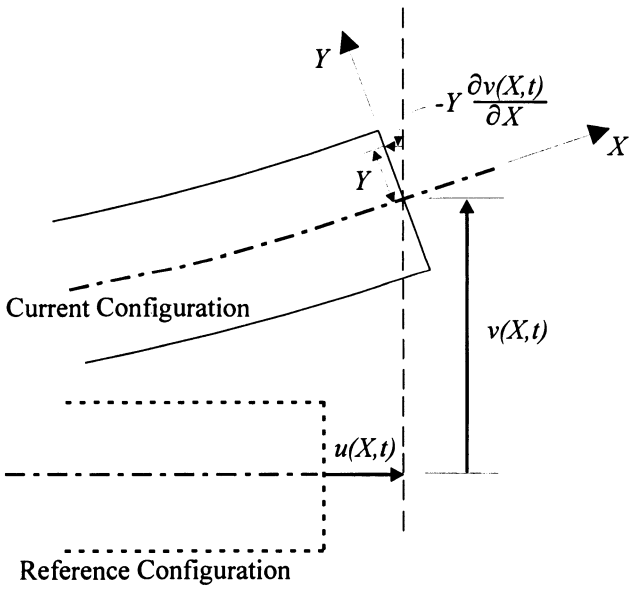

Figure 5.2. Kirchhoff's Hypothesis

varies linearly with the in-plane-coordinate as shown in Figure 5.2. The form of the displacement field implies that the shear effect is negligible when compared to that of the bending moment. Therefore, we are assuming that the beam is slender enough so that such an assumption is valid.

Assuming a symmetrical cross-section, u is also the average deflection of the beam element X. We assume that the strain is small, but the rotation can be moderate. Mathematically, we write

$$\frac{\partial u_1}{\partial X} \sim \left(\frac{\partial u_2}{\partial X}\right)^2 << 1. \tag{5.4}$$

In terms of midplane deflections, we can write

$$\frac{\partial u}{\partial X} \sim \left(\frac{\partial v}{\partial X}\right)^2 << 1. \tag{5.5}$$

It should be noted that in order for Kirchhoff's hypothesis to be valid, the only condition that has to be satisfied is that the strains be small when compared to the rotation [59][1]. Therefore, by using Kirchhoff's hypothesis, we have already assumed small strains and moderate rotation.

The general form of Green's strains are given by

$$\begin{aligned}
\mathcal{E}_{11} &= \frac{\partial u_1}{\partial X} + \frac{1}{2}\left[\left(\frac{\partial u_1}{\partial X}\right)^2 + \left(\frac{\partial u_2}{\partial X}\right)^2 + \left(\frac{\partial u_3}{\partial X}\right)^2\right] \\
\mathcal{E}_{22} &= \frac{\partial u_2}{\partial Y} + \frac{1}{2}\left[\left(\frac{\partial u_1}{\partial Y}\right)^2 + \left(\frac{\partial u_2}{\partial Y}\right)^2 + \left(\frac{\partial u_3}{\partial Y}\right)^2\right] \\
\mathcal{E}_{33} &= \frac{\partial u_3}{\partial Z} + \frac{1}{2}\left[\left(\frac{\partial u_1}{\partial Z}\right)^2 + \left(\frac{\partial u_2}{\partial Z}\right)^2 + \left(\frac{\partial u_3}{\partial Z}\right)^2\right] \\
\mathcal{E}_{12} &= \frac{1}{2}\left[\frac{\partial u_2}{\partial X} + \frac{\partial u_1}{\partial Y} + \frac{\partial u_1}{\partial X}\frac{\partial u_1}{\partial Y} + \frac{\partial u_2}{\partial X}\frac{\partial u_2}{\partial Y} + \frac{\partial u_3}{\partial X}\frac{\partial u_3}{\partial Y}\right] \\
\mathcal{E}_{23} &= \frac{1}{2}\left[\frac{\partial u_3}{\partial Y} + \frac{\partial u_2}{\partial Z} + \frac{\partial u_1}{\partial Y}\frac{\partial u_1}{\partial Z} + \frac{\partial u_2}{\partial Y}\frac{\partial u_2}{\partial Z} + \frac{\partial u_3}{\partial Y}\frac{\partial u_3}{\partial Z}\right] \\
\mathcal{E}_{13} &= \frac{1}{2}\left[\frac{\partial u_3}{\partial X} + \frac{\partial u_1}{\partial Z} + \frac{\partial u_1}{\partial X}\frac{\partial u_1}{\partial Z} + \frac{\partial u_2}{\partial X}\frac{\partial u_2}{\partial Z} + \frac{\partial u_3}{\partial X}\frac{\partial u_3}{\partial Z}\right].
\end{aligned} \tag{5.6}$$

[1] See pg. 197.

Using the assumptions stated in Equations 5.4 and 5.5, Green's strains are given by

$$\begin{aligned}
\mathcal{E}_{XX} &= \frac{\partial u_1}{\partial X} + \frac{1}{2}\left(\frac{\partial u_2}{\partial X}\right)^2 \\
\mathcal{E}_{YY} &= \frac{\partial u_2}{\partial Y} \\
\mathcal{E}_{XY} &= \frac{1}{2}\left[\frac{\partial u_2}{\partial X} + \frac{\partial u_1}{\partial Y}\right] \\
\mathcal{E}_{YZ} &= 0 \\
\mathcal{E}_{XZ} &= 0 \\
\mathcal{E}_{ZZ} &= 0.
\end{aligned} \tag{5.7}$$

Using the assumed displacement field given in Equation 5.3, Green's strains are given by

$$\begin{aligned}
\mathcal{E}_{XX} &= \frac{\partial u}{\partial X} - Y\frac{\partial^2 v}{\partial X^2} + \frac{1}{2}\left(\frac{\partial v}{\partial X}\right)^2 \\
\mathcal{E}_{YY} &= 0 \\
\mathcal{E}_{XY} &= 0,
\end{aligned} \tag{5.8}$$

where we keep in mind that u and v are functions of X and t. The form of strain written above assumes that Poisson's ratio is zero. Then, the second Piola-Kirchhoff stress is given by

$$\tilde{\sigma}_{XX} = E\mathcal{E}_{XX}. \tag{5.9}$$

2.2 Lagrangian

The general expression for the strain energy is given by

$$PE_{strain} = \frac{1}{2}\int_{V_o} \bar{\sigma}_{ij}\mathcal{E}_{ij}dV_o, \tag{5.10}$$

where V_o is the volume of the undeformed beam. Using the expressions for the second Piola-Kirchhoff stress and Green's strain, we obtain

$$PE_{strain} = \frac{E}{2}\int_X\int_A \left(u' - Yv'' + \frac{1}{2}v'^2\right)^2 dAdX, \tag{5.11}$$

where prime notation is used for derivatives with respect to X. Expanding the integrand, we obtain

$$PE_{strain} = \frac{E}{2}\int_0^L \int_A \left(u'^2 - 2u'v''Y + v'^2u' + Y^2v''^2 - v'^2Yv'' + \frac{1}{4}v'^4\right) dAdX. \tag{5.12}$$

Integrating over the cross-sectional area, the terms with odd functions of Y (second and fifth) disappear due to the assumption of a symmetric cross-section. Y^2 integrated over the cross-sectional area becomes the area moment of inertia about the neutral axis and is denoted as I. Therefore, we can write

$$\begin{aligned} PE_{strain} &= \frac{E}{2}\int_0^L \left[\left(u'^2 + v'^2u' + \frac{1}{4}v'^4\right)A + v''^2I\right] dX \\ &= \int_0^L \left[\frac{1}{2}EA\left(u' + \frac{1}{2}v'^2\right)^2 + \frac{1}{2}EIv''^2\right] dX, \end{aligned} \tag{5.13}$$

where the first term is the membrane energy, and second is the bending energy.

The potential energy stored in the torsional spring is given by

$$PE_{spring} = \frac{1}{2}k\theta^2, \tag{5.14}$$

where θ is the angle of twist of the torsional spring. The angle of twist can be approximated by the first derivative of the transverse deflection $v'(0,t)$ using the small angle assumption.

Therefore, we can write the total potential energy as

$$PE = \frac{1}{2}\int_0^L \left[EA\left(u' + \frac{1}{2}v'^2\right)^2 + EIv''^2\right] dX + \frac{1}{2}kv'(0,t)^2 \tag{5.15}$$

The kinetic energy has two components: kinetic energy of the beam and kinetic energy of the point mass. The kinetic energy of the beam is given by

$$KE_{beam} = \frac{1}{2}\int_0^L \int_A \left[\rho(\dot{u}_1^2 + \dot{u}_2^2)\right] dAdX, \tag{5.16}$$

where dot notation is used for derivatives with respect to time. Replacing the axial displacements u_1 and u_2 and using Equation 5.3, we can write

$$\begin{aligned}\frac{\rho}{2}\int_0^L\int_A(\dot{u}_1^2+\dot{u}_2^2)dAdX &= \frac{\rho}{2}\int_0^L\int_A\left[\left(\dot{u}-Y\dot{v}'\right)^2+\dot{v}^2\right]dAdX\\ &= \frac{\rho}{2}\int_0^L\int_A\left(\dot{u}^2-2Y\dot{u}\dot{v}'+Y^2\dot{v}'^2+\dot{v}^2\right)dAdX\\ &= \frac{1}{2}\int_0^L\left[\rho A(\dot{u}^2+\dot{v}^2)+\rho I\dot{v}'^{\,2}\right]dX, \qquad (5.17)\end{aligned}$$

where the term with factor Y integrated over the cross-section disappeared, and the term with factor Y^2 integrated over the cross-section became I as before. The kinetic energy of the point mass is given by

$$KE_{\text{point mass}} = \frac{1}{2}M_p\left[\dot{v}^2(L,t)+\dot{u}^2(L,t)\right]. \qquad (5.18)$$

The total kinetic energy of the system is then written as

$$KE = \frac{1}{2}\int_0^L\left[\rho A(\dot{u}^2+\dot{v}^2)+\rho I\dot{v}'^{\,2}\right]dX+\frac{1}{2}M_p\left[\dot{v}^2(L,t)+\dot{u}^2(L,t)\right]. \qquad (5.19)$$

The term $\rho I\dot{v}'^{\,2}$ is Rayleigh's rotational term. It is the kinetic energy due to the rotation of the cross-section and is usually small compared to the kinetic energy due to translation, $\rho A(\dot{u}^2+\dot{v}^2)$.

The Lagrangian integrated over time, $\int_{t_i}^{t_f}\mathcal{L}dt = \int_{t_i}^{t_f}(KE-PE)\,dt$, is given by

$$\begin{aligned}&\int_{t_i}^{t_f}\mathcal{L}dt\\ &=\frac{1}{2}\int_{t_i}^{t_f}\left\{\int_0^L\left[\rho A(\dot{u}^2+\dot{v}^2)+\rho I\dot{v}'^{\,2}-EA\left(u'+\frac{1}{2}v'^{\,2}\right)^2-EIv''^2\right]dX\right.\\ &\left.+\frac{1}{2}M_p\left[\dot{v}^2(L,t)+\dot{u}^2(L,t)\right]-\frac{1}{2}kv'(0,t)^2\right\}dt, \qquad (5.20)\end{aligned}$$

and the virtual work done by the distributed transverse and axial loads is given by

$$\delta W = \int_0^L\left(f(X,t)\,\delta v+p(X,t)\,\delta u\right)dX. \qquad (5.21)$$

If the axial point load, N_o, acts at $X=L$, the virtual work done by N_o is given by

$$\delta W = N_o\delta u(L,t). \qquad (5.22)$$

2.3 Equations of Motion and Boundary Conditions via Hamilton's Principle

The variation of Equation 5.20 is

$$\delta\int_{t_i}^{t_f}\mathcal{L}dt=\int_{t_i}^{t_f}\left\{\int_0^L\left[\rho A(\dot{u}\delta\dot{u}+\dot{v}\delta\dot{v})+\rho I\dot{v}'\delta\dot{v}'\right.\right.$$
$$\left.-EA\left(u'+\frac{1}{2}v'^{\,2}\right)\left(\delta u'+v'\delta v'\right)-EIv''\delta v''\right]dX$$
$$\left.+M_p\left[\dot{v}\left(L,t\right)\delta\dot{v}\left(L,t\right)+\dot{u}\left(L,t\right)\delta\dot{u}\left(L,t\right)\right]-kv'\left(0,t\right)\delta v'\left(0,t\right)\right\}dt. \tag{5.23}$$

Integrating by parts, we obtain

$$\delta\int_{t_i}^{t_f}\mathcal{L}dt=\int_{t_i}^{t_f}\int_0^L\left\{-\rho A\ddot{u}+\left[EA\left(u'+\frac{1}{2}v'^{\,2}\right)\right]'\right\}\delta u$$
$$+\left\{-\rho A\ddot{v}+\left(EA\left(u'+\frac{1}{2}v'^{\,2}\right)v'\right)'+\rho I\ddot{v}''-\left(EIv''\right)''\right\}\delta vdX$$
$$+\int_{t_i}^{t_f}\left\{\left[\left(EIv''\right)'-\rho I\ddot{v}'-EA\left(u'+\frac{1}{2}v'^{\,2}\right)v'\right]\delta v\right\}\Big|_0^L dt$$
$$+\int_{t_i}^{t_f}\left\{-EA\left(u'+\frac{1}{2}v'^{\,2}\right)\delta u-EIv''\delta v'\right\}\Big|_0^L dt$$
$$-\int_{t_i}^{t_f}M_p\left[\ddot{v}\left(L,t\right)\delta v\left(L,t\right)+\ddot{u}\left(L,t\right)\delta u\left(L,t\right)\right]\Big\}dt$$
$$+\int_{t_i}^{t_f}kv'\left(0,t\right)\delta v'\left(0,t\right)dt. \tag{5.24}$$

Note that variations at the two end points in time is assumed to be zero. Hamilton's principle states that $\delta\int_{t_i}^{t_f}\left(\mathcal{L}+W\right)dt=0$, and thus the nonlinear coupled equations of motion are given by

$$\rho A\ddot{u}-\left(EA\left(u'+\frac{1}{2}v'^{\,2}\right)\right)'=p \tag{5.25}$$

$$\rho A\ddot{v}-\left(EA\left(u'+\frac{1}{2}v'^{\,2}\right)v'\right)'-\left(\rho I\ddot{v}'\right)'+\left(EIv''\right)''=f, \tag{5.26}$$

and the corresponding boundary conditions are given by

$$\begin{aligned}
\left[EA\left(u' + \frac{1}{2}v'^{\,2}\right)\right]\Big|_{(0,t)} \delta u\,(0,t) &= 0 \\
\left[EA\left(u' + \frac{1}{2}v'^{\,2}\right) - N_o + M_p\ddot{u}\right]\Big|_{(L,t)} \delta u\,(L,t) &= 0 \\
\left[\left(EIv''\right)' - \rho I\ddot{v}' - EA\left(u' + \frac{1}{2}v'^{\,2}\right)v'\right]\Big|_{(0,t)} \delta v\,(0,t) &= 0 \\
\left[\left(EIv''\right)' - \rho I\ddot{v}' - EA\left(u' + \frac{1}{2}v'^{\,2}\right)v' - M_p\ddot{v}\,(L,t)\right]\Big|_{(L,t)} \delta v\,(L,t) &= 0 \\
\left[EIv'' + kv'\right]\big|_{(0,t)} \delta v'\,(0,t) &= 0. \\
\left[EIv''\right]\big|_{(L,t)} \delta v'\,(L,t) &= 0
\end{aligned} \tag{5.27}$$

In our case, the boundary conditions are given by

$$\begin{aligned}
u(0,t) &= 0 \\
\left[EA\left(u' + \frac{1}{2}v'^{\,2}\right) - N_o + M_p\ddot{u}\right]\Big|_{(L,t)} &= 0 \\
v(0,t) &= 0 \\
\left[kv' - EIv''\right]\big|_{(0,t)} &= 0 \\
\left[\left(EIv''\right)' - \rho I\ddot{v}' - EA\left(u' + \frac{1}{2}v'^{\,2}\right)v' - M_p\ddot{v}\right]\Big|_{(L,t)} &= 0 \\
EIv''\,(L,t) &= 0.
\end{aligned} \tag{5.28}$$

Note that similar equations of motion and boundary conditions are obtained by Bottega [16], Yigit and Christoforou[82], Adrezin and Benaroya [3][4]. Also note that Adrezin uses the Eulerian formulation instead of the Lagrangian formulation used in this chapter.

2.4 Non-dimensionalization

Now, let us non-dimensionalize our equations of motion. The length scales X, $v\,(X,t)$, $u\,(X,t)$ are normalized by the length of the beam L, the time t is normalized by $1/\bar{\omega}$ where $\bar{\omega}$ is some characteristic angular frequency. The energy is normalized by the bending energy. We find

that the equations of motions are then given by

$$\bar{m}\frac{\partial^2\bar{u}}{\partial\bar{t}^2} - \frac{\partial}{\partial\bar{x}}\left(s^2\left(\frac{\partial\bar{u}}{\partial\bar{x}} + \frac{1}{2}\left(\frac{\partial\bar{v}}{\partial\bar{x}}\right)^2\right)\right) = \bar{p}$$

$$\bar{m}\frac{\partial^2\bar{v}}{\partial\bar{t}^2} - \frac{\partial}{\partial\bar{x}}\left(s^2\left(\frac{\partial\bar{u}}{\partial\bar{x}} + \frac{1}{2}\left(\frac{\partial\bar{v}}{\partial\bar{x}}\right)^2\right)\frac{\partial\bar{v}}{\partial\bar{x}}\right) - \frac{\partial}{\partial\bar{x}}\left(\bar{J}\frac{\partial^3\bar{v}}{\partial\bar{t}^2\partial\bar{x}}\right) + \frac{\partial^4\bar{v}}{\partial\bar{x}^4} = \bar{f}, \tag{5.29}$$

and the boundary conditions are given by

$$\begin{aligned}
\bar{u}(0,t) &= 0 \\
\left[s^2\left(\frac{\partial\bar{u}}{\partial\bar{x}} + \frac{1}{2}\left(\frac{\partial\bar{v}}{\partial\bar{x}}\right)^2\right) - \bar{N}_o + \bar{M}_p\frac{\partial^2\bar{u}}{\partial\bar{t}^2}\right]\Bigg|_{(1,t)} &= 0 \\
\bar{v}(0,t) &= 0 \\
\left[\bar{k}\frac{\partial\bar{v}}{\partial\bar{x}} - \frac{\partial^2\bar{v}}{\partial\bar{x}^2}\right]\Bigg|_{(0,t)} &= 0 \\
\left[\frac{\partial^3\bar{v}}{\partial\bar{x}^3} - s^2\left(\frac{\partial\bar{u}}{\partial\bar{x}} + \frac{1}{2}\left(\frac{\partial\bar{v}}{\partial\bar{x}}\right)^2\right)\frac{\partial\bar{v}}{\partial\bar{x}} - \bar{J}\frac{\partial^3\bar{v}}{\partial\bar{t}^2\partial\bar{x}} - \bar{M}_p\frac{\partial^2\bar{v}}{\partial\bar{t}^2}\right]\Bigg|_{(1,t)} &= 0 \\
\frac{\partial^2\bar{v}}{\partial\bar{x}^2}(1,t) &= 0,
\end{aligned} \tag{5.30}$$

where barred quantities are non-dimensional quantities, and their expressions are given by

$$\begin{aligned}
\bar{t} = t\bar{\omega},\ \bar{x} = X/L,\ \bar{m} &= \rho A\frac{\bar{\omega}^2L^4}{EI}, \\
s^2 = \frac{L^2}{I/A},\ \bar{J} = \rho I\frac{L^2\bar{\omega}^2}{EI},\ \bar{p} &= p\frac{L^3}{EI}, \\
\bar{f} = f\frac{L^3}{EI},\ \bar{N}_o &= \frac{N_oL^2}{EI}, \\
\bar{M}_p = M_p\frac{\bar{\omega}^2L^3}{EI},\ \bar{k} &= k\frac{L}{EI}.
\end{aligned} \tag{5.31}$$

Note that the nonlinear coupling terms in the equations of motion have an s^2 factor in common. s is the slenderness ratio, the ratio of the length of the beam to the radius of gyration of the cross-section. If the beam is slender, the contribution of the nonlinear coupling term becomes large. Therefore, this nonlinear coupling term may be important for offshore structures which tend to be long.

2.5 Linear Transverse Vibration with Tension

Now, let us consider the special case when the longitudinal vibration can be neglected. The longitudinal part of the equation of motion (Equation 5.25) is reduced to

$$N' = -p(X,t), \tag{5.32}$$

where N is the axial force given by

$$N = EA\left(u' + \frac{1}{2}v'^2\right). \tag{5.33}$$

Equation 5.32 can be integrated to yield

$$N(X,t) = -\int_{X_o}^{X} p(x_o,t)\,dx_o + N(X_o,t), \tag{5.34}$$

where X_o is an arbitrary location in the beam where $N(X_o,t)$ is known. Since $N(L,t) = N_o - M_p\ddot{u}(L,t)$ from the second boundary condition in Equations 5.28, we can write

$$N(X,t) = -\int_{L}^{X} p(x_o,t)\,dx_o + N_o - M_p\ddot{u}(L,t). \tag{5.35}$$

Since it is assumed that the axial vibration is negligible, we have

$$N(X,t) = -\int_{L}^{X} p(x_o,t)\,dx_o + N_o. \tag{5.36}$$

Therefore, the equation for the transverse vibration (Equation 5.26) can be written as

$$\rho A\ddot{v} - \left(\left[\int_X^L p dx_o + N_o\right]v'\right)' - (\rho I\ddot{v}')' + (EIv'')'' = f. \tag{5.37}$$

The corresponding boundary conditions are given by

$$\begin{aligned} v(0,t) &= 0 \\ \left[kv' - EIv''\right]\big|_{(0,t)} &= 0 \\ \left[(EIv'')' - \rho I\ddot{v}' - Nv' - M_p\ddot{v}\right]\Big|_{(L,t)} &= 0 \\ EIv''(L,t) &= 0. \end{aligned} \tag{5.38}$$

Another way of obtaining the differential equation is to formulate the Lagrangian given by

$$\mathcal{L} = \frac{1}{2}\int_0^L \left[\rho A\dot{v}^2 + \rho I\dot{v}'^2 - EIv''^2 - Nv'^2\right]dX - \frac{1}{2}kv'(0)^2, \tag{5.39}$$

which results in

$$\rho A\ddot{v} - \left[Nv'\right]' - \left(\rho I\ddot{v}'\right)' + \left(EIv''\right)'' = f, \tag{5.40}$$

where $N(X,t)$ is given in Equation 5.36.

In the case where N is constant (when $p(X,t)$ is zero), the analytical solution can be obtained using the methods of separation of variables and eigenfunction expansion[2]. When N is not constant, but a function of X, we resort to a numerical solution using the finite difference method.

2.6 Linear Response without Tension

In this section, we examine the response of the linear models without the tension. Analytical solutions are obtained for the longitudinal and transverse motion. This is done so that we can compare the results of the nonlinear problem with those of the equivalent linear problems. Specifically, the natural frequencies of the linear systems will be compared to those of the nonlinear system.

2.6.1 Longitudinal Motion

Here, we use the linear formulations in order to obtain the natural frequencies of the system. The linear equation of motion for the axial motion is given by Equation 5.1 or

$$EAu'' = \rho A\ddot{u}. \tag{5.41}$$

The corresponding boundary conditions are given by

$$\begin{aligned} u(0,t) &= 0 \\ EAu'(L,t) - N_o + M_p\ddot{u}(L,t) &= 0, \end{aligned} \tag{5.42}$$

where the second boundary condition is non-homogeneous. If we let $w(X,t) = u(X,t) - N_o X/EA$, the equation of motion and the boundary conditions become homogeneous, and they are given by

$$EAw'' = \rho A\ddot{w}, \tag{5.43}$$

and

$$\begin{aligned} u(0,t) &= 0 \\ EAu'(L,t) + M_p\ddot{u}(L,t) &= 0. \end{aligned} \tag{5.44}$$

[2]The axial force N is constant when $p(X,t) = 0$ and a point axial force is applied at $X = L$.

Separating $w(X,t)$ into $U(X)\,T_u(t)$, we obtain two ordinary differential equations

$$\begin{aligned} U'' + \frac{\rho}{E}\omega^2 U &= 0 \\ \ddot{T}_u + \omega^2 T_u &= 0. \end{aligned} \tag{5.45}$$

The general or homogeneous solution of the spatial equation is given by

$$U = C_1 \sin \beta X + C_2 \cos \beta X, \tag{5.46}$$

where β is given by

$$\beta = \sqrt{\frac{\rho}{E}}\omega.$$

The spatial variable $U(X)$ satisfies the boundary conditions given by

$$\begin{aligned} U(0) &= 0 \\ EAU'(L) - M_p\omega^2 U(L) &= 0. \end{aligned} \tag{5.47}$$

There are an infinite number of spatial solutions $U(X)$ because of the nature of the boundary value problem. Solving the ordinary differential equation for $U(X)$ and applying the boundary conditions, we obtain

$$U_n(X) = c_n \sin \beta_n x \text{ for } n = 1, 2, \cdots, \tag{5.48}$$

where β_n are solutions to transcendental equation given by

$$\tan \beta L = \frac{\rho A}{M_p}\frac{1}{\beta}, \tag{5.49}$$

and the natural frequencies are given by

$$\omega_n = \beta_n \sqrt{\frac{E}{\rho}} \text{ for } n = 1, 2, \cdots. \tag{5.50}$$

2.6.2 Transverse Motion

The equation of motion for the transverse motion is given by Equation 5.2 or

$$EIv'''' = -\rho A\ddot{v}, \tag{5.51}$$

and the boundary conditions are given by

$$\begin{aligned} v(0,t) &= 0 \\ kv'(0,t) - EIv''(0,t) &= 0 \\ EIv'''(L,t) - M_p\ddot{v}(L) &= 0 \\ EIv''(L) &= 0. \end{aligned} \tag{5.52}$$

Separating $v(X,t)$ into $V(X)\,T_v(t)$, we obtain two ordinary differential equations given by

$$\begin{aligned} V'''' + \frac{\rho A}{EI}\omega^2 V &= 0 \\ \ddot{T}_v + \omega^2 T_v &= 0. \end{aligned} \tag{5.53}$$

The spatial solution $V(X)$ satisfies the boundary conditions given by

$$\begin{aligned} V(0) &= 0 \\ kV'(0) - EIV''(0) &= 0 \\ V'''(L) + M_p\omega^2 V(L) &= 0 \\ V''(L) &= 0. \end{aligned} \tag{5.54}$$

The general solution for $V(X)$ is given by

$$V(X) = c_1 \sin\beta X + c_2 \cos\beta X + c_3 \sinh\beta X + c_4 \cosh\beta X, \tag{5.55}$$

where

$$\beta^4 = \frac{\rho A}{EI}\omega^2. \tag{5.56}$$

Applying boundary conditions, we have four simultaneous equations given by

$$[A]\begin{bmatrix} c_1 \\ c_2 \\ c_3 \\ c_4 \end{bmatrix} = \begin{bmatrix} 0 \\ 0 \\ 0 \\ 0 \end{bmatrix}, \tag{5.57}$$

where $[A]$ is given by

$$[A] = \begin{bmatrix} 0 & 1 & 0 & 1 \\ k & EI\beta & K & -EI\beta \\ A_{31} & A_{32} & A_{33} & A_{34} \\ -\sin\beta L & -\cos\beta L & \sinh\beta L & \cosh\beta L \end{bmatrix}, \tag{5.58}$$

where

$$\begin{aligned} A_{31} &= -\cos\beta L + \frac{M_p EI}{\rho A}\beta \sin\beta L \\ A_{32} &= \sin\beta L + \frac{M_p EI}{\rho A}\beta \cos\beta L \\ A_{33} &= \cosh\beta L + \frac{M_p EI}{\rho A}\beta \sinh\beta L \\ A_{34} &= \sinh\beta L + \frac{M_p EI}{\rho A}\beta \cosh\beta L. \end{aligned} \tag{5.59}$$

Table 5.1. Beam Properties

Material	Aluminium
Young's Modulus, E	73 GPa
Density, ρ	2770 kg/m^3
Point Mass, M_p	0.236 kg
Torsional Spring Constant, k	38.8 N/m
Length, L	1.27 m
Outer Radius, r_o	0.0127 m
Inner Radius r_i	0.011 m

Table 5.2. Fluid Properties

Density of Water, ρ_f	999 kg/m^3
Water Depth, d	1.05 m
Added Mass Coefficient, C_A	1
Modified Drag Coefficient, C_D	1
Reynold's Number, Re	2718.7

In order to have a non-trivial solution, the determinant of the matrix in Equation 5.58 has to be zero. The characteristic equation is given by

$$0 = k\rho A + k\rho A\cos(\beta L)\cosh(\beta L) - (Mpk\beta + EI\rho A\beta)\sin(\beta L)\cosh(\beta L) - 2EIM_p\beta^2\sin(\beta L)\sinh(\beta L) + (\rho AEI\beta + Mpk\beta)\cos(\beta L)\sinh(\beta L). \tag{5.60}$$

There are infinitely many β that satisfy the characteristic equation. The angular frequencies ω_n are obtained using Equation 5.56.Therefore, the characteristic equation is also called the frequency equation.

3. Free and Damped-Free Response using the Two-Dimensional Coupled Model

In Section 2, we have formulated the equations of motion of a nonlinear coupled transverse and axial model. The responses are obtained numerically for a beam with properties given in Table 5.1. When the damped-free response is considered, the fluid properties in Table 5.2 are used.

First, we consider a uniform beam vibrating freely in vacua in a gravity-free environment. This will provide us with the nonlinear structural characteristics such as frequencies and shapes of free response.

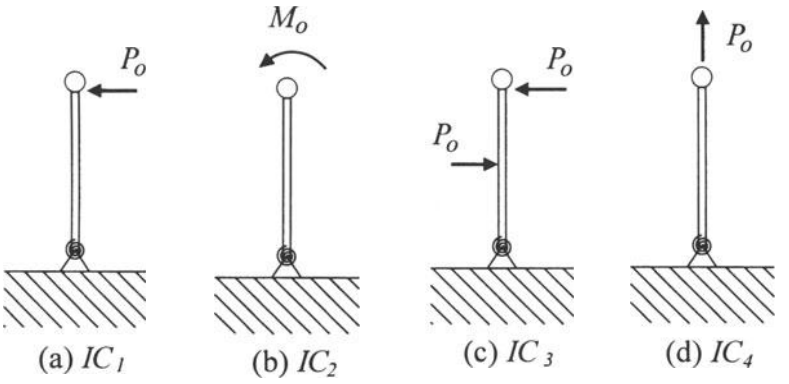

Figure 5.3. Four Sets of Initial Displacements.

Second, we consider a beam vibrating in still water under gravity and buoyancy. The Morison equation with damping and added mass terms is used to simulate this condition. This will provide us with the damped characteristics such as the frequencies and shapes of oscillation of the damped response. In both cases, free and damped-free, the beam will oscillate due to non-zero initial conditions: initial displacement and/or initial velocity.

Nonlinearities can influence the response in many ways. For example, the frequencies of vibration may vary with the initial conditions and vibration amplitude whereas frequencies are constant quantities in linear systems. Let us consider four initial conditions in order to demonstrate the sensitivity to these. Here, we assume that the initial velocity is zero and the displacement fields correspond to the physical configurations shown in Figure 5.3.

The four sets of initial displacements are listed in Table 5.3[3]. The parameters (point loads and applied moment) are chosen such that the static transverse end deflection is 0.05 m, which is approximately 4% of the beam length. The corresponding axial end deflections are about 0.001 m for IC_1 and IC_3 and 0.002 m for IC_2. These end deflections may be seen in the experiments and are small enough so that the small angle assumption is valid.

The corresponding initial transverse displacements that can be used for the linear transverse model are given in Table 5.5.

The finite difference approach is employed to obtain the responses. The finite difference equations are written for the spatial derivatives

[3]See Appendix B for detailed derivations.

Table 5.3. Four Sets of Initial Displacements

$$
\begin{aligned}
IC_1: \quad & u(X,0) = -\tfrac{1}{2}\left(\tfrac{P_o}{EI}\right)^2\left(\tfrac{X^5}{20} - \tfrac{LX^4}{4} + \left(L^2 - \tfrac{EIL}{k}\right)\tfrac{X^3}{3} + \tfrac{EIL^2X^2}{k} + \left(\tfrac{EIL}{k}\right)^2 X\right) \\
& v(X,0) = -\tfrac{P_o}{EI}\left(\tfrac{X^3}{6} - \tfrac{LX^2}{2} - \tfrac{EILX}{k}\right) \\
IC_2: \quad & u(X,0) = -\tfrac{1}{2}\left(\tfrac{M_o}{EI}\tfrac{X^3}{3} + \tfrac{M_o^2}{EIk}X^2 + \tfrac{M_o^2}{k^2}X\right) \\
& v(X,0) = M_o\left(\tfrac{X^2}{2EI} + \tfrac{X}{k}\right) \\
IC_3: \quad & u(X,0) = P_o^2L^2\left[\tfrac{X^3}{48(EI)^2} + \tfrac{X^2}{16EIk} + \tfrac{X}{16k^2}\right] \text{ for } 0 < X \le \tfrac{L}{2} \\
& u(X,0) = \left(\tfrac{P_o}{2EI}\right)^2\left[\tfrac{X^5}{20} - \tfrac{LX^4}{4} + \left(\tfrac{3L^2}{8} - \tfrac{LEI}{6k}\right)X^3\right. \\
& \quad \left. - \left(\tfrac{L^2}{8} - \tfrac{LEI}{2k}\right)LX^2 + \left(\tfrac{L^2}{8} - \tfrac{LEI}{2k}\right)^2 X\right] \text{ for } \tfrac{L}{2} < X < L \\
& v(X,0) = \tfrac{P_oL}{2}\left(\tfrac{X^2}{2EI} + \tfrac{X}{k}\right) \text{ for } 0 < X < \tfrac{L}{2} \\
& v(X,0) = -\tfrac{P_o}{EI}\left(\tfrac{X^3}{6} - \tfrac{LX^2}{2} + \left(\tfrac{LEI}{2k} - \tfrac{L^2}{8}\right)X - \tfrac{L^3}{48}\right) \text{ for } \tfrac{L}{2} < X < L \\
IC_4: \quad & u(X,0) = \tfrac{P_o}{EA_o}X \\
& v(X,0) = 0
\end{aligned}
$$

Table 5.4. Natural Frequencies Obtained Using Linear Models

Linear Longitudinal model	Linear Transverse model
$f_{u1} = 677.65$ Hz	$f_{v1} = 1.2337$ Hz
$f_{u2} = 2313.7$ Hz	$f_{v2} = 47.549$ Hz
$f_{u3} = 4190.6$ Hz	$f_{v3} = 172.728$ Hz

Table 5.5. Four Sets of Initial Displacements for Linear Model

$$
\begin{aligned}
IC_1 \quad & v(X,0) = -\tfrac{P_o}{EI}\left(\tfrac{X^3}{6} - \tfrac{LX^2}{2} - \tfrac{EILX}{k}\right) \\
IC_2 \quad & v(X,0) = -M_o\left(\tfrac{X^2}{2EI} + \tfrac{X}{k}\right) \\
IC_3 \quad & v(X,0) = \tfrac{P_oL}{2}\left(\tfrac{X^2}{2EI} + \tfrac{X}{k}\right) \text{ for } 0 < X < \tfrac{L}{2} \\
& v(X,0) = -\tfrac{P_o}{EI}\left(\tfrac{X^3}{6} - \tfrac{LX^2}{2} + \tfrac{L}{8k}(Lk - 4EI)X + \tfrac{L^3}{48}\right) \text{ for } \tfrac{L}{2} < X < L
\end{aligned}
$$

for N nodes leading to the equations of motion in terms of $4N$ second order ordinary differential equations in time. These ordinary differential equations are solved using the 4th or 5th order Runge-Kutta method in

MATLAB[4]. Between 8 and 30 nodes are used initially to determine the fewest number of nodes that can be used to ensure convergence. Here, 14 nodes are used. It was found that the response obtained using 14 nodes and 30 nodes do not deviate significantly from each other.

The natural frequencies predicted by the linear models of Equations 5.1 and 5.2, with appropriate boundary conditions, are given in Table 5.4. This data will be useful for comparisons and discussions when we obtain the frequencies of vibration for the nonlinear system. The physical configuration that is used for the linear longitudinal model is a beam that is fixed at one end and has a point mass at the other end. The physical configuration for the linear transverse model is a beam that is supported by a torsional spring at one end and has a point mass at the other end.

3.1 Free Response - Displacements, Phase Plots, and Spectral Density Plots

This is the case where the external loads, $p(X,t)$, N_o, and $f(X,t)$, equal zero in Equations 5.25 and 5.26. Then the equations of motion become

$$\rho A\ddot{u} - EA\left(u' + \frac{1}{2}v'^{\,2}\right)' = 0 \tag{5.61}$$

$$\rho A\ddot{v} - EA\left(\left(u' + \frac{1}{2}v'^{\,2}\right)v'\right)' - \rho I\ddot{v}'' + EIv'''' = 0. \tag{5.62}$$

Figures 5.4 to 5.7 show the responses of the beam when subjected to initial conditions IC_1 to IC_4 in Table 5.3. There are four plots in each figure. They are the tip displacements versus time and phase plots for the tip. The plots in the left column are for the axial vibration and those in the right column are for the transverse vibration.

Let us look at the responses when the first three sets of initial conditions are used. From the displacement plots, we notice that the motions in both transverse and axial direction look sinusoidal. Only the axial displacement in Figure 5.5(a) seems to have high frequency components. However, the phase plots for all three cases show the high frequency components, which indicates that all responses have high frequency components and only the amplitude of the high frequency component varies from case to case. The low frequency or the fundamental frequency com-

[4]See Appendix C for a detailed description of the finite difference method used to solve the coupled beam model.

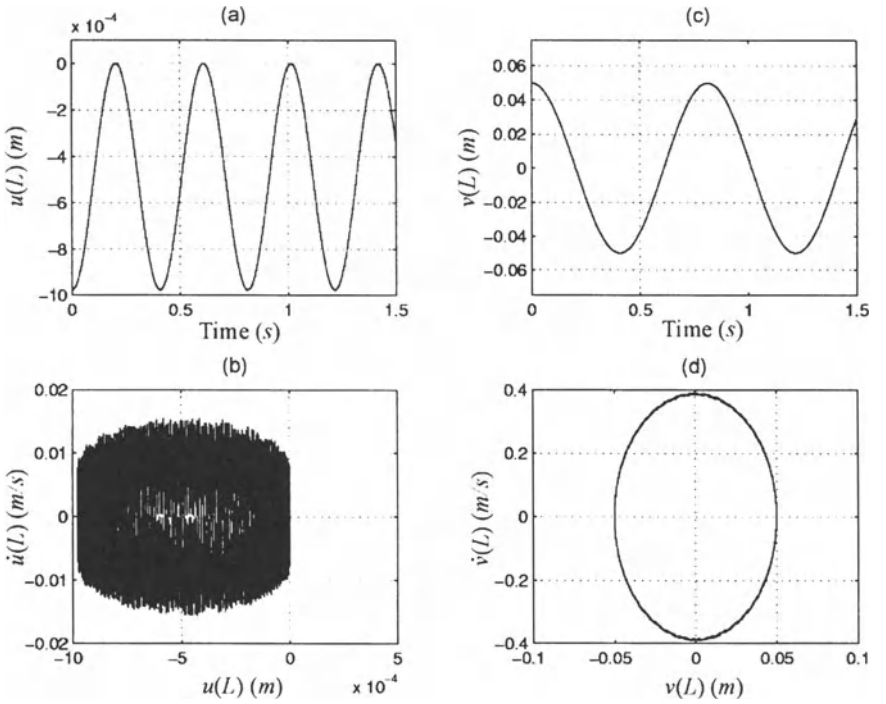

Figure 5.4. Free Response Plots using IC_1. (a) Axial Tip Displacement vs. Time, (b) Phase Plot for the Tip Axial Motion, (c) Transverse Tip Displacement vs. Time, (d) Phase Plot for the Tip Transverse Motion

ponent describes the dominant motion or an envelope which can be seen easily in the displacement plots.

Now, let us look at the transverse displacement plots in Figures 5.4(c) to 5.6(c). They are shown superimposed in Figure 5.8. We find from the figures that the period for the transverse response is about 0.81 s (1.23 Hz) when IC_1 and IC_3 are used. This frequency is close to the one predicted by the linear model. The period for the transverse responses are about 0.74 s (1.35Hz) when IC_2 is used. These fundamental frequencies of the transverse motion varied with initial conditions, which is a characteristic of a nonlinear system.

The transverse tip displacements shown in Figures 5.4(c) to 5.6(c) are plotted again in Figure 5.9 against the transverse tip displacements obtained using the linear model. The responses look similar except for when IC_2 is used.

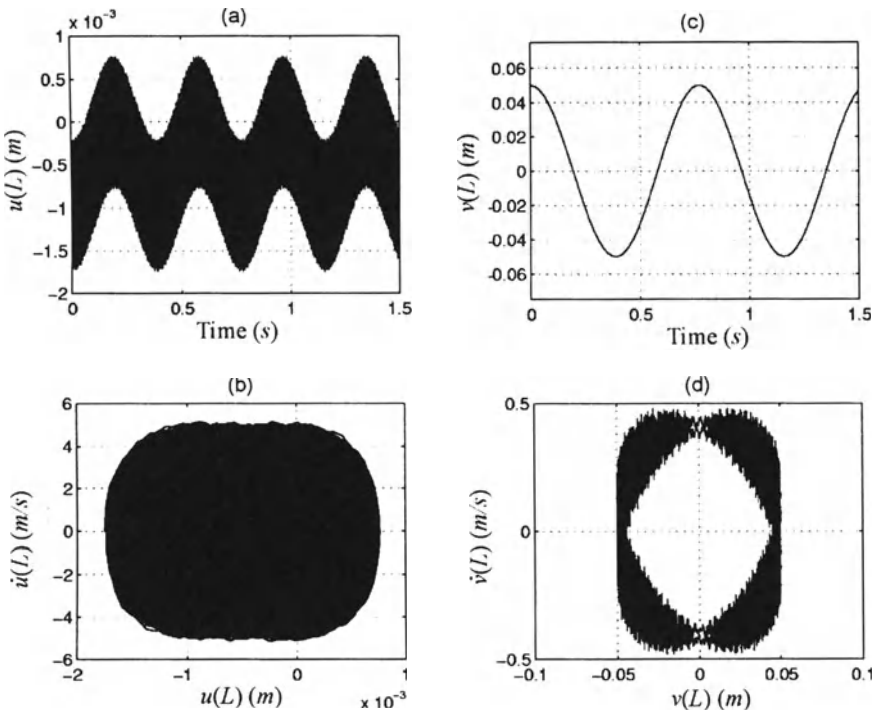

Figure 5.5. Free Response Plots using IC_2. (a) Axial Tip Displacement vs. Time, (b) Phase Plot for the Tip Axial Motion, (c) Transverse Tip Displacement vs. Time, (d) Phase Plot for the Tip Transverse Motion

Figure 5.10 shows the spectral density plots of axial and transverse motion when IC_2 is used[5,6]. The frequencies at which the peaks occur

[5]The resolution of the power spectral density plot is

$$\text{sampling frequency} \div \text{number of total data points},$$

and the reading error is half the resolution.

[6]Note that the power spectral densities are plotted in logarithmic scales. The decibel is defined by

$$dB = 20 \log_{10} \frac{W(f)}{\text{unit of } W(f)}, \tag{5.63}$$

where $W(f)$ is the discrete one-sided power spectrum. If $W(f)$ is the discrete one-sided power spectrum of u, then the units of $W(f)$ are the units of u squared.

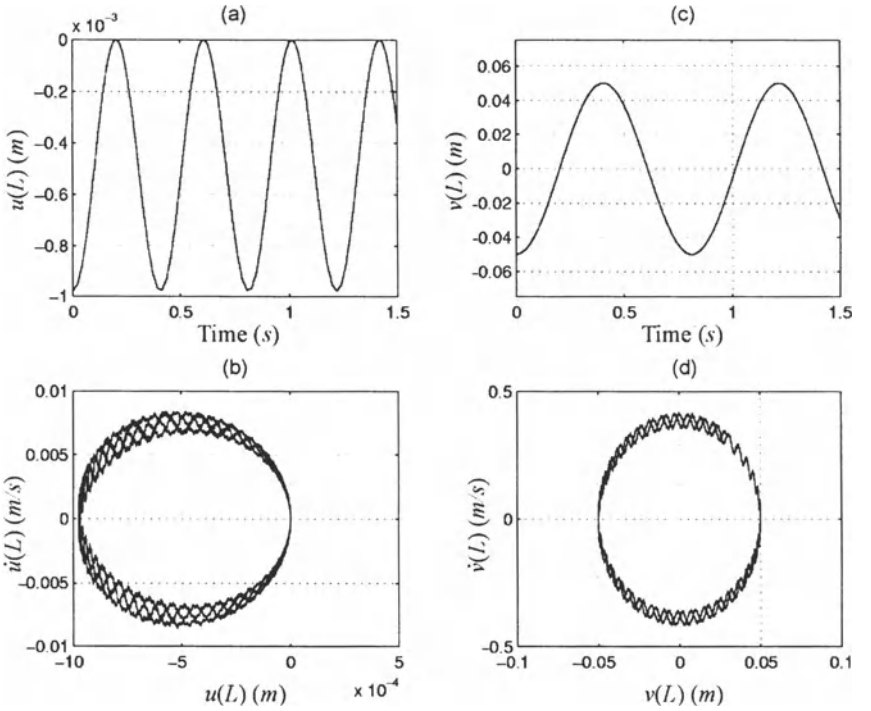

Figure 5.6. Free Response Plots using IC_3, (a) Axial Tip Displacement vs. Time. (b) Phase Plot for the Tip Axial Motion, (c) Transverse Tip Displacement vs. Time, (d) Phase Plot for the Tip Transverse Motion

are

$$f_u = 2.6,\ 47.3,\ 678,\ 2307, \cdots\ [Hz]$$
$$f_v = 1.3,\ 47.3,\ 170,\ 317,\ 361,\ 508,\ 622,\ 630,\ 678,\ 725,$$
$$848,\ 931,\ 1273,\ 1631,\ 1988,\ 2138,\ 2307, \cdots\ [Hz]\,.$$

Comparing the frequencies obtained using the linear models in Table 5.4, we find that the frequencies, 678 and 2307 Hz for the axial vibration and 1.3, 47.3, and 170 Hz for the transverse vibration can be found approximately using the linear models. The rest can only be obtained using the nonlinear model.

Note that the fundamental frequencies of the axial motion are twice those of transverse vibration. In order to explain why this is the case, let us look at a typical path taken by the free end of the beam shown in Figure 5.11. When the free end goes through points 1, 2 and 3, the transverse displacement makes half a cycle while the axial displacement makes one complete cycle. This is true even when there is no longitudinal

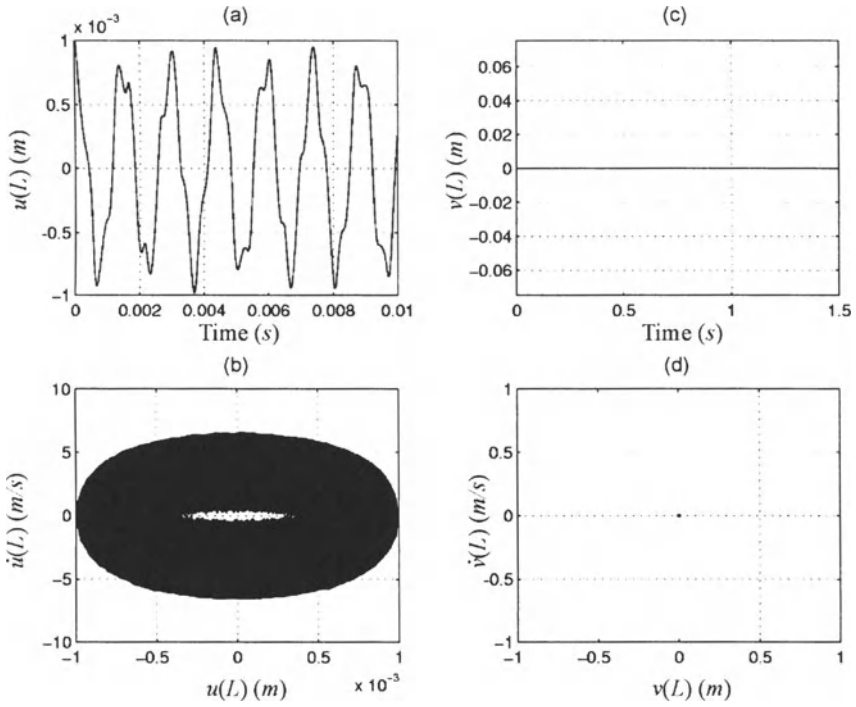

Figure 5.7. Free Response Plots using IC_4. (a) Axial Tip Displacement vs. Time, (b) Phase Plot for the Tip Axial Motion, (c) Transverse Tip Displacement vs. Time, (d) Phase Plot for the Tip Transverse Motion

strain. Therefore, the fundamental frequency in the axial displacement is purely due to the geometry. The tip transverse displacement $v(L,t)$ is plotted in Figure 5.12 against the axial tip displacement $u(L,t)$ when IC_1 is used. The shape describes the actual path taken by the free end. The schematic in Figure 5.11 indeed resembles the actual path.

In order to explain analytically why the fundamental frequency of the axial motion is twice of that of the transverse motion, let us go back to the axial equation of motion in Equation 5.25 with $p(x,t) = 0$, or

$$\rho A_o \ddot{u} - E A_o u'' = E A_o v' v''. \tag{5.64}$$

From the response plots, we know that the transverse motion is approximately sinusoidal with frequency ω_v. Then we can say v is approximately given by

$$v \approx g(X)\, e^{i\omega_v t}. \tag{5.65}$$

Therefore, we can think of Equation 5.64 as being forced by $E A_o g'(X)$ $g''(X)\, e^{i(2\omega_v)t}$ which has a frequency of $2\omega_v$. Therefore, the solution of

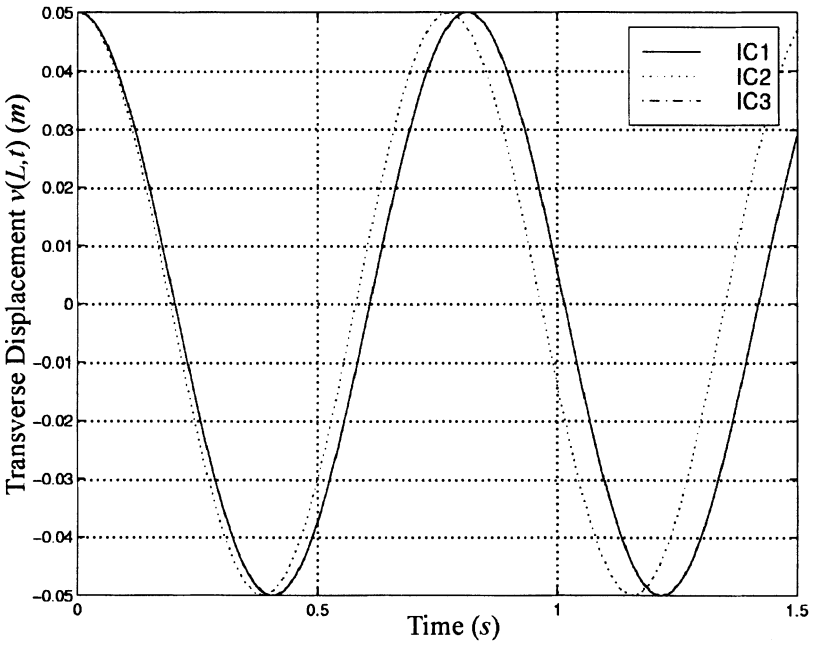

Figure 5.8. Transverse Tip Displacements for the Free Vibrations

Equation 5.64 has frequencies that are natural frequencies of the linear model (solution of $\rho A_o \ddot{u} - EA_o u'' = 0$) and the forcing frequency $2\omega_v$.

Let us look at the response plots in Figure 5.7 when the fourth initial condition is used. Recall that this is the case when there is an axial initial displacement only. The response plots show that the transverse displacement stays zero.

This shows that it is possible to excite the axial motion without affecting the transverse motion. Physically, it is possible to have longitudinal stress without generating moments. On the other hand, the reverse is not true. It is not possible to have moments without generating longitudinal stress. Therefore, it is not possible to excite the transverse motion without affecting the axial motion.

The axial motion in this case can be described by the linear longitudinal model given by

$$\rho A_o \ddot{u} - EA_o u'' = 0. \tag{5.66}$$

Figure 5.13 shows the elongation of the beam as a function of time for all four cases. It should be noted that the physical stretch or elongation of the beam can be obtained using the combination of the axial transverse displacements. The expression for the elongation $d\Delta$ of a beam

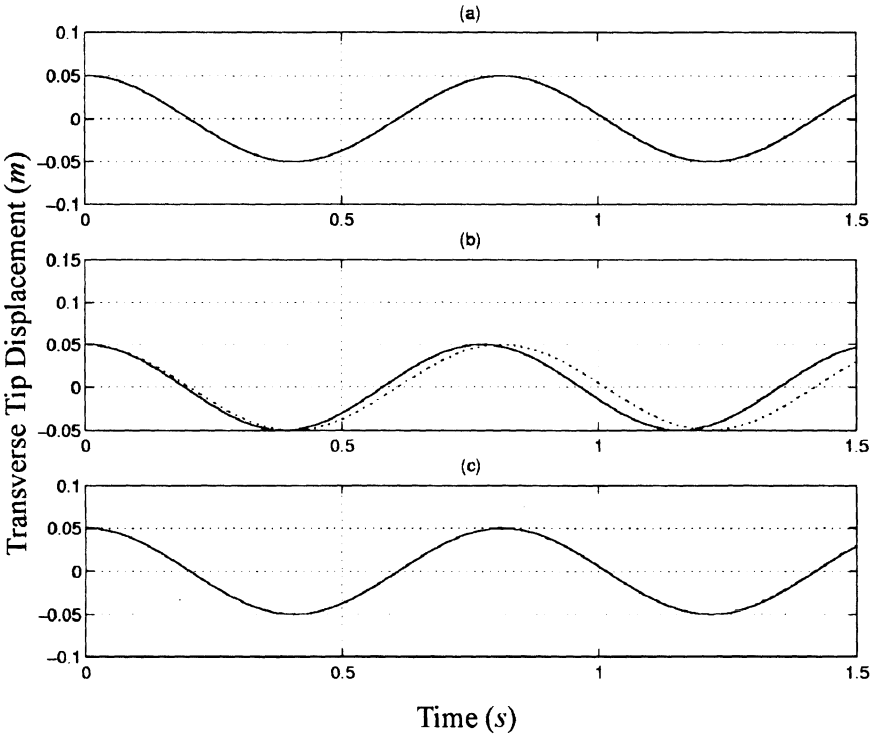

Figure 5.9. Transverse Tip Displacement Obtained using Both Linear and Nonlinear Models. (a) IC_1, (b) IC_2, (c) IC_3. – nonlinear model; ·· linear model

element shown in Figure 5.14 is given by

$$d\Delta = \sqrt{[dX + u(X + dX) - u(X)]^2 + [v(X + dX) - v(X)]^2} - dX. \tag{5.67}$$

Summing these $d\Delta$ gives the total elongation Δ of the beam.

The elongations for all cases are mostly positive. The shapes do not resemble sinusoidal functions. Instead, peaks tend to be sharper when the beam is at the extreme position. Figure 5.15 shows the power spectral density plot of the elongation of the beam for IC_2. Note that it resembles the power spectral density plot of the axial motion in Figure 5.10 (a).

So far, we have only examined the tip responses (displacement and phase plots). It may be interesting to look at the whole beam at different times. Figure 5.16 shows the responses when IC_1 is used for time from zero to 0.4 seconds at 0.05 second intervals. The beam goes through approximately a half cycle. We observe that the overall motion is similar to the first mode shape of the linear beam. Therefore, if we are

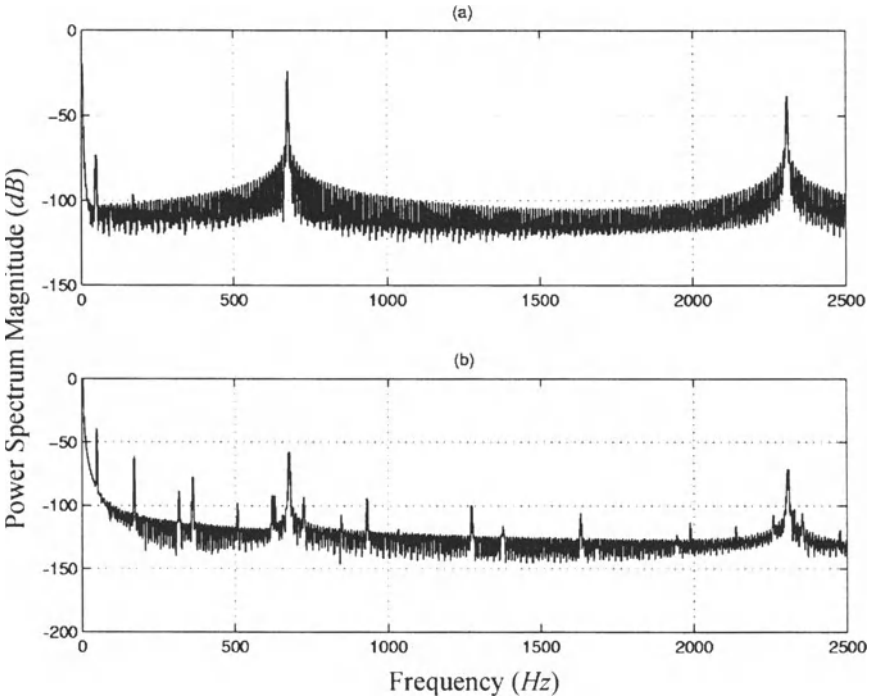

Figure 5.10. Power Spectral Density Plots using IC_2. (a) Axial Motion (b) Transverse Motion

concerned with the overall motion only, discarding the small amplitude high frequency component may be reasonable, and the linear model may be sufficient.

3.2 Free Response - Potential and Kinetic Energies

So far, we have examined the tip displacements, phase plots for the free end, spectral density plots for the free end, and elongation of the beam. Next, we consider how the energy distributes between the various types in order to understand the physical system better.

Figures 5.17 to 5.19 show the potential energies, and Figures 5.20 to 5.22 show the kinetic energies using the first three sets of initial conditions. The potential energies are the bending energy, membrane energy, and the potential energy stored in the torsional spring. Their expressions

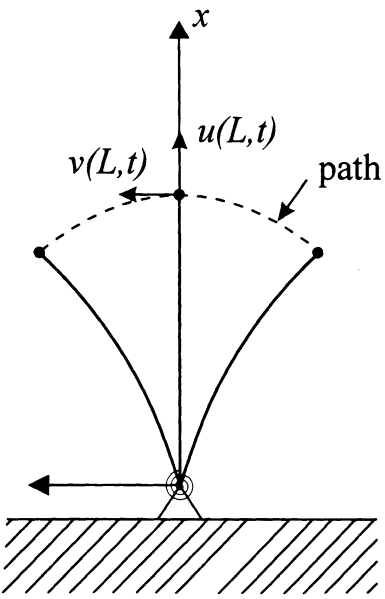

Figure 5.11. A Typical Path Taken by the Free End

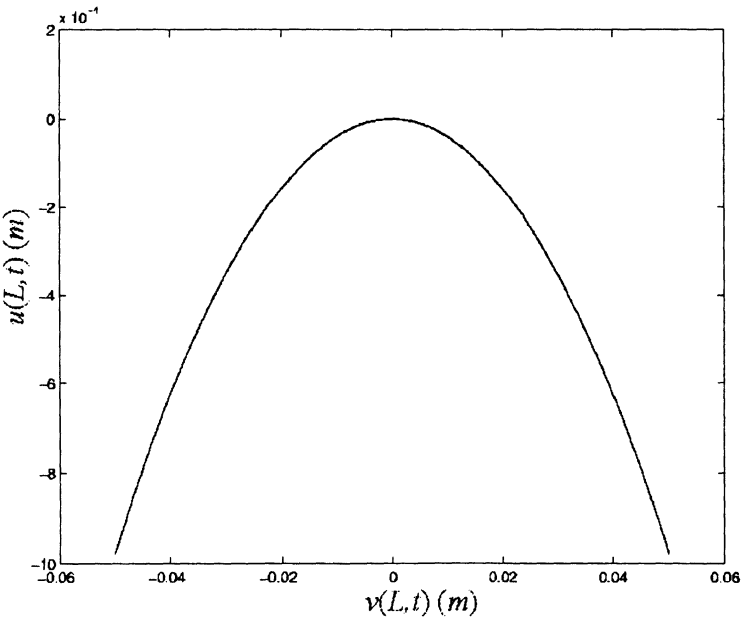

Figure 5.12. $v(L,t)$ vs. $u(L,t)$ using IC_1

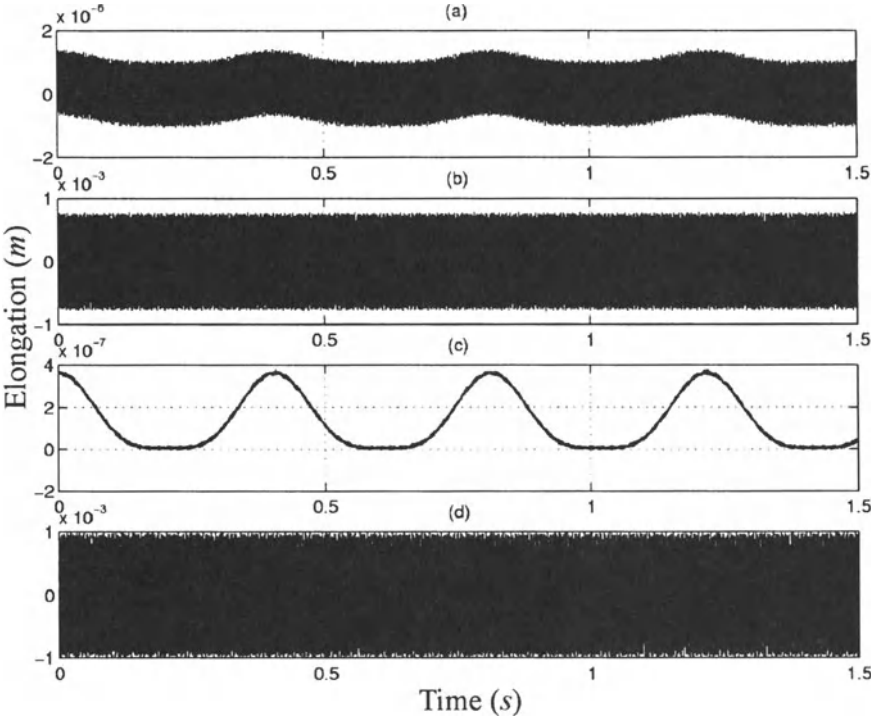

Figure 5.13. Elongation vs. Time for the Free Vibration Using Four Sets of Initial Conditions. (a) IC_1, (b) IC_2, (c) IC_3, (d) IC_4 (The high frequency is at 678 Hz.)

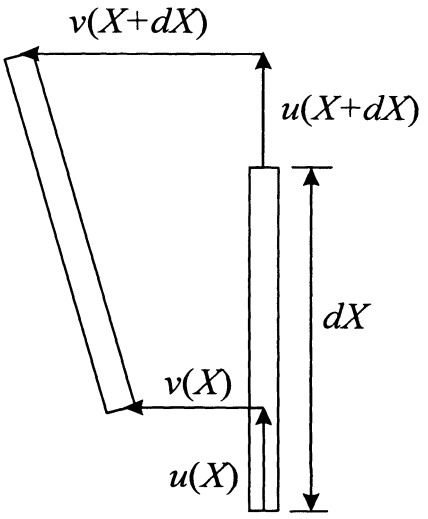

Figure 5.14. A Beam Element

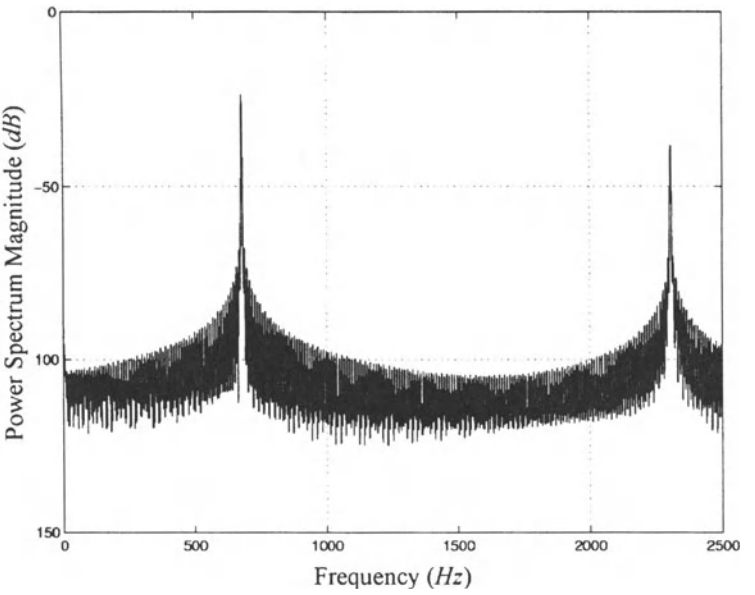

Figure 5.15. Power Spectral Density Plot of Elongation using IC_2

are given by

$$PE_{\text{bending}} = \frac{1}{2}\int_0^L EI_o v''^2 dX$$

$$PE_{\text{membrane}} = \frac{1}{2}\int_0^L EA_o \left(u' + \frac{1}{2}v'^2\right)^2 dX$$

$$PE_{\text{spring}} = \frac{1}{2}kv'(0,t)^2 . \tag{5.68}$$

The kinetic energies are the translational kinetic energy of the beam, rotational kinetic energy of the beam, and the translational kinetic energy of the point mass. Their expressions are given by

$$KE_{\text{translation}} = \frac{1}{2}\int_0^L \rho A_o \left(\dot{u}^2 + \dot{v}^2\right) dX$$

$$KE_{\text{rotation}} = \frac{1}{2}\int_0^L \rho I_o \dot{v}'^2 dX$$

$$KE_{\text{point mass}} = \frac{1}{2}M_p \left(\dot{v}(L,t)^2 + \dot{u}(L,t)^2\right) . \tag{5.69}$$

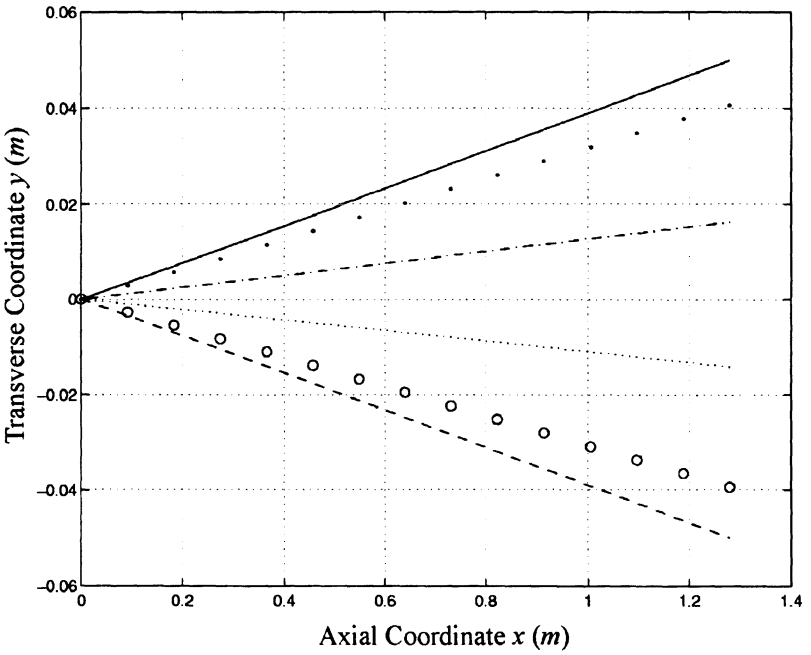

Figure 5.16. Free Response at 0.08 Second Intervals. $-$ $t = 0$; $\cdots$ $t = 0.08$; $-\cdot$ $t = 0.16$; $-$ $t = 0.24$; oo $t = 0.32$; $--$ $t = 0.40$

From the energy plots, we observe that the magnitude of the high frequency component varied from case to case. This was seen in the tip displacement plots in Section 4.1.1.

The amplitudes of the potential energy stored in the torsional spring are almost same for all three cases. Recall that the end deflections for all three cases are set to 0.05 m. The beam is almost rigid in our case such that the initial deflections of the torsional spring, $v'(0,t)$, for all three cases are near $0.05/L$. Therefore, it is reasonable that the energy stored in the spring is almost the same for all three cases. The potential energies are then distributed between the bending and the membrane energies. The bending energy is the dominant term for IC_1 where the high frequency extensional effects are small, and the membrane energy is the dominant term for IC_2 and IC_3 where the high frequency extensional effects are significant.

Notice the similarity between the shapes of the membrane energy and the elongation of the beam shown in Figure 5.13. This can be explained

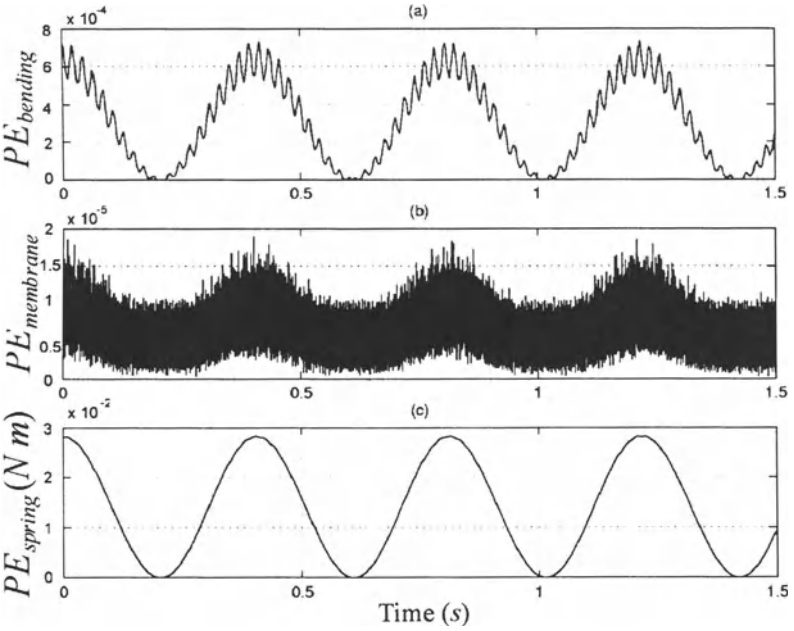

Figure 5.17. Potential Energies of Free Vibration Using IC_1

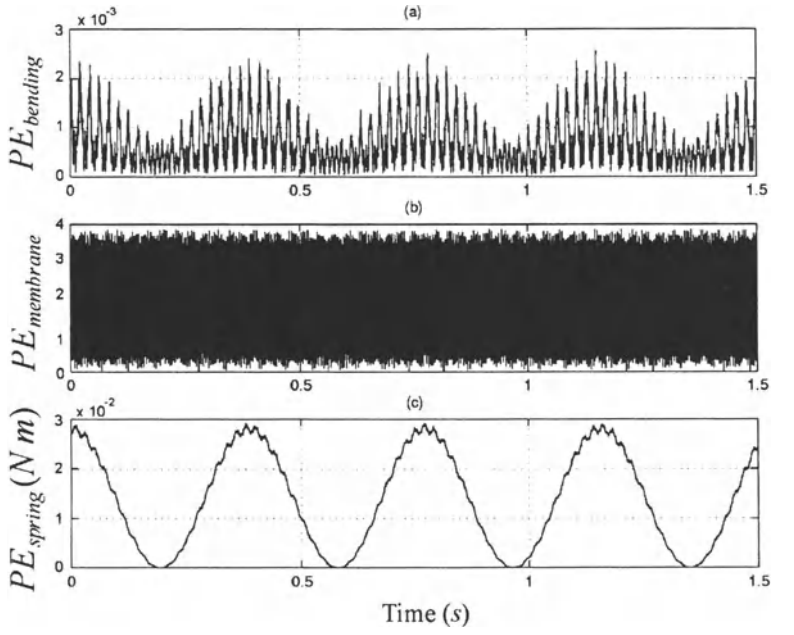

Figure 5.18. Potential Energies of Free Vibration Using IC_2

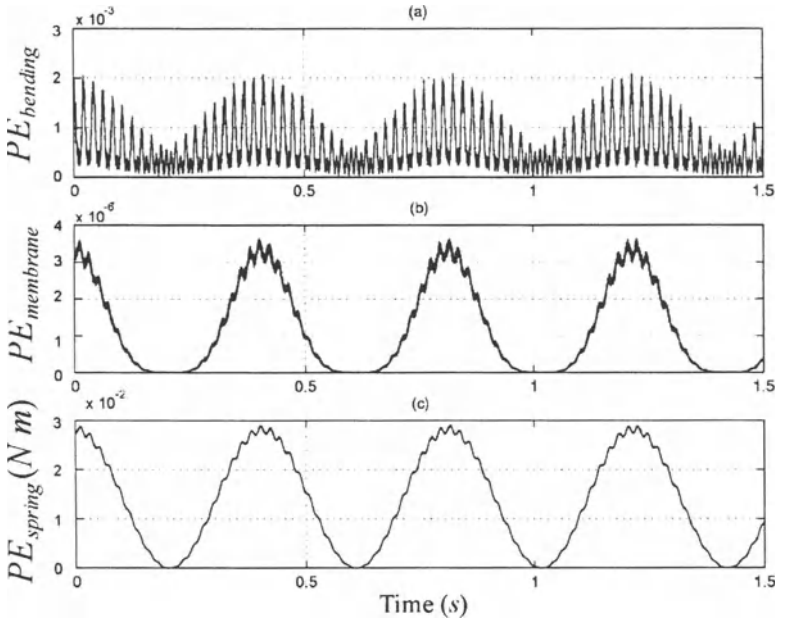

Figure 5.19. Potential Energies of Free Vibration Using IC_3

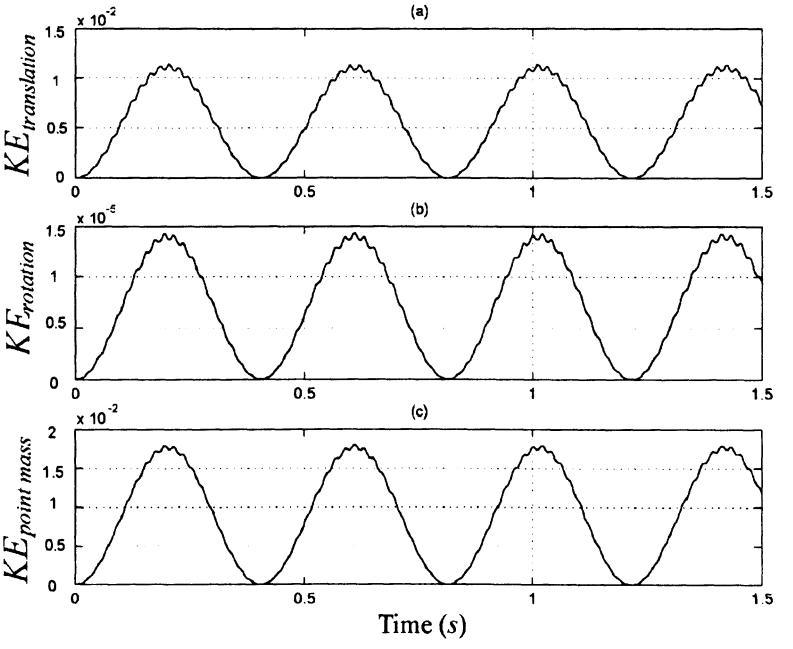

Figure 5.20. Kinetic Energies of Free Vibration Using IC_1

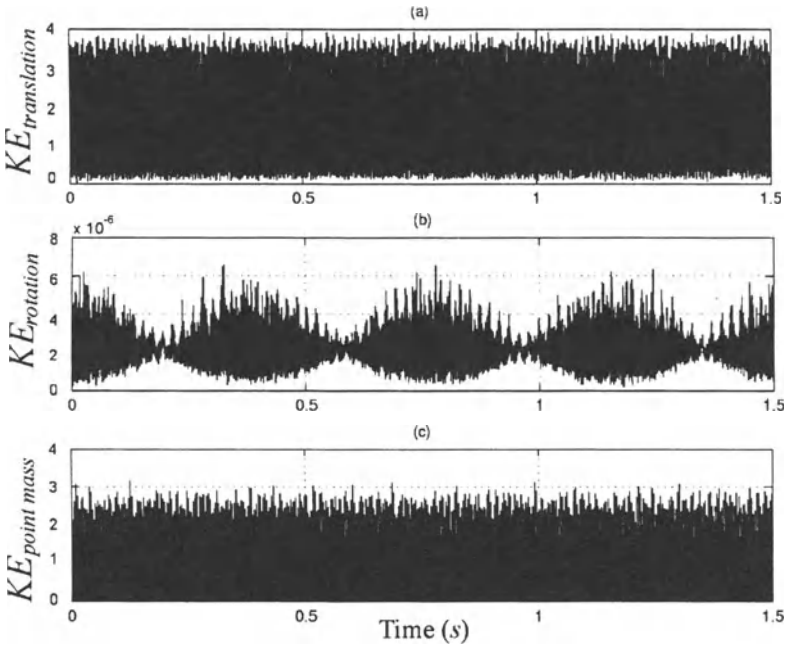

Figure 5.21. Kinetic Energies of Free Vibration Using IC_2

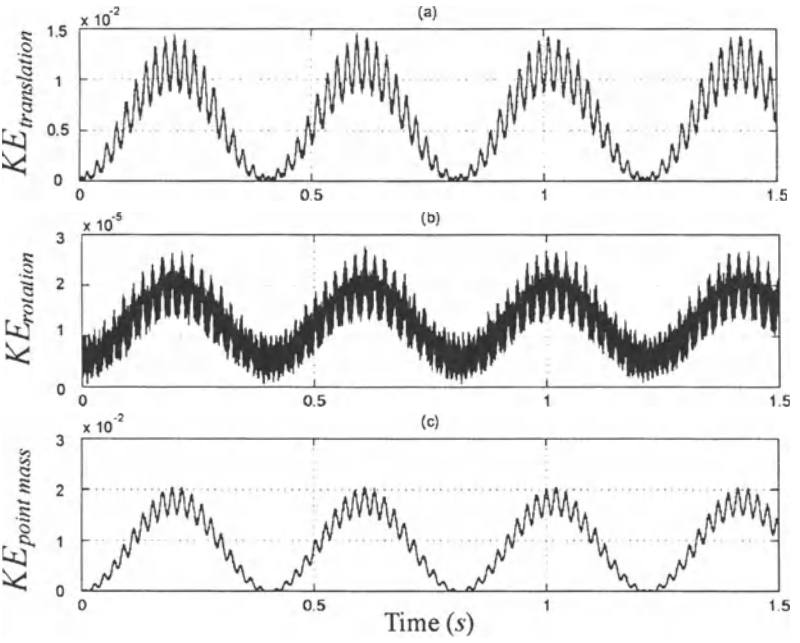

Figure 5.22. Kinetic Energies of Free Vibration Using IC_3

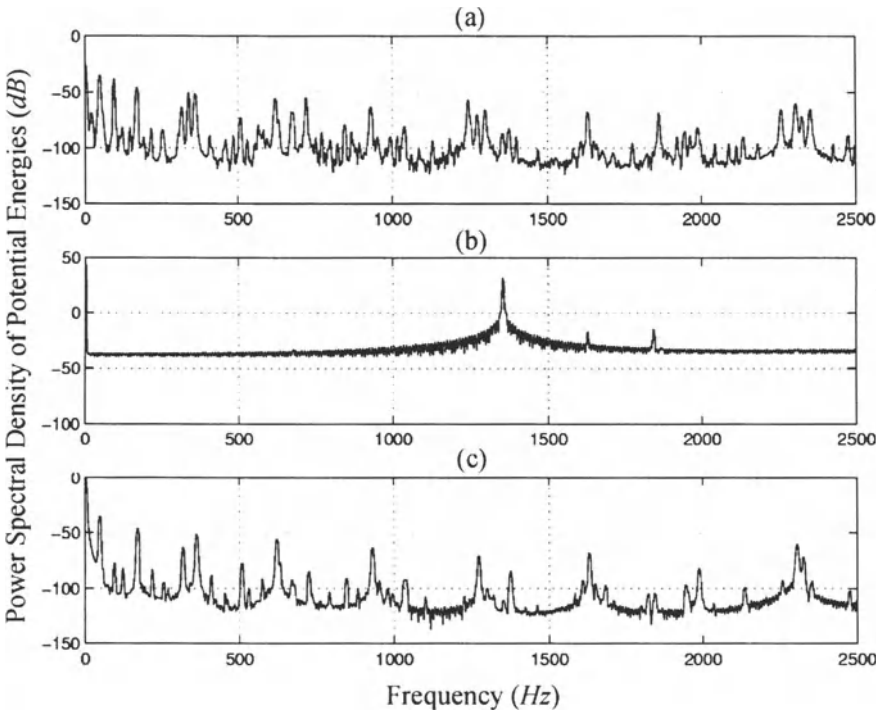

Figure 5.23. Power Spectral Density Plots of Potential Energies Using IC_2. (a) $PE_{bending}$, (b) $PE_{membrane}$, (c) PE_{spring}

by rewriting the incremental elongation in Equation 5.67 as

$$d\Delta = \left[\sqrt{\left(1+\frac{du}{dX}\right)^2+\left(\frac{dv}{dX}\right)^2}-1\right]dX. \tag{5.70}$$

Using the Taylor expansion around $du/dX \approx 0$ and $dv/dX \approx 0$, we can rewrite the incremental elongation as

$$d\Delta = \left[\frac{du}{dX}+\frac{1}{2}\left(\frac{dv}{dX}\right)^2+O\left(\left(\frac{du}{dX}\right)^3+\left(\frac{dv}{dX}\right)^3\right)\right]dX. \tag{5.71}$$

Assuming small strain and moderate rotation given in Equation 5.5, we can write

$$d\Delta \approx \left[\frac{du}{dX}+\frac{1}{2}\left(\frac{dv}{dX}\right)^2\right]dX. \tag{5.72}$$

This expression is seen in the membrane energy expression. Therefore, the membrane energy directly translates into the elongation of the beam.

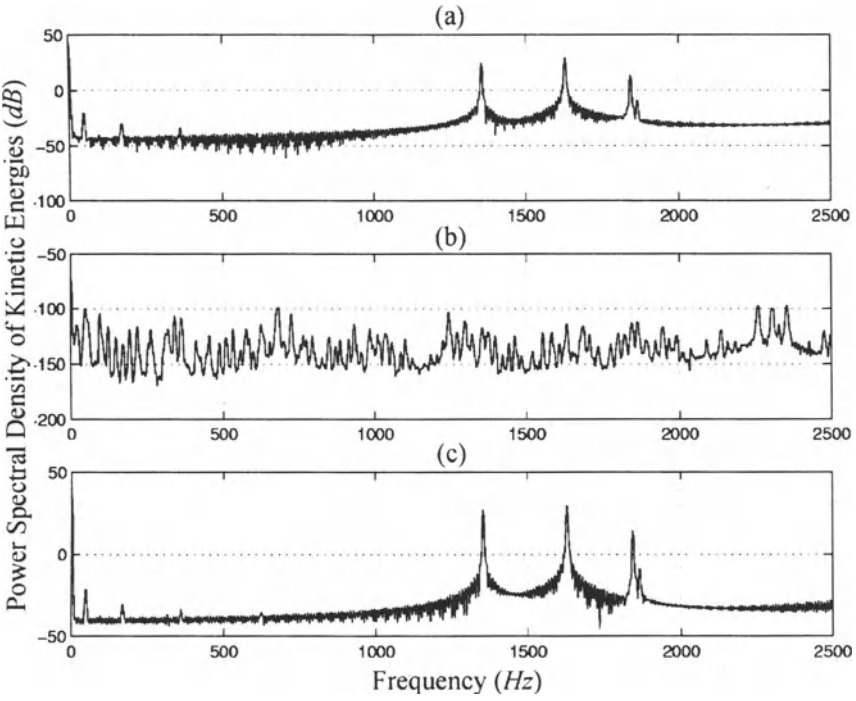

Figure 5.24. Power Spectral Density Plots of Kinetic Energies Using IC_2. (a) $KE_{\text{translation}}$, (b) KE_{rotation}, (c) $KE_{\text{point mass}}$

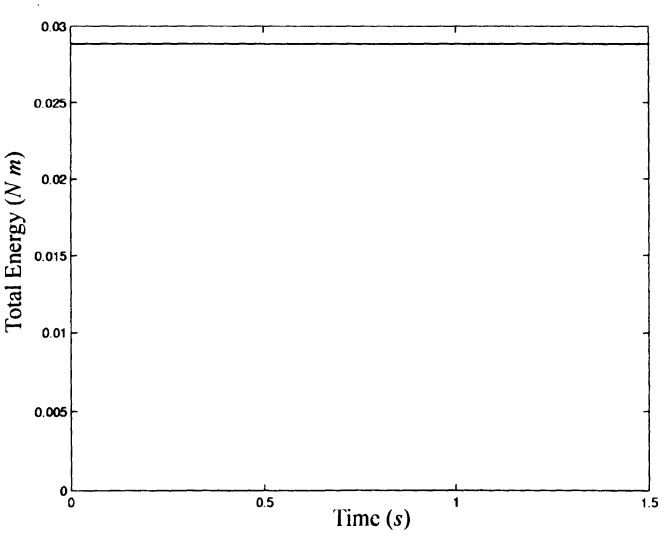

Figure 5.25. Total Energy of the System for IC_1

We also notice that the potential energy and the kinetic energy are 180° out of phase.

Figures 5.23 and 5.24 show the power spectral density plots of the potential and kinetic energy when IC_2 is used. The high frequency shown in $PE_{membrane}$, KE_{trans}, and KE_{mass} is 1356 Hz. This is twice the frequency seen in the axial displacement. This makes sense because those energies are quadratic functions of $u(X,t)$ or derivatives of $u(X,t)$. The power spectral density plots for $PE_{bending}$, PE_{spring}, and $KE_{rotation}$ have many more peaks. This is because those energies are functions of $v(X,t)$ or derivatives of $v(X,t)$, which has many more peaks in their power spectral density plots.

Figure 5.25 shows the total energy of the system when IC_1 is used. The total energy is constant because the system is conservative. The total energies for IC_2 and IC_3 (not shown here) show more numerical errors that grow with time.

3.3 Damped-Free Response - Displacements, Phase Plots, and Spectral Density Plots

Let us now examine the response of the beam assuming that it is placed in still water under the influence of gravity and buoyancy. If we assume that the fluid does not exert force tangent to the structure, the axial load is only due to gravity and gravity. Therefore, the distributed axial load, $p(X,t)$, can be immediately written as

$$\begin{aligned} p(X,t) &= \left(\rho_f A_f - \rho A\right) g \text{ for } 0 < X < d \\ &= -\rho g A \text{ for } d < X < L, \end{aligned} \tag{5.73}$$

where ρ_f is the density of the surrounding medium, ρ is the density of the structure, g is the gravitational acceleration, A is the cross-sectional area, and d is the water depth. The distributed axial load can be thought of as the body force multiplied by the cross-sectional area. The transverse force is given in Equation 4.14. Note that there are no wave nor current in this case. Therefore, w_x, w_y, and U_c are all set to zero, and the distributed transverse load is given by

$$f(X,t) = C_D \rho_f r_o \left(\dot{u}v' - \dot{v}\right) \left|\dot{u}v' - \dot{v}\right| - C_A \rho_f \pi r_o^2 \left(-\ddot{u}v' + \ddot{v}\right). \tag{5.74}$$

The tip displacements with time and phase plots for the tip are shown in Figures 5.26 to 5.29 for the same four sets of initial conditions used for the undamped cases. Let us first consider responses obtained using the first three sets of initial conditions.

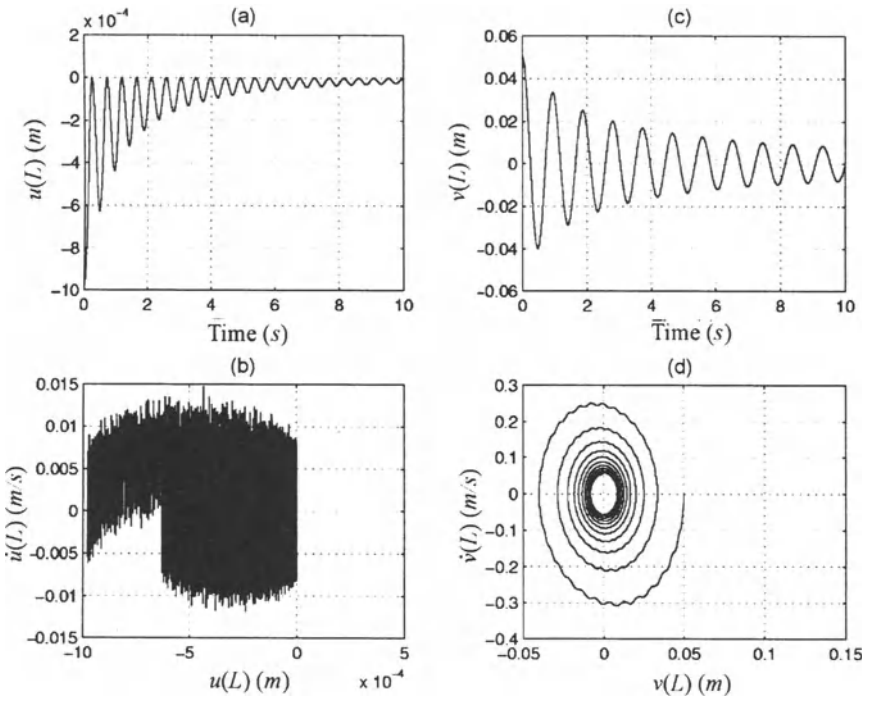

Figure 5.26. Damped Free Response Plots using IC_1. (a) Axial Tip Displacement vs. Time, (b) Phase Plot for the Tip Axial Motion, (c) Transverse Tip Displacement vs. Time, (d) Phase Plot for the Tip Transverse Motion

The frequencies of vibration vary with initial conditions as in the free responses. The tip transverse displacements when IC_1, IC_2 and IC_3 are used are plotted in Figure 5.30 for an easy comparison. The fundamental frequencies for the transverse response are about 1.08 Hz (0.93 s) when IC_1 and IC_3 are used, and 1.12 Hz (0.89 s) when IC_2 is used. When the periods of damped motion are compared with those of the corresponding free cases, damped responses are slower than undamped responses as we expected. It is interesting to note that the IC_2 produces the fastest response for both undamped and damped cases.

The fundamental frequencies of the corresponding tip axial displacements in Figures 5.26(a) to 5.28(a) are twice those of the transverse vibration as we have seen in the free undamped case.

Figure 5.31 shows the spectral density plots when IC_2 is used. The peaks occur at

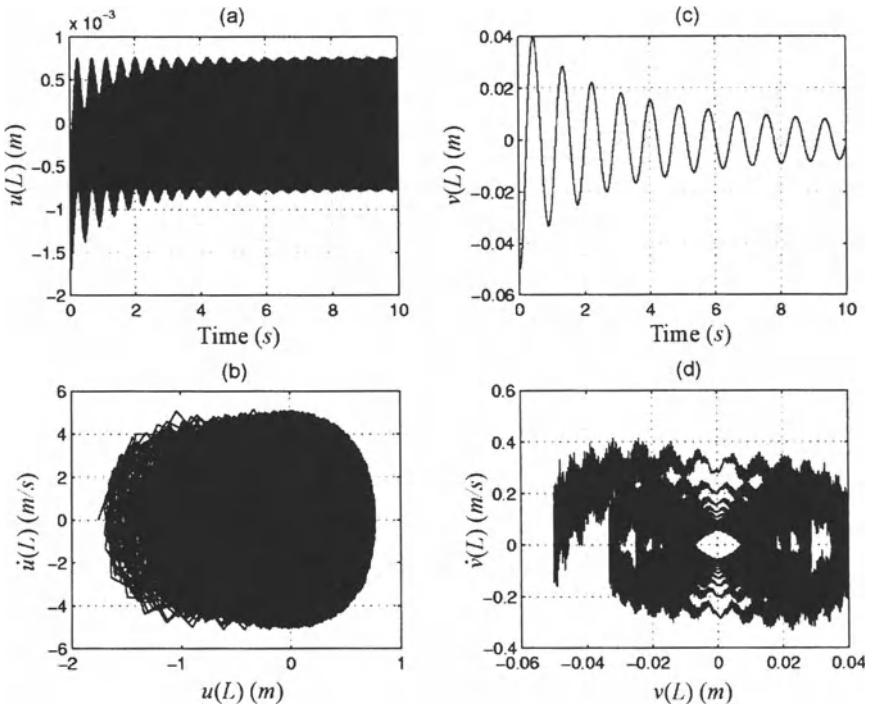

Figure 5.27. Damped Free Response Plots using IC_2. (a) Axial Tip Displacement vs. Time, (b) Phase Plot for the Tip Axial Motion, (c) Transverse Tip Displacement vs. Time, (d) Phase Plot for the Tip Transverse Motion

$$f_u = 2.24,\ 32.5,\ 677,\ 2300,\ \cdots\ [Hz]$$
$$f_v = 1.12,\ 33.6,\ 114,\ 247,\ 429,\ 564,\ 650,\ 677,\ 688,\ 711,\cdots\ [Hz]\,.$$

When compared with the spectral density plots for the free vibration in Figure 5.10, peaks in Figure 5.31 generally are shifted to the left, some more so than others.

The transverse motion in all cases in Figures 5.26(b) to 5.28(b) approaches its asymptote at zero by oscillating around it. However, the axial motion approaches its asymptote oscillating (at twice the fundamental frequency of the transverse motion) without overshooting the asymptote. It is helpful to recall that the axial displacement is the displacement from the reference configuration in the axial direction (x direction), and the axial motion at the fundamental frequency is geometrically induced due to the transverse motion. Therefore, the axial displacement should not overshoot.

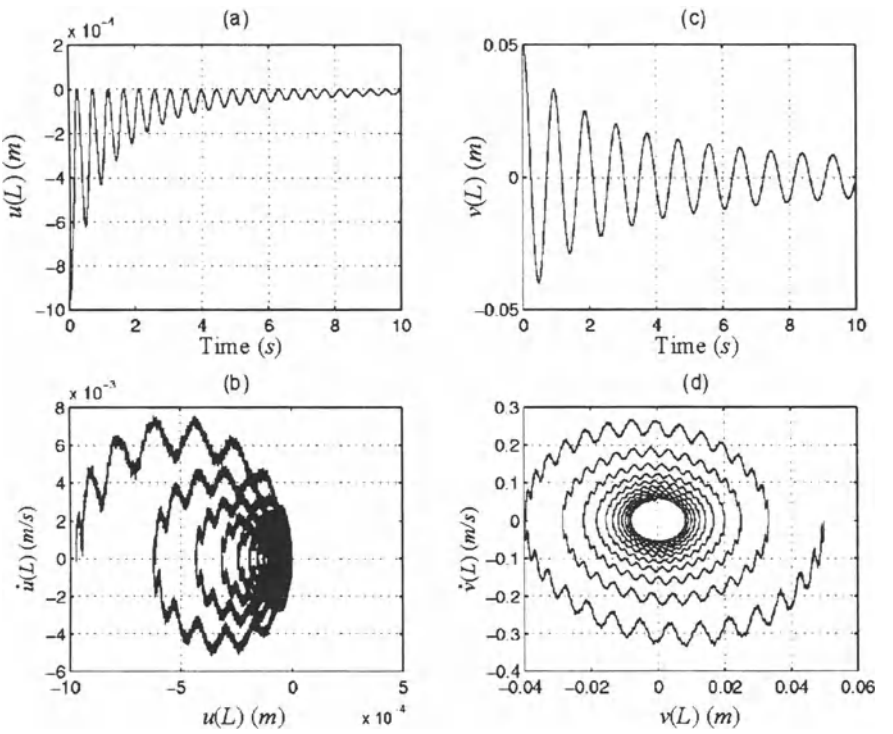

Figure 5.28. Damped Free Response Plots using IC_3. (a) Axial Tip Displacement vs. Time, (b) Phase Plot for the Tip Axial Motion, (c) Transverse Tip Displacement vs. Time, (d) Phase Plot for the Tip Transverse Motion

The axial displacement plots show that the fundamental frequency motions damp out and only the high frequency response remains. After a while, the axial motion seems to be decoupled from the transverse motion. In order to examine why this happens, it is noted that the Morison equation is formulated to act perpendicular to the beam. We assumed that the rotation is small enough so that the Morison force only acts in the transverse direction. Therefore, the Morison fluid force directly affects the transverse motion, and affects the axial motion indirectly through the coupling of the transverse and the axial motions. The magnitude of its influence on the axial motion depends on the magnitude of the transverse motion and the coupling.

The Morison force in our case damps the transverse motion and therefore weakens the coupling between two motions. In the end, the axial motion becomes effectively decoupled from the transverse motion and the Morison fluid forcing. At this point, there is no mechanism for the

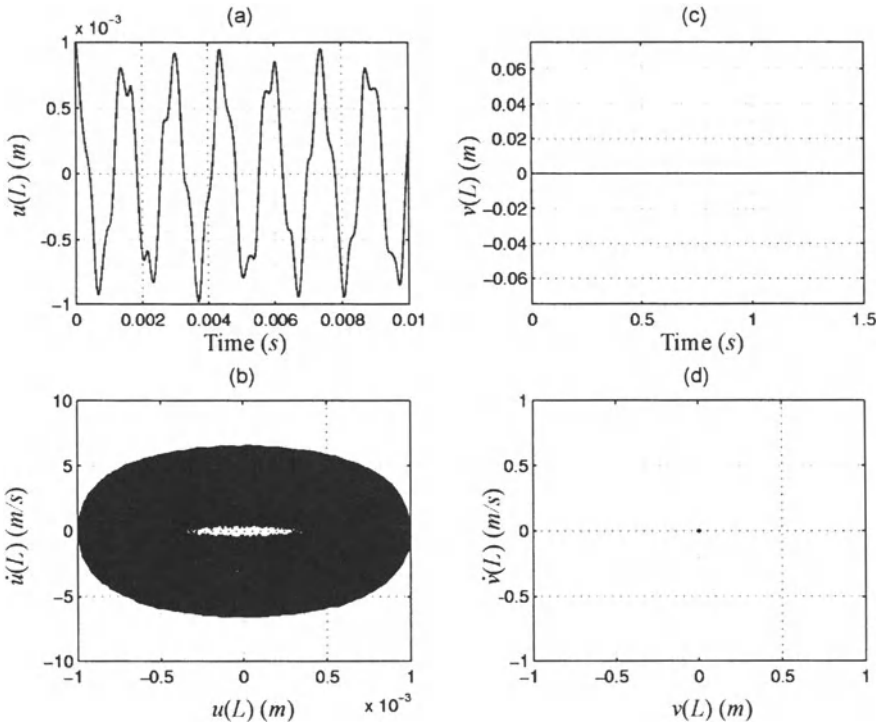

Figure 5.29. Damped Free Response Plots using IC_4. (a) Axial Tip Displacement vs. Time, (b) Phase Plot for the Tip Axial Motion, (c) Transverse Tip Displacement vs. Time, (d) Phase Plot for the Tip Transverse Motion

fluid forces to slow down the axial motion. Since the transverse motion has exponentially decayed, we no longer see the fundamental frequency response in the axial motion. This is, of course, an approximation that can be removed if necessary.

Analytically, the change in total energy between $t = \tau_o$ and τ is given by[7]

$$E(\tau) - E(\tau_o) = \int_0^L \left[\int_{\tau_o}^{\tau} \left\{ C_D \rho_f r_o \left(\dot{u}v' - \dot{v} \right) \left| \dot{u}v' - \dot{v} \right| + C_A \rho_f \pi r_o^2 \left(\ddot{u}v' - \ddot{v} \right) \right\} \dot{v} dt \right] dX. \tag{5.75}$$

[7]See Appendix D for derivation.

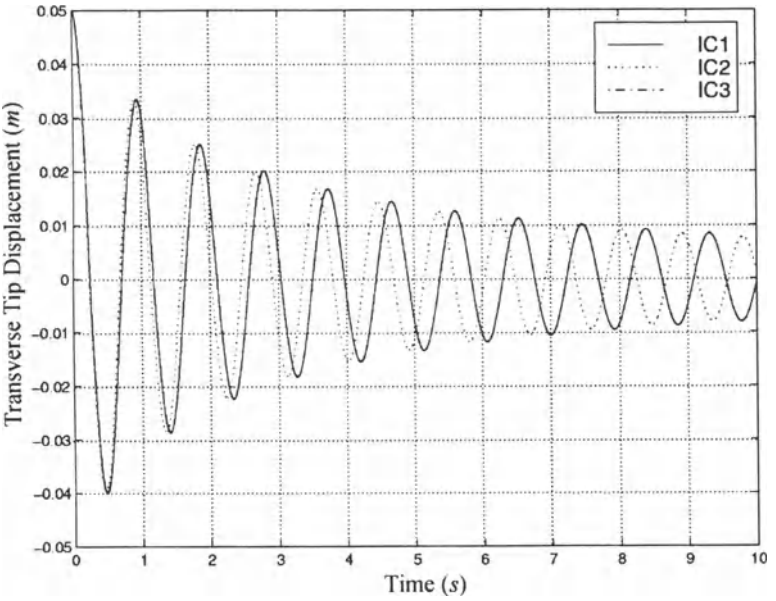

Figure 5.30. Transverse Tip Displacements for the Damped Free Vibrations

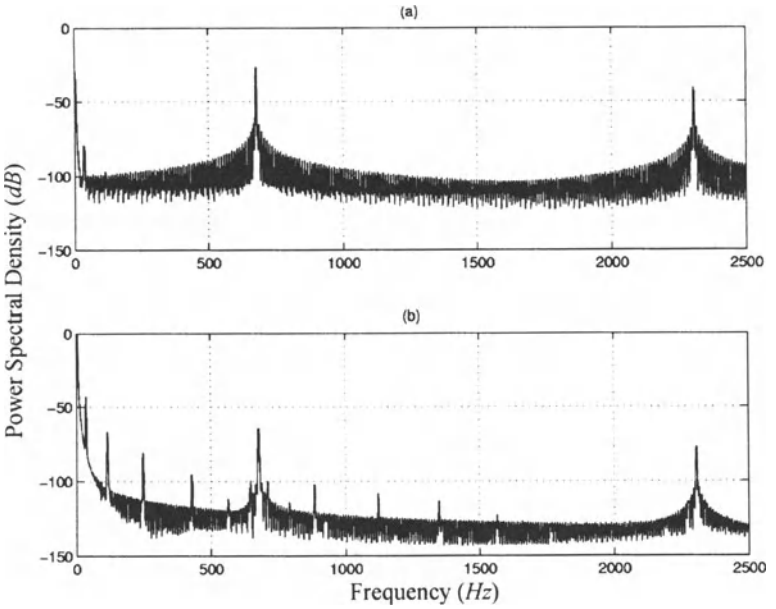

Figure 5.31. Power Spectral Density Plots for the Damped System Using IC_2. (a) Axial Motion, (b) Transverse Motion

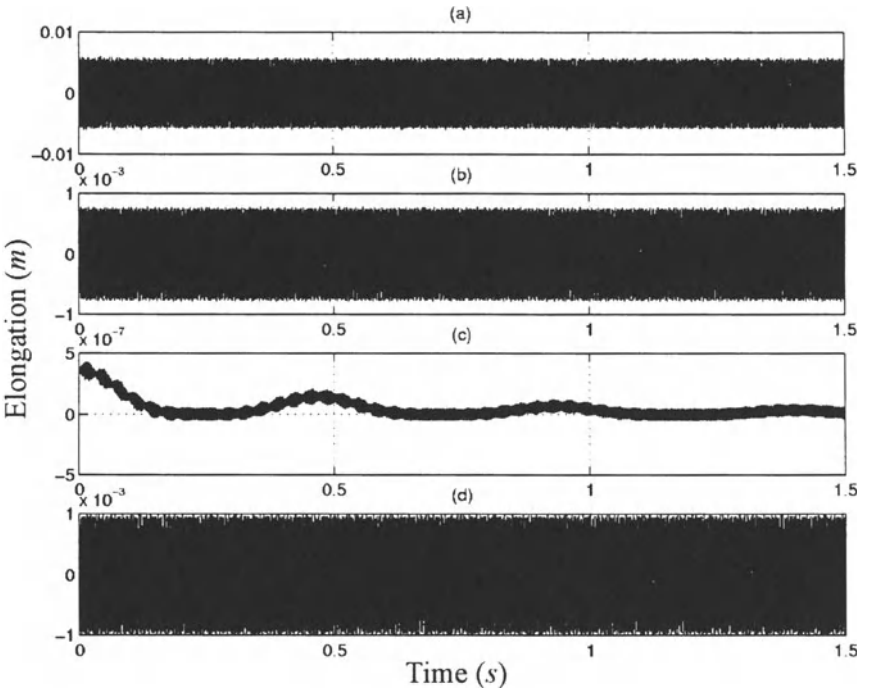

Figure 5.32. Elongation vs. Time for the Damped Free Vibration Using Four Sets of Initial Conditions. (a) IC_1, (b) IC_2, (c) IC_3, (d) IC_4 (The high frequency is at 677 Hz.)

If there is no transverse vibration, $\dot{v}(X,t) = 0$, there is no energy loss. Therefore, it is possible that the undamped axial motion can still exist after the transverse motion has died out.

The phase plots in Figures 5.26(c),(d) to 5.28(c),(d), when the transverse motion exists, show decreasing spirals, which means that the system is dissipative.

Figure 5.29, when there is no transverse motion, shows that the influence of the fluid forcing and the coupling between the transverse and the axial motion no longer exist. The axial motion in this case can be described by the linear longitudinal model given in Equation 5.66.

The physical elongation in Figure 5.32 seems to persist with time. This is the result of having the axial motion that does not damp out. The elongations in all cases barely show the effect of diminishing transverse motion.

For the transverse response produced using IC_1, we obtain the equivalent damping ratio using consecutive peaks. The equivalent damping

Table 5.6. Equivalent Damping Ratios for the Transverse Motion obtained using IC_1

n	t	$v(L,t)$	δ	ζ
1	0	0.05	0.4716	0.0748
2	0.847	0.0312	0.3158	0.0502
3	1.692	0.02275	0.2411	0.0384
4	2.536	0.01787	0.1932	0.0307
5	3.379	0.01473	0.1626	0.0259
6	4.223	0.01252	-	-

ratio is given by

$$\zeta = \frac{\delta}{\sqrt{4\pi^2 + \delta^2}}, \tag{5.76}$$

where δ is the logarithmic decrement, defined by the logarithm of the ratio of consecutive peaks,

$$\delta_n = \ln \frac{\text{height of } (n+1)th \text{ peak}}{\text{height of } nth \text{ peak}}. \tag{5.77}$$

This analysis is based on the linear mass-spring-damper system which does not apply in this case. However, this will give us some idea about the degree of nonlinearity that we are dealing with. For example, if the system is linear, the damping ratio calculated in this manner should be constant for any nth and $(n+1)\,th$ peaks we choose. Therefore, if the equivalent damping ratio ζ stays roughly the same, then the system is nearly linear.

As a numerical example, Table 5.6 shows the logarithmic decrement and equivalent damping ratio for the transverse response obtained using IC_1.

3.4 Damped-Free Response - Potential and Kinetic Energies

Figures 5.33 to 5.35 show the potential energies, and Figures 5.36 to 5.38 show the kinetic energies of the system for the first three initial conditions. The energies of the damped system show some of the same characteristics that we have seen in the free system: shape of elongation resembles the shape of membrane energy, the potential energies themselves are in phase, the kinetic energies themselves are in phase, the potential energy and the kinetic energy are 180° out of phase.

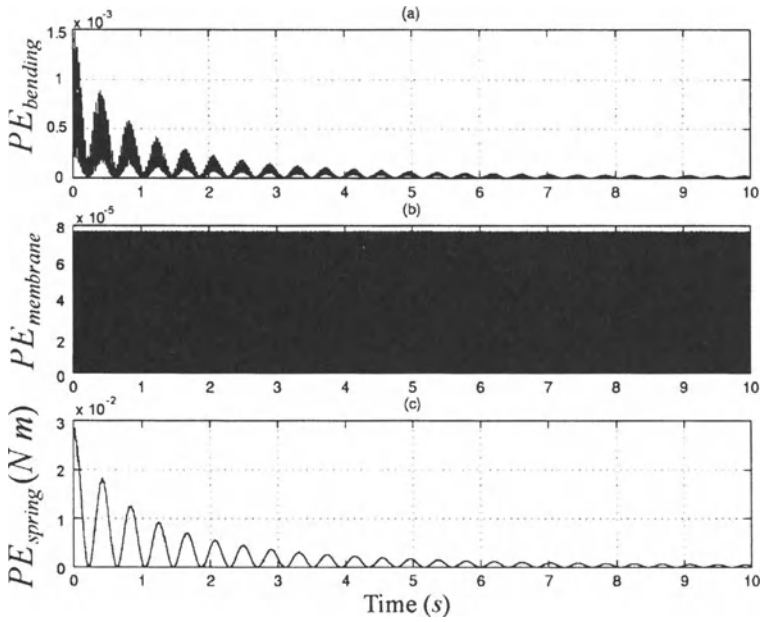

Figure 5.33. Potential Energies of the Damped Free System Using IC_1

Now, let us look at how the energy is transferred between the potential energy and kinetic energy. Looking at the potential energies, only the membrane energy persists with time while the bending and spring energy seem to diminish with time.

Looking at the kinetic energies obtained using IC_2 and IC_3, membrane energy shows up as the translational kinetic energy of the beam and the kinetic energy of the point mass. The expressions for the membrane energy, translational kinetic energy and the kinetic energy of the point mass have axial displacement in common. This is consistent with our previous result that only the axial motion persists in the system when the Morison force is applied.

Figures 5.39 show the total energies of the system with time for all three initial conditions. The total energy decays while oscillating when IC_1 is used. The total energy fluctuates due to the phase difference between the kinetic and potential energy. When IC_2 and IC_3 are used, the total energy does not seem to decrease. This is because the most energy is in the axial motion. Note that fifty and one hundred nodes are used in order to produce energies associated with IC_2 and IC_3, respectively. This is because the error was noticeable when only fourteen nodes are used in those cases.

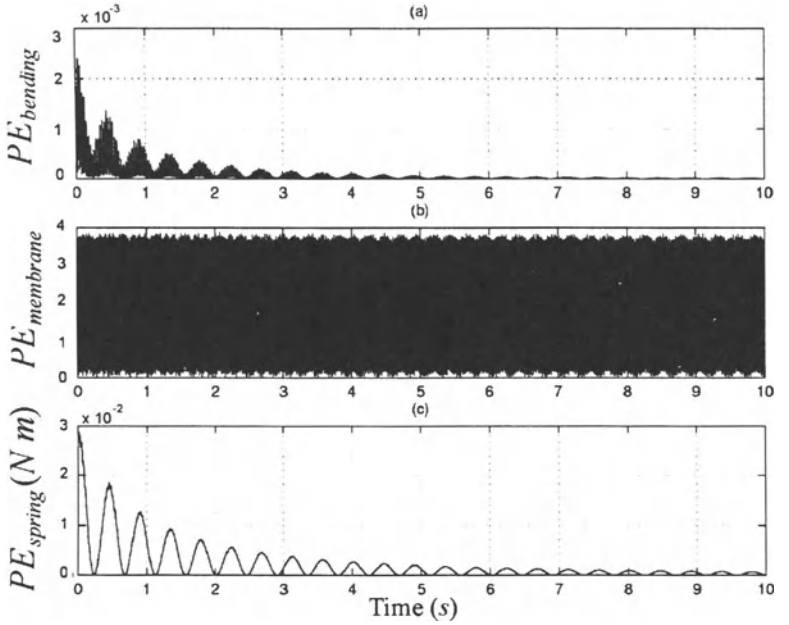

Figure 5.34. Potential Energies of the Damped Free System Using IC_2

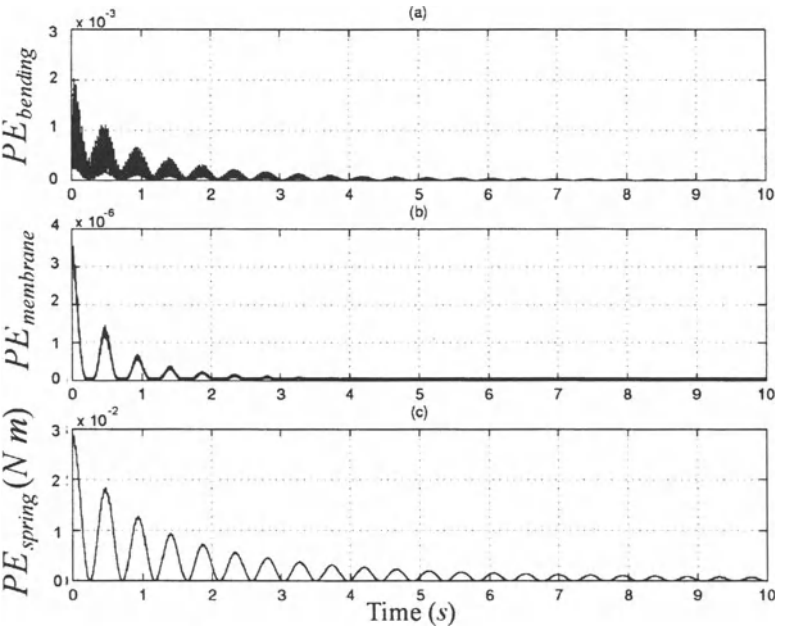

Figure 5.35. Potential Energies of the Damped Free System Using IC_3

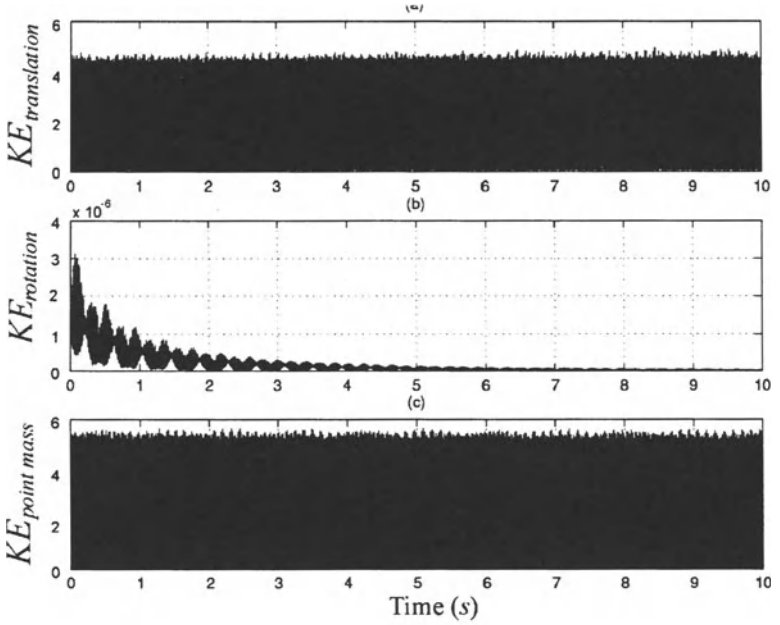

Figure 5.36. Kinetic Energies of the Damped Free System Using IC_1

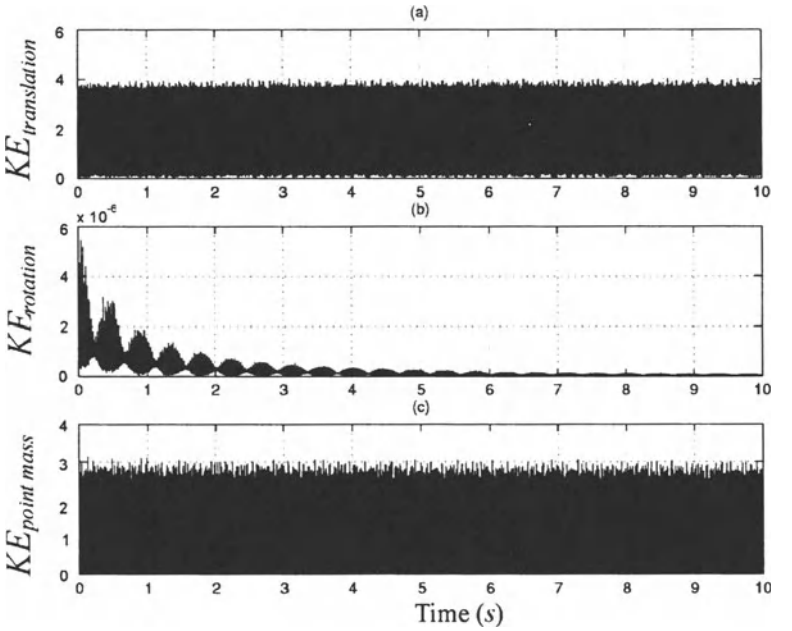

Figure 5.37. Kinetic Energies of the Damped Free System Using IC_2

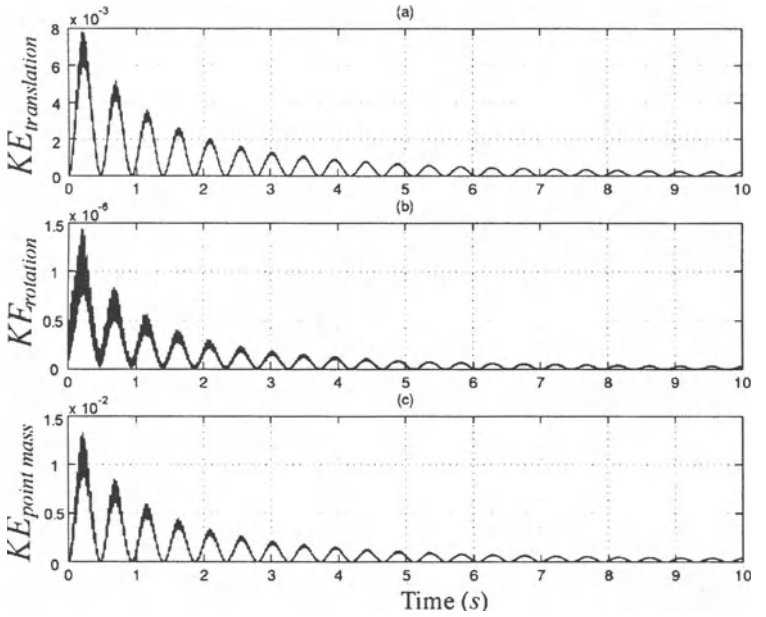

Figure 5.38. Kinetic Energies of the Damped Free System Using IC_3

3.5 Effect of Varying Fluid Coefficients

The added mass coefficient, C_A, changes the effective mass length density ($\rho A_{effective}$) of the beam. Therefore, larger C_A means longer period and smaller decay rate. Increasing the drag coefficient, C_D, will increase the damping in the system. Here, the coefficients are varied $\pm 50\%$ of their nominal values of $C_A = 1$ and $C_D = 1$.

Figure 5.40 shows the transverse tip displacement for $C_A = 0.5$, 1, and 1.5. The periods of oscillation are 0.877, 0.933, 0.987 s. The amplitude ratios of the second to the first peaks are 0.640, 0.670, and 0.694. The period varied from -6.00% to $+5.79\%$, and the amplitude ratio varied from -4.48% to $+3.58\%$.

Figure 5.41 shows the transverse tip displacement for $C_D = 0.5$, 1, and 1.5. The amplitude ratios of the second to the first peaks are 0.800, 0.670, and 0.570. The amplitude ratio varied from $+19.4\%$ to -14.9%.

The responses are more sensitive to the drag coefficient than the added mass coefficient.

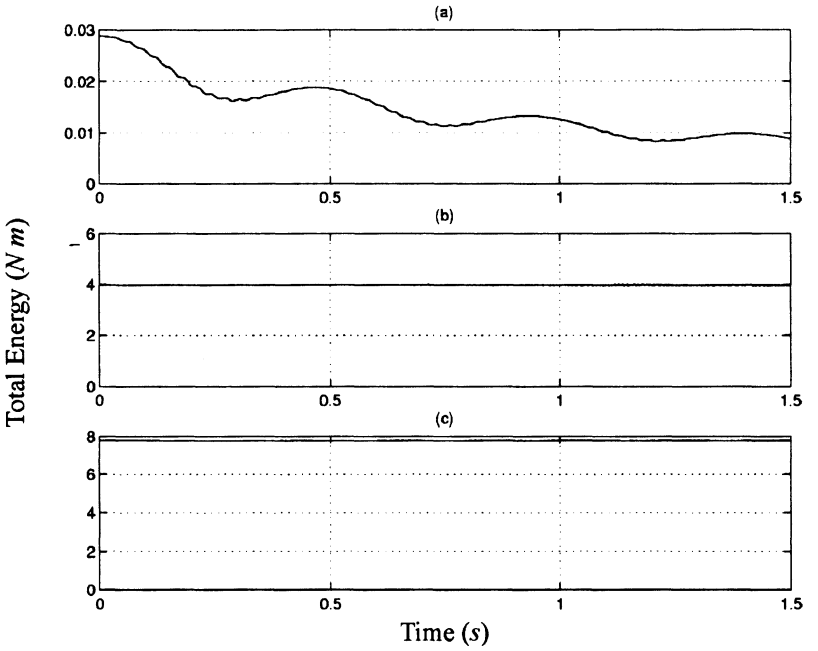

Figure 5.39. Total Energy of the Damped System. (a) IC_1 (14 nodes), (b) IC_2 (50 nodes), (c) IC_3 (100 nodes)

4. Forced Response using the Two-Dimensional Coupled Model

For numerical purposes, we consider a beam identical to that used in the investigation of the free response. The beam and the fluid properties are given in Tables 5.1 and 5.2. In addition, the current velocity $U_c = 0.12\ m/s$ and the inertia coefficient $C_M = 2$ are used.

The drag coefficient of 1 is a reasonable value for the Reynolds number of our flow [61]. For a long cylinder, the inertia coefficient approaches its theoretical value (the value for a uniformly accelerated flow) of 2, and the added mass coefficient related to the inertia coefficient by

$$C_A = C_M - 1 \tag{5.78}$$

approaches 1. We use these theoretical values for numerical purposes.

Here, we consider either zero initial conditions or initial displacements obtained from the physical configuration shown in Figure 5.42 with zero initial velocities.

The point load is determined such that the end transverse deflection is 0.05 m. The expressions for the displacements are given in Equation

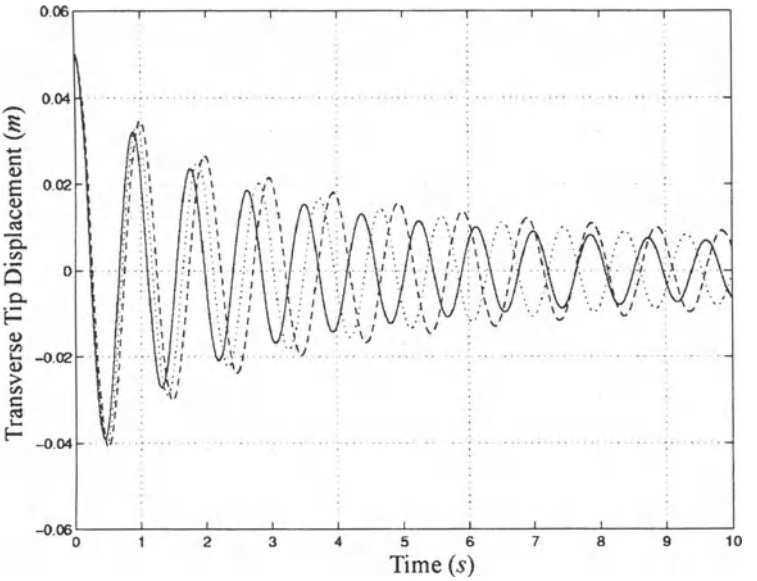

Figure 5.40. Transverse Tip Displacement Using IC_1 and $C_D = 1$. $-$ $C_A = 0.5$; $\cdots$ $C_A = 1$; $--$ $C_A = 1.5$

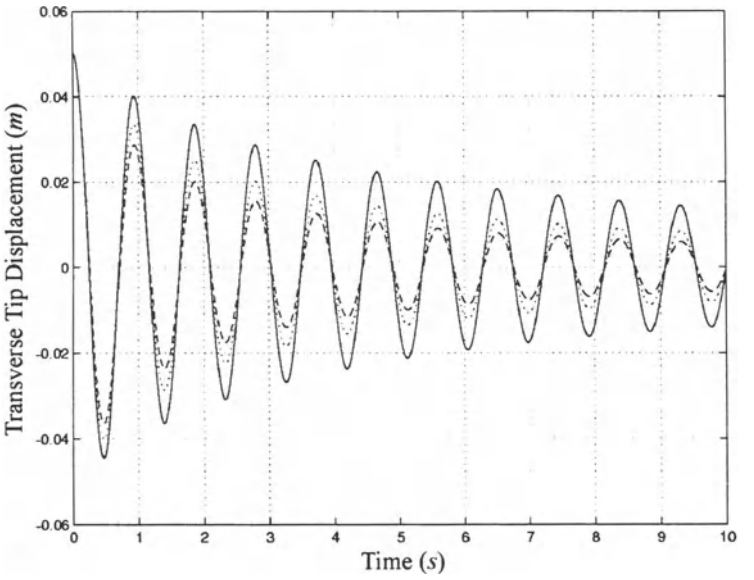

Figure 5.41. Transverse Tip Displacement Using IC_1 and $C_A = 1$. $-$ $C_D = 0.5$; $\cdots$ $C_D = 1$; $--$ $C_D = 1.5$

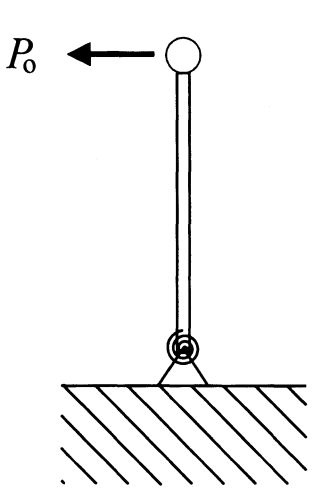

Figure 5.42. Initial Configuration

5.79,

$$u(X,0) = -\frac{1}{2}\left(\frac{P_o}{EI}\right)^2\left(\frac{X^5}{20} - \frac{LX^4}{4} + \left(L^2 - \frac{EIL}{k}\right)\frac{X^3}{3} + \frac{EIL^2X^2}{k} + \left(\frac{EIL}{k}\right)^2 X\right)$$

$$v(X,0) = -\frac{P_o}{EI}\left(\frac{X^3}{6} - \frac{LX^2}{2} - \frac{EILX}{k}\right). \tag{5.79}$$

Note that these displacements are identical to the initial displacements IC_1 used in the free and damped vibration studies in Section 3.

In free vibration, we found that the fundamental frequency of the transverse motion is 7.75 rad/s in vacua and 6.78 rad/s in still water.

Here, we apply two kinds of distributed transverse loads: a simple harmonic and a random force. The fluid force due to random waves has many frequency components. Therefore, it may be useful to first consider a transverse load with single frequency. The distributed axial load in Equation 5.73 is used for all cases.

4.1 Harmonic Forcing

Let us assume that the distributed transverse load is constant over the length of the beam and varies harmonically with time. That is, $f(X,t) = \rho_f A_f \cos\omega_f t$. The coefficient of the harmonic function is chosen as $\rho_f A_f$ to give a reasonable deflection amplitude.

4.1.1 Subharmonics

If we see a periodic response to a forcing frequency that is a multiple of the natural frequency, it is called a subharmonic response. Similarly, if we see a periodic response to a forcing frequency that is a fraction of the natural frequency, it is called a superharmonic or ultraharmonic response. In both cases, the system responds at the lower frequency of the two. That is, the system responds at the natural frequency for the subharmonics and at the forcing frequency for the superharmonics. The superharmonics are called ordinary harmonics in the sense that the system response is at the input forcing frequency.

Subharmonics and superharmonics can be seen in both linear and nonlinear systems. Those seen in linear systems are due to exact relations between the natural and forcing frequencies. That is, the forcing frequency has to be an exact multiple or an exact fraction of the natural frequency. Recall that there are two parts to the solution to the linear oscillator; the homogeneous and the particular solution. The homogeneous part oscillates at the natural frequency, and the particular part oscillates at the forcing frequency. The magnitude of the homogeneous part is determined exactly from initial conditions, the forcing frequency, and the amplitude of the force. The subharmonic state enters when the forcing frequency is twice the natural frequency, and the magnitude of the homogeneous solution is large compared to that of the particular solution. Similarly, the superharmonic state enters when the forcing frequency is half the natural frequency, and the magnitude of the homogeneous solution is small compared to that of the particular solution. Therefore, subharmonics and superharmonics may or may not appear depending on the initial conditions and the amplitude of forcing when a suitable forcing frequency is set for each case[8].

Nonlinear systems are slightly different in that the nonlinearity of the system can generate stable harmonics that can appear for a range of forcing frequencies, instead of at exact values of forcing frequency. Again, subharmonics and superharmonics may or may not appear depending on the initial conditions and forcing amplitude.

The governing equations of motion, Equations 5.25 and 5.26, have second order nonlinear terms. This indicates that the response may exhibit subharmonics of order 1/2 and superharmonics of order 2. Therefore, we look for subharmonics for the forcing frequency near twice the natural frequency and superharmonics near half the natural frequency.

[8]For detailed treatment of subharmonics and superharmonics, readers are refered to [52].

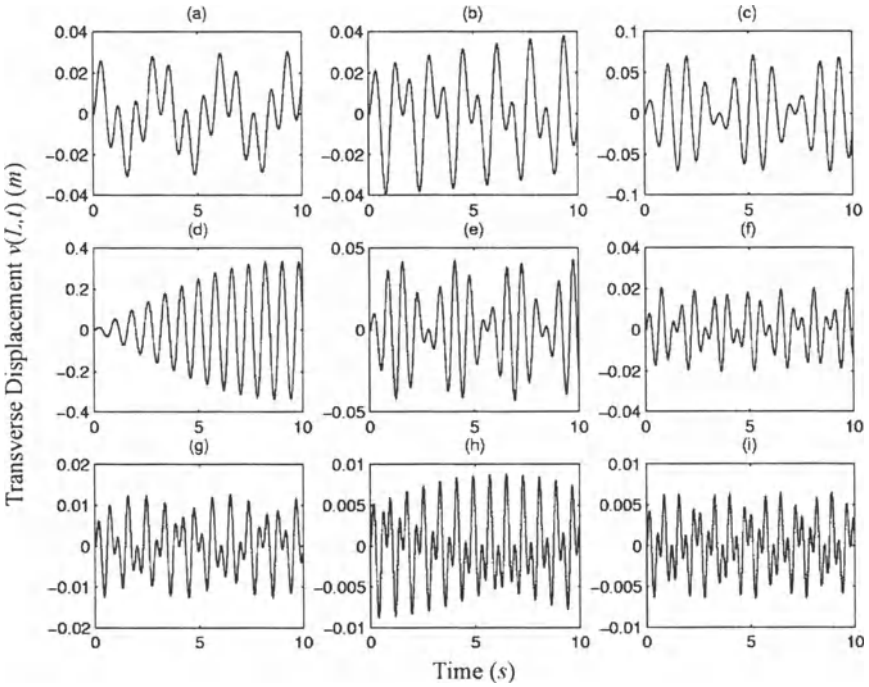

Figure 5.43. Transverse Tip Displacement when Zero Initial conditions are used. (a) $\omega_f = 2$, (b) $\omega_f = 4$, (c) $\omega_f = 6$, (d) $\omega_f = 8$, (e) $\omega_f = 10$, (f) $\omega_f = 12$, (g) $\omega_f = 14$, (h) $\omega_f = 16$, (i) $\omega_f = 18$ rad/s

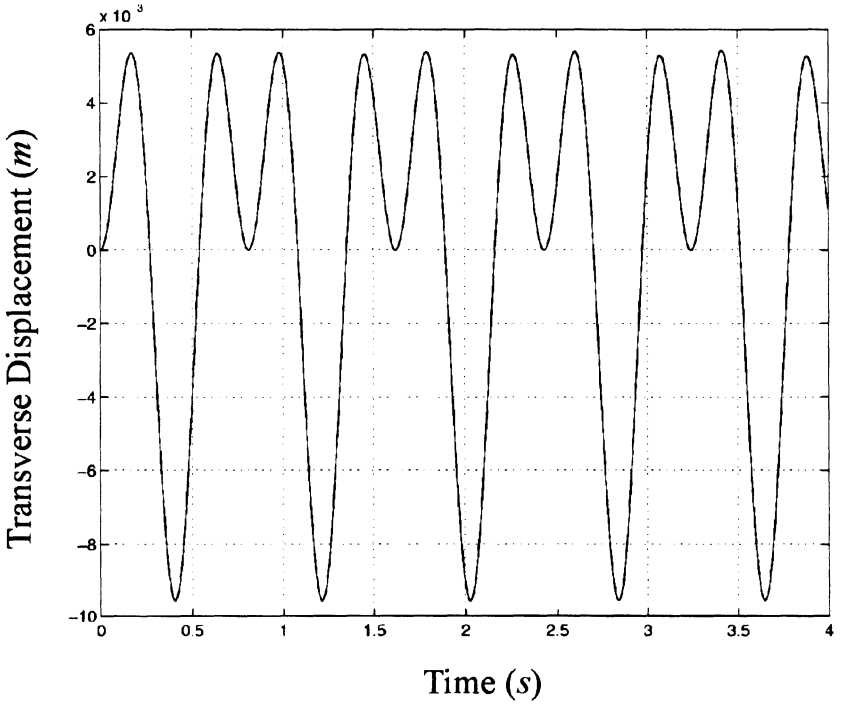

Figure 5.44. Transverse Tip Displacement when $\omega_f = 15.5\ rad/s$

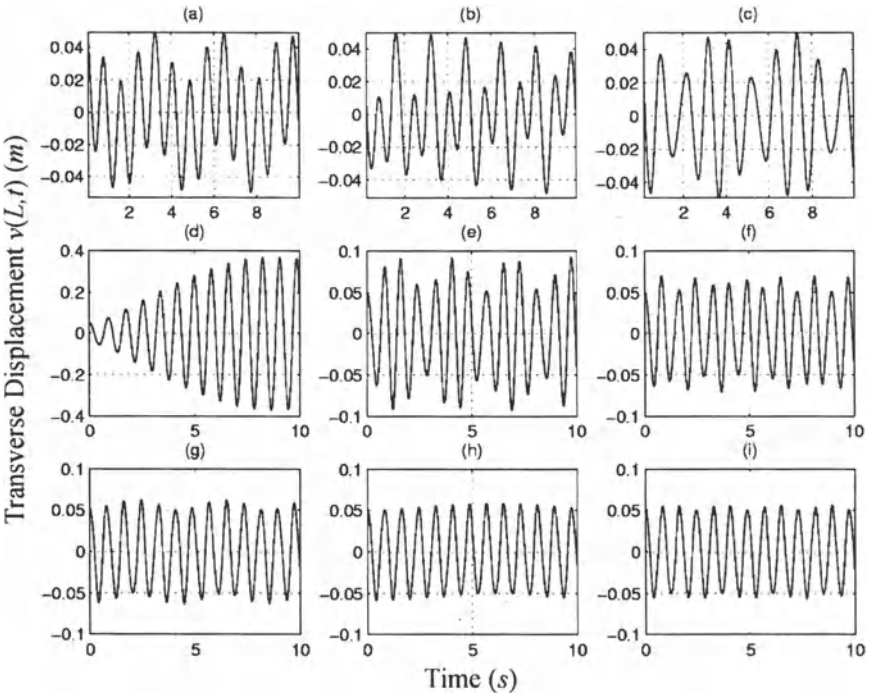

Figure 5.45. Transverse Tip Displacement when IC_1 is used. (a) $\omega_f = 2$, (b) $\omega_f = 4$, (c) $\omega_f = 6$, (d) $\omega_f = 8$, (e) $\omega_f = 10$, (f) $\omega_f = 12$, (g) $\omega_f = 14$, (h) $\omega_f = 16$, (i) $\omega_f = 18$ rad/s

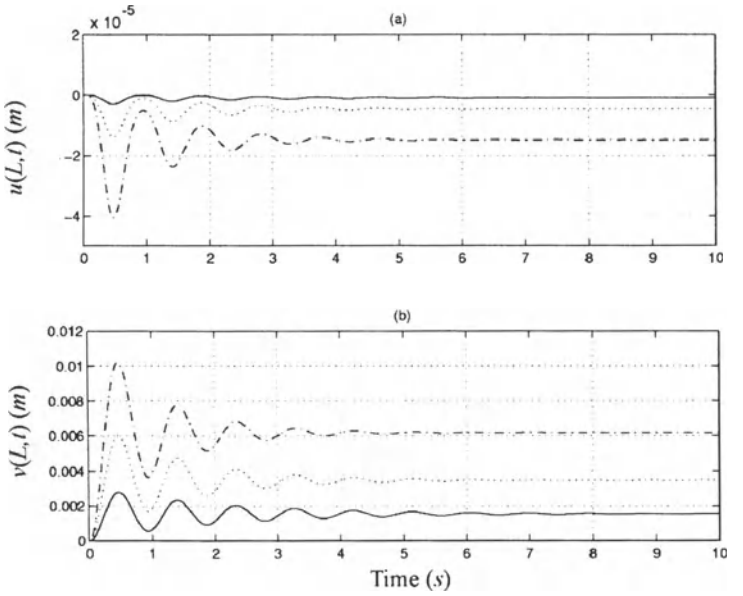

Figure 5.46. Tip Displacements when the Beam is Subjected to Current. – $U_c = 0.08$; - - $U_c = 0.12$; –. $U_c = 0.16$ m/s. (a) $u(L,t)$, (b) $v(L,t)$

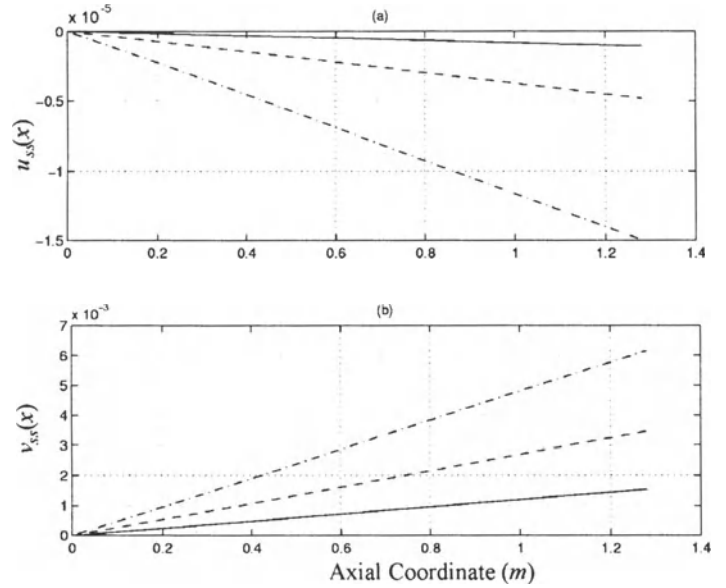

Figure 5.47. Steady State Response when the Beam is Subjected to Current. – $U_c = 0.08$; - - $U_c = 0.12$; –. $U_c = 0.16$ m/s. (a) $u_{ss}(L,t)$, (b) $v_{ss}(L,t)$

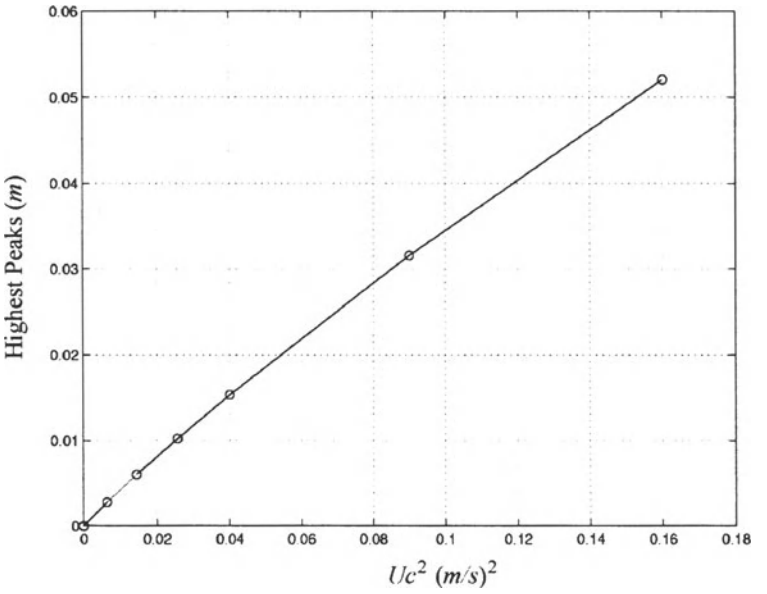

Figure 5.48. Peak Amplitude of Tip Transverse Displacement

It has been observed that the subharmonics exist in offshore structures such as landing ships tanks (LST's) during mooring [55]. Here, let us only consider subharmonic responses.

The forcing frequency is varied from 2 to 18 rad/s at 2 rad/s increment. Figure 5.43 shows the transverse displacement when zero initial conditions are used. We notice that the response grows when the forcing frequency approaches the natural frequency (around 7.75-8.48 rad/s). The subharmonic state did not enter here. The subharmonic response can be seen only when the forcing frequency is 15.5 rad/s, as shown in Figure 5.44 where the system responds at half the input forcing frequency. This behavior is similar to what we see in the linear responses where an exact relationship between the natural and forcing frequency is required in order for the subharmonic state to enter.

On the other hand, the transverse displacement in Figure 5.45, obtained using the initial conditions given in Equation 5.79, shows the subharmonic response for forcing frequencies that are not exactly twice the natural frequency. In Figures 5.45(g) to (i), we observed that the system responds at the natural frequency when it is forced at a frequency close to twice the natural frequency. This is a characteristic of a nonlinear system.

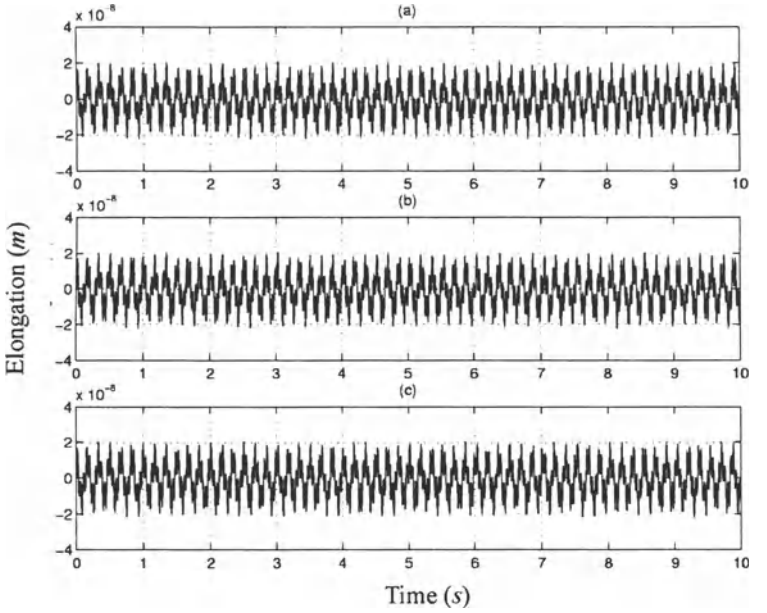

Figure 5.49. Elongation of the Beam. (a) $U_c = 0.08$, (b) $U_c = 0.12$, (c) $U_c = 0.16$ m/s

4.2 Effects of Current

Figure 5.46 shows the transverse and axial displacement plots for current velocities of 0.8, 1.2 and 1.6 m/s. Note that the steady-state response can be found by solving the equations of motion in Equations 5.25 and 5.26 by setting the time derivatives equal to zero, or

$$-EA\left(u'_{ss} + \frac{1}{2}v'^{2}_{ss}\right)' = p \tag{5.80}$$

$$-\left(EA\left(u'_{ss} + \frac{1}{2}v'^{2}_{ss}\right)v'_{ss}\right)' + \left(EIv''_{ss}\right)'' = f, \tag{5.81}$$

where

$$\begin{aligned} p(X,t) &= -\rho gA + \rho_f g A_f \text{ for } 0 < x < d \\ &= -\rho gA \text{ for } d < x < L \\ f(X,t) &= C_D \rho_f r_o U_c^2 \text{ for } 0 < x < d \\ &= 0 \text{ for } d < x < L. \end{aligned} \tag{5.82}$$

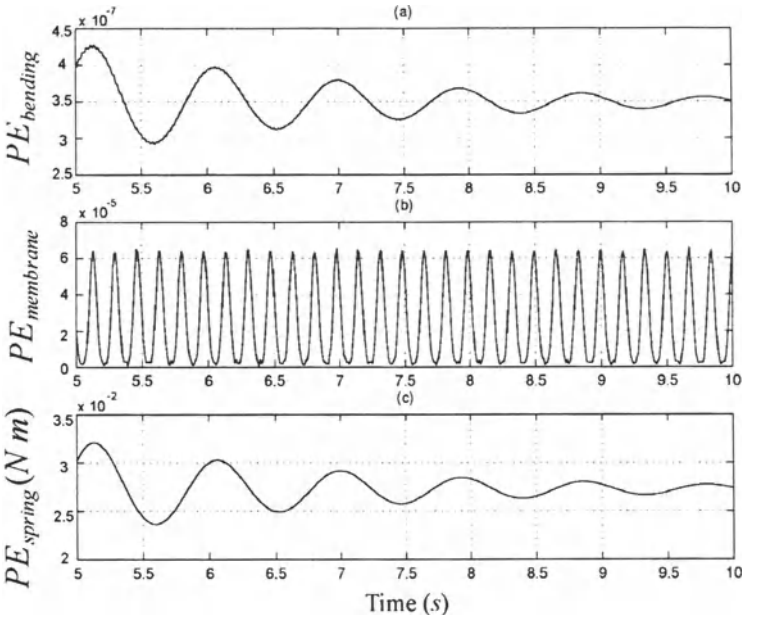

Figure 5.50. Potential Energy for $U_c = 0.08m/s$

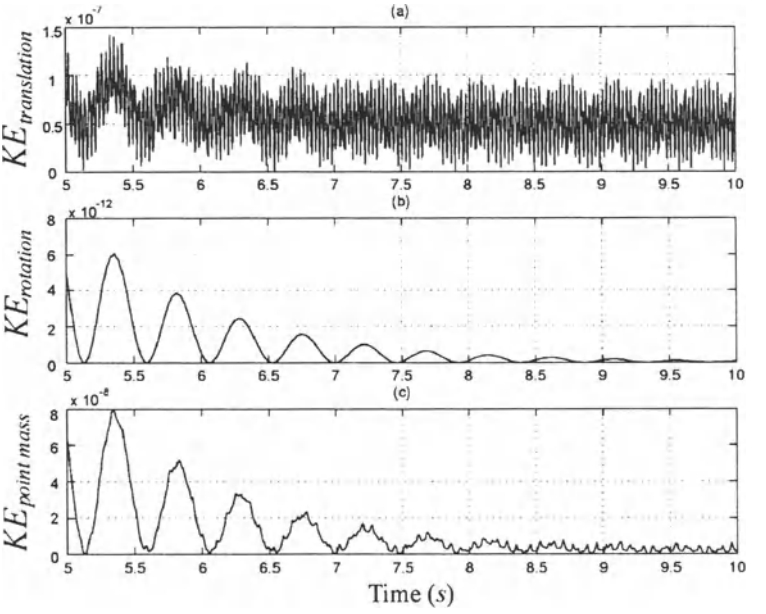

Figure 5.51. Kinetic Energy for $U_c = 0.08m/s$

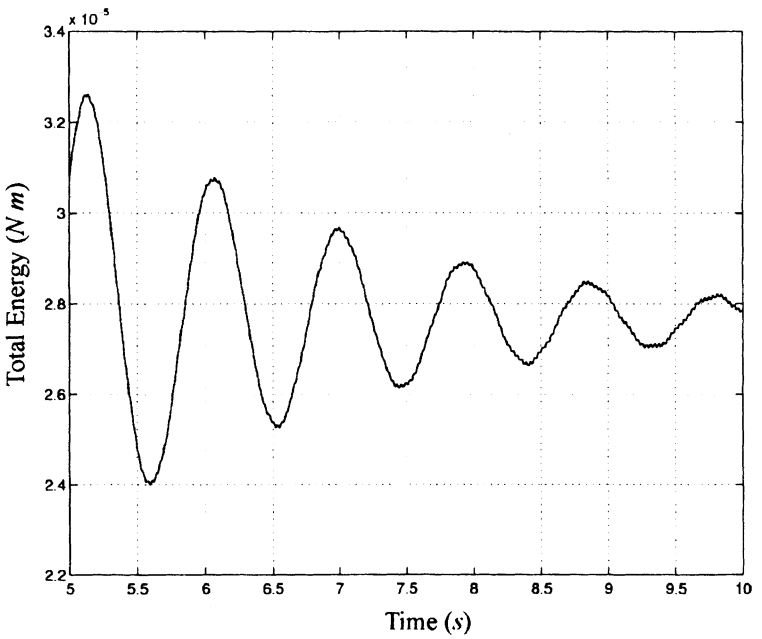

Figure 5.52. Total Energy for $U_c = 0.08\ m$

The subscript ss is used for the steady-state response. It is not difficult to solve for the steady-state response numerically[9]. The steady-state axial and transverse displacements along the beam are shown in Figure 5.47. The steady-state transverse tip displacements are 0.00154, 0.00346, and $0.00616m$ for $U_c = 0.08$, 0.12, and 0.16 m/s, respectively. The ratio of the transverse tip displacements is $1 : 2.25 : 4$. Looking at this ratio, we note that the transverse displacement is proportional to the current velocity squared. This can also be shown by manipulating Equations 5.80 and 5.81. Therefore, we can write

$$v_{ss}(X) = k_v(X) U_c^2, \tag{5.83}$$

where k_v is the proportionality constant that depends on the location of the beam. Using the data, $v_{ss}(L) = 0.00616\ m$ when $U_c = 0.16\ m/s$, the proportionality constant for $X = L$ is found to be $0.241\ s^2/m$. On the other hand, the steady-state axial displacement is not proportional to the current velocity squared. Instead, it is determined using Equation 5.80.

[9]See Appendix E for details.

Now, let us look at the transient response. The maximum transverse displacements are plotted in Figure 5.48 for the current velocities 0.08, 0.12, 0.16, 0.2, 0.3, and 0.4 m/s. Note that the abscissa is the current velocity squared. The figure shows decreasing slope for increasing current velocities, which means that the maximum transverse tip displacement is proportional to the current velocity to the power slightly less than 2, if it is proportional at all.

As the current velocity increases, the drag increases. This is analogous to increasing the damping coefficient in the linear system. As the damping coefficient increases in the linear system, the damped natural frequency decreases. Therefore, in our case, increasing the current velocity slows the response. Figure 5.49 shows corresponding physical elongation of the beam for current velocities, 0.08. 0.12, and 0.16 m/s. Surprisingly, the magnitudes are about the same. In fact, the time response looks almost identical. We also notice that the elongations do not decay with time. Now, let us look at the energies of the system. Figures 5.50 and 5.51 show the potential and kinetic energies of the system when $U_c = 0.08\ m/s$. The bending energy and the potential energy stored in the spring approach a non-zero value as time passes. The membrane energy and translational kinetic energy do not decay nor approach steady-state value. It was shown in Section 3 that the membrane energy is directly related to the elongation of the beam. It is no surprise that the shapes of the membrane energy and the elongation resemble one another. The non-decaying elongation, membrane energy, and translational kinetic energy indicate that the Morison force is unable to damp the axial motion as shown previously in damped-free vibration. However, the axial motion is small compared to the transverse motion so that the steady-state analysis in Equations 5.80 and 5.81 are still valid. The total energy shown in Figure 5.52 approaches a non-zero value, which is mainly the potential energy stored in the system.

4.3 Effect of Random Waves

The significant wave height is varied such that the peak angular frequency is varied from 2 to 18 rad/s at 2 rad/s intervals. That is, the corresponding significant wave heights, from Equation 4.28, are 0.3957, 0.0989, 0.0440, 0.0247, 0.0158, 0.0110, 0.0081, 0.0062, and 0.0049 m. The Pierson-Moskowitz spectra are plotted in Figure 5.53. In the laboratory setting, a significant wave height of 0.1 m may be plausible. Note that the magnitude of power spectral density decreases with decreasing significant wave height or increasing peak frequency.

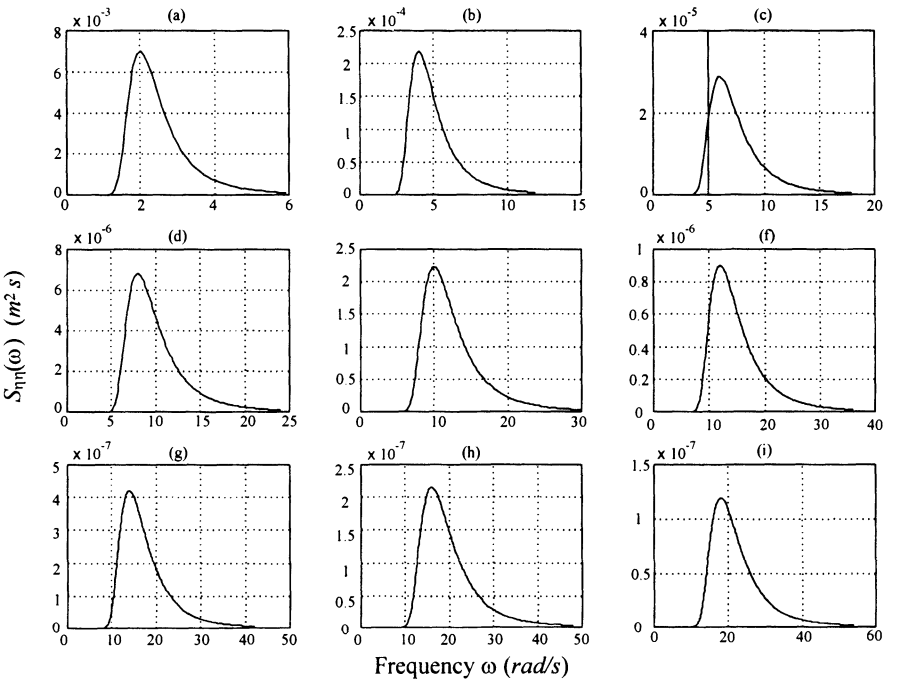

Figure 5.53. Pierson-Moskowitz Spectrum. (a) $\omega_{peak} = 2$, (b) $\omega_{peak} = 4$, (c) $\omega_{peak} = 6$, (d) $\omega_{peak} = 8$, (e) $\omega_{peak} = 10$, (f) $\omega_{peak} = 12$, (g) $\omega_{peak} = 14$, (h) $\omega_{peak} = 16$, (i) $\omega_{peak} = 18\ rad/s$

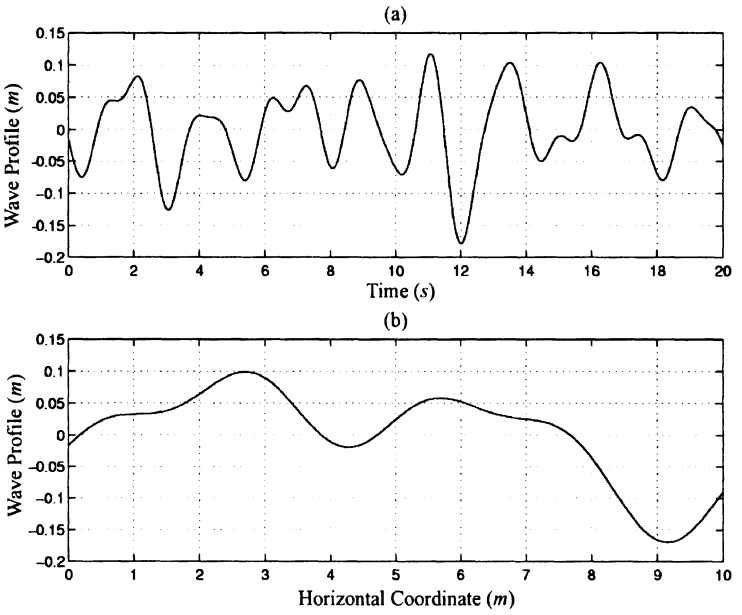

Figure 5.54. Wave Height for $\omega_{peak} = 2\ rad/s$. (a) Wave Height vs. Time, (b) Wave Height vs. Horizontal Coordinate

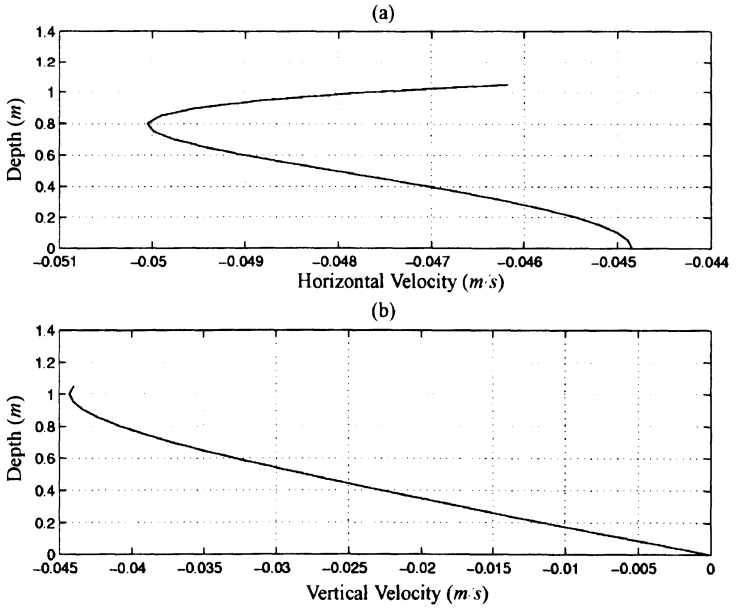

Figure 5.55. Wave Velocities for $\omega_{peak} = 2\ rad/s$. (a) Horizontal Velocity, (b) Vertical Velocity

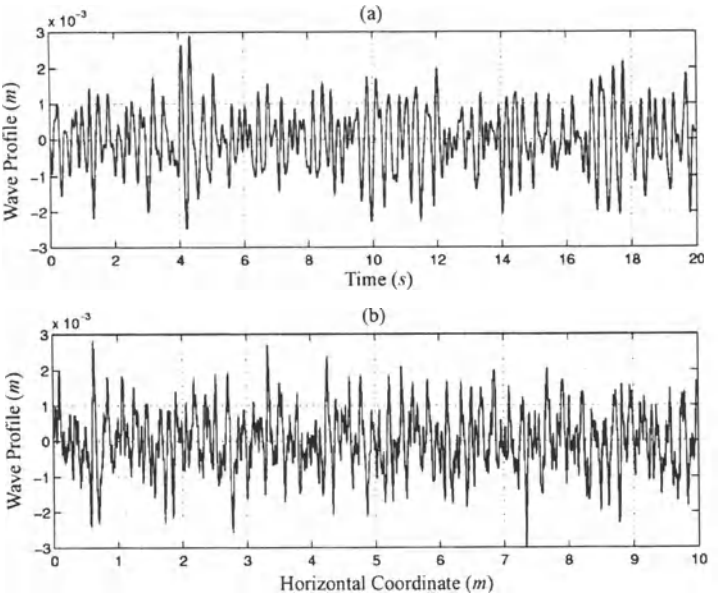

Figure 5.56. Wave Height for $\omega_{peak} = 18\ rad/s$. (a) Wave Height vs. Time, (b) Wave Height vs. Horizontal Coordinate

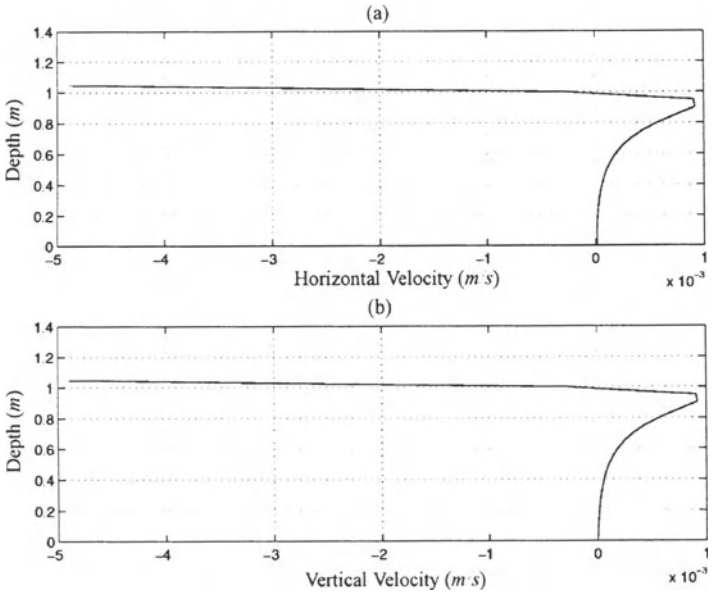

Figure 5.57. Wave Velocities for $\omega_{peak} = 18\ rad/s$. (a) Horizontal Velocity, (b) Vertical Velocity

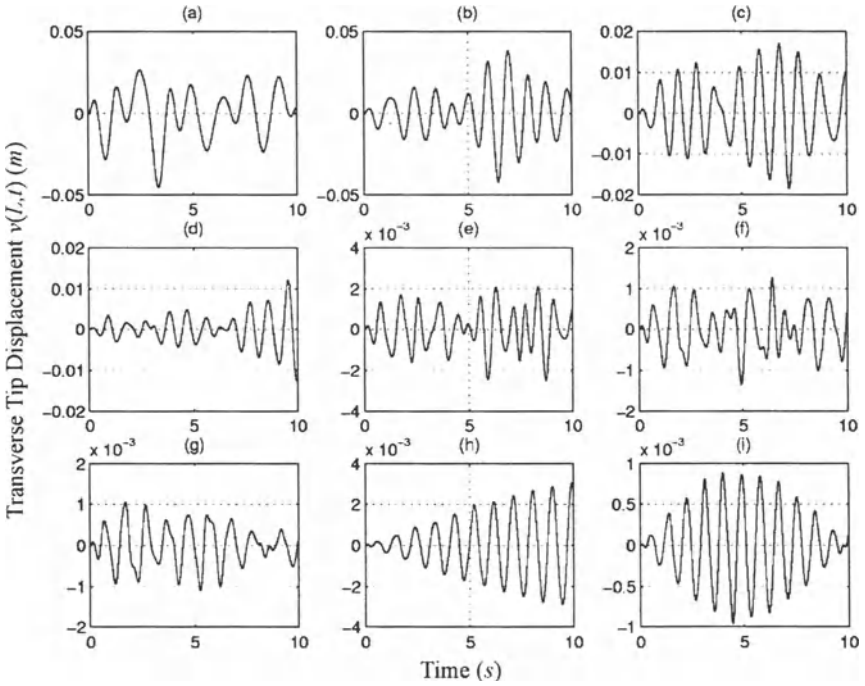

Figure 5.58. Transverse Tip Displacement when Zero Initial Conditions are used. (a) $\omega_{peak} = 2$, (b) $\omega_{peak} = 4$, (c) $\omega_{peak} = 6$, (d) $\omega_{peak} = 8$, (e) $\omega_{peak} = 10$, (f) $\omega_{peak} = 12$, (g) $\omega_{peak} = 14$, (h) $\omega_{peak} = 16$, (i) $\omega_{peak} = 18$ rad/s

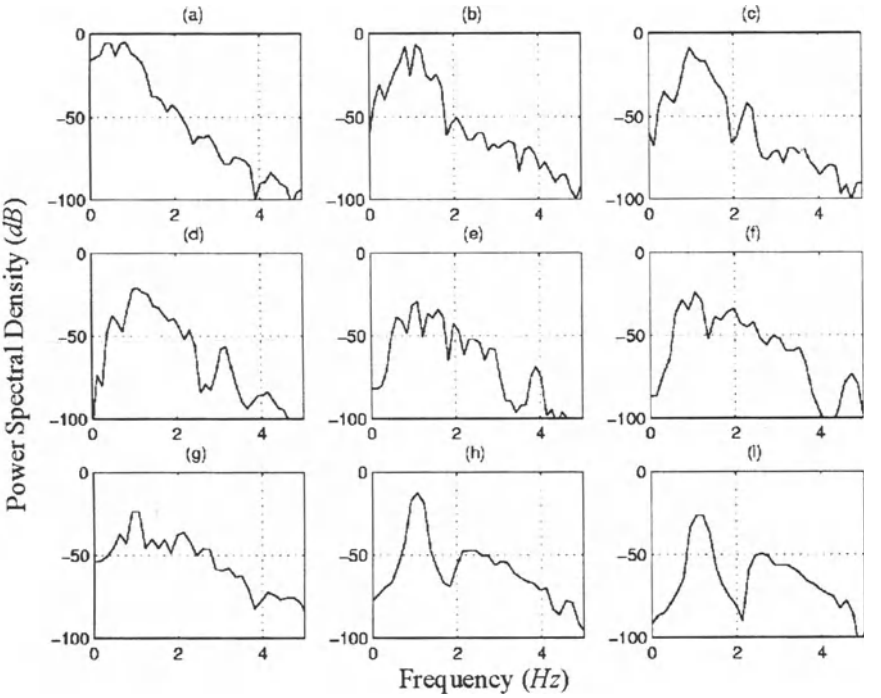

Figure 5.59. Power Spectral Density Plots for the Transverse Tip Displacements when Zero Initial Conditions are used. (a) $\omega_{peak} = 2$, (b) $\omega_{peak} = 4$, (c) $\omega_{peak} = 6$, (d) $\omega_{peak} = 8$, (e) $\omega_{peak} = 10$, (f) $\omega_{peak} = 12$, (g) $\omega_{peak} = 14$, (h) $\omega_{peak} = 16$, (i) $\omega_{peak} = 18\ rad/s$

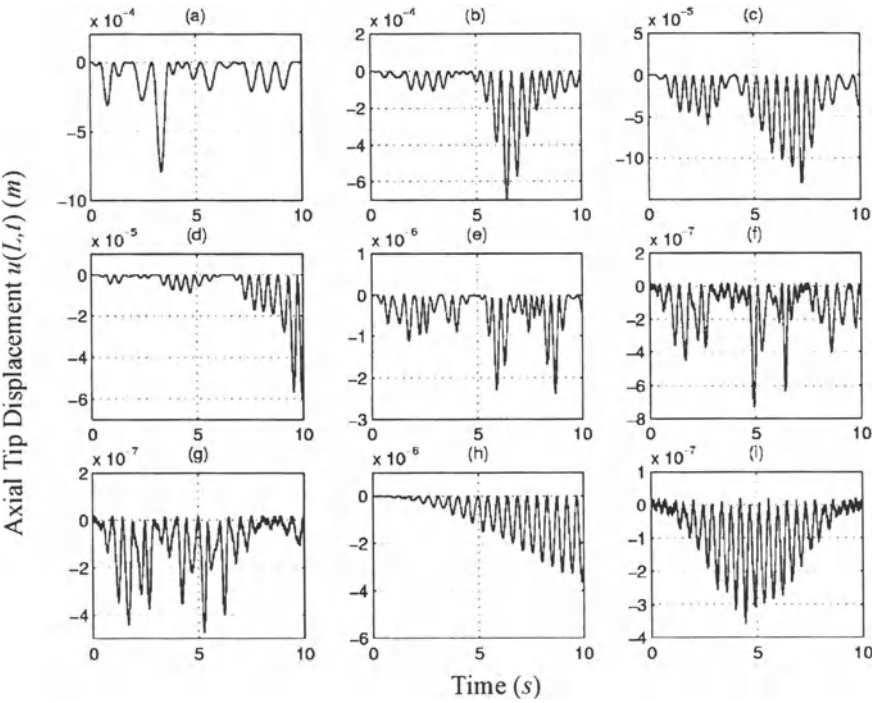

Figure 5.60. Axial Displacement when Zero Initial Conditions are used. (a) $\omega_{peak} = 2$, (b) $\omega_{peak} = 4$, (c) $\omega_{peak} = 6$, (d) $\omega_{peak} = 8$, (e) $\omega_{peak} = 10$, (f) $\omega_{peak} = 12$, (g) $\omega_{peak} = 14$, (h) $\omega_{peak} = 16$, (i) $\omega_{peak} = 18\ rad/s$

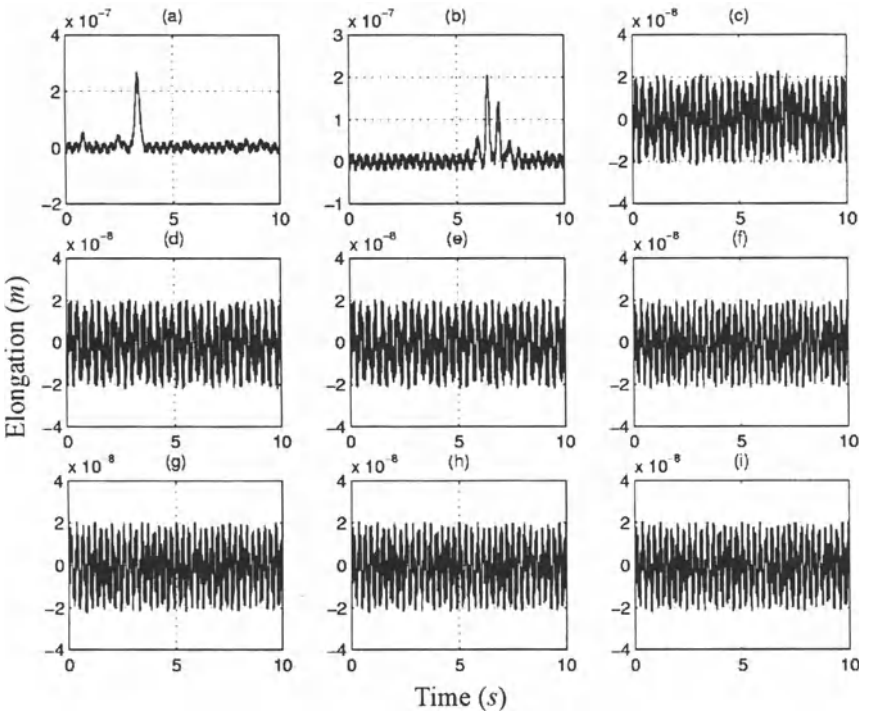

Figure 5.61. Elongation when Zero Initial Conditions are used. (a) $\omega_{peak} = 2$, (b) $\omega_{peak} = 4$, (c) $\omega_{peak} = 6$, (d) $\omega_{peak} = 8$, (e) $\omega_{peak} = 10$, (f) $\omega_{peak} = 12$, (g) $\omega_{peak} = 14$, (h) $\omega_{peak} = 16$, (i) $\omega_{peak} = 18\ rad/s$

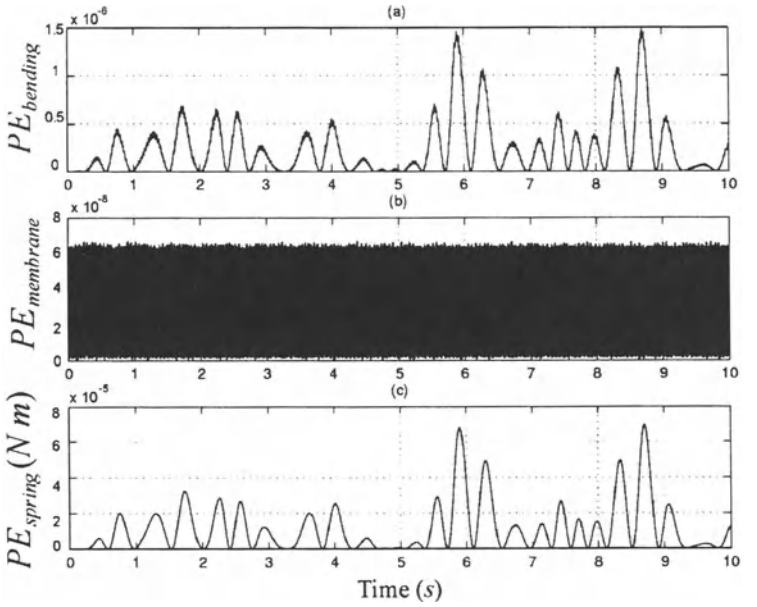

Figure 5.62. Potential Energies when Zero Initial Conditions and $\omega_{peak} = 10\ rad/s$ are used

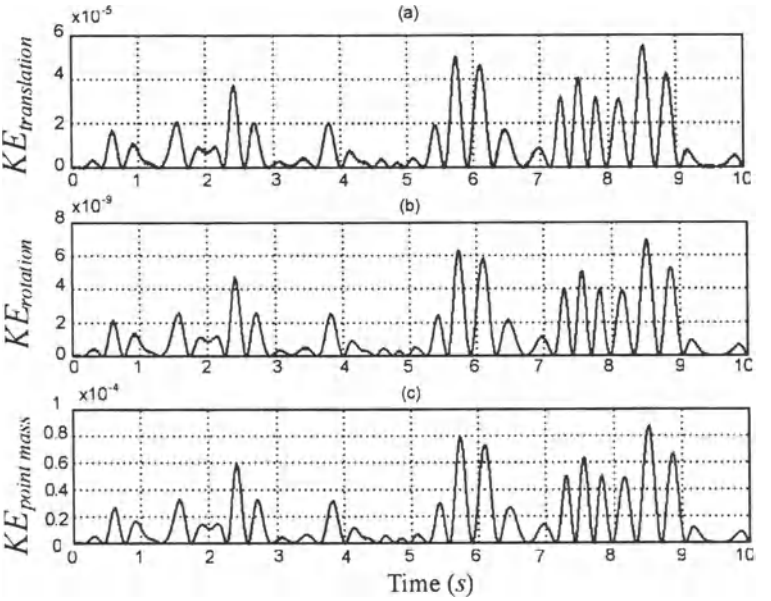

Figure 5.63. Kinetic Energies when Zero Initial Conditions and $\omega_{peak} = 10\ rad/s$ are used

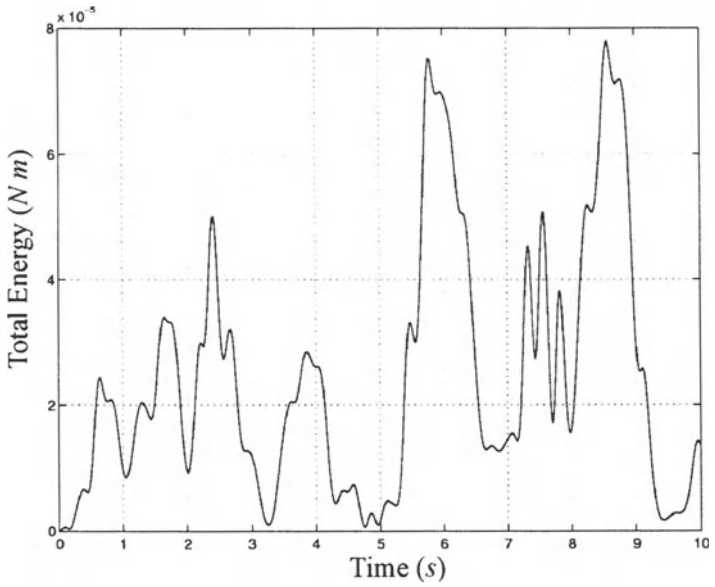

Figure 5.64. Total Energy when Zero Initial Conditions and $\omega_{peak} = 10\ rad/s$ are used

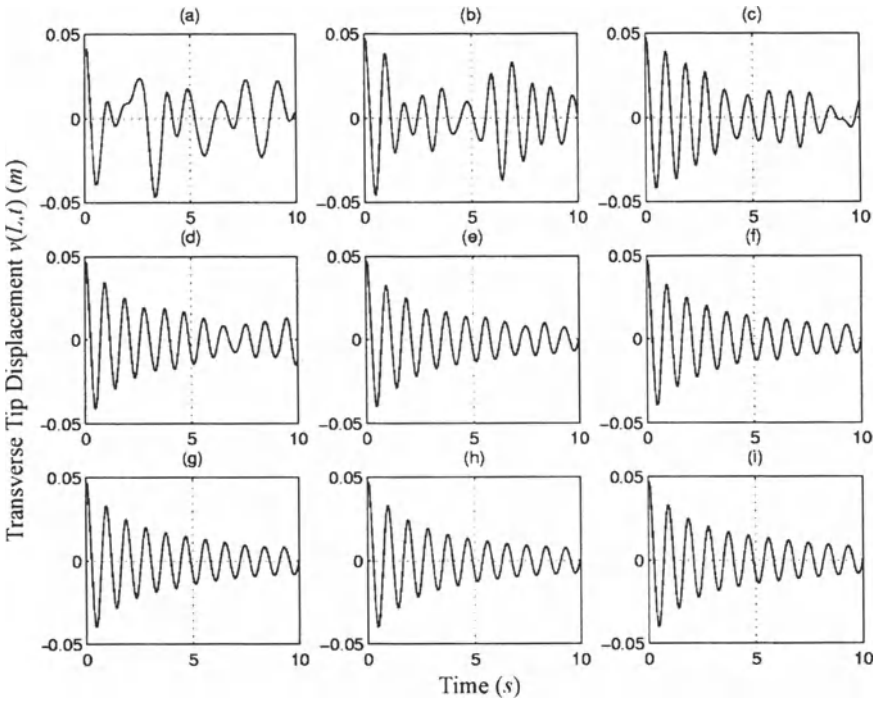

Figure 5.65. Transverse Displacement when Nonzero Initial Conditions are used. (a) $\omega_{peak} = 2$, (b) $\omega_{peak} = 4$, (c) $\omega_{peak} = 6$, (d) $\omega_{peak} = 8$, (e) $\omega_{peak} = 10$, (f) $\omega_{peak} = 12$, (g) $\omega_{peak} = 14$, (h) $\omega_{peak} = 16$, (i) $\omega_{peak} = 18\ rad/s$

For $\omega_{peak} = 2\ rad/s$, the wave elevations, $\eta(y = 0, t)$ and $\eta(y, t = 0)$, are plotted in Figures 5.54 (a) and (b). The corresponding horizontal and vertical wave velocities at $t = 0$ and $y = 0$ are plotted as a function of depth in Figures 5.55 (a) and (b). For $\omega_{peak} = 18\ rad/s$, similar plots are shown in Figures 5.56 and 5.57. Note that the magnitude of wave elevations and velocities also decreased with increasing peak frequency.

The transverse displacements are plotted in Figure 5.58 where zero initial conditions are used. We observe a beating phenomenon in many of the responses. They are not well defined as in the linear case. The magnitude of the response generally decreased with increasing peak frequency. This is because the wave velocities decrease with the peak frequency. Figure 5.59 shows power spectral density plots for the transverse tip displacements. The data points are sampled at 0.0005 second intervals. We obtain a consistent peak at about 1 Hz. This frequency must be the damped natural frequency of the system. Note that it is different from the damped natural frequency obtained in still water or the

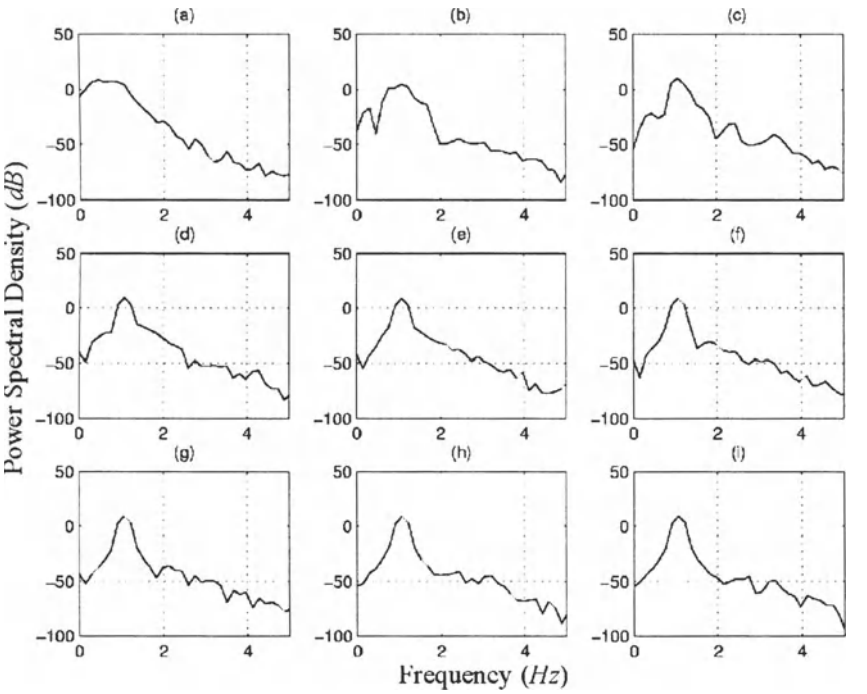

Figure 5.66. Power Spectral Density Plots for the Tip Transverse Displacement when Nonzero Initial Conditions are used

damped natural frequency when there is only current. This is because the damping force is different in each case.

Figure 5.60 shows the corresponding axial displacements. The general shape of the axial response is similar to those shown in Section 3: the fundamental frequency of the axial motion is twice that of the transverse motion, and the maximum of each peak of the dominant axial motion is the same, so that the dominant axial motion seems to have a ceiling. It was shown in Section 3 that this is due to the geometry of the system.

Figure 5.61 shows the elongation of the beam as a function of time. The amplitudes in most cases are about 2×10^{-8} m. When $\omega_{peak} = 2$ and 4 rad/s, we observe spurious peaks in elongations.

Figures 5.62 and 5.63 show the potential and kinetic energies when $\omega_{peak} = 10$ rad/s. The energies have some of the same characteristics observed in the free vibration: shape of elongation resembles the shape of the membrane energy, the potential energies and the kinetic energies are in phase, the potential energies and the kinetic energies are 180° out of phase. Figure 5.64 shows the total energy of the system. It shows

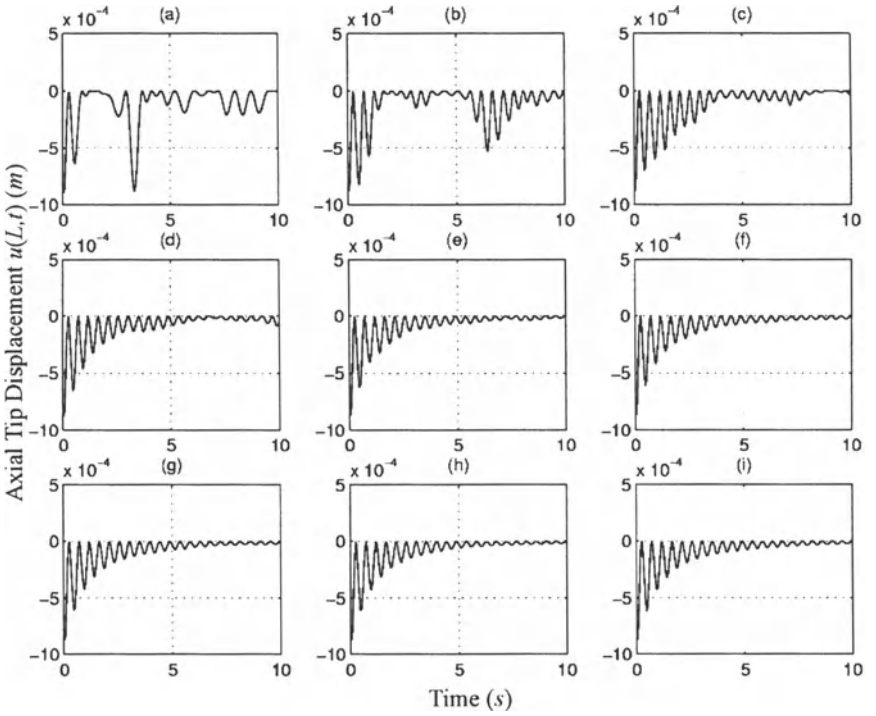

Figure 5.67. Axial Displacement when Nonzero Initial Conditions are used. (a) $\omega_{peak} = 2$, (b) $\omega_{peak} = 4$, (c) $\omega_{peak} = 6$, (d) $\omega_{peak} = 8$, (e) $\omega_{peak} = 10$, (f) $\omega_{peak} = 12$, (g) $\omega_{peak} = 14$, (h) $\omega_{peak} = 16$, (i) $\omega_{peak} = 18\ rad/s$

that the total energy does not decay. Instead, it fluctuates randomly due to the random forcing.

The transverse displacements are plotted in Figure 5.65, where the initial displacements in Equation 5.79 are used. The power spectral densities are plotted in Figure 5.66. The dominant frequency in all the responses is the damped natural frequency at about 1 Hz. We observe subharmonic resonances in Figures 5.65 (c) – (i). Note that we observe that the subharmonic resonance occurs for a relatively wide range of the peak frequency, ω_{peak}. This is due to the fact that the transverse force is random and the forcing frequency is spread out around ω_{peak}. Figure 5.68 shows the elongation of the beam. The amplitudes are about 10^{-6} m for all cases. It should be noted that the responses look similar to the ones we saw in the damped-free vibration where water was still. That is, the damping effect in the Morison force must be dominant when non-zero initial conditions are applied. Figures 5.69 and 5.70 show potential and kinetic energies of the system when $\omega_{peak} = 10\ rad/s$. Figure 5.71

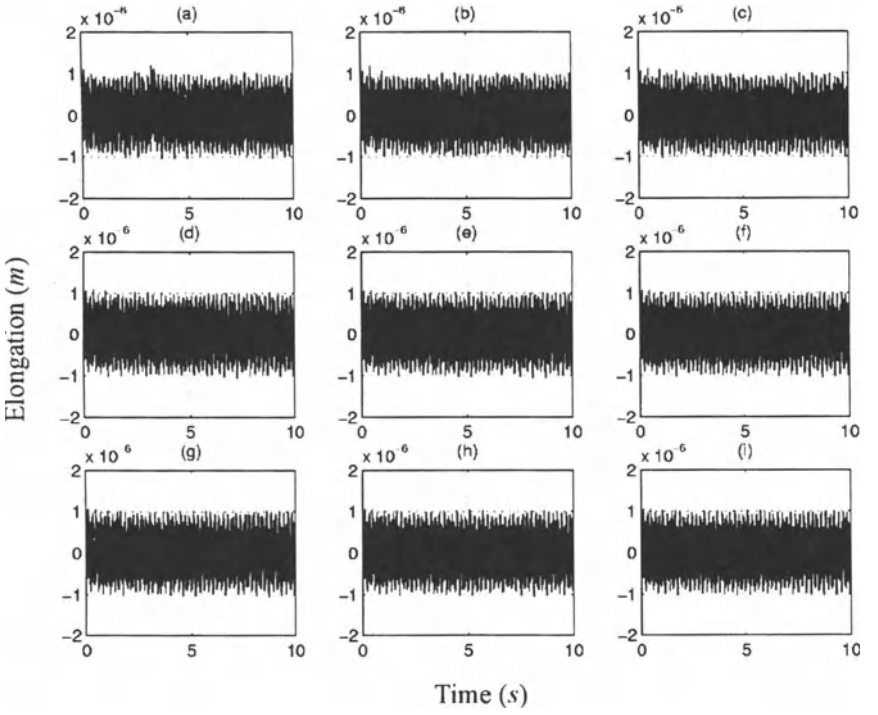

Figure 5.68. Elongation when Nonzero Initial Conditions are used. (a) $\omega_{peak} = 2$, (b) $\omega_{peak} = 4$, (c) $\omega_{peak} = 6$, (d) $\omega_{peak} = 8$, (e) $\omega_{peak} = 10$, (f) $\omega_{peak} = 12$, (g) $\omega_{peak} = 14$, (h) $\omega_{peak} = 16$, (i) $\omega_{peak} = 18$ rad/s

shows the total energy of the system. These plots show that the energies decay with time due to damping. After the transient response dies out, we expect to see similar random patterns as when zero initial conditions were used.

5. Chapter Summary

Analysis showed that the fundamental frequency for the free transverse motion ranged from 1.23 to 1.3 rad/s for the initial conditions used. The fundamental frequency for the transverse motion with damping ranged from 1.08 to 1.12 rad/s. The fundamental frequency of the axial motion was twice the fundamental frequency of the corresponding transverse motion. The axial motion at this frequency is geometrically induced from the transverse motion. It is possible to excite the axial motion without inducing the transverse motion, while the reverse is not possible. The fluid damping force modeled using the Morison equation

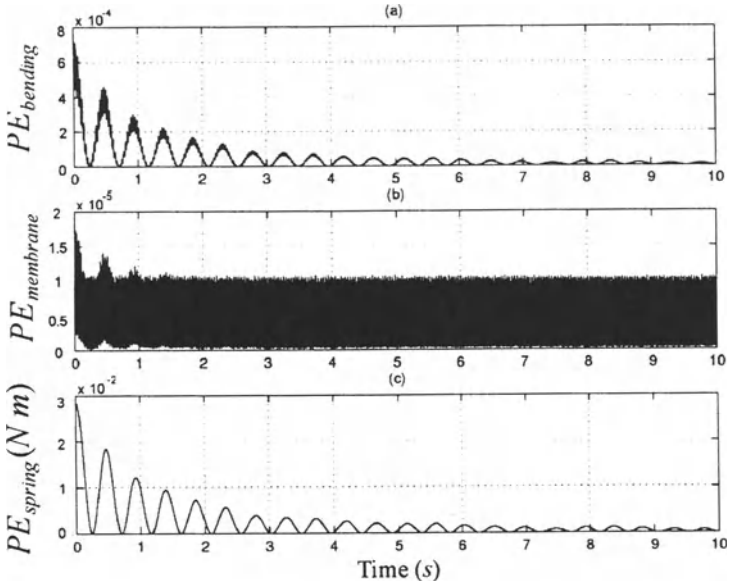

Figure 5.69. Potential Energies when Nonzero Initial Conditions and $\omega_{peak} = 10$ rad/s are used. (a) PE_{bending}, (b) PE_{membrane}, (c) PE_{spring}

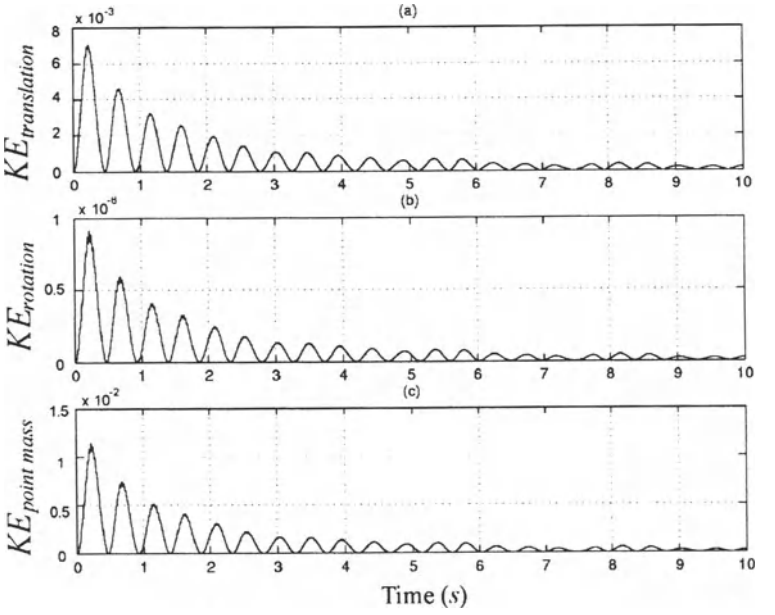

Figure 5.70. Kinetic Energies when Nonzero Initial Conditions and $\omega_{peak} = 10\ rad/s$ are used. (a) $KE_{\text{translation}}$, (b) KE_{rotation}, (c) $KE_{\text{point mass}}$

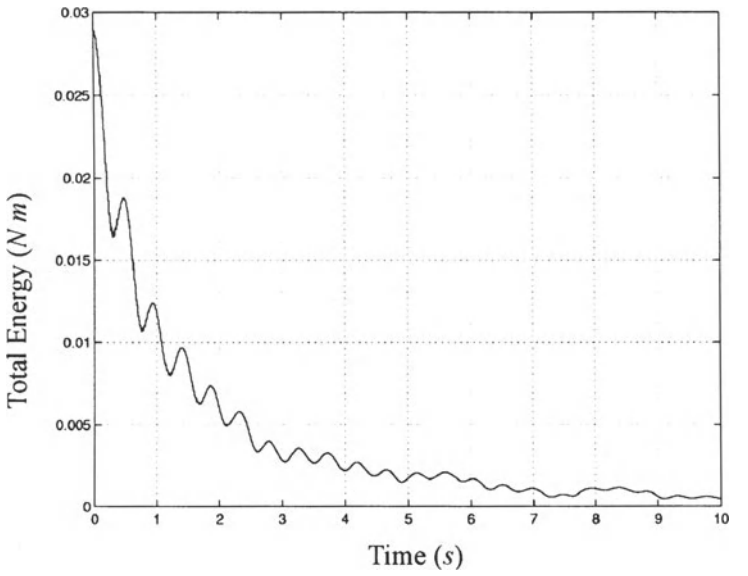

Figure 5.71. Total Energy when Nonzero Initial Conditions are used

affects the transverse motion directly, and then the transverse motion affects the axial motion through the system coupling. The influence on the axial motion by the Morison fluid forcing depends on the magnitude of the transverse motion.

When a harmonic force was applied, we observed a subharmonic resonance for the forcing frequency near twice the natural frequency. When only a current was present, the steady-state transverse offset from the vertical at the tip was proportional to the current velocity squared. The magnitude of the highest transverse peak in the transient response did not quite follow the same rule. Instead, the magnitudes were slightly less than what was predicted by the current-velocity-squared rule.

When a random fluid force was applied, a subharmonic resonance was not observed when zero initial conditions were used. When non-zero initial conditions were used, a subharmonic resonance of order 1/2 was observed for a wide range of significant wave heights. In all cases, the axial displacement had the same characteristics as in the free vibration case. The fundamental frequency was twice that of the transverse vibration, and the maximum of each peak of the dominant axial motion is the same. The amplitude of elongation for various peak frequencies was similar for each initial condition.

When zero initial conditions were used, we observed spurious peaks in elongations for $\omega_{peak} = 2$ and 4 rad/s. The total energy of the system varied randomly with time. When non-zero initial conditions were used, we saw uniform elongations for all cases. The responses look similar to those for the damped-free cases. The total energy of the system decayed with time. However, we expect that the random effects may become more pronounced after the transient response dies out.

Chapter 6

THREE-DIMENSIONAL VIBRATION

The purpose of this chapter is to explore the three-dimensional vibration of an offshore platform. First, the equations of motion of the three-dimensional model are derived for two cases: a rigid structure and an elastic structure. Second, the free responses of the rigid and the elastic models are compared. The free response obtained using the rigid model allows us to gain confidence in the formulation and the numerical results obtained using the elastic model. Finally, the forced responses due to deterministic loads are investigated. Two cases are studied in particular. The first case is when a harmonic (in time) load is applied in one direction, and the second case is when steady and harmonic loads are applied in mutually perpendicular directions. The second case can be thought of as the three-dimensional loading arising from a current that also induces vortex shedding. The responses due to these simple fluid force models will prepare us for the study of responses due to more complicated fluid loading models. This subject has also been treated by Han and Benaroya [26].

1. Nomenclature

Symbol	Description	Units
A_o	cross-sectional area of the reference beam	m^2
E	Young's Modulus	N/m^2
$\mathcal{E}_{ij}$	Green's strain	-
f_y	transversely distributed load in the y direction	N/m
f_z	transversely distributed load in the z direction	N/m
$f_{\theta,\,\text{linear}}$	natural frequency of the rigid beam	rad/s
$[I_o]$	mass moment of inertia matrix of the rigid beam about the base	$kg \cdot m^2$

S. M. Han et al., *Nonlinear and Stochastic Dynamics of Compliant Offshore Structures*

I_y	area moment of inertia of the beam cross-section about the Y axis	m^4
I_z	area moment of inertia of the beam cross-section about the Z axis	m^4
k	torsional spring constant	$N \cdot m/rad$
KE	kinetic energy	$N \cdot m$
L	length of the beam	m
$\mathcal{L}$	Lagrangian	$N \cdot m$
M	total mass of the beam	kg
M_p	point mass	kg
p	distributed axial load	N/m
r_i	inner radius of the cylinder	m
r_o	outer radius of the cylinder	m
$\mathbf{r_p}$	displacement vector of the point mass	m
t	time	s
u, v, w	midplane displacements in the x, y, z directions	m
u_1, u_2, u_3	displacement of the cross-section in the x, y, z directions	m
V_p	velocity of the point mass	m/s
W	work done by $p(X,t)$, $f_y(X,t)$, and $f_z(X,t)$	$N \cdot m$
X, Y, Z	original location of a beam element	m
ϕ	polar angle	rad
ν	Poisson's ratio	-
θ	spherical angle	rad
ρ	density of the beam	kg/m^3
$\tilde{\sigma}$	the second Piola-Kirchhoff stress	N/m^2
ω	angular frequency	rad/s

2. Mathematical Formulation

2.1 Rigid Model

In this study, the vertical member of an articulated tower or a leg of a tension leg platform is modeled as a smooth cylindrical beam, the support at the base as a torsional spring, and the structures above the water line as a point mass. It is assumed that the base of the torsional spring is free to rotate in any direction.

The equations of motion when the beam is considered rigid are derived in this section. From Figure 6.1, the system can be described with two angular degrees of freedom. The equations of motion for a similar system were obtained by Jain and Kirk [34], and Bar-Avi and Benaroya [8][10]. The equations of motion are re-derived here.

The kinetic energy of the system is given by

$$KE = \frac{1}{2}\{\omega\}^T [I_o] \{\omega\} + \frac{1}{2} M_p \{V_p\}^T \{V_p\}, \tag{6.1}$$

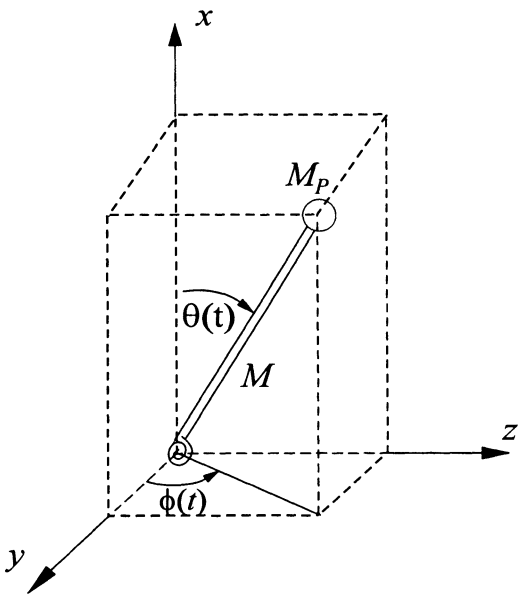

Figure 6.1. Rigid Beam Model

where $[I_o]$ is the mass moment of inertia matrix of the beam about the base, M_p is the point mass, and V_p is the velocity of the point mass. The first term is the kinetic energy of the beam, and the second term is the kinetic energy of the point mass.

We consider three frames of reference, xyz, $x'y'z'$, and $x_by_bz_b$, as shown in Figure 6.2. xyz is the inertial reference frame, $x'y'z'$ is obtained by rotating xyz by angle ϕ about the x axis. $x_by_bz_b$ is obtained by rotating $x'y'z'$ by θ about the z' axis. $x_by_bz_b$ is also called the body frame of reference since axis x_b coincides with the axis of the beam.

The beam experiences two angular velocities, $\dot{\phi}$ about the x axis and $\dot{\theta}$ about the z' axis. The angular velocity of the beam is then

$$\omega = \dot{\phi}\mathbf{i} + \dot{\theta}\mathbf{k}', \tag{6.2}$$

where $\mathbf{i}$ and $\mathbf{k}'$ are unit vectors in the x and z' directions, respectively. We choose to express the angular velocity in the body frame of reference. The transformations between the unit vectors $\mathbf{i}$ and $\mathbf{k}'$ and the unit vectors of the body frame of reference are

$$\begin{aligned} \mathbf{i} &= \cos\theta\mathbf{i}_b - \sin\theta\mathbf{j}_b \\ \mathbf{k}' &= \mathbf{k}_b. \end{aligned} \tag{6.3}$$

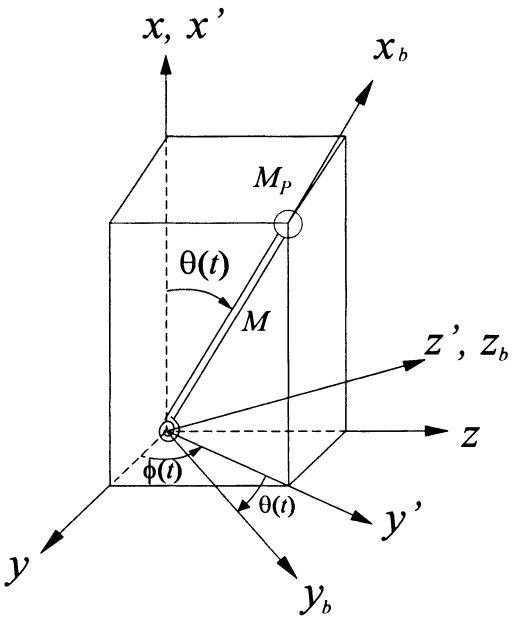

Figure 6.2. Reference and Body Frames

Therefore, the angular velocity in the body frame of reference is given by

$$\boldsymbol{\omega} = \dot{\phi}\cos\theta \mathbf{i}_b - \dot{\phi}\sin\theta \mathbf{j}_b + \dot{\theta}\mathbf{k}_b, \tag{6.4}$$

or in matrix form

$$\{\omega\}_{x_b y_b z_b} = \begin{bmatrix} \dot{\phi}\cos\theta \\ -\dot{\phi}\sin\theta \\ \dot{\theta} \end{bmatrix}. \tag{6.5}$$

The mass moment of inertia about the base expressed in the body frame of reference is given by

$$[I_o]_{x_b y_b z_b} = \begin{bmatrix} \frac{M}{2}\left(r_o^2 + r_i^2\right) & 0 & 0 \\ 0 & \frac{M}{4}\left(r_o^2 + r_i^2\right) + \frac{ML^2}{3} & 0 \\ 0 & 0 & \frac{M}{4}\left(r_o^2 + r_i^2\right) + \frac{ML^2}{3} \end{bmatrix}, \tag{6.6}$$

where r_o and r_i are outer and inner radii of the beam, M is the total mass of the beam, and L is the length of the beam.

The kinetic energy of the beam is given by

$$\begin{aligned} KE_{\text{beam}} &= \frac{1}{2}\{\omega\}^T [I_o]\{\omega\} \\ &= \frac{1}{4}M\left(r_o^2 + r_i^2\right)\dot{\phi}^2 \cos^2\theta \\ &+ \frac{1}{2}\left(\frac{1}{4}M\left(r_o^2 + r_i^2\right) + \frac{1}{3}ML^2\right)\dot{\phi}^2 \sin^2\theta \\ &+ \dot{\theta}^2\left(\frac{1}{4}M\left(r_o^2 + r_i^2\right) + \frac{1}{3}ML^2\right). \end{aligned} \tag{6.7}$$

The velocity of the point mass is expressed in the reference frame of reference. First, the displacement of the point mass is

$$\mathbf{r}_p = L\cos\theta\mathbf{i} + L\sin\theta\cos\phi\mathbf{j} + L\sin\theta\sin\phi\mathbf{k}. \tag{6.8}$$

The velocity is obtained by taking the derivative with respect to time. Since the displacement is expressed in the reference frame, the derivatives of the unit vectors are zero. The velocity of the point mass is then given by

$$\{V_p\}_{xyz} = L\begin{bmatrix} -\dot{\theta}\sin\theta \\ \dot{\theta}\cos\theta\cos\phi - \dot{\phi}\sin\theta\sin\phi \\ \dot{\theta}\cos\theta\sin\phi + \dot{\phi}\sin\theta\cos\phi \end{bmatrix}. \tag{6.9}$$

The kinetic energy of the point mass is then

$$\begin{aligned} KE_{\text{point mass}} &= \frac{1}{2}M_p\{V_p\}^T\{V_p\} \\ &= \frac{1}{2}M_pL^2\left(\dot{\theta}^2\sin^2\theta + \dot{\theta}^2\cos^2\theta\cos^2\phi\right. \\ &- 2\dot{\theta}\dot{\phi}\cos\theta\cos\phi\sin\theta\sin\phi + \dot{\phi}^2\sin^2\theta\sin^2\phi + \dot{\theta}^2\cos^2\theta\sin^2\phi \\ &\left.+ 2\dot{\theta}\dot{\phi}\cos\theta\sin\phi\sin\theta\cos\phi + \dot{\phi}^2\sin^2\theta\cos^2\phi\right) \\ &= \frac{1}{2}M_pL^2\left(\dot{\theta}^2 + \dot{\phi}^2\sin^2\theta\right). \end{aligned} \tag{6.10}$$

Combining Equations 6.7 and 6.10, the kinetic energy of the system is given by

$$KE = \frac{1}{2}J_2\left(\dot{\theta}^2 + \dot{\phi}^2\sin^2\theta\right) + \frac{1}{2}J_1\dot{\phi}^2\cos^2\theta, \tag{6.11}$$

where we let

$$J_1 = \frac{1}{2}M\left(r_o^2 + r_i^2\right),\ J_2 = \frac{1}{3}ML^2 + M_pL^2 + \frac{1}{4}M\left(r_o^2 + r_i^2\right). \tag{6.12}$$

The potential energy is stored in the torsional spring and is given by

$$PE = \frac{1}{2}k\theta^2. \tag{6.13}$$

This assumes that the structure can only bend, not twist. Therefore, the Lagrangian is given by

$$\mathcal{L} = \frac{1}{2}\left[\frac{1}{3}ML^2 + M_pL^2 + \frac{1}{4}M\left(r_o^2 + r_i^2\right)\right]\left(\dot{\theta}^2 + \dot{\phi}^2\sin^2\theta\right) + \frac{1}{4}M\left(r_o^2 + r_i^2\right)\dot{\phi}^2\cos^2\theta - \frac{1}{2}k\theta^2. \tag{6.14}$$

Lagrange's equations are given by

$$\frac{d}{dt}\left(\frac{\partial\mathcal{L}}{\partial\dot{q}_k}\right) - \frac{\partial\mathcal{L}}{\partial q_k} = Q_{knc},\ k = 1, 2, \tag{6.15}$$

where Q_{knc} is the generalized non-conservative force associated with q_k, and q_1 and q_2 are θ and ϕ, respectively. For an unforced system, the equations of motion are given by

$$J_2\ddot{\theta} - (J_2 - J_1)\dot{\phi}^2\sin\theta\cos\theta + k\theta = 0 \tag{6.16}$$

$$\frac{d}{dt}\left[\dot{\phi}\left(J_2\sin^2\theta + J_1\cos^2\theta\right)\right] = 0, \tag{6.17}$$

where J_1 and J_2 are given in Equation 6.12. Note that Equation 6.17 implies that $\phi(t)$ is a cyclic or ignorable coordinate[1]. Further, the generalized momentum associated with $\phi(t)$ is conserved as long as $Q_{\phi nc}$ is zero.

The generalized momentum associated with $\phi(t)$, p_ϕ, is given by

$$p_\phi = \dot{\phi}\left(J_2\sin^2\theta + J_1\cos^2\theta\right), \tag{6.18}$$

and its value can be obtained from the initial conditions. Then, $\dot{\phi}(t)$ at any time t can be written as

$$\dot{\phi}(t) = \frac{p_\phi}{J_2\sin^2\theta(t) + J_1\cos^2\theta(t)} = \frac{\dot{\phi}(0)\left(J_2\sin^2\theta(0) + J_1\cos^2\theta(0)\right)}{J_2\sin^2\theta(t) + J_1\cos^2\theta(t)}. \tag{6.19}$$

[1] $q(t)$ is an ignorable coordinate if $q(t)$ does not explicitly appear in the Lagrangian. Then,

$$\frac{d}{dt}\left(\frac{\partial\mathcal{L}}{\partial\dot{q}_k}\right) = Q_{knc}.$$

In words, the rate of change of the generalized momentum associated with q_k is equal to the generalized force Q_{knc} in this case.

The equation of motion in Equation 6.16 can be written in terms of θ only such that

$$J_2\ddot{\theta} - (J_2 - J_1)\frac{p_\phi^2 \sin\theta\cos\theta}{\left(J_2\sin^2\theta + J_1\cos^2\theta\right)^2} + k\theta = 0. \tag{6.20}$$

2.2 Elastic Model

The displacement field is obtained using Kirchhoff's hypothesis, and the corresponding strain and stress fields are obtained accordingly as done in Chapter 5. The potential and kinetic energies are then obtained to form the Lagrangian. The equations of motion are obtained using Hamilton's principle.

2.2.1 Displacements, Strains and Stress

Using Kirchhoff's hypothesis, the displacement field is given by

$$\begin{aligned} u_1 &= u(X,t) - Y\frac{\partial u_2(X,t)}{\partial X} - Z\frac{\partial u_3(X,t)}{\partial X} \\ u_2 &= v(X,t) \\ u_3 &= w(X,t), \end{aligned} \tag{6.21}$$

where u_1, u_2, and u_3 are displacements in the x, y, and z directions, respectively. u, v, and w are the midplane displacements of the cross-section in the x, y, and z directions, respectively. They are also the average displacements for a symmetric cross-section. It should be noted that the displacements are measured from the original configuration as shown in Figure 6.3. The coordinates X, Y, and Z mark the original location of a beam element. Note that the average displacements are functions of X and t only.

We assume that the strain is small, but the rotation can be moderate. Mathematically, we can write

$$\frac{\partial u_1}{\partial X} \sim \left(\frac{\partial u_2}{\partial X}\right)^2 \sim \left(\frac{\partial u_3}{\partial X}\right)^2 << 1. \tag{6.22}$$

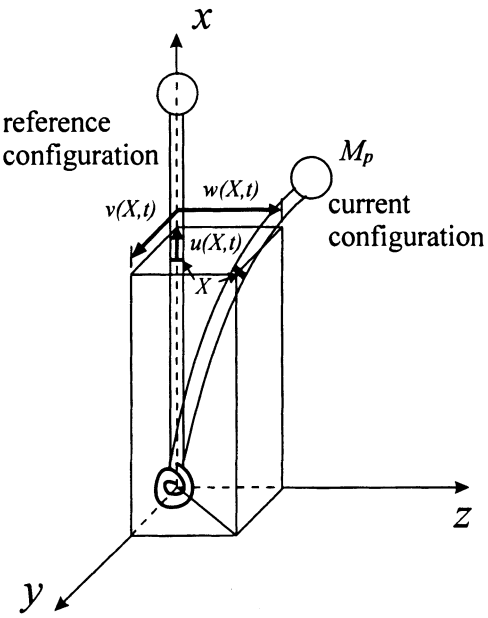

Figure 6.3. Three-dimensional Beam Model

The general form of Green's strains are given in Equation 5.6 or

$$\mathcal{E}_{11} = \frac{\partial u_1}{\partial X} + \frac{1}{2}\left[\left(\frac{\partial u_1}{\partial X}\right)^2 + \left(\frac{\partial u_2}{\partial X}\right)^2 + \left(\frac{\partial u_3}{\partial X}\right)^2\right]$$

$$\mathcal{E}_{22} = \frac{\partial u_2}{\partial Y} + \frac{1}{2}\left[\left(\frac{\partial u_1}{\partial Y}\right)^2 + \left(\frac{\partial u_2}{\partial Y}\right)^2 + \left(\frac{\partial u_3}{\partial Y}\right)^2\right]$$

$$\mathcal{E}_{33} = \frac{\partial u_3}{\partial Z} + \frac{1}{2}\left[\left(\frac{\partial u_1}{\partial Z}\right)^2 + \left(\frac{\partial u_2}{\partial Z}\right)^2 + \left(\frac{\partial u_3}{\partial Z}\right)^2\right]$$

$$\mathcal{E}_{12} = \frac{1}{2}\left[\frac{\partial u_2}{\partial X} + \frac{\partial u_1}{\partial Y} + \frac{\partial u_1}{\partial X}\frac{\partial u_1}{\partial Y} + \frac{\partial u_2}{\partial X}\frac{\partial u_2}{\partial Y} + \frac{\partial u_3}{\partial X}\frac{\partial u_3}{\partial Y}\right]$$

$$\mathcal{E}_{23} = \frac{1}{2}\left[\frac{\partial u_3}{\partial Y} + \frac{\partial u_2}{\partial Z} + \frac{\partial u_1}{\partial Y}\frac{\partial u_1}{\partial Z} + \frac{\partial u_2}{\partial Y}\frac{\partial u_2}{\partial Z} + \frac{\partial u_3}{\partial Y}\frac{\partial u_3}{\partial Z}\right]$$

$$\mathcal{E}_{13} = \frac{1}{2}\left[\frac{\partial u_3}{\partial X} + \frac{\partial u_1}{\partial Z} + \frac{\partial u_1}{\partial X}\frac{\partial u_1}{\partial Z} + \frac{\partial u_2}{\partial X}\frac{\partial u_2}{\partial Z} + \frac{\partial u_3}{\partial X}\frac{\partial u_3}{\partial Z}\right]. \qquad (6.23)$$

Substituting these strains into the assumed displacement field, Equation 6.21, Green's strains are then given by

$$\begin{aligned}\mathcal{E}_{11} &= \frac{\partial u_1}{\partial X} + \frac{1}{2}\left[\left(\frac{\partial u_2}{\partial X}\right)^2 + \left(\frac{\partial u_3}{\partial X}\right)^2\right] \\ &= u' - Yv'' + Zw'' + \frac{1}{2}v'^2 + \frac{1}{2}w'^2 \\ \mathcal{E}_{12} &= \mathcal{E}_{22} = \mathcal{E}_{33} = \mathcal{E}_{23} = \mathcal{E}_{13} = 0. \end{aligned} \tag{6.24}$$

The notation used are: $(') \equiv \partial/\partial X$ and $(\dot{}) \equiv \partial/\partial t$.

2.2.2 Potential and Kinetic Energies

The strain energy is given by

$$PE_{strain} = \frac{1}{2}\int_{V_o} \tilde{\sigma}_{ij}\mathcal{E}_{ij} dV_o, \tag{6.25}$$

where $\tilde{\sigma}$ is the second Piola-Kirchhoff stress. Since $\mathcal{E}_{11}$ is the only non-zero strain, the strain energy is simply

$$PE_{strain} = \frac{1}{2}\int_0^L \int_{A_o} \tilde{\sigma}_{11}\mathcal{E}_{11} dA_o dX. \tag{6.26}$$

The stress is related to strain by the constitutive relationship given by

$$\tilde{\sigma}_{ij} = \lambda \mathcal{E}_{kk}\delta_{ij} + 2G\mathcal{E}_{ij}. \tag{6.27}$$

The stress, $\tilde{\sigma}_{11}$, is then

$$\begin{aligned}\tilde{\sigma}_{11} &= (\lambda + 2G)\,\mathcal{E}_{11} \\ &= E\left(\frac{1-\nu}{(1+\nu)(1-2\nu)}\right)\mathcal{E}_{11}. \end{aligned} \tag{6.28}$$

If we neglect Poisson's effect, since the transverse energies are at least an order of magnitude smaller than the axial energies, $\nu = 0$, the strain energy is given by

$$PE_{strain} = \int_0^L \int_{A_o} \frac{E}{2}\mathcal{E}_{11}^2 dA_o dX. \tag{6.29}$$

The strain energy can be reduced to

$$\begin{aligned} PE_{strain} &= \frac{E}{2}\int_0^L \int_{A_o} \left(u' - Yv'' - Zw'' + \frac{1}{2}v'^2 + \frac{1}{2}w'^2\right)^2 dA_o dX \\ &= \frac{E}{2}\int_0^L \left\{ A_o\left(u' + \frac{1}{2}v'^2 + \frac{1}{2}w'^2\right)^2 \right. \\ &\left. + I_z v''^2 + I_y w''^2 \right\} dX, \end{aligned} \tag{6.30}$$

where I_z is the area moment of inertia about the Z axis, and I_y is the moment of inertia about the Y axis through the centroid. Note that the expressions are significantly reduced due to the symmetrical cross-section.

The potential energy stored in the base support spring is given by

$$PE_{spring} = \frac{1}{2}k\left(v'^2 + w'^2\right)\Big|_{0,t}. \tag{6.31}$$

This assumes that the structure can only bend, not twist.

The kinetic energy of the beam is simply

$$\begin{aligned} KE &= \frac{1}{2}\int_0^L \int_{A_o} \rho\left[\dot{u}_1^2 + \dot{u}_2^2 + \dot{u}_3^2\right] dA_o dX \\ &= \frac{1}{2}\int_0^L \int_{A_o} \rho A_o\left[\left(\dot{u} - Y\dot{v}' - Z\dot{w}'\right)^2 + \dot{v}^2 + \dot{w}^2\right] dA_o dX \\ &= \frac{\rho}{2}\int_0^L \left[A_o\left(\dot{u}^2 + \dot{v}^2 + \dot{w}^2\right) + I_z\dot{v}'^2 + I_y\dot{w}'^2\right] dX, \end{aligned} \tag{6.32}$$

and the kinetic energy of the point mass is

$$KE_{\text{point mass}} = \frac{1}{2}M_p\left(\dot{u}^2 + \dot{v}^2 + \dot{w}^2\right)\Big|_{L,t}. \tag{6.33}$$

2.2.3 Equations of Motion and Boundary Conditions Using Variational Principles

The Lagrangian is given by

$$\begin{aligned} L &= KE - PE \\ &= \frac{1}{2}\int_0^L \left\{\rho\left[A_o\left(\dot{u}^2 + \dot{v}^2 + \dot{w}^2\right) + I_z\dot{v}'^2 + I_y\dot{w}'^2\right]\right. \\ &\left. -E\left[A_o\left(u' + \frac{1}{2}v'^2 + \frac{1}{2}w'^2\right)^2 + I_z v''^2 + I_y w''^2\right]\right\} dX \\ &+ \frac{1}{2}M_p\left(\dot{u}^2 + \dot{v}^2 + \dot{w}^2\right)\Big|_{L,t} - \frac{1}{2}k\left(v'^2 + w'^2\right)\Big|_{0,t}. \end{aligned} \tag{6.34}$$

Let $p(X,t)$, $f_y(X,t)$ and $f_z(X,t)$ be distributed loads in the x, y and z directions, respectively. The virtual work done by these distributed loads is given by

$$\delta W = \int_0^L \left[p\delta u + f_y\delta v + f_z\delta w\right] dX. \tag{6.35}$$

The variation of the Lagrangian in Equation 6.34 integrated over time is given by

$$\begin{aligned}
\delta\int_{to}^{t_f} L dt = \int_{to}^{t_f}\int_0^L \Bigg\{ & \left[-\rho A_o \ddot{u} + EA_o\left(u' + \frac{1}{2}v'^2 + \frac{1}{2}w'^2\right)'\right]\delta u \\
& - \left[\rho A_o \ddot{v} - \left(\rho I_z \ddot{v}'\right)' - \left(EA_o\left(u' + \frac{1}{2}v'^2 + \frac{1}{2}w'^2\right)v'\right)'\right. \\
& \left. + \left(EI_z v''\right)''\right]\delta v \\
& - \left[\rho A_o \ddot{w} - \left(\rho I_y \ddot{w}'\right)' - \left(EA_o\left(u' + \frac{1}{2}v'^2 + \frac{1}{2}w'^2\right)w'\right)'\right. \\
& \left. + \left(EI_y w''\right)''\right]\delta w \Bigg\} dX dt \\
& - \int_{to}^{t_f}\Bigg\{ EA_o\left(u' + \frac{1}{2}v'^2 + \frac{1}{2}w'^2\right)\delta u\Big|_0^L \\
& + \left[\rho I_z \ddot{v}' + EA_o\left(u' + \frac{1}{2}v'^2 + \frac{1}{2}w'^2\right)v' - \left(EI_z v''\right)'\right]\delta v\Big|_0^L \\
& - M_p\left(\ddot{u}(L,t)\,\delta u(L,t) + \ddot{v}(L,t)\,\delta v(L,t) + \ddot{w}(L,t)\,\delta w(L,t)\right) \\
& + EI_z v''\delta v'\Big|_0^L + kv'\delta v'(0,t) \\
& + \left[\rho I_y \ddot{w}' + EA_o\left(u' + \frac{1}{2}v'^2 + \frac{1}{2}w'^2\right)w' - \left(EI_y w''\right)'\right]\delta w\Big|_0^L \\
& + EI_y w''\delta w'\Big|_0^L + kw'\delta w'(0,t)\Bigg\} dt. \qquad (6.36)
\end{aligned}$$

Using the extended Hamilton's principle,

$$\delta\int_{to}^{t_f}(L+W)\,dt = 0, \qquad (6.37)$$

the equations of motion are given by

$$\begin{aligned}
\rho A_o \ddot{u} - \left(EA_o\left(u' + \frac{1}{2}v'^2 + \frac{1}{2}w'^2\right)\right)' &= p \\
\rho A_o \ddot{v} - \left(EA_o\left(u' + \frac{1}{2}v'^2 + \frac{1}{2}w'^2\right)v'\right)' - \left(\rho I_z \ddot{v}'\right)' + \left(EI_z v''\right)'' &= f_y \\
\rho A_o \ddot{w} - \left(EA_o\left(u' + \frac{1}{2}v'^2 + \frac{1}{2}w'^2\right)w'\right)' - \left(\rho I_y \ddot{w}'\right)' + \left(EI_y w''\right)'' &= f_z, \qquad (6.38)
\end{aligned}$$

and the boundary conditions are given by

$$u(0,t) = 0 \tag{6.39}$$

$$v(0,t) = 0 \tag{6.40}$$

$$w(0,t) = 0 \tag{6.41}$$

$$\left(EI_z v'' - kv'\right)\Big|_{0,t} = 0 \tag{6.42}$$

$$\left(EI_y w'' - kw'\right)\Big|_{0,t} = 0 \tag{6.43}$$

$$EI_z v''\Big|_{L,t} = 0 \tag{6.44}$$

$$EI_y w''\Big|_{L,t} = 0 \tag{6.45}$$

$$\left[EA_o\left(u' + \frac{1}{2}v'^2 + \frac{1}{2}w'^2\right) + M_p\ddot{u}\right]\Big|_{L,t} = 0 \tag{6.46}$$

$$\left[\rho I_z\ddot{v}' + EA_o\left(u' + \frac{1}{2}v'^2 + \frac{1}{2}w'^2\right)v' - \left(EI_z v''\right)' + M_p\ddot{v}\right]\Big|_{L,t} = 0 \tag{6.47}$$

$$\left[\rho I_y\ddot{w}' + EA_o\left(u' + \frac{1}{2}v'^2 + \frac{1}{2}w'^2\right)w' - \left(EI_y w''\right)' + M_p\ddot{w}\right]\Big|_{L,t} = 0 \tag{6.48}$$

The boundary conditions in Equations 6.39 to 6.41 indicate that there are no displacements at $X = 0$. Equations 6.42 and 6.43 are the moment conditions at $X = 0$. The bending moments in the y and z directions are proportional to the deflection of the torsional spring in these directions. Equations 6.44 and 6.45 state that there are no bending moments at the free end ($X = L$). Equation 6.46 expresses the fact that the normal force in the x direction is balanced by the inertia force of the point mass in that direction. Equations 6.47 and 6.48 indicate that the transverse shear forces are balanced by the inertial forces of the point mass in the respective transverse directions.

Note that $u(X,t)$, $v(X,t)$, and $w(X,t)$ are nonlinearly coupled, and therefore, the equations need to be solved simultaneously using numerical methods.

2.3 Linearization of Equations of Motion

If we further assume that the rotation squared be small when compared to the linear strain,

$$(\partial v/\partial X)^2 << \partial u/\partial X << 1 \text{ and } (\partial w/\partial X)^2 << \partial u/\partial X << 1, \quad (6.49)$$

the Lagrangian in Equation 6.34 becomes

$$\begin{aligned} L &= KE - PE \\ &= \frac{1}{2}\int_0^L \left\{\rho\left[A_o\left(\dot{u}^2+\dot{v}^2+\dot{w}^2\right)+I_z\dot{v}'^2+I_y\dot{w}'^2\right]\right. \\ &\left.-E\left[A_o u'^2+I_z v''^2+I_y w''^2\right]\right\}dX \\ &+\frac{1}{2}M_p\left(\dot{u}^2+\dot{v}^2+\dot{w}^2\right)\Big|_{L,t}-\frac{1}{2}k\left(v'^2+w'^2\right)\Big|_{0,t}. \end{aligned} \quad (6.50)$$

Then the equations of motion and boundary conditions are given by

$$\begin{aligned} \rho A_o\ddot{u}-\left(EA_o u'\right)' &= p \\ \rho A_o\ddot{v}-\left(\rho I_z\ddot{v}'\right)'+\left(EI_z v''\right)'' &= f_y \\ \rho A_o\ddot{w}-\left(\rho I_y\ddot{w}'\right)'+\left(EI_y w''\right)'' &= f_z, \end{aligned} \quad (6.51)$$

with boundary conditions

$$\begin{aligned} u(0,t) &= 0 \\ v(0,t) &= 0 \\ w(0,t) &= 0 \\ \left(EI_z v''-kv'\right)\Big|_{0,t} &= 0 \\ \left(EI_y w''-kw'\right)\Big|_{0,t} &= 0 \\ EI_z v''\Big|_{L,t} &= 0 \\ EI_y w''\Big|_{L,t} &= 0 \\ \left[EA_o u'+M_p\ddot{u}\right]\Big|_{L,t} &= 0 \\ \left[\rho I_z\ddot{v}'-\left(EI_z v''\right)'+M_p\ddot{v}\right]\Big|_{L,t} &= 0 \\ \left[\rho I_y\ddot{w}'-\left(EI_y w''\right)'+M_p\ddot{w}\right]\Big|_{L,t} &= 0. \end{aligned} \quad (6.52)$$

The equations of motion are decoupled, and we recover the linear elastic equations of motion for each direction.

Table 6.1. Beam Properties

Material	Aluminum
Young's Modulus, E	73.0 GPa
Density, ρ	2770 kg/m^3
Point Mass, M_p	0.236 kg
Torsional Spring Constant, k	38.8 N/m
Length, L	1.27 m
Outer Radius, r_o	0.0127 m
Inner Radius r_i	0.0101 m

3. Results on the Free Vibration

The free responses of the nonlinear three-dimensional rigid and elastic models are considered next. The free response of the rigid beam will then be used to gain confidence in the results obtained by the elastic model. For numerical purposes, the properties of the structure given in Table 6.1 will be used.

The rigid and elastic models are solved numerically using MATLAB. The Runge-Kutta method of order 4 or 5 is used. Fourteen nodes are used for the elastic model[2].

We can consider two different types of vibration behavior: when the beam moves back and forth in an arbitrary plane and when the beam rotates in three dimensions as shown in Figure 6.4.

The first type of behavior, Figure 6.4(a), can be induced by non-zero $\theta(0)$ and zero $\dot{\phi}(0)$ for any $\dot{\theta}(0)$ and $\phi(0)$. When the motion is small enough that the small angle assumption is valid, the natural frequency of $\theta(t)$ is approximately given by

$$f_{\theta,\,\text{linear}} = \frac{1}{2\pi}\sqrt{\frac{k}{ML^2/3 + M_pL^2 + M\left(r_o^2 + r_i^2\right)/4}}. \tag{6.53}$$

In our case, $f_{\theta,\,\text{linear}} = 1.25\ Hz$. When the motion is in two dimensions, θ is allowed to turn negative once it passes through $\theta = 0\ rad$ as shown in Figure 6.5(a)

The second type, Figure 6.4(b), can be induced by non-zero $\theta(0)$ and $\dot{\phi}(0)$ for any $\dot{\theta}(0)$ and $\phi(0)$. For the rigid case, only a single coordinate, θ, is required to describe the motion for the planar model. This coordinate can take on positive or negative values as the beam swings back and

[2]See Appendix C for a detailed description of the finite difference method and sample MATLAB codes.

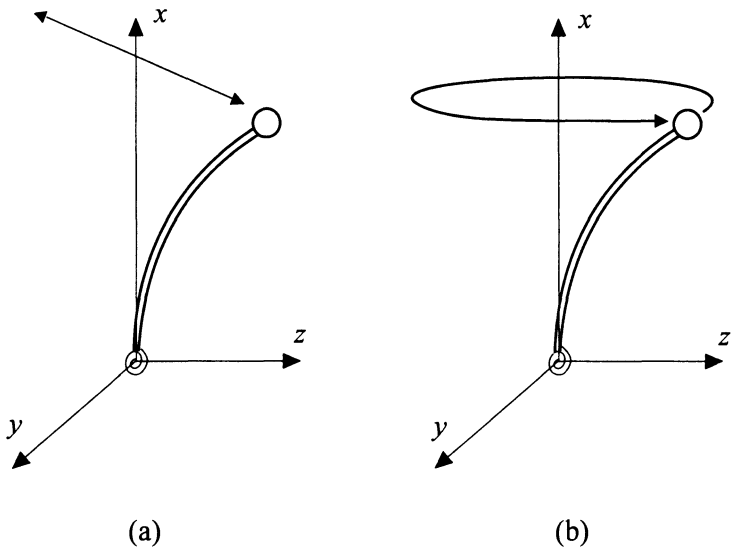

Figure 6.4. Two Types of Three-dimensional Motions in the Absence of External Loads. (a) Planar 3D Motion, (b) Full 3D Motion

forth through the vertical. On the other hand, for the three-dimensional model, two coordinates, θ and ϕ, are required to describe the motion. In this case, θ, which is defined as the angle between the vertical and the beam, is always positive. This can be observed in Figure 6.5(b).

Let us imagine two paths taken by the point mass viewed from the top as shown in Figure 6.6. Figure 6.6(a) describes a two-dimensional motion and Figure 6.6(b) a three-dimensional motion generated by slightly disturbing the two-dimensional motion such that points A and C in Figure 6.6(a) coincide with points A and C in Figure 6.6(b), respectively.

As the point mass in two dimensions goes through ABCBA, the point mass in three dimensions goes through ABCDA. $\theta(t)$ at point C in Figure 6.6(a) is negative, where $\theta(t)$ at point C in Figure 6.6(b) is positive but with the same magnitude. Therefore, the fundamental frequency of $\theta(t)$ calculated in three dimensions is equivalent to the fundamental frequency of $|\theta(t)|$ in two dimensions, 2.5 Hz. However, this is a highly idealized case, and we expect that the fundamental frequency of $\theta(t)$ in three dimensions will vary with initial conditions, but be near 2.5 Hz.

In summary, Figures 6.4(a), 6.5(a), and 6.6(a) depict planar motion and Figures 6.4(b), 6.5(b), and 6.6(b) depict fully three-dimensional motion.

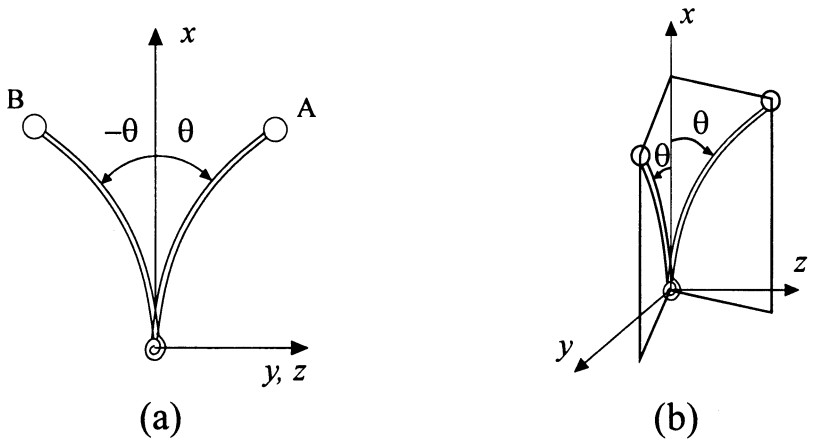

Figure 6.5. Sign Convensions for $\theta(t)$. (a) Planar Model, (b) Three-dimensional Model

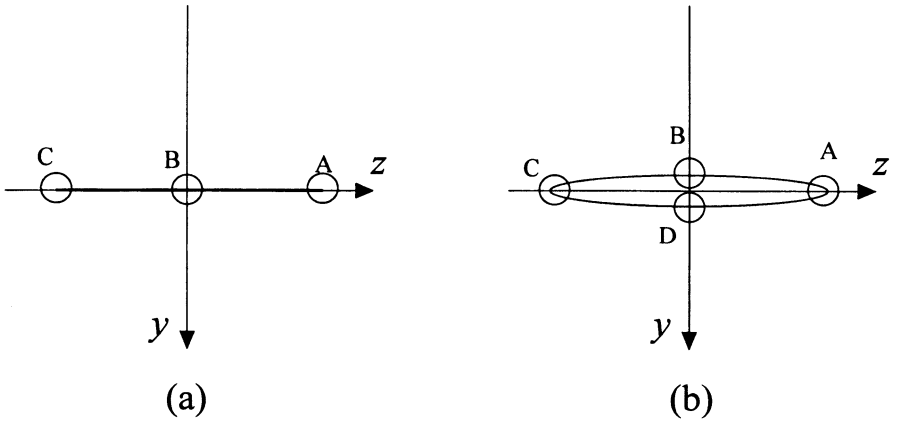

Figure 6.6. A Sample Path Taken by the Tip of the Beam

3.1 Three-Dimensional Rigid Model

Let us keep in mind that the nonlinear rigid model formulation does not make any assumptions regarding the angle of rotation. Therefore, the results are valid for any angle of deflection θ. Here, let us examine the case where the motion is in three dimensions by considering the following initial conditions:

$$\begin{aligned} &\theta(0) = 0.2\ rad,\ \dot{\theta}(0) = 0 \\ &\phi(0) = 0,\ \dot{\phi}(0) = 2\ rad/s. \end{aligned} \tag{6.54}$$

Figure 6.7 shows $\theta(t)$ and its power spectral density plot, and Figure 6.8 shows $\phi(t)$ and its power spectral density plot. The power spectral density plot reveals that the fundamental frequency is about 2.48 Hz for both $\theta(t)$ and $\phi(t)$. It should be noted that the natural frequency of 2.48 Hz for $\theta(t)$ is consistent with the frequency of 1.25 Hz obtained in Equation 6.53 when the motion is planar and linear.

Figure 6.9 shows the tip axial displacement, $u(L,t)$. The PSD plot shows that the fundamental frequency is at about $2.5Hz$. This frequency is close to the fundamental frequency of $\theta(t)$ since $\theta(t)$ completes one cycle while $u(L,t)$ also completes one cycle, as shown in Figure 6.6(b). Note that the transverse displacements, $v(L,t)$ and $w(L,t)$, complete half a cycle for each cycle of $\theta(t)$ and $u(L,t)$.

Figures 6.10 and 6.11 show the tip transverse displacements, $v(L)$ and $w(L)$, in the y and z directions and their power spectral density plots. The displacements are related to $\theta(t)$ and $\phi(t)$ as shown in Figure 6.1 and, therefore, by the following relationships,

$$\begin{aligned} u(X,t) &= X\cos\theta(t) - X \\ v(X,t) &= X\sin\theta(t)\cos\phi(t) \\ w(X,t) &= X\sin\theta(t)\sin\phi(t), \end{aligned} \tag{6.55}$$

where the units are all in *meters*.

The transverse displacements show a beating phenomenon with two visible frequencies at 1.25 Hz and 0.035 Hz. The envelope or the beat frequency 0.035 Hz is unexpected from the linear analysis. The consequence of this beating phenomenon on the overall response is clearer when the motion is viewed from top in Figure 6.12. The horizontal axis in Figure 6.12 is the transverse displacement in the y direction, and the vertical axis is the transverse displacement in the z direction. The free end follows an elliptical path that rotates in the counterclockwise direction at 0.035 Hz.

In order to understand why the path rotates, let us look at what happens for the first 0.81 seconds as shown in Figure 6.13. From the figure, we find that θ makes two cycles in about 0.81 s, and ϕ varies from 0 to 2π rad in about 0.76 s. After two cycles of θ have been completed, the free end does not return to its original location so that the path seems to be rotating counterclockwise, and the transverse displacements, $v(X,t)$ and $w(X,t)$, show beating. It is interesting to note that this beating phenomenon does not appear in $\theta(t)$, $\phi(t)$ nor in $u(L,t)$.

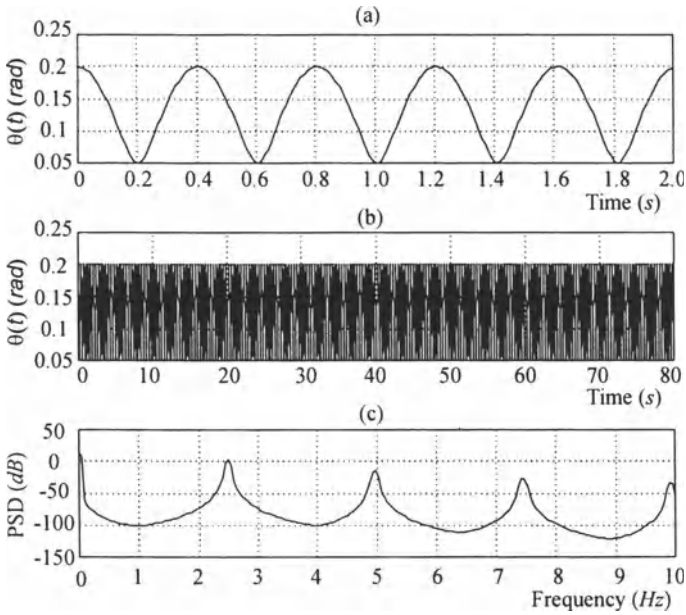

Figure 6.7. Angle of Deflection $\theta(t)$ and its PSD Plot

Let us further investigate the beating phenomenon that appears in the transverse displacements plot. Let us vary $\theta(0)$ and $\phi(0)$ one at a time. Figure 6.14 shows $v(L,t)$ and Figure 6.15 shows the top views for $\dot{\phi}(0) = 4\ rad/s$ and $\theta(0) = 0.07$, 0.09, 0.11, and 0.13 *rad*. They show that as the initial angle increases, the amplitude increases and the beat frequency decreases. Comparing 6.14(a) with 6.14(d), where the initial angle is almost doubled, the beat frequency decreased almost by a factor of three. While the beat frequency varied with the initial conditions, the 'high' frequency inside the envelope stayed at about 1.25 Hz.

Figures 6.16 and 6.17 show $v(L,t)$ and the top views for $\theta(0) = 0.05$ *rad* and $\dot{\phi}(0) = 4$, 6, 8, and 10 rad/s. It shows that as $\dot{\phi}(0)$ increases, the beat frequency decreases. Comparing 6.16(a) and (b), where the initial angle is increased by 50%, the frequency decreases by about a factor of two. Again, while the beat frequency varies with initial conditions, the 'high' frequency inside the envelope stayed at about 1.25 Hz.

In Figures 6.16(a,b) and 6.17(a,b), the major axis of the response path coincides with the x axis at the start of the response. When $\dot{\phi}(0) = 8$ rad/s, the length of the major and minor axes of the elliptical path are very close to each other so that the path is almost circular. Therefore, the path seems stationary. As $\dot{\phi}(0)$ is increased as shown in Figure

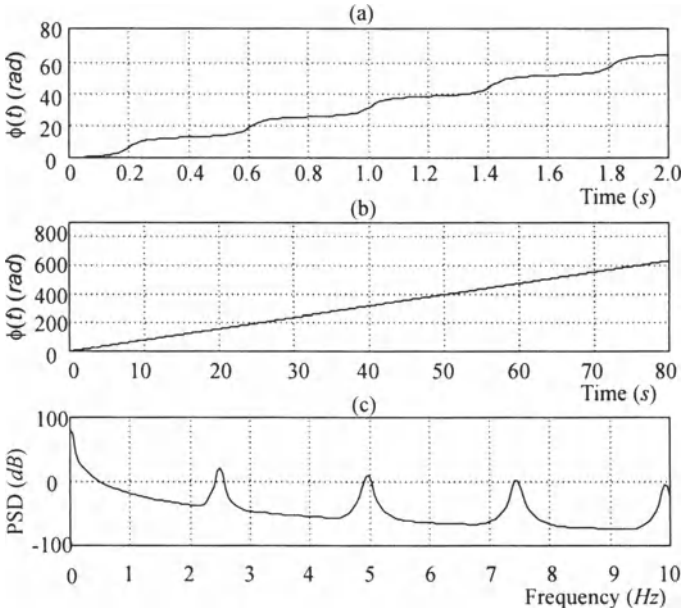

Figure 6.8. Angle of Rotation $\phi(t)$ and its PSD Plot

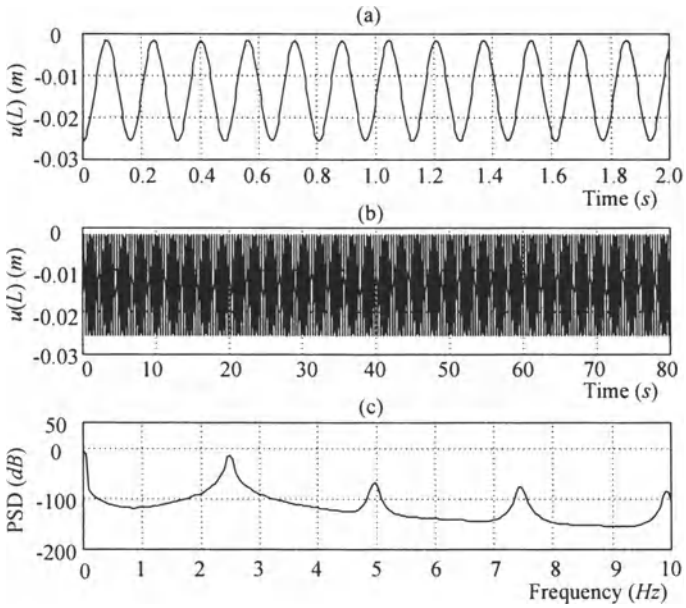

Figure 6.9. Axial Displacment $u(L,t)$ and its PSD Plot Predicted by the Rigid Model

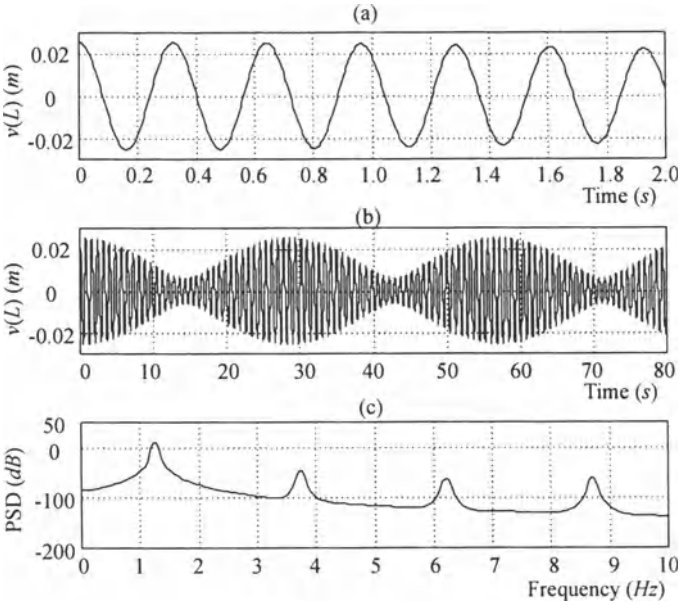

Figure 6.10. Transverse Displacment $v(L,t)$ and its PSD Plot Predicted by the Rigid Model

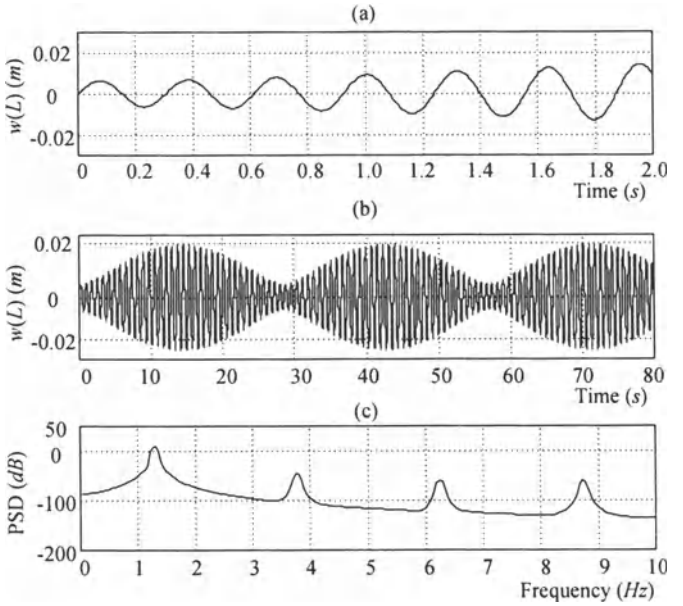

Figure 6.11. Transverse Displacment $w(L,t)$ and its PSD Plot Predicted by the Rigid Model

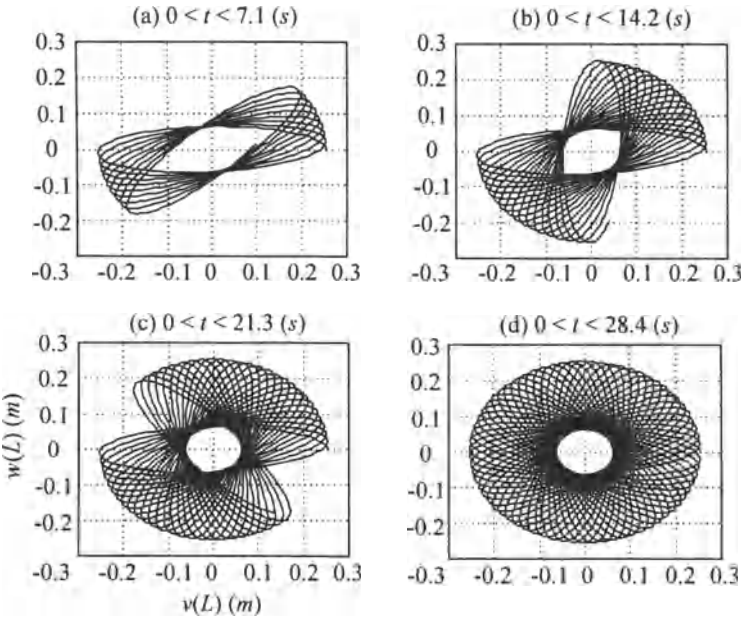

Figure 6.12. Free Response Viewed from the Top, Predicted by the Rigid Model

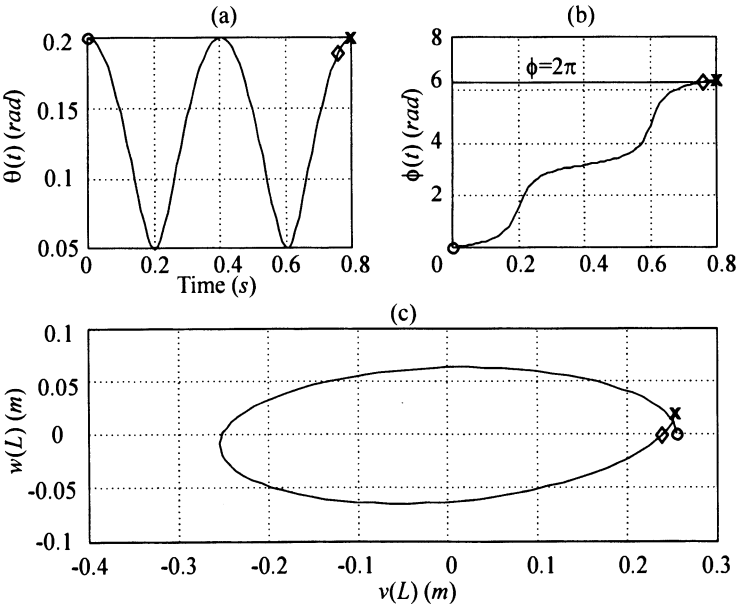

Figure 6.13. Free Response for 0.81 s (The symbol o is placed at the initial location, $\diamond$ at $\phi = 2\pi$, and $*$ after θ completes two cycles, respectively.)

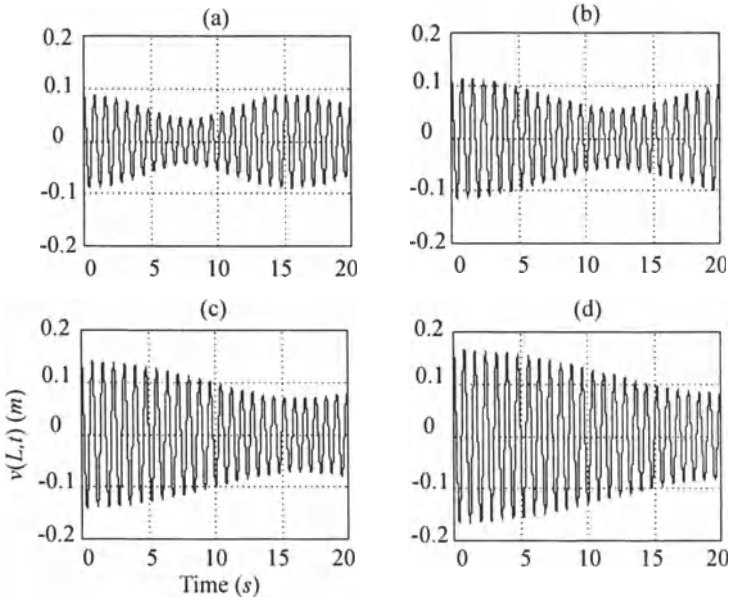

Figure 6.14. Transverse Displacements $v(L,t)$ when $\dot{\phi}(0) = 4\ rad/s$, (a) $\theta(0) = 0.07$, (b) $\theta(0) = 0.09$, (c) $\theta(0) = 0.11$, (d) $\theta(0) = 0.13\ rad$

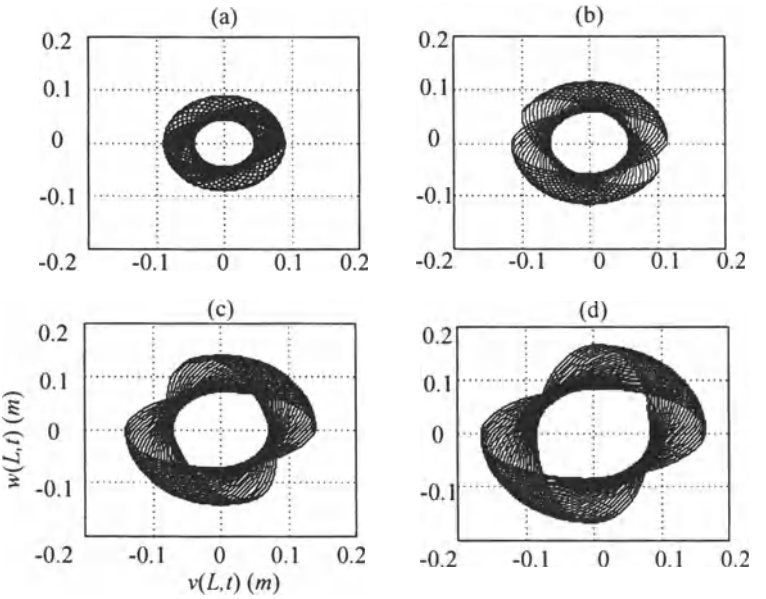

Figure 6.15. Free Response Viewed from the Top when $\dot{\phi}(0) = 4\ rad/s$. (a) $\theta(0) = 0.07$, (b) $\theta(0) = 0.09$, (c) $\theta(0) = 0.11$, (d) $\theta(0) = 0.13\ rad$

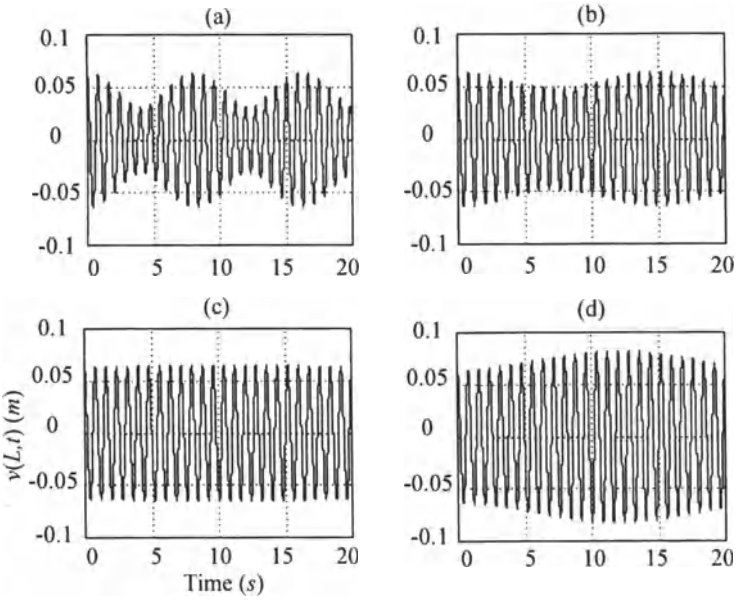

Figure 6.16. Transverse Displacements $v(L,t)$ when $\theta(0) = 0.05\ rad.$ (a) $\dot{\phi}(0) = 4$, (b) $\dot{\phi}(0) = 6$, (c) $\dot{\phi}(0) = 8$, (d) $\dot{\phi}(0) = 10\ rad/s$

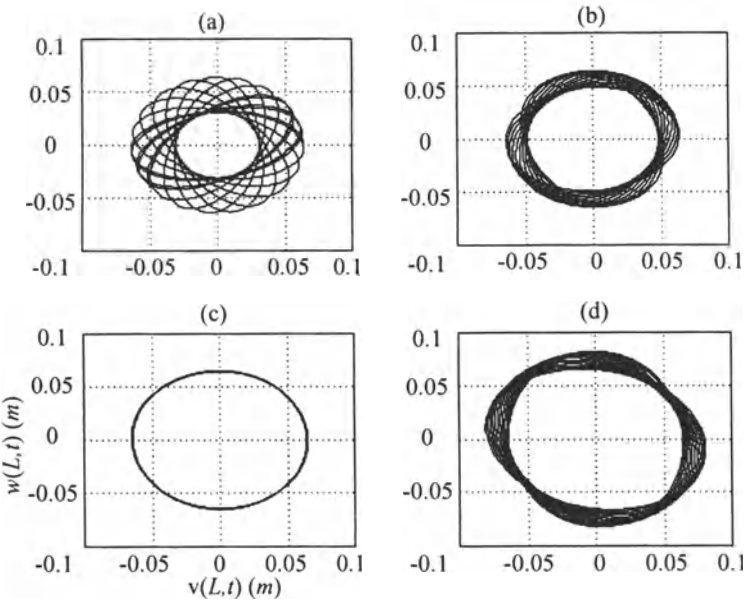

Figure 6.17. Free Response Viewed from the Top when $\theta(0) = 0.05\ rad.$ (a) $\dot{\phi}(0) = 4$, (b) $\dot{\phi}(0) = 6$, (c) $\dot{\phi}(0) = 8$, (d) $\dot{\phi}(0) = 10\ rad/s$

6.16(d), the path continues to rotate in the same direction. In this case, the minor axis coincides with the x axis in the beginning.

From the response plots, we can conclude the following:

1 The fundamental frequencies of $\theta(t)$ and $\phi(t)$ in three dimensions can be approximated by twice the fundamental frequency of $\theta(t)$ in two dimensions.

2 The rotation rate of the elliptical path varies with initial conditions, decreasing with increasing $\theta(0)$ and $\dot{\phi}(0)$.

3 The high frequency component of the response at 1.25 Hz in the transverse displacements was not affected or affected minimally by the initial conditions.

4 The rotation rate of the elliptical path is more sensitive to $\theta(0)$ than $\dot{\phi}(0)$. Therefore, for a small enough $\theta(0)$, the elliptical path may seem stationary (not rotating). A stationary path indicates that the motions in the xy and the xz plane are *independent* of each other. This is an important result since it implies that if the motion is small (small $\theta(0)$), the motion can be approximated by two planar models. This is also seen in the equations of motion for the elastic model in Equation 6.51. Three displacements are decoupled when the angle of rotation squared is small compared to the linear strain (Equation 6.49). For the rigid model, we can make the same analysis such that the transverse displacement of the tip can be obtained by solving the two decoupled equations of motion given by

$$\begin{aligned} J_2\ddot{\theta}_1 + k\theta_1 &= 0 \\ J_2\ddot{\theta}_2 + k\theta_2 &= 0, \end{aligned} \tag{6.56}$$

where J_2 is given in Equation 6.12, and $\theta_1(t)$ and $\theta_2(t)$ are the angles of deflection in xy and xz planes, as shown in Figure 6.18. The transverse displacements are then

$$\begin{aligned} v(L,t) &= L\cos\theta_1(t) \\ w(L,t) &= L\cos\theta_2(t). \end{aligned} \tag{6.57}$$

3.2 Three-Dimensional Elastic Model

Similar response plots are obtained using the nonlinear elastic model. The corresponding initial conditions are obtained using Equation 6.55

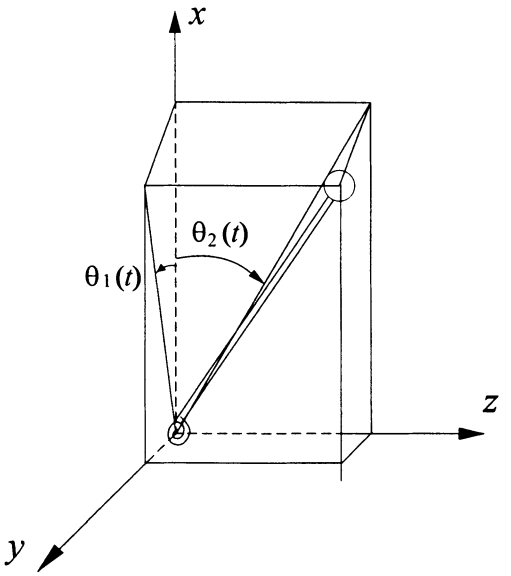

Figure 6.18. Superposition of Two Planar Models

and are given by

$$\begin{aligned}
u(X,0) &= X(\cos\theta(0) - 1) = -0.0199X \ m \\
v(X,0) &= X\sin\theta(0)\cos\phi(0) = 0.199X \ m \\
\dot{w}(X,0) &= X\dot{\theta}(0)\cos\theta(0)\sin\phi(0) + X\dot{\phi}(0)\sin\theta(0)\cos\phi(0) \\
&= 0.397X \ m/s \\
\dot{u}(X,0) &= 0 \\
\dot{v}(X,0) &= 0 \\
w(X,0) &= 0.
\end{aligned} \tag{6.58}$$

The nonlinear elastic model is valid for a wider range of angles of deflection from the x axis ($\partial v/\partial X$ and $\partial w/\partial X$) than the linear elastic model. Recall that the linear elastic model requires that the rotation squared be small when compared to the linear strain,

$$(\partial v/\partial X)^2 << \partial u/\partial X << 1 \text{ and } (\partial w/\partial X)^2 << \partial u/\partial X << 1, \tag{6.59}$$

so that the equations of motion are decoupled.

In the nonlinear elastic model, the rotation is assumed to be moderate such that

$$(\partial v/\partial X)^2 \sim \partial u/\partial X << 1 \text{ and } (\partial w/\partial X)^2 \sim \partial u/\partial X << 1. \tag{6.60}$$

Table 6.2. Free Vibration Results

	Fundamental Frequency of $u(L,t)$	Fundamental Frequencies of $v(L,t)$ and $w(L,t)$	Beat Frequency of $v(L,t)$ and $w(L,t)$
Rigid	2.50 Hz	1.25 Hz	0.0350 Hz
Elastic	2.44 Hz	1.22 Hz	0.0126 Hz

The initial conditions in Equation 6.58 are chosen such that the rotation from the x axis squared, $(\partial v/\partial X)^2$, is comparable to the linear strain, $\partial u/\partial X$. Therefore, the linear model is not valid for this set of initial conditions.

Figures 6.21 and 6.22 show the tip transverse displacements, $v(L,t)$ and $w(L,t)$, in the y and z directions and their power spectral density plots. The average natural frequency is found in the PSD plots to be 1.22 Hz, which is lower than that of the rigid beam. This is consistent with our intuition since the rigid beam is 'stiffer' than the elastic beam, and the stiffer beam vibrates at a higher frequency. When we look at the transverse displacement plots in Figures 6.21(b) and 6.22(b), the beat frequency seems to be at 0.0126 Hz (period of 79.5 s), which is lower than that of the rigid beam. The top views in Figure 6.23 show rotating ellipses at 0.0126 Hz. For an easy comparison, the free vibration results are summarized in Table 6.2. Note that the fundamental and beat frequencies for two transverse displacements are the same.

Figure 6.24 shows the axial displacement $u(L,t)$ and its PSD. The PSD plot shows a dominant frequency at 2.44 Hz, which is twice the fundamental frequency of the transverse motion. This was seen in the rigid case and also in Chapter 5.

The numerical results obtained using the three-dimensional elastic model appear reasonable when compared with those of the rigid model.

4. Sample Results for the Forced Response of the Elastic Model

In this section, we consider two loading situations. The first case is when a harmonically varying (in time) transverse load is applied in the y direction, and the second is when a non-harmonic load in applied in the y direction along with a harmonic load in the z direction. In all cases, the transverse loads are exponential in X. The distributed transverse loads in Figure 6.19 are given in Table 6.3.

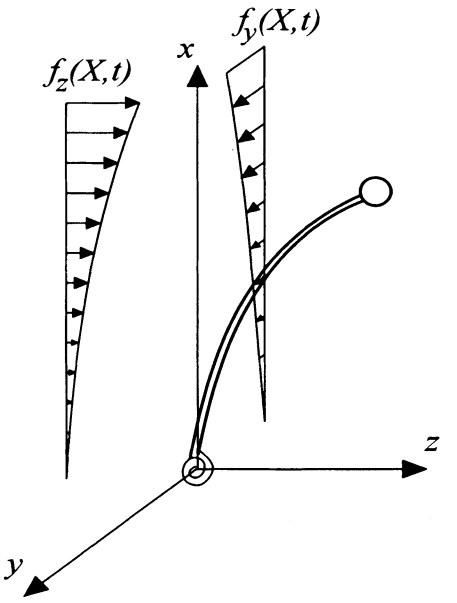

Figure 6.19. Distributed Transverse Loads

Table 6.3. Transverse Loads

Case I	$f_y(X,t) = 2(\exp(X) - 1)\cos\omega_f t$	$f_z(X,t) = 0$
Case II	$f_y(X,t) = 2(\exp(X) - 1)\cos\omega_f t$	$f_z(X,t) = 2(\exp(X) - 1)$

4.1 Case I: Harmonic Loading in the y Direction

In this section, we investigate the forced response by varying the forcing frequencies. The initial velocities are set to zero and the initial displacements are given by

$$u(X,0) = -0.002503X \ m, \ v(X,0) = w(X,0) = 0.05X \ m. \quad (6.61)$$

This is when the beam is rotated about 0.05 *rad* from the vertical without any elastic deformation and placed in the first octant. Note that when the initial transverse displacements are given, the initial axial displacement can be found from the equations of motion and boundary conditions. In this case, the axial displacement is negative since all the beam elements need to move in the negative x direction to achieve given initial configuration shown in Figure 6.20.

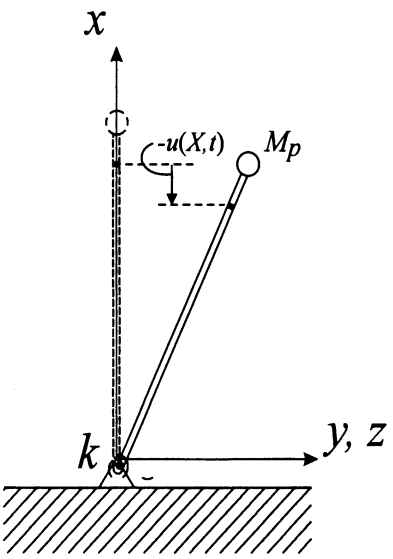

Figure 6.20. Initial Configuration

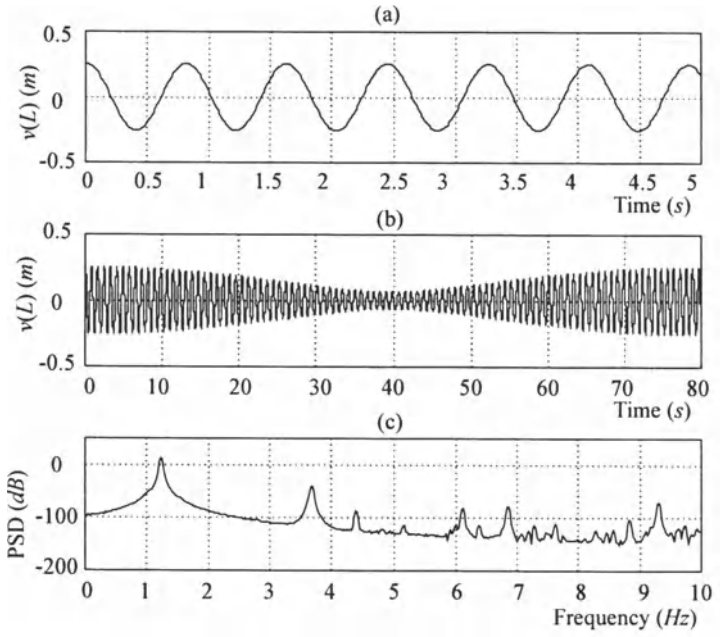

Figure 6.21. Transverse Displacement $v(L,t)$ Predicted by the Elastic Model

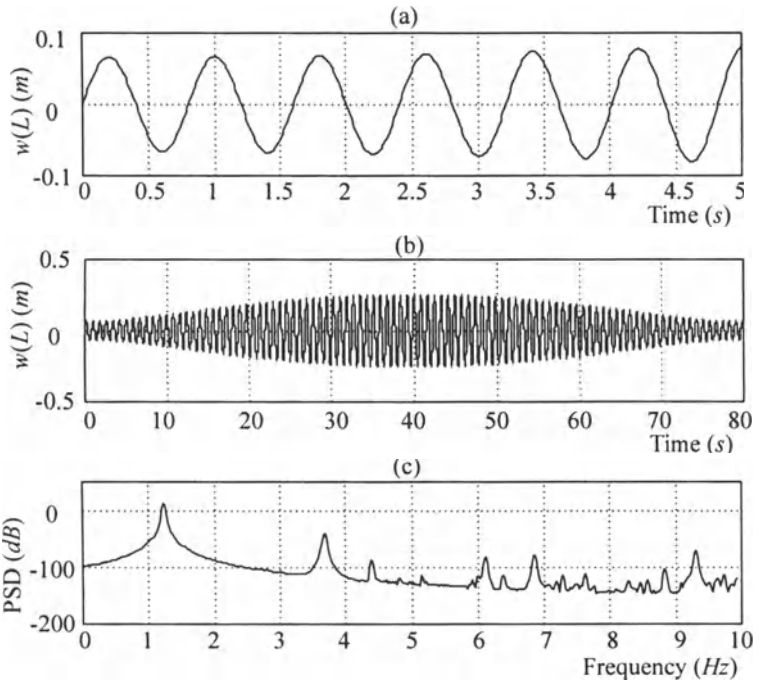

Figure 6.22. Transverse Displacement $w(L,t)$ Predicted by the Elastic Model

Figures 6.25 and 6.26 show the transverse displacements $v(L,t)$ and their PSD plots when the forcing frequencies are varied from π to 9π at π rad/s increments. The vertical lines in the PSD plots mark the forcing frequencies. When the forcing frequency is below the fundamental frequency, as shown in Figure 6.25(a), $v(L,t)$ responds dominantly at the forcing frequency. When the forcing frequency is increased to the vicinity of the fundamental frequency, beating occurs as shown in Figures 6.25(b,c) and 6.26(b,c). When this happens, the amplitude of vibration also increases. When the forcing frequency is increased even more, in Figures 6.25(d-f) and 6.26(d-f), we see a subharmonic resonance of order 1/2, where the system responds at the natural frequency when the forcing frequency is close to twice the natural frequency, and in Figures 6.25(g-i) and 6.26(g-i) we see subharmonic resonances of order 1/3. It should be noted that when $v(L,t)$ enters subharmonic resonance, the response looks similar to the free response. That is, $v(L,t)$ vibrates mostly at the fundamental frequency.

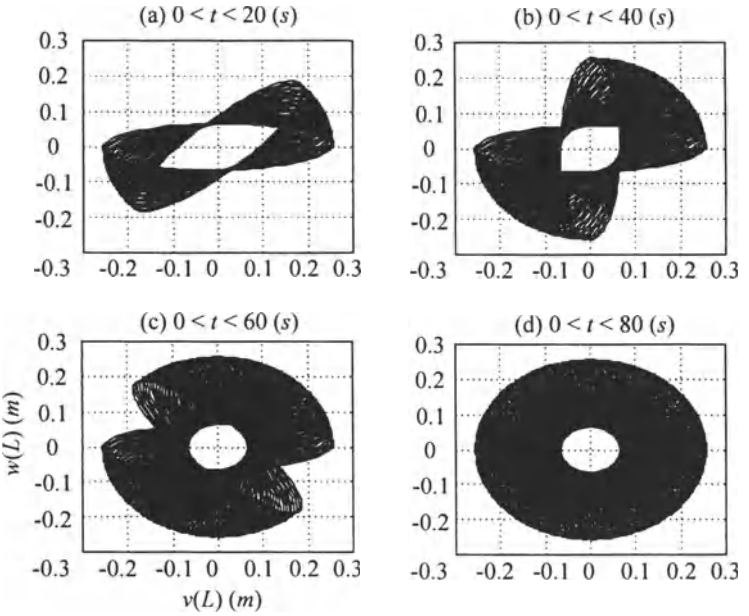

Figure 6.23. Free Response Viewed from the Top, Predicted by the Elastic Model

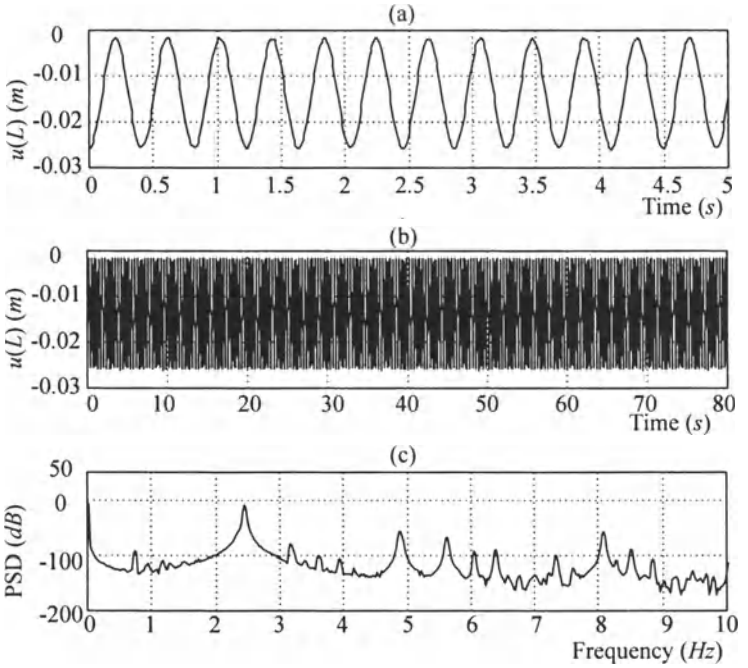

Figure 6.24. Axial Displacement $u(L,t)$ and its PSD Plot

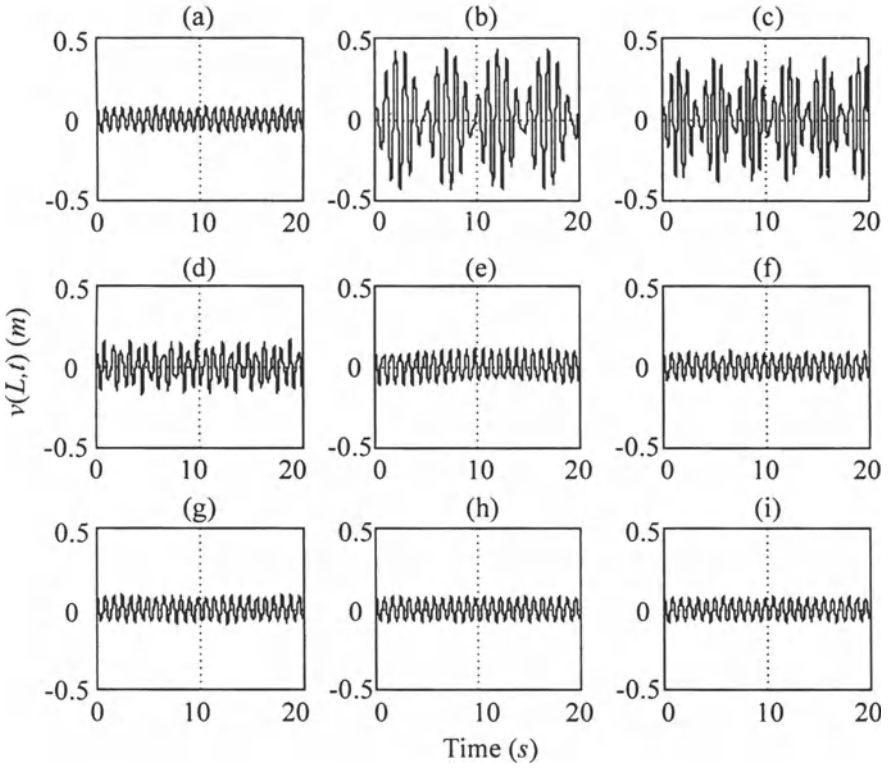

Figure 6.25. Transverse Displacement $v(L,t)$ when $f_y = 2(\exp(X) - 1)\cos\omega_f t$. (a) $\omega_f = \pi$, (b) $\omega_f = 2\pi$, (c) $\omega_f = 3\pi$, (d) $\omega_f = 4\pi$, (e) $\omega_f = 5\pi$, (f) $\omega_f = 6\pi$, (g) $\omega_f = 7\pi$, (h) $\omega_f = 8\pi$, (i) $\omega_f = 9\pi$ *rad/s*

Figures 6.27 and 6.28 show the transverse displacements $w(L,t)$ and their PSD plots. The transverse displacement in the z direction is minimally affected except for $\omega_f = 2\pi$ and 3π, at which $v(L,t)$ shows beating. However, the amplitude of $w(L,t)$ stays almost constant throughout. In all nine cases, $w(L,t)$ responds at or near the fundamental frequency.

Figure 6.29 shows the view from the top for the first 5 seconds of motion. Due to the subharmonic response in $v(L,t)$, which resembles the free response and virtually unaffected $w(L,t)$, Figures 6.29(d-i) look similar to the top views of the free response, the response that we would obtain when the beam is released from the initial position given by Equation 6.61.

Figure 6.30 shows the phase plots, $v(L,t)$ versus $\dot{v}(L,t)$, and Figure 6.31 shows the Poincaré maps strobed at the forcing frequency. If the

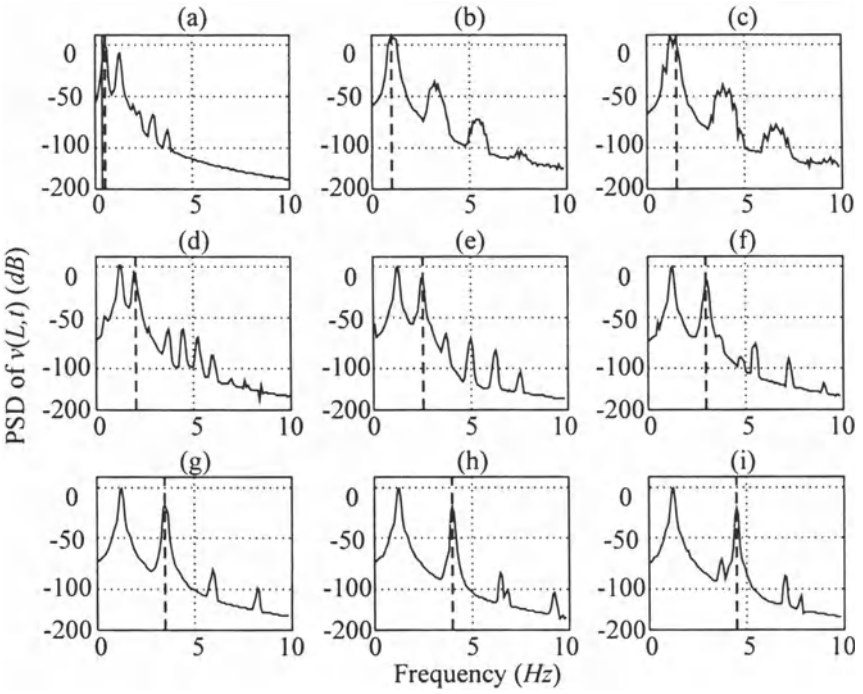

Figure 6.26. PSD Plots for $v(L,t)$ when $f_y = 2(\exp(X) - 1)\cos\omega_f t$. (a) $\omega_f = \pi$, (b) $\omega_f = 2\pi$, (c) $\omega_f = 3\pi$, (d) $\omega_f = 4\pi$, (e) $\omega_f = 5\pi$, (f) $\omega_f = 6\pi$, (g) $\omega_f = 7\pi$, (h) $\omega_f = 8\pi$, (i) $\omega_f = 9\pi$ rad/s

ratio of the forcing frequency to the natural frequency of $v(L,t)$ is a rational number, the Poincaré map will show a discrete number of points. However, in our case, the ratio of the forcing frequency to the natural frequency of $v(L,t)$ may be an irrational number. In that case, $v(L,t)$ does not return exactly to its initial value, and the strobe points of the Poincaré map will never repeat. On the Poincaré map, the strobe point will eventually fill in a circle, and the motion is called quasiperiodic [7]. The Poincaré maps in Figure 6.31 show circular patterns without repeating points, which indicates that our system is quasiperiodic.

4.2 Case II: Harmonic and Non-harmonic Loadings in the Perpendicular Directions

Figures 6.32 and 6.33 show the response plots when the forcing frequency is π rad/s, and Figures 6.35 and 6.36 when the forcing frequency is 6π rad/s. The initial conditions given in Equation 6.61 are used in all cases.

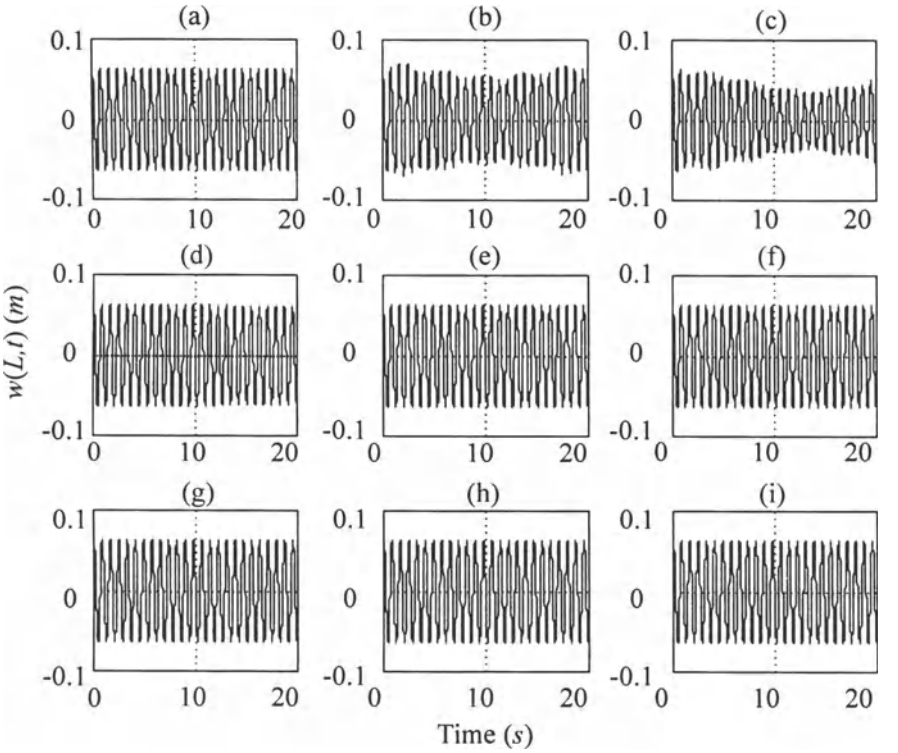

Figure 6.27. Transverse Displacement $w(L,t)$ when $f_y = 2(\exp(X) - 1)\cos\omega_f t$. (a) $\omega_f = \pi$, (b) $\omega_f = 2\pi$, (c) $\omega_f = 3\pi$, (d) $\omega_f = 4\pi$, (e) $\omega_f = 5\pi$, (f) $\omega_f = 6\pi$, (g) $\omega_f = 7\pi$, (h) $\omega_f = 8\pi$, (i) $\omega_f = 9\pi$ rad/s

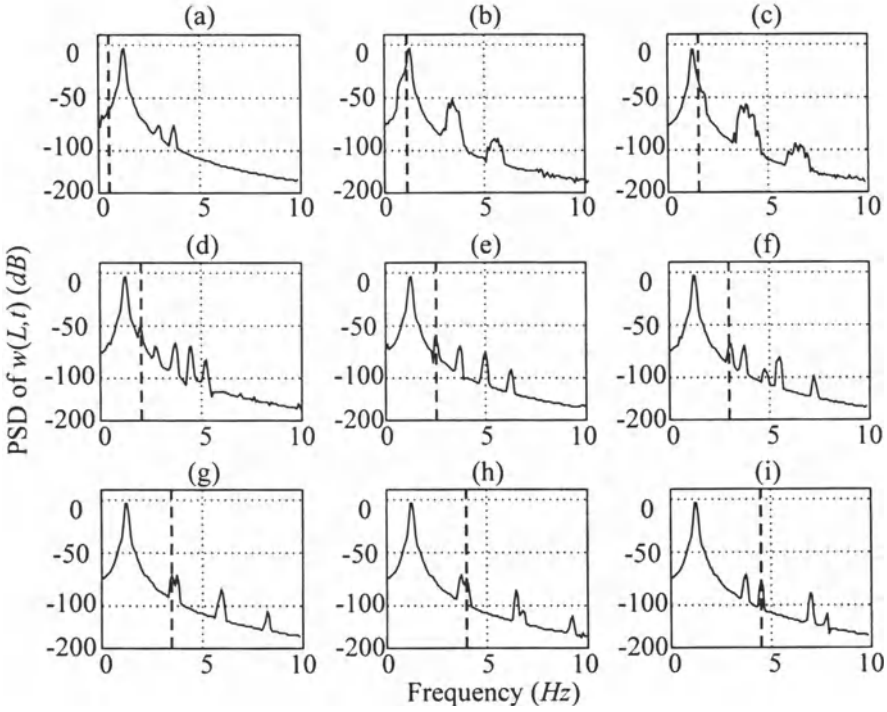

Figure 6.28. PSD Plots for $w(L,t)$ when $f_y = 2(\exp(X) - 1)\cos\omega_f t$. (a) $\omega_f = \pi$, (b) $\omega_f = 2\pi$, (c) $\omega_f = 3\pi$, (d) $\omega_f = 4\pi$, (e) $\omega_f = 5\pi$, (f) $\omega_f = 6\pi$, (g) $\omega_f = 7\pi$, (h) $\omega_f = 8\pi$, (i) $\omega_f = 9\pi$ rad/s

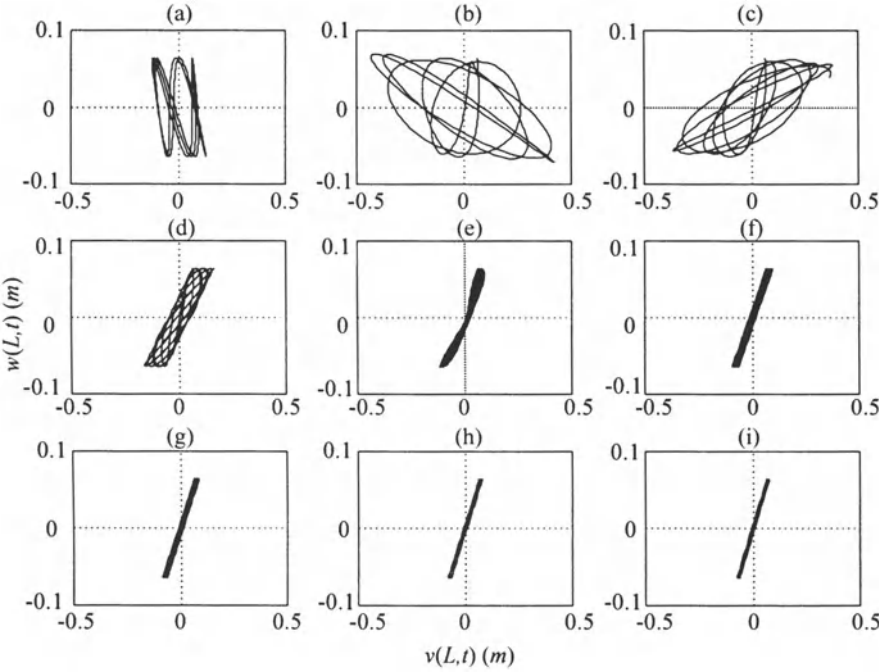

Figure 6.29. Forced Response Viewed from the Top when $f_y = 2(\exp(X) - 1)\cos\omega_f t$. (a) $\omega_f = \pi$, (b) $\omega_f = 2\pi$, (c) $\omega_f = 3\pi$, (d) $\omega_f = 4\pi$, (e) $\omega_f = 5\pi$, (f) $\omega_f = 6\pi$, (g) $\omega_f = 7\pi$, (h) $\omega_f = 8\pi$, (i) $\omega_f = 9\pi$ rad/s

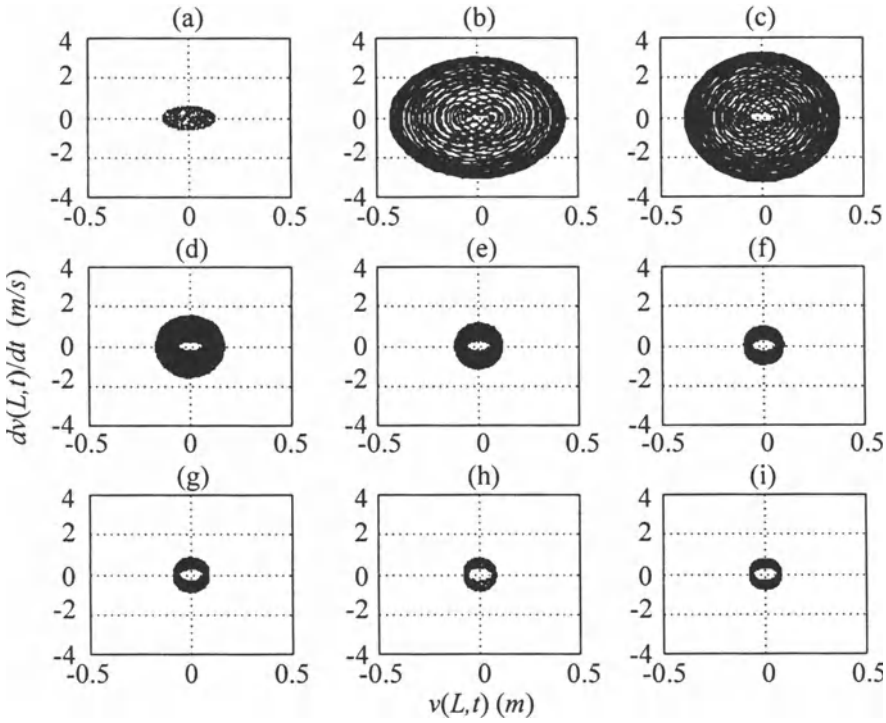

Figure 6.30. Phase Plots for $v(L,t)$. (a) $\omega_f = \pi$, (b) $\omega_f = 2\pi$, (c) $\omega_f = 3\pi$, (d) $\omega_f = 4\pi$, (e) $\omega_f = 5\pi$, (f) $\omega_f = 6\pi$, (g) $\omega_f = 7\pi$, (h) $\omega_f = 8\pi$, (i) $\omega_f = 9\pi$ rad/s

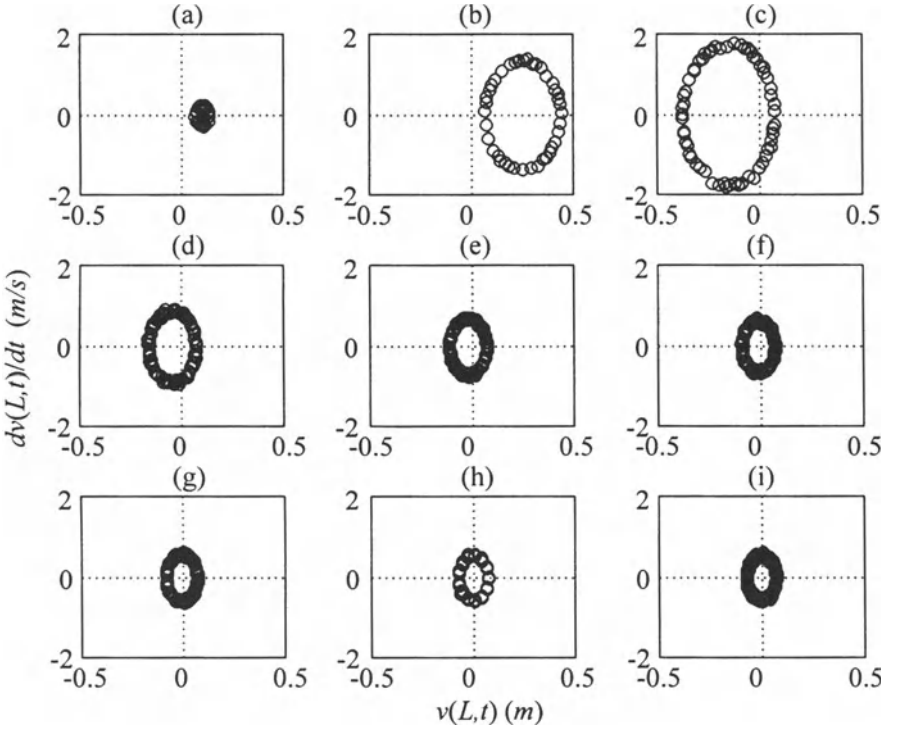

Figure 6.31. Poincaré Maps for $v(L,t)$ that Correspond to Figure 6.30. (a) $\omega_f = \pi$, (b) $\omega_f = 2\pi$, (c) $\omega_f = 3\pi$, (d) $\omega_f = 4\pi$, (e) $\omega_f = 5\pi$, (f) $\omega_f = 6\pi$, (g) $\omega_f = 7\pi$, (h) $\omega_f = 8\pi$, (i) $\omega_f = 9\pi$ rad/s

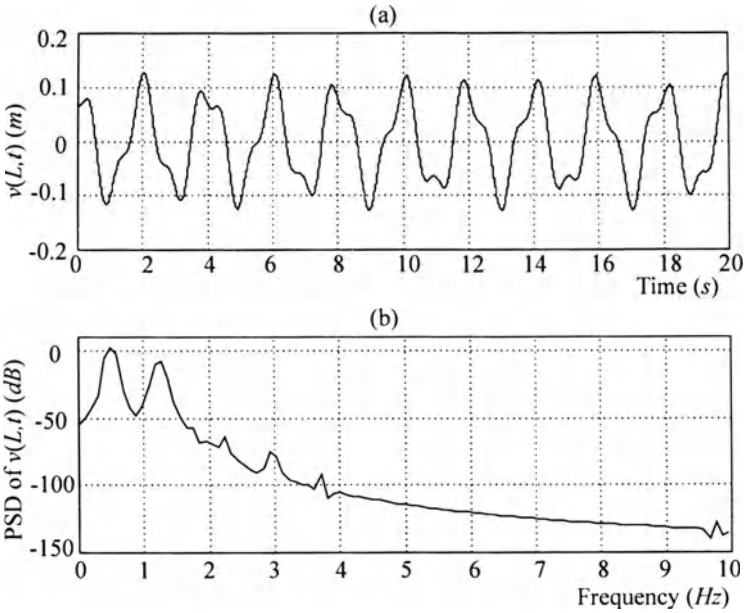

Figure 6.32. Transverse Displacement $v(L,t)$ and its PSD Plot when $f_y = 2(\exp(X) - 1)\cos \pi t$ and $f_z = 2(\exp(X) - 1)$

The transverse displacement in the y direction, $v(L,t)$, is almost unchanged from Figure 6.25(a), where the non-harmonic force in the z direction was not used. In fact, if they were plotted on the same figure, they would overlap. On the other hand, the transverse displacement in the z direction, $w(L,t)$, is shifted to the positive direction from Figure 6.27(a). However, the frequency of oscillation remains the same. Therefore, for this particular case, we can see that transverse motions in each direction are minimally affected by the forces in the perpendicular directions. That is, the force in the z direction has a minimal affect on the displacement in the y direction, and vice versa. The same can be said for the second case when the forcing frequency is 6π rad/s.

5. Chapter Summary

The equations of motion of a beam supported by a torsional spring at the base and with a point mass at the top were obtained, first by assuming the beam to be rigid and second by assuming it to be elastic. For the rigid model, a two degree of freedom model, with the two angular degrees of spherical coordinates, was employed. When the beam was modeled as elastic, the equations of motion were in terms of displace-

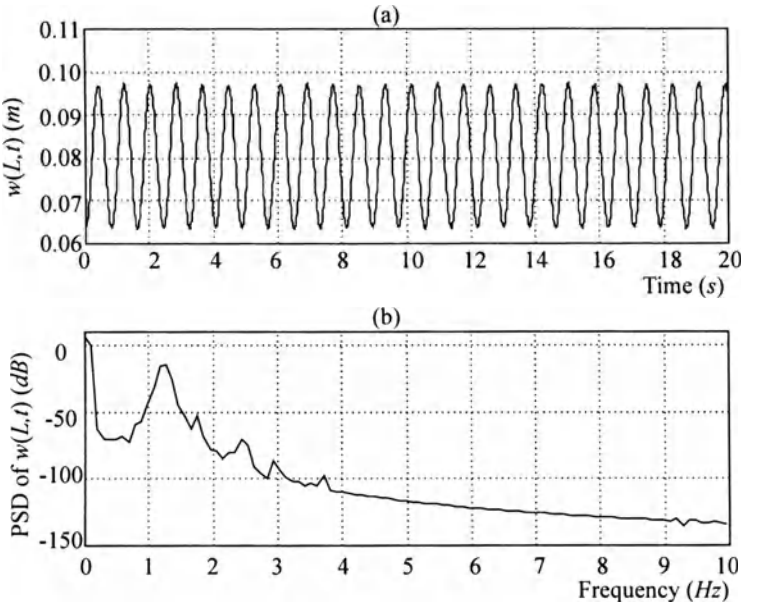

Figure 6.33. Transverse Displacement $w(L,t)$ and its PSD Plot when $f_y = 2(\exp(X) - 1)\cos \pi t$ and $f_z = 2(\exp(X) - 1)$

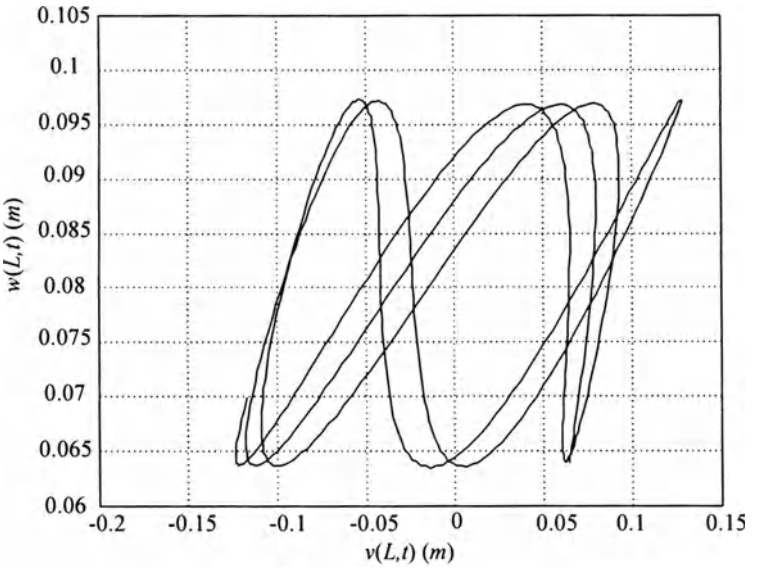

Figure 6.34. Forced Response Viewed from the Top when $f_y = 2(\exp(X) - 1)\cos \pi t$ and $f_z = 2(\exp(X) - 1)$ for $0 < t < 5$ s

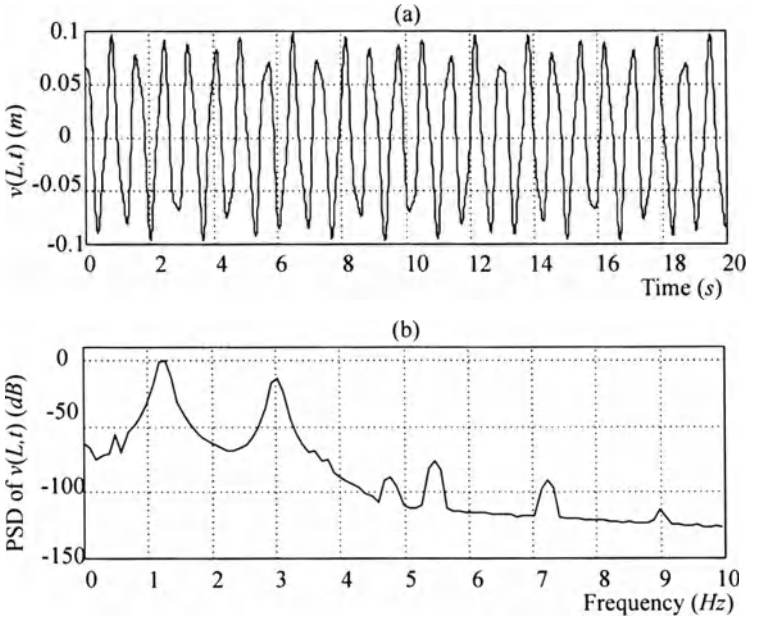

Figure 6.35. Transverse Displacement $v(L,t)$ and its PSD Plot when $f_y = 2(\exp(X) - 1)\cos 6\pi t$ and $f_z = 2(\exp(X) - 1)$

ments in the three directions measured from the original configuration. Kirchhoff's hypothesis and Hamilton's principle were used to obtain the equations of motion and boundary conditions. The equations of motion of the elastic model were coupled nonlinear partial differential equations.

Free responses were obtained using both models, and the numerical results show similar results in terms of the fundamental frequency and the nonlinear behavior. A rotating path is unique to the nonlinear three-dimensional models. It was found that the precession rate increases with increasing $\theta(0)$ and $\dot{\phi}(0)$, or, equivalently, increasing $v(X,0)$, $w(X,0)$, $\dot{v}(X,0)$, and $\dot{w}(X,0)$. Therefore, if those quantities are small enough, the motion in the xy and xz planes can be assumed to be independent, and the response can be analyzed using two planar models.

Once the numerical results of the elastic model were verified, the forced responses due to harmonic and non-harmonic loads were investigated. When a harmonic load was applied in the y direction, the transverse displacement in the y direction goes through a series of responses including beating and subharmonic resonance of order 1/2. On the other hand, the transverse displacement in the perpendicular direction (z direction) was minimally affected. When the non-harmonic force is added in the z direction, the transverse displacement in the z direction shifted

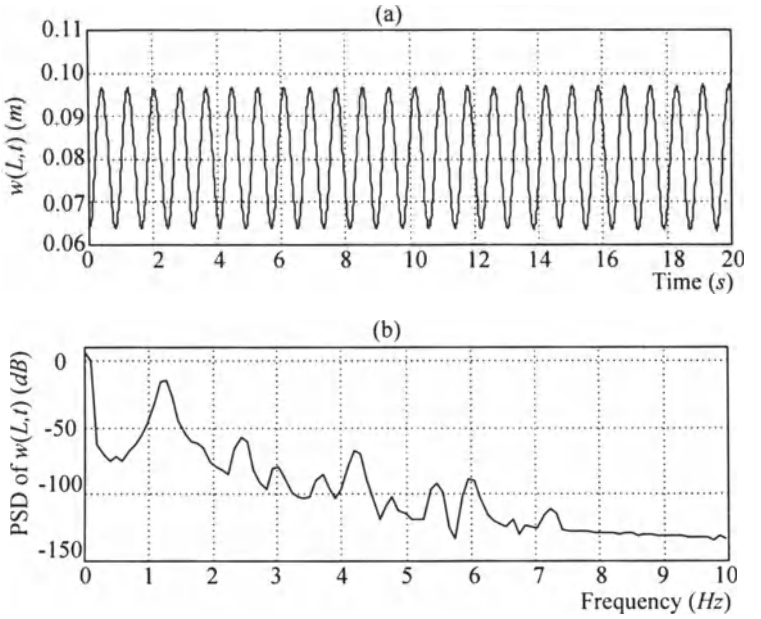

Figure 6.36. Transverse Displacement $w(L,t)$ and its PSD Plot when $f_y = 2(\exp(X) - 1)\cos 6\pi t$ and $f_z = 2(\exp(X) - 1)$

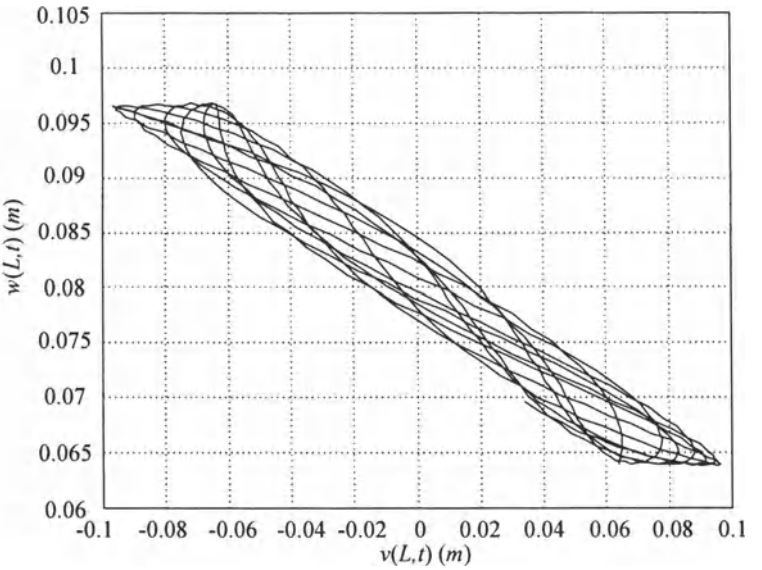

Figure 6.37. Forced Response Viewed from the Top when $f_y = 2(\exp(X) - 1)\cos 6\pi t$ and $f_z = 2(\exp(X) - 1)$ for $0 < t < 5$ s

and its amplitude changed while the displacement in the perpendicular direction (y direction) stayed about the same. Poincaré maps strobed at the forcing frequency were plotted, and they reveal that the responses were quasiperiodic for the conditions tested.

Chapter 7

SUMMARY

The derivation of the equations of motion and numerical responses for two and three-dimensional beam models are presented. These beam models can be used to model the tendons of a TLP.

In Chapter 2, variational methods are derived for use in the subsequent chapters. In Chapter 3, the existing transverse beam models are thoroughly reviewed and compared. They are the Euler-Bernoulli, Rayleigh, shear and Timoshenko models. For engineering purposes, the natural frequencies are presented graphically in terms of normalized wave numbers. The natural frequencies and the mode shapes are functions of the geometry and the material properties such as slenderness ratio, shear factor, and Poisson's ratio. The equations of motion are solved analytically, and a numerical example is given for a non-slender beam. A brief discussion on the second frequency spectrum of the Timoshenko beam model is included. The shear and rotary effects are secondary effects that are neglected by the Euler Bernoulli model. It is found that the shear and rotary effects become more significant for a beam with a small slenderness ratio, a small shape factor, or a large Poisson's ratio with the slenderness ratio being the most important. It is also found that the shear effect is more important than the rotary effect. Therefore, the shear model (the Timoshenko model without the rotary effect) can give reasonable results with less complexity.

The next step is to review the environmental loads that a TLP may experience. Morison's in-plane force and random waves modeled using the Airy linear wave theory with the Pierson-Moskowitz spectrum are reviewed in Chapter 4. A method to obtain a sample time history of random waves is presented.

S. M. Han et al., *Nonlinear and Stochastic Dynamics of Compliant Offshore Structures*

In Chapter 5, a set of nonlinear equations of motion is derived using Kirchhoff's hypothesis for a beam that can vibrate in both the axial and transverse directions. This is done because significant high frequency nonlinear effects appear to be caused by extensional or longitudinal vibration of tendons. Also, the nonlinear coupling between the axial and the transverse motions increases with increasing slenderness ratio. The free and damped-free vibration are investigated in the first part of the chapter. It is found that the fundamental frequency of the axial motion is twice the fundamental frequency of the corresponding transverse motion. The axial motion at this frequency is geometrically induced from the transverse motion. When the vibration of the beam in still water is investigated, it is found that the fluid damping force affects the transverse motion directly, and then the transverse motion affects the axial motion through the system coupling. The influence on the axial motion by the Morison fluid forcing depends on the magnitude of the transverse motion.

In the second part of the chapter, the deterministic and random wave forces are applied. When a harmonic force is applied with non-zero initial conditions, we observed subharmonic resonance of order 1/2 for forcing frequency near twice the natural frequency. When random fluid force is applied, the subharmonic resonance is also observed when non-zero initial conditions were used for a wide range of significant wave heights. In all cases, the axial displacement has the same characteristics as in the free vibration case. The fundamental frequency is twice that of the transverse vibration.

In Chapter 6, the three dimensional motion of a beam is examined. The equations of motion is derived for two cases: for an assumed rigid beam and for an elastic beam. The rigid model has two degrees of freedom, the two spherical angular coordinates. When the beam is modeled as elastic, the equations of motion are found in terms of displacements in the three directions measured from the original configuration. Kirchhoff's hypothesis and Hamilton's principle are used to obtain the equations of motion and boundary conditions. Free responses are obtained using both models, and the numerical results are in close agreement with respect to the fundamental frequency and the nonlinear behavior. In both cases, the path taken by the free end of the beam rotates. This phenomenon is unique to nonlinear three-dimensional models.

Harmonic and non-harmonic loads are then applied to the three-dimensional elastic model. When the harmonic load is applied in the y direction, the transverse displacement in the y direction, $v(X,t)$, revealed a series of responses including beating and subharmonic resonances of order 1/2 or 1/3 when the forcing frequency is near twice or

three times the natural frequency. On the other hand, the transverse displacement in the perpendicular direction, $w(X,t)$, is minimally affected. When a non-harmonic force is added in the z direction, the transverse displacement in the z direction, $w(X,t)$, shifted and its amplitude changed while the displacement in the perpendicular direction, $v(X,t)$, stayed about the same. Poincaré maps strobed at the forcing frequency revealed that the responses were quasiperiodic for the conditions tested.

In this monograph, the tendons are modeled as beams and the platform as a point mass. In reality, the dynamics of the platform may be equally important as the dynamics of the tendons. They are certainly coupled. In future studies, a rigid six degree of freedom model for the platform can be incorporated. Also, the three-dimensional beam model does not include torsion of the beam, which exists for typical TLP geometries. Finally, the harmonic vortex shedding force should be replaced by a coupled model that takes the nonlinear interaction between the fluid and the structure into account. Each of these proposed studies are significant in their scope and difficulty.

Appendix A
Fourier Representation of a Gaussian Random Process

If $\eta(t)$ is a result of many effects that are independent or nearly independent, $\eta(t)$ is a Gaussian random process according to the central limit theorem [66][1]. If $\eta(t)$ is a stationary process on $[0, T]$, its realization can be represented as a Fourier series as

$$\eta(t) = \sum_{n=1}^{N} a_n \cos \omega_n t + b_n \sin \omega_n t, \tag{A.1}$$

where the coefficients a_n and b_n are random variables that have identical normal distribution with zero means,

$$\begin{aligned} E\{a_n\} &= E\{b_n\} = 0 \\ E\{a_n^2\} &= E\{b_n^2\} = \sigma_n^2, \end{aligned} \tag{A.2}$$

and they are independent. That is,

$$\begin{aligned} E\{a_n b_m\} &= 0, \quad \text{for } 1 \leq n, m \leq N \\ E\{a_n a_m\} &= 0, \quad \text{for } 1 \leq n, m \leq N \text{ and } n \neq m \\ E\{b_n b_m\} &= 0, \quad \text{for } 1 \leq n, m \leq N \text{ and } n \neq m. \end{aligned} \tag{A.3}$$

For example, a_1 is independent of all coefficients except for itself.

[1] The article is reprinted in N. Wax, *Selected papers on Noise and Stochastic Processes*, Dover, New York, pages 133-294, 1954.

The autocorrelation function, $R_{\eta\eta}(\tau)$, is then given by

$$\begin{aligned} R_{\eta\eta}(\tau) &= E\{\eta(t)\,\eta(t+\tau)\} \\ &= E\left\{\left(\sum_{n=1}^{N} a_n \cos\omega_n t + b_n \sin\omega_n t\right)\right. \\ &\quad \left.\left(\sum_{m=1}^{N} a_m \cos\omega_m t + b_m \sin\omega_m t\right)\right\} \\ &= \sum_{n=1}^{N}\sum_{m=1}^{N} E\{a_n a_m + a_n b_m\}\cos\omega_n t \cos\omega_m t \\ &\quad + \sum_{n=1}^{N}\sum_{m=1}^{N} E\{b_n a_m + b_n b_m\}\sin\omega_n t \cos\omega_m t. \end{aligned} \tag{A.4}$$

Since $E\{a_n b_m\} = 0$ for any n and m, we can write

$$R_{\eta\eta}(\tau) = \sum_{n=1}^{N}\sum_{m=1}^{N} E\{a_n a_m\}\cos\omega_n t \cos\omega_m t + E\{b_n b_m\}\sin\omega_n t \cos\omega_m t. \tag{A.5}$$

Using $E\{a_n a_m\} = 0$ for $n \neq m$ and $E\{a_n^2\} = E\{b_n^2\} = \sigma_n^2$, we have

$$\begin{aligned} R_{\eta\eta}(\tau) &= \sum_{n=1}^{N} \sigma_n^2 (\cos\omega_n t \cos\omega_n t + \sin\omega_n t \cos\omega_n t) \\ &= \sum_{n=1}^{N} \sigma_n^2 \cos\omega_n \tau. \end{aligned} \tag{A.6}$$

If the mean of $\eta(t)$ is zero, the variance of $\eta(t)$, the autocorrelation function evaluated at $\tau = 0$, is simply the sum of individual variances associated with each frequency,

$$\sigma_\eta^2 = \sum_{n=1}^{N} \sigma_n^2. \tag{A.7}$$

Since σ_η^2 is the total area under the power spectral density, each individual variance σ_n^2 is the area under the spectral density between $\omega_n - \Delta\omega/2$ and $\omega_n + \Delta\omega/2$, as shown in Figure A.1,

$$\sigma_n^2 = \int_{\omega_n - \Delta\omega/2}^{\omega_n + \Delta\omega/2} S_{\eta\eta}^{o}(\omega)\, d\omega, \tag{A.8}$$

or

$$\sigma_n^2 \simeq S_{\eta\eta}^{o}(\omega_n)\,\Delta\omega. \tag{A.9}$$

If the functional form of $S_{\eta\eta}^{o}(\omega)$ is given, the integral expression can be used for accuracy. If $S_{\eta\eta}^{o}(\omega)$ is given as discrete data, the approximation to the integral is used. Note that $S_{\eta\eta}^{o}(\omega)$ is one-sided in this case.

This suggests that a sample time history of the Gaussian random process $\eta(t)$ can be expressed as a Fourier series with normally distributed and independent a_n and b_n with variance σ_n.

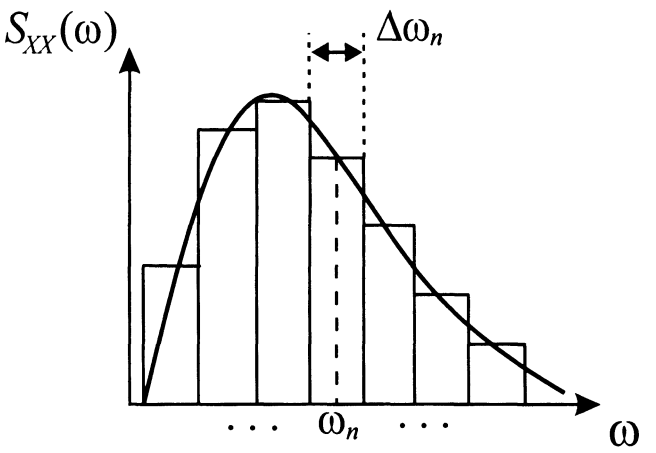

Figure A.1. Area under the Spectral Density

However, this is not the only nor the most convenient representation of $\eta(t)$. Another representation is given by

$$\eta(t) = \sum_{n=1}^{N} \sqrt{2}\sigma_n \cos(\omega_n t - \varphi_n), \tag{A.10}$$

where σ_n is given in either Equation A.8 or A.9, and φ is distributed uniformly on $[0, 2\pi]$. It can be shown that the representations in Equations A.1 and A.10 of $\eta(t)$ lead to the same statistical properties as long as they are used in a way that the central limit theorem may be applied. For example, the autocorrelation function is

$$\begin{aligned} R_{\eta\eta}(\tau) &= E\{\eta(t)\,\eta(t+\tau)\} \\ &= \int_0^{2\pi} \cdots \int_0^{2\pi} \eta(t)\,\eta(t+\tau)\, f_{\Phi_1 \cdots \Phi_N}(\varphi_1, \cdots, \varphi_N)\, d\varphi_1 \cdots d\varphi_N. \end{aligned} \tag{A.11}$$

Since φ are independent of each other, the probability density function is

$$f_{\Phi_1 \cdots \Phi_N}(\varphi_1, \cdots, \varphi_N) = \left(\frac{1}{2\pi}\right)^N. \tag{A.12}$$

Then,

$$
\begin{aligned}
R_{\eta\eta}(\tau) &= \left(\frac{1}{2\pi}\right)^N \int_0^{2\pi} \cdots \int_0^{2\pi} \left[\sum_{n=1}^{N} \sqrt{2}\sigma_n \cos(\omega_n t - \varphi_n)\right. \\
&\quad \left. \times \sum_{m=1}^{N} \sqrt{2}\sigma_m \cos(\omega_m (t+\tau) - \varphi_m)\right] d\varphi_1 \cdots d\varphi_N . \\
&= \left(\frac{1}{2\pi}\right)^N \int_0^{2\pi} \cdots \int_0^{2\pi} \sum_{n=1}^{N} \sum_{m=1}^{N} 2\sigma_n \sigma_m \cos(\omega_n t - \varphi_n) \\
&\quad \cos(\omega_m (t+\tau) - \varphi_m) \\
&= \sum_{n=1}^{N} \sigma_n^2 \left[\cos(\omega_n t)\cos(\omega_m (t+\tau)) + \sin(\omega_n t)\sin(\omega_m (t+\tau))\right] \\
&= \sum_{n=1}^{N} \sigma_n^2 \cos(\omega_n \tau), \qquad \text{(A.13)}
\end{aligned}
$$

which is identical to the autocorrelation function when the Fourier representation in Equation A.1 is used.

In this expression, $\eta(t)$ is represented as the sum of sinusoids with fixed amplitude but random phase shifts. Note that the representation in Equation A.1 requires $2 \times N$ normal random numbers (a_n and b_n), but Equation A.10 requires only N uniform random numbers (φ_n). Therefore, the latter representation is more convenient to use. Using Equation A.9, we can rewrite Equation A.10 as

$$
\eta(t) = \sum_{n=1}^{N} \sqrt{2S_{\eta\eta}^{o}(\omega_n)\,\Delta\omega} \cos(\omega_n t - \varphi_n). \qquad \text{(A.14)}
$$

Since the surface elevation $\eta(t)$ is also harmonic in space (in the horizontal direction) with wave number k_n, we can write

$$
\eta(t,y) = \sum_{n=1}^{N} \sqrt{2S_{\eta\eta}^{o}(\omega_n)\,\Delta\omega} \cos(\omega_n t - k_n y - \varphi_n). \qquad \text{(A.15)}
$$

Without losing generality, we can also write

$$
\eta(t,y) = \sum_{n=1}^{N} \sqrt{2S_{\eta\eta}^{o}(\omega_n)\,\Delta\omega} \cos(k_n y - \omega_n t - \varphi_n). \qquad \text{(A.16)}
$$

This expression is identical to Equation 4.30.

Appendix B
Physically Plausible Initial Displacements

The expressions for the moment and shear for a static case are given by

$$\begin{aligned} M &= EIv'' \\ Q &= EIv''' - EA\left(u' + \frac{1}{2}v'^2\right)v', \end{aligned} \tag{B.1}$$

where the moment and shear is defined positive as shown in Figure B.1.

For the first configuration in Figure 5.3, the moment and shear are given by

$$\begin{aligned} M &= P_o(L - X) \\ Q &= -P_o. \end{aligned} \tag{B.2}$$

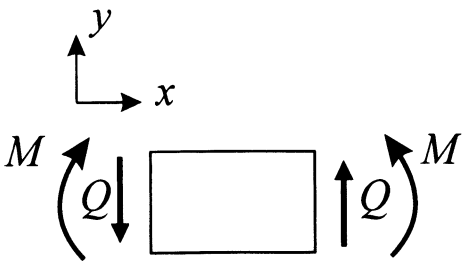

Figure B.1. Definition of Positive Moment and Positive Shear

The boundary conditions that must be satisfied are taken from Equation 5.28 without the time derivatives,

$$\begin{aligned} u(0) &= 0 \\ EA\left(u' + \frac{1}{2}v'^2\right)\Big|_L &= 0 \\ v(0) &= 0 \\ Kv' - EIv''\big|_0 &= 0 \\ (EIv'')' - EA\left(u' + \frac{1}{2}v'^2\right)v'\Big|_L &= P_o \\ EIv''(L) &= 0. \end{aligned} \tag{B.3}$$

Note that the shear at $X = L$ is set to P_o in order to take into account the end point load. The displacement field that satisfies Equations B.1, B.2, and B.3 are given below:

IC_1 :

$$\begin{aligned} u(X,0) &= -\frac{1}{2}\left(\frac{P_o}{EI}\right)^2\left[\frac{X^5}{20} - \frac{LX^4}{4} + \left(L^2 - \frac{EIL}{K}\right)\frac{X^3}{3}\right. \\ &\quad \left. + \frac{EIL^2X^2}{K} + \left(\frac{EIL}{K}\right)^2 X\right] \\ v(X,0) &= -\frac{P_o}{EI}\left(\frac{X^3}{6} - \frac{LX^2}{2} - \frac{EILX}{K}\right). \end{aligned} \tag{B.4}$$

Similarly, the displacement field that satisfies the other three initial configurations in Figure 5.3 are given by

IC_2 :

$$\begin{aligned} u(X,0) &= \frac{1}{2}\left(\frac{M_o}{EI}\frac{X^3}{3} - \frac{M_o^2}{EIK}X^2 - \frac{M_o^2}{K^2}X\right) \\ v(X,0) &= -M_o\left(\frac{X^2}{2EI} + \frac{X}{K}\right). \end{aligned} \tag{B.5}$$

IC_3 :

$$\begin{aligned} u(X,0) &= \frac{1}{24}P_oL^2\left[(XK + EI)^3 + \frac{EI}{K^3}\right] \\ v(X,0) &= \frac{P_oL}{2}\left(\frac{X^2}{2EI} + \frac{X}{K}\right) \end{aligned} \tag{B.6}$$

for $0 < X < L/2$ and

$$\begin{aligned} u(X,0) &= \frac{1}{11520}\left(\frac{P_o}{EIK}\right)^2\left[-288K^2X^5 + 1440LK^2X^4\right. \\ &\quad + (960EI - 2080LK)\,LKX^3 + (480LK - 2880EI)\,L^2KX^2 \\ &\quad \left. + \left(480LKEI - 40L^2K^2 - 1440\,(EI)^2\right)L^2X + 19L^5K^2\right] \\ v(X,0) &= -\frac{P_o}{EI}\left(\frac{X^3}{6} - \frac{LX^2}{2} + \frac{L}{12K}\,(LK - 6EI)\,X\right) \end{aligned} \tag{B.7}$$

for $\frac{L}{2} < X < L$.

IC_4 :

$$u(X,0) = \frac{P_o}{EA}X$$
$$v(X,0) = 0. \tag{B.8}$$

Appendix C
Finite Difference Method

1. Two Dimensional Equations of Motion and Boundary Conditions

In Chapter 5, we obtained the equations of motion (Equations 5.25 and 5.26) and the boundary conditions (Equation 5.28) for a beam vibrating both transversely and axially. The axial force term p is due to gravity, and the transverse force term f is due to current and random waves. The transverse forcing term is formulated in Chapter 4.

The equations of motion are nonlinear. Therefore, we use the finite difference method to obtain the response numerically. Here, it will be shown how this can be done. In order to remind ourselves, the equations of motion (Equations 5.25 and 5.26) are given by

$$\rho A\ddot{u} - \left(EA\left(u' + \frac{1}{2}v'^{\,2}\right)\right)' = p \tag{C.1}$$

$$\rho A\ddot{v} - \left(EA\left(u' + \frac{1}{2}v'^{\,2}\right)v'\right)' - (\rho I\ddot{v}')' + (EIv'')'' = f, \tag{C.2}$$

and the boundary conditions (5.28) are given by

$$u(0,t) = 0 \tag{C.3}$$

$$EA\left(u' + \frac{1}{2}v'^{\,2}\right) + M_p\ddot{u}(L,t)\Big|_{L,t} = 0 \tag{C.4}$$

$$v(0,t) = 0 \tag{C.5}$$

$$kv' - EIv''\big|_{0,t} = 0 \tag{C.6}$$

$$EIv''(L,t) = 0 \tag{C.7}$$

$$(EIv'')' - \rho I\ddot{v}' - EA\left(u' + \frac{1}{2}v'^{\,2}\right)v' - M_p\ddot{v}\Big|_{L,t} = 0. \tag{C.8}$$

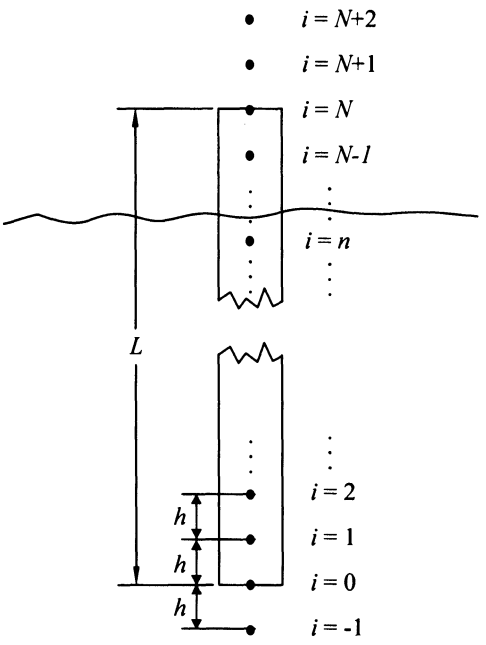

Figure C.1. Node Distribution

Using Equation C.4, Equation C.8 can also be written as

$$\left(EIv''\right)' + M_p\ddot{u}v' - \rho I\ddot{v}' - M_p\ddot{v}\Big|_{L,t} = 0. \tag{C.9}$$

The axial and transverse distributed loads are given in Equations 5.73 and 4.14 or

$$\begin{aligned} p &= \left(\rho_f A_f - \rho A\right) g \text{ for } 0 < x < d \\ &= -\rho g A \text{ for } d < x < L \end{aligned} \tag{C.10}$$

$$\begin{aligned} f\left(X,t\right) = {} & C_D \rho_f r_o \left(-w_x v' + \dot{u}v' + w_y + U_c - \dot{v}\right) \\ & \times \left|-w_x v' + \dot{u}v' + w_y + U_c - \dot{v}\right| \\ & -C_A \rho_f \pi r_o^2 \left(-\ddot{u}v' + \ddot{v}\right) + C_M \rho_f \pi r_o^2 \left(\dot{w}_y - \dot{w}_x v'\right) \text{ for } X < d. \end{aligned} \tag{C.11}$$

1.1 Discretized Equations of Motion

The goal here is to express the partial differential equations for $u\left(X,t\right)$ and $v\left(X,t\right)$ in Equations C.1 and C.2 in terms of ordinary differential equations in time for each node shown in Figure C.1. Displacements for each node, $u_i\left(t\right)$ and $v_i\left(t\right)$, are equivalent to $u\left(ih,t\right)$ and $v\left(ih,t\right)$. First, we write a discretized equation of motion in time for each node, $i = 0$ to $i = N$. Therefore, only the spatial derivatives are written in terms of finite difference equations. The finite difference equations for the spatial

derivatives are given by

$$
\begin{aligned}
v_i' &= \frac{v_{i+1} - v_{i-1}}{2h} \\
v_i'' &= \frac{v_{i+1} - 2v_i + v_{i-1}}{h^2} \\
v_i''' &= \frac{v_{i+2} - 2v_{i+1} + 2v_{i-1} - v_{i-2}}{2h^3} \\
v_i'''' &= \frac{v_{i+2} - 4v_{i+1} + 6v_i - 4v_{i-1} + v_{i-2}}{h^4}.
\end{aligned} \tag{C.12}
$$

For each node, the differential equations are given by

$$\rho A \ddot{u}_i = EA\left(u_i'' + v_i' v_i''\right) + p_i \tag{C.13}$$

$$
\begin{aligned}
\rho A \ddot{v}_i - \rho I \ddot{v}_i'' = &-EI v_i'''' + EA\left(u_i'' + v_i' v_i''\right) v_i' \\
&+ EA\left(u_i' + \frac{1}{2} v_i'^{\,2}\right) v_i'' + f_i,
\end{aligned} \tag{C.14}
$$

for $i = 0 \cdots N$. Since $u(0,t) = 0$ and $v(0,t) = 0$, the equation of motion for $i = 0$ can be omitted. The distributed loads are given by

$$
\begin{aligned}
p_i &= \left(\rho_f A_f - \rho A\right) g \qquad \text{for } i = 1, \cdots, n \\
&= -\rho g A \qquad\qquad\quad \text{for } i = n+1, \cdots, N,
\end{aligned} \tag{C.15}
$$

and

$$
\begin{aligned}
f_i = {} & C_M \frac{\rho_f \pi r_o^2}{\rho A}\left(\dot{w}_{y\,i} - \dot{w}_{x\,i} v_i'\right) \\
& + C_D \frac{\rho_f r_o}{\rho A}\left(-w_{x\,i} v_i' + \dot{u}_i v_i' + w_{y\,i} + U_{c\,i} - \dot{v}_i\right) \\
& \times \left|-w_x v_i' + \dot{u}_i v_i' + w_{y\,i} + U_{c\,i} - \dot{v}_i\right| \\
& - C_A \frac{\rho_f \pi r_o^2}{\rho A}\left(-\ddot{u}_i v_i' + \ddot{v}_i\right) \qquad \text{for } i = 1, \cdots, n \\
= {} & 0 \qquad\qquad\qquad\qquad\qquad\quad \text{for } i = n+1, \cdots, N.
\end{aligned} \tag{C.16}
$$

Note that the nodes from $i = 1$ to n are submerged in water. The term $\ddot{u}_i$ in the added mass term (in Equation C.16) can be replaced by the equation of motion for the i^{th} axial displacement given in Equation C.13.

The boundary conditions in terms of finite difference equations are given by

$$0 = u_0 \tag{C.17}$$

$$0 = EA\left[\frac{u_{N+1} - u_{N-1}}{2h} + \frac{1}{2}\left(\frac{v_{N+1} - v_{N-1}}{2h}\right)^2\right] + M_p \ddot{u}_N \tag{C.18}$$

$$0 = v_0 \tag{C.19}$$

$$0 = k\frac{v_1 - v_{-1}}{2h} - EI\frac{v_1 - 2v_0 + v_{-1}}{h^2} \tag{C.20}$$

$$0 = \frac{v_{N+1} - 2v_N + v_{N-1}}{h^2} \tag{C.21}$$

$$
\begin{aligned}
0 = {} & EI\frac{v_{N+2} - 2v_{N+1} + 2v_{N-1} - v_{N-2}}{2h^3} - \rho I\left(\frac{\ddot{v}_{N+1} - \ddot{v}_{N-1}}{2h}\right) \\
& + M_p \ddot{u}_N\left(\frac{v_{N+1} - v_{N-1}}{2h}\right) - M_p \ddot{v}_N.
\end{aligned} \tag{C.22}
$$

Using these boundary conditions, we can write the displacements of the fictitious nodes as

$$u_{N+1} = u_{N-1} - \frac{(v_N - v_{N-1})^2}{h} - \frac{M_p}{EA}(2h)\ddot{u}_N \tag{C.23}$$

$$v_{-1} = \frac{kh - 2EI}{kh + EI} v_1 \tag{C.24}$$

$$v_{N+1} = 2v_N - v_{N-1} \tag{C.25}$$

$$v_{N+2} = 4v_N - 4v_{N-1} + v_{N-2} + 2h^3 \frac{M_p}{EI}\ddot{v}_N - 2h^2 \frac{M_p}{EI}(v_N - v_{N-1})\ddot{u}_N + 2h^2 \frac{\rho I}{EI}(\ddot{v}_N - \ddot{v}_{N-1}). \tag{C.26}$$

The finite difference Equation C.12 is valid for interior nodes. For nodes $i = 1$, N, and $N-1$, we need to utilize Equations C.23 to C.26. For instance, the spatial derivatives of the axial displacement at $i = 1$ are given by

$$u_1' = \frac{u_2 - u_0}{2h}$$
$$u_1'' = \frac{u_2 - 2u_1 + u_0}{h^2}. \tag{C.27}$$

The axial displacement at $i = 0$ is zero from Equation C.17 ($u_0 = 0$). Therefore,

$$u_1' = \frac{u_2}{2h}$$
$$u_1'' = \frac{u_2 - 2u_1}{h^2}. \tag{C.28}$$

At $i = N$, the spatial derivatives of u are given by

$$u_1' = \frac{u_{N+1} - u_{N-1}}{2h}$$
$$u_1'' = \frac{u_{N+1} - 2u_N + u_{N-1}}{h^2}. \tag{C.29}$$

The fictitious displacement u_{N+1} is replaced by Equation C.23 so that

$$u_N' = -\frac{(v_N - v_{N-1})^2}{2h^2} - \frac{M_p}{EA}\ddot{u}_N$$
$$u_N'' = \frac{-2u_N + 2u_{N-1}}{h^2} - \frac{(v_N - v_{N-1})^2}{h^3} - \frac{M_p}{EA}\left(\frac{2}{h}\right)\ddot{u}_N. \tag{C.30}$$

Similarly, the first, second, and fourth spatial derivatives of v at $i = 1$ are given by

$$v_1' = \frac{v_2}{2h}$$
$$v_1'' = \frac{v_2 - 2v_1}{h^2}$$
$$v_1'''' = \frac{v_3 - 4v_2 + \left(6 + \frac{kh-2EI}{kh+EI}\right) v_1}{h^4}, \tag{C.31}$$

the spatial derivatives of v at $i = N-1$ are given by

$$\begin{aligned} v'_{N-1} &= \frac{v_N - v_{N-2}}{2h} \\ v''_{N-1} &= \frac{v_N - 2v_{N-1} + v_{N-2}}{h^2} \\ v''''_{N-1} &= \frac{-2v_N + 5v_{N-1} - 4v_{N-2} + v_{N-3}}{h^4}, \end{aligned} \tag{C.32}$$

and the spatial derivatives of v at $i = N$ are given by

$$\begin{aligned} v'_N &= \frac{2v_N - 2v_{N-1}}{2h} \\ v''_N &= 0 \\ v''''_N &= \frac{2v_N - 4v_{N-1} + 2v_{N-2}}{h^4} + \frac{1}{h}\frac{M_p}{EI}\ddot{v}_N \\ &\quad - \frac{2}{h^2}\frac{M_p}{EI}(v_N - v_{N-1})\ddot{u}_N + \frac{2}{h^2}\frac{\rho I}{EI}(\ddot{v}_N - \ddot{v}_{N-1}). \end{aligned} \tag{C.33}$$

The equations of motion for the 1^{st} node can be written as

$$\rho A\ddot{u}_1 = EA\left(\frac{u_{N+1} - u_{N-1}}{2h} + \frac{v_2}{2h}\frac{v_2 - 2v_1}{h^2}\right) + p_1$$

$$\begin{aligned} \left(\rho A + \frac{2\rho I}{h^2}\right)\ddot{v}_1 - \frac{\rho I}{h^2}\ddot{v}_2 &= -EI\frac{v_3 - 4v_2 + \left(6 + \frac{kh-2EI}{kh+EI}\right)v_1}{h^4} \\ &\quad + EA\left(\frac{u_2 - 2u_1}{h^2} + \frac{v_2}{2h}\frac{v_2 - 2v_1}{h^2}\right)\frac{v_2}{2h} \\ &\quad + EA\left(\frac{u_2}{2h} + \frac{1}{2}\left(\frac{v_2}{2h}\right)^2\right)\left(\frac{v_2 - 2v_1}{h^2}\right) + f_1. \end{aligned} \tag{C.34}$$

The equations of motion for the $(N-1)^{th}$ node are given by

$$\begin{aligned} \rho A\ddot{u}_{N-1} &= EA\frac{u_N - 2u_{N-1} + u_{N-2}}{h^2} \\ &\quad + EA\frac{v_N - v_{N-2}}{2h}\frac{v_N - 2v_{N-1} + v_{N-2}}{h^2} + p_{N-1} \end{aligned} \tag{C.35}$$

and

$$\begin{aligned} &\rho A\ddot{v}_{N-1} - \rho I\frac{\ddot{v}_N - 2\ddot{v}_{N-1} + \ddot{v}_{N-2}}{h^2} \\ &= -EI\frac{-2v_N + 5v_{N-1} - 4v_{N-2} + v_{N-3}}{h^4} \\ &+ EA\left(\frac{u_N - 2u_{N-1} + u_{N-2}}{h^2} + \frac{v_N - v_{N-2}}{2h}\frac{v_N - 2v_{N-1} + v_{N-2}}{h^2}\right) \\ &\times \frac{v_N - v_{N-2}}{2h} \\ &+ EA\left(\frac{u_N - u_{N-2}}{2h} + \frac{1}{2}\left(\frac{v_N - v_{N-2}}{2h}\right)^2\right)\left(\frac{v_N - 2v_{N-1} + v_{N-2}}{h^2}\right) \\ &+ f_{N-1}, \end{aligned} \tag{C.36}$$

and the equations motion for the N^{th} node are given by

$$\left(\rho A + \frac{2M_p}{h}\right)\ddot{u}_N = EA\frac{-2u_N + 2u_{N-1}}{h^2} - EA\frac{(v_N - v_{N-1})^2}{h^3} + p_N \tag{C.37}$$

and

$$\begin{aligned}\left(\rho A - \frac{1}{h}\frac{M_p}{EI} + \frac{2}{h^2}\rho I\right)\ddot{v}_N - \frac{2}{h^2}\rho I\ddot{v}_{N-1} \\ = -EI\frac{2v_N - 4v_{N-1} + 2v_{N-2}}{h^4} \\ + EA\left(\frac{-2u_N + 2u_{N-1}}{h^2}\right)\left(\frac{2v_N - 2v_{N-1}}{2h}\right) \\ - EA\frac{(v_N - v_{N-1})^3}{h^4} + f_N.\end{aligned} \tag{C.38}$$

The equations of motion can be simplified if we use matrix notation such that

$$[M_u]\{\ddot{u}\} = EA[U_2]\{u\} + EA([V_1]\{v\})\cdot([V_2]\{v\}) + \{N_1\} + \{p\} \tag{C.39}$$

$$\begin{aligned}[M_v]\{\ddot{v}\} &= -EI[V_4]\{v\} + EA([V_1]\{v\}) \\ &\quad \cdot [[U_2]\{u\} + ([V_1]\{v\})\cdot([V_2]\{v\})] \\ &\quad + EA\left([U_1]\{u\} + \frac{1}{2}([V_1]\{v\})\cdot([V_1]\{v\})\right)\cdot([V_2]\{v\}) \\ &\quad + \{N_2\} + \{f\},\end{aligned} \tag{C.40}$$

where

$$[M_u] = \begin{bmatrix} \rho A & 0 & 0 & 0 & 0 \\ 0 & \rho A & 0 & 0 & 0 \\ 0 & 0 & \rho A & 0 & 0 \\ 0 & 0 & 0 & \rho A & 0 \\ 0 & 0 & 0 & 0 & \rho A + \frac{2}{h}M_p \end{bmatrix}, \tag{C.41}$$

$$\begin{aligned}&[M_v] \\ &= \begin{bmatrix} \rho A + 2\frac{\rho I}{h^2} & -\frac{\rho I}{h^2} & 0 & 0 & 0 \\ -\frac{\rho I}{h^2} & \rho A + 2\frac{\rho I}{h^2} & -\frac{\rho I}{h^2} & 0 & 0 \\ 0 & -\frac{\rho I}{h^2} & \rho A + 2\frac{\rho I}{h^2} & -\frac{\rho I}{h^2} & 0 \\ 0 & 0 & -\frac{\rho I}{h^2} & \rho A + 2\frac{\rho I}{h^2} & -\frac{\rho I}{h^2} \\ 0 & 0 & 0 & -2\frac{\rho I}{h^2} & \rho A + \frac{2}{h}M_p + 2\frac{\rho I}{h^2} \end{bmatrix}\end{aligned} \tag{C.42}$$

$$+ C_A\rho A_f \begin{bmatrix} 1 & 0 & 0 & 0 & 0 \\ 0 & 1 & 0 & 0 & 0 \\ 0 & 0 & 1 & 0 & 0 \\ 0 & 0 & 0 & 0 & 0 \\ 0 & 0 & 0 & 0 & 0 \end{bmatrix} \begin{matrix} \left.\begin{matrix}\\\\\\\end{matrix}\right\} 1 \sim n \\ \left.\begin{matrix}\\\end{matrix}\right\} n+1 \sim N \end{matrix}, \tag{C.43}$$

$$[U_1] = [V_1] = \frac{1}{2h}\begin{bmatrix} 0 & 1 & 0 & 0 & 0 & 0 \\ -1 & 0 & 1 & 0 & 0 & 0 \\ 0 & -1 & 0 & 1 & 0 & 0 \\ 0 & 0 & -1 & 0 & 1 & 0 \\ 0 & 0 & 0 & 0 & -2 & 2 \end{bmatrix}, \tag{C.44}$$

$$[U_2] = \frac{1}{h^2}\begin{bmatrix} -2 & 1 & 0 & 0 & 0 \\ 1 & -2 & 1 & 0 & 0 \\ 0 & 1 & -2 & 1 & 0 \\ 0 & 0 & 1 & -2 & 1 \\ 0 & 0 & 0 & 2 & -2 \end{bmatrix}, \tag{C.45}$$

$$[V_2] = \frac{1}{h^2}\begin{bmatrix} -2 & 1 & 0 & 0 & 0 \\ 1 & -2 & 1 & 0 & 0 \\ 0 & 1 & -2 & 1 & 0 \\ 0 & 0 & 1 & -2 & 1 \\ 0 & 0 & 0 & 0 & 0 \end{bmatrix}, \tag{C.46}$$

$$[V_4] = \frac{1}{h^4}\begin{bmatrix} 6+\frac{kh-2EI}{kh+2EI} & -4 & 1 & 0 & 0 & 0 & 0 \\ -4 & 6 & -4 & 1 & 0 & 0 & 0 \\ 1 & -4 & 6 & -4 & 1 & 0 & 0 \\ 0 & 1 & -4 & 6 & -4 & 1 & 0 \\ 0 & 0 & 1 & -4 & 6 & -4 & 1 \\ 0 & 0 & 0 & 1 & -4 & 5 & -2 \\ 0 & 0 & 0 & 0 & 2 & -4 & 2 \end{bmatrix}, \tag{C.47}$$

$$\{N_1\} = \begin{bmatrix} 0 \\ 0 \\ 0 \\ 0 \\ -\frac{EA}{h^3}(v_N - v_{N-1})^2 \end{bmatrix}, \{N_2\} = \frac{(v_N - v_{N-1})}{h}\{N_1\} \tag{C.48}$$

and

$$\begin{aligned} \{f\} = {} & C_A\rho_f A_f([V_1]\{v\}\cdot\{\ddot{u}\}) + C_M\rho_f A_f(\{\dot{w}_y\} - \{\dot{w}_x\}\cdot([V_1]\{v\})) \\ & + C_D\rho_f r_o((\{\dot{u}\} - \{w_x\})\cdot([V_1]\{v\}) + \{w_y\} + \{U_c\} - \{\dot{v}\})\cdot \\ & |(\{\dot{u}\} - \{w_x\})\cdot([V_1]\{v\}) + \{w_y\} + \{U_c\} - \{\dot{v}\}| \end{aligned} \tag{C.49}$$

for the first n terms. The term$\{\ddot{u}\}$ in Equation C.49 should be replaced using Equation C.39. The $\cdot$ notation is used for term by term multiplication instead of matrix multiplication. For example,

$$\begin{bmatrix} 1 \\ 2 \\ 3 \end{bmatrix} \cdot \begin{bmatrix} -2 \\ 5 \\ 7 \end{bmatrix} = \begin{bmatrix} 1 \times -2 = -2 \\ 2 \times 5 = 10 \\ 3 \times 7 = 21 \end{bmatrix}.$$

The equations of motion in Equations C.39 and C.40 can be written as $4N$ coupled first order nonlinear ordinary differential equations by letting $\{u\} = \{Y_{(1)}\}$, $\{\dot{u}\} =$

$\{Y_{(2)}\}$, $\{v\} = \{Y_{(3)}\}$, and $\{\dot{v}\} = \{Y_{(4)}\}$ such that

$$\begin{aligned}
\frac{d}{dt}\{Y_{(1)}\} &= \{Y_{(2)}\} \\
\frac{d}{dt}\{Y_{(2)}\} &= [M_u]^{-1}\left(EA[U_2]\{Y_{(1)}\} + EA\left([V_1]\{Y_{(3)}\}\right)\cdot\left([V_2]\{Y_{(3)}\}\right)\right) \\
&\quad + [M_u]^{-1}\left(\{N_1\} + \{p\}\right) \\
\frac{d}{dt}\{Y_{(3)}\} &= \{Y_{(4)}\} \\
\frac{d}{dt}\{Y_{(4)}\} &= [M_v]^{-1}\left(-EI[V_4]\{Y_{(3)}\} + EA\left([V_1]\{Y_{(3)}\}\right)\cdot[U_2]\{Y_{(1)}\}\right. \\
&\quad + EA\left([V_1]\{Y_{(3)}\}\right)\cdot\left([V_1]\{Y_{(3)}\}\right)\cdot\left([V_2]\{Y_{(3)}\}\right) + \{N_2\} + \{f\} \\
&\quad + EA\left([U_1]\{Y_{(1)}\}\right)\cdot\left([V_2]\{Y_{(3)}\}\right) \\
&\quad \left. + EA\left(\frac{1}{2}\left([V_1]\{Y_{(3)}\}\right)\cdot\left([V_1]\{Y_{(3)}\}\right)\right)\cdot\left([V_2]\{Y_{(3)}\}\right)\right),
\end{aligned} \tag{C.50}$$

where

$$\begin{aligned}
\{f\} &= C_A\rho_f A_f\left([V_1]\{Y_{(3)}\}\cdot\left\{\dot{Y}_{(2)}\right\}\right) \\
&\quad + C_M\rho_f A_f\left(\{\dot{w}_y\} - \{\dot{w}_x\}\cdot\left([V_1]\{Y_{(3)}\}\right)\right) \\
&\quad + C_D\rho_f r_o\left(\left(\{Y_{(2)}\} - \{w_x\}\right)\cdot\left([V_1]\{Y_{(3)}\}\right) + \{w_y\} + \{U_c\} - \{Y_{(4)}\}\right)\cdot \\
&\quad \left|\left(\{Y_{(2)}\} - \{w_x\}\right)\cdot\left([V_1]\{Y_{(3)}\}\right) + \{w_y\} + \{U_c\} - \{Y_{(4)}\}\right|,
\end{aligned} \tag{C.51}$$

and the term $\left\{\dot{Y}_{(2)}\right\}$ is to replaced by

$$\begin{aligned}
\left\{\dot{Y}_{(2)}\right\} &= [M_u]^{-1}\left(EA[U_2]\{Y_{(1)}\}\right) \\
&\quad + [M_u]^{-1}\left(EA\left([V_1]\{Y_{(3)}\}\right)\cdot\left([V_2]\{Y_{(3)}\}\right) + \{N_1\} + \{p\}\right).
\end{aligned} \tag{C.52}$$

These systems of ODEs can be solved using numerical algorithms such as the Runge-Kutta method. We used 4th order Runge-Kutta method (using MATLAB) to generate the results.

2. Three-Dimensional Equations of Motion and Boundary Conditions

In Chapter 6, we expanded our analysis to three dimensions. The equations of motion and boundary conditions are given by

$$\begin{aligned}
\rho A\ddot{u} - \left(EA\left(u' + \frac{1}{2}v'^2 + \frac{1}{2}w'^2\right)\right)' &= p \\
\rho A\ddot{v} - \left(EA\left(u' + \frac{1}{2}v'^2 + \frac{1}{2}w'^2\right)v'\right)' - \left(\rho I_z\ddot{v}'\right)' + \left(EI_z v''\right)'' &= f_y \\
\rho A\ddot{w} - \left(EA\left(u' + \frac{1}{2}v'^2 + \frac{1}{2}w'^2\right)w'\right)' - \left(\rho I_y\ddot{w}'\right)' + \left(EI_y w''\right)'' &= f_z,
\end{aligned} \tag{C.53}$$

and the boundary conditions are given by

$$
\begin{aligned}
u(0,t) &= 0 \\
\left[EA\left(u' + \frac{1}{2}v'^2 + \frac{1}{2}w'^2\right) + M_p\ddot{u}\right]\Big|_{L,t} &= 0 \\
v(0,t) &= 0 \\
\left(kv' - EI_z v''\right)\big|_{0,t} &= 0 \\
EI_z v''\big|_{L,t} &= 0 \\
\left[\left(EI_z v''\right)' - \rho I_z \ddot{v}' - EA\left(u' + \frac{1}{2}v'^2 + \frac{1}{2}w'^2\right)v' - M_p\ddot{v}\right]\Big|_{L,t} &= 0
\end{aligned}
$$

$$
\begin{aligned}
w(0,t) &= 0 \\
\left(kw' - EI_y w''\right)\big|_{0,t} &= 0 \\
EI_y w''\big|_{L,t} &= 0 \\
\left[\left(EI_y w''\right)' - \rho I_y \ddot{w}' - EA\left(u' + \frac{1}{2}v'^2 + \frac{1}{2}w'^2\right)w' - M_p\ddot{w}\right]\Big|_{L,t} &= 0.
\end{aligned} \tag{C.54}
$$

The term w is the transverse displacement in the z direction, not to be confused with the wave velocities w_x and w_y.

The axial and transverse distributed loads are given by

$$
\begin{aligned}
p &= \left(\rho_f A_f - \rho A\right) g \text{ for } 0 < x < d \\
&= -\rho g A \text{ for } d < x < L \\
f_y(X,t) &= 2\left(\exp(X) - 1\right)\cos\omega_f t \\
f_z(X,t) &= 2\left(\exp(X) - 1\right).
\end{aligned} \tag{C.55}
$$

2.1 Discretized Equations of Motion

For each node, the differential equations are given by

$$
\rho A\ddot{u}_i = EA\left(u_i'' + v_i'v_i'' + w_i'w_i''\right) + p_i \tag{C.56}
$$

$$
\begin{aligned}
\rho A\ddot{v}_i - \rho I_z\ddot{v}_i'' &= -EI_z v_i'''' + EA\left(u_i'' + v_i'v_i'' + w_i'w_i''\right)v_i' \\
&\quad + EA\left(u_i' + \frac{1}{2}v_i'^2 + \frac{1}{2}w_i'^2\right)v_i'' + f_{yi},
\end{aligned} \tag{C.57}
$$

$$
\begin{aligned}
\rho A\ddot{w}_i - \rho I_y\ddot{w}_i'' &= -EI_y w_i'''' + EA\left(u_i'' + v_i'v_i'' + w_i'w_i''\right)w_i' \\
&\quad + EA\left(u_i' + \frac{1}{2}v_i'^2 + \frac{1}{2}w_i'^2\right)w_i'' + f_{zi},
\end{aligned} \tag{C.58}
$$

where the spatial derivatives, v_i', v_i'', $\cdots$, are expressed in terms of finite difference equations, and

$$
\begin{aligned}
p_i &= \left(\rho_f A_f - \rho A\right) g && \text{for } i = 1, \cdots, n \\
&= -\rho g A && \text{for } i = 1+n, \cdots, N \\
f_{yi} &= 2\left(\exp(x_i) - 1\right)\cos\omega_f t && \text{for } i = 1, \cdots, N \\
f_{zi} &= 2\left(\exp(x_i) - 1\right) && \text{for } i = 1, \cdots, N,
\end{aligned} \tag{C.59}
$$

where $x_i = h \times i$.

The boundary conditions can be written as

$$
\begin{aligned}
0 &= u \\
0 &= \left[\frac{u_{N+1} - u_{N-1}}{2h} + \frac{1}{2}\left(\frac{v_{N+1} - v_{N-1}}{2h}\right)^2 + \frac{1}{2}\left(\frac{w_{N+1} - w_{N-1}}{2h}\right)^2\right]\Bigg|_{L,t} \\
&\quad + M_p \ddot{u}_N|_{L,t} \\
0 &= v_0 \\
0 &= k\frac{v_1 - v_{-1}}{2h} - EI_z \frac{v_1 - 2v_0 + v_{-1}}{h^2}\Bigg|_{0,t} \\
0 &= \frac{v_{N+1} - 2v_N + v_{N-1}}{h^2}\Bigg|_{L,t} \\
0 &= EI_z \frac{v_{N+2} - 2v_{N+1} + 2v_{N-1} - v_{N-2}}{2h^3} - \rho I_z \left(\frac{\ddot{v}_{N+1} - \ddot{v}_{N-1}}{2h}\right) \\
&\quad + M_p \ddot{u}_N \left(\frac{v_{N+1} - v_{N-1}}{2h}\right) - M_p \ddot{v}_N \\
0 &= w_0 \\
0 &= k\frac{w_1 - w_{-1}}{2h} - EI_y \frac{w_1 - 2w_0 + w_{-1}}{h^2}\Bigg|_{0,t} \\
0 &= \frac{w_{N+1} - 2w_N + w_{N-1}}{h^2}\Bigg|_{L,t} \\
0 &= EI_y \frac{w_{N+2} - 2w_{N+1} + 2w_{N-1} - w_{N-2}}{2h^3} - \rho I_y \left(\frac{\ddot{w}_{N+1} - \ddot{w}_{N-1}}{2h}\right) \\
&\quad + M_p \ddot{u}_N \left(\frac{w_{N+1} - w_{N-1}}{2h}\right) - M_p \ddot{w}_N,
\end{aligned}
\tag{C.60}
$$

from which we deduce that

$$
\begin{aligned}
u_{N+1} &= u_{N-1} - \frac{(v_N - v_{N-1})^2}{h} - \frac{(w_N - w_{N-1})^2}{h} - \frac{M_p}{EA}(2h)\ddot{u}_N \\
v_{-1} &= \frac{kh - 2EI_z}{kh + EI_z} v_1 \\
v_{N+1} &= 2v_N - v_{N-1} \\
v_{N+2} &= 4v_N - 4v_{N-1} + v_{N-2} + 2h^3 \frac{M_p}{EI_z}\ddot{v}_N \\
&\quad - 2h^2 \frac{M_p}{EI_z}(v_N - v_{N-1})\ddot{u}_N + 2h^2 \frac{\rho I_z}{EI_z}(\ddot{v}_N - \ddot{v}_{N-1}) \\
w_{-1} &= \frac{kh - 2EI_y}{kh + EI_y} w_1 \\
w_{N+1} &= 2w_N - w_{N-1} \\
w_{N+2} &= 4w_N - 4w_{N-1} + w_{N-2} + 2h^3 \frac{M_p}{EI_y}\ddot{w}_N - 2h^2 \frac{M_p}{EI_y}(w_N - w_{N-1})\ddot{u}_N \\
&\quad + 2h^2 \frac{\rho I_y}{EI_y}(\ddot{w}_N - \ddot{w}_{N-1}).
\end{aligned}
\tag{C.61}
$$

Now, we can write the equations of motion in matrix form as

$$[M_u]\{\ddot{u}\} = EA[U_2]\{u\} + EA([V_1]\{v\}) \cdot ([V_2]\{v\}) + EA([V_1]\{w\}) \cdot ([V_2]\{w\}) + \{N_1\} + \{p\} \tag{C.62}$$

$$\begin{aligned}[M_v]\{\ddot{v}\} = &-EI_z[V_4]\{v\} + EA([V_1]\{v\}) \cdot ([U_2]\{u\}) \\ &+ EA([V_1]\{v\}) \cdot ([V_2]\{v\}) + EA([V_1]\{w\}) \cdot ([V_2]\{w\}) \\ &+ EA\left([U_1]\{u\} + \frac{1}{2}([V_1]\{v\}) \cdot ([V_1]\{v\})\right) \\ &+ EA\left(\frac{1}{2}([V_1]\{w\}) \cdot ([V_1]\{w\})\right) \\ &\cdot ([V_2]\{v\}) + \{N_2\} + \{f_y\}\end{aligned} \tag{C.63}$$

and

$$\begin{aligned}[M_w]\{\ddot{w}\} = &-EI_y[W_4]\{w\} + EA([V_1]\{w\}) \cdot ([U_2]\{u\}) \\ &+ EA([V_1]\{v\}) \cdot ([V_2]\{v\}) \\ &+ EA([V_1]\{w\}) \cdot ([V_2]\{w\}) \\ &+ EA\left([U_1]\{u\} + \frac{1}{2}([V_1]\{v\}) \cdot ([V_1]\{v\})\right) \\ &+ EA\left(\frac{1}{2}([V_1]\{w\}) \cdot ([V_1]\{w\})\right) \\ &\cdot ([V_2]\{w\}) + \{N_3\} + \{f_z\},\end{aligned} \tag{C.64}$$

where $[M_u]$, $[U_1]$, $[U_2]$, $[V_1]$, and $[V_2]$ are given in Equations C.41, C.44, and C.45, and

$$[M_v] = \begin{bmatrix} \rho A + \frac{2\rho I_z}{h^2} & -\frac{\rho I_z}{h^2} & 0 & 0 \\ -\frac{\rho I_z}{h^2} & \rho A + \frac{2\rho I_z}{h^2} & -\frac{\rho I_z}{h^2} & 0 \\ 0 & -\frac{\rho I_z}{h^2} & \rho A + \frac{2\rho I_z}{h^2} & -\frac{\rho I_z}{h^2} \\ 0 & 0 & -\frac{2\rho I_z}{h^2} & \rho A + \frac{2M_p}{h} + \frac{2\rho I_z}{h^2} \end{bmatrix} \tag{C.65}$$

$$[M_w] = \begin{bmatrix} \rho A + \frac{2\rho I_y}{h^2} & -\frac{\rho I_y}{h^2} & 0 & 0 \\ -\frac{\rho I_y}{h^2} & \rho A + \frac{2\rho I_y}{h^2} & -\frac{\rho I_y}{h^2} & 0 \\ 0 & -\frac{\rho I_y}{h^2} & \rho A + \frac{2\rho I_y}{h^2} & -\frac{\rho I_y}{h^2} \\ 0 & 0 & -\frac{2\rho I_y}{h^2} & \rho A + \frac{2M_p}{h} + \frac{2\rho I_y}{h^2} \end{bmatrix} \tag{C.66}$$

$$[V_4] = \frac{1}{h^4}\begin{bmatrix} 6+\frac{kh-2EI_z}{kh+2EI_z} & -4 & 1 & 0 & 0 & 0 \\ -4 & 6 & -4 & 1 & 0 & 0 \\ 1 & -4 & 6 & -4 & 1 & 0 \\ 0 & 1 & -4 & 6 & -4 & 1 \\ 0 & 0 & 1 & -4 & 5 & -2 \\ 0 & 0 & 0 & 0 & -4 & 2 \end{bmatrix} \tag{C.67}$$

$$[W_4] = \frac{1}{h^4}\begin{bmatrix} 6+\frac{kh-2EI_y}{kh+2EI_y} & -4 & 1 & 0 & 0 & 0 \\ -4 & 6 & -4 & 1 & 0 & 0 \\ 1 & -4 & 6 & -4 & 1 & 0 \\ 0 & 1 & -4 & 6 & -4 & 1 \\ 0 & 0 & 1 & -4 & 5 & -2 \\ 0 & 0 & 0 & 0 & -4 & 2 \end{bmatrix} \tag{C.68}$$

and

$$\{N_1\} = -\frac{EA}{h^3}\begin{bmatrix} 0 \\ 0 \\ 0 \\ 0 \\ (v_N - v_{N-1})^2 + (w_N - w_{N-1})^2 \end{bmatrix}$$

$$\{N_2\} = \frac{(v_N - v_{N-1})}{h}\{N_1\}$$

$$\{N_3\} = \frac{(w_N - w_{N-1})}{h}\{N_1\}. \tag{C.69}$$

The equations of motion in Equations C.62, C.63, and C.64 can be written as $6N$ coupled first order nonlinear ordinary differential equations by letting $\{u\} = \{Y_{(1)}\}$, $\{\dot{u}\} = \{Y_{(2)}\}$, $\{v\} = \{Y_{(3)}\}$, $\{\dot{v}\} = \{Y_{(4)}\}$, $\{w\} = \{Y_{(5)}\}$, $\{\dot{w}\} = \{Y_{(6)}\}$. Again, these ordinary differential equations are solved using the 4^{th} order Runge-Kutta algorithm. Sample MATLAB codes are included next.

2.2 Sample MATLAB Codes for 3D System

2.2.1 Main Program

```
clear
tic
global counter cn N nd h U1 U2 V1 V2 V4 W4 EI1 EI2 EA p m IMT1 IMT2 IML x
wf
N=14; %number of nodes
%properties
rho=2770; E=73e9; ro=0.0127; ri=0.011; L=1.28;
I1=pi*(ro^4-ri^4)/4; I2=pi*(ro^4-ri^4)/4; A=pi*(ro^2-ri^2);
K=38.8; Mp=0.236;
wf=0;
PLOT=1;
Tf=80;
tint=0.01;
qn=800; %qn is number of intervals
EI1=E*I1;
EI2=E*I2;
```

```
EA=E*A;
m=rho*A;
Er=E/rho;
J1=rho*I1;
J2=rho*I2;
h=L/N; % inverval between nodes The first node is not at x=0
x=[h:h:L]';
int=Tf/qn; %int=time interval
%-----------------------------------------------------------
%mass matrix for the transverse equation
Q2=2*eye(N)+[zeros(N-1,1) -eye(N-1);zeros(1,N)]+...
   [zeros(1,N);-eye(N-1) zeros(N-1,1)];
MT1=diag([m*ones(N-1,1); m+2*Mp/h])+J1/h^2*Q2; MT(N,N-1)
   =J1/h^2*(-2);
MT2=diag([m*ones(N-1,1); m+2*Mp/h])+J2/h^2*Q2; MT(N,N-1)
   =J2/h^2*(-2);
IMT1=inv(MT1);
IMT2=inv(MT2);
ML=[m*ones(N-1,1); m+2*Mp/h];
IML=1./ML;
%-----------------------------------------------------------
%Forming the V4 matrix. It is the linear part and same as MS
K1=(K*h-2*EI1)/(K*h+2*EI1);
K2=(K*h-2*EI2)/(K*h+2*EI2);
TMP= 6*eye(N)+[zeros(1,N);-4*eye(N-1) zeros(N-1,1)]+...
[zeros(2,N);eye(N-2) zeros(N-2,2)]+...
[zeros(N-1,1) -4*eye(N-1); zeros(1,N)]+...
[zeros(N-2,2) eye(N-2); zeros(2,N)];
%at both ends
TMP(1,1)=6+K1; TMP(N,N)=2; TMP(N,N-1)=-4; TMP(N,N-2)=2;
TMP(N-1,N)=-2; TMP(N-1,N-1)=5;
V4=TMP./h^4;
W4=V4; W4(1,1)=(6+K2)/h^4;
%-----------------------------------------------------------
% necessary matrices for nonlinear terms
Q1=[zeros(N-1,1) eye(N-1);zeros(1,N)]+[zeros(1,N); -eye(N-1) zeros(N-1,1)];
V1=Q1; V1(N,N-1)=-2; V1(N,N)=2; V1=1/(2*h)*V1;
V2=-Q2; V2(N,N-1)=0; V2(N,N)=0; V2=(1/h^2)*V2;
U1=V1;
U2=-Q2; U2(N,N-1)=2; U2(N,N)=-2; U2=1/h^2*U2;
%-----------------------------------------------------------
%external forcing
p=[(rhof*Af-rho*A)*ones(nd,1); -rho*A*ones(N-nd,1)]*g;
%f1 and f2 defined inside of fdiffun3.m
%-----------------------------------------------------------
%initial diplacement
Uo=-0.00125*x; Vo=0.05*x; Wo=zeros(N,1);
Udo=zeros(N,1); Vdo=zeros(N,1); Wdo=0.1*x;
uo=[Uo; Udo];
vo=[Vo; Vdo];
```

```
wo=[Wo; Wdo];
Yo=[uo;vo;wo];
Ys=Yo';
ts=0;
save prac ts Yo Ys
options=odeset('RelTol',1e-4,'AbsTol', 1e-7);
for q=1:qn;
   to=int*(q-1); tf=int*q;
   tspan=[to:tint:tf]';
   load prac
   counter=0; cn=1;
   [t,Y]=ode45('fdiffun3',tspan,Yo,options);
   ts=[ts;t(2:size(t,1))];
   NN=size(t,1); tmp=Y(2:size(Y,1),:);
   Yo=Y(NN,:); Ys=[Ys;tmp];
   save prac ts Yo Ys
   if PLOT==1;
   figure(1)
   subplot(3,1,1)
   plot(ts,Ys(:,N),'b:')
   subplot(3,1,2)
   plot(ts,Ys(:,3*N),'b:')
   subplot(3,1,3)
   plot(ts,Ys(:,5*N),'b:')
   pause(1)
   end
end
save efn2 ts Yo Ys
toc
```

2.2.2 Function Used in the Main Program

```
function dot=fdiffun3(t,Y)
global counter cn N nd h U1 U2 V1 V2 V4 W4 EI1 EI2 EA p m IMT1 IMT2 IML x
wf
u=Y(1:N); v=Y(2*N+1:3*N); w=Y(4*N+1:5*N);
ud=Y(N+1:2*N); vd=Y(3*N+1:4*N); wd=Y(5*N+1:6*N);
vp=V1*v; vpp=V2*v; wp=V1*w; wpp=V2*w;
NN1=-EA/h^3*((v(N)-v(N-1))^2+(w(N)-w(N-1))^2);
f1=2*(exp(x)-1)*cos(wf*t); %
f2=zeros(N,1);
mudd=EA*(U2*u+vp.*vpp+wp.*wpp)+[zeros(N-1,1); NN1];
udd=IML.*(mudd+p);
vdd=IMT1*(-EI1*V4*v+mudd.*vp+EA*(U1*u+0.5*vp.*vp
   +0.5*wp.*wp).*vpp+f1);
wdd=IMT2*(-EI2*W4*w+mudd.*wp+EA*(U1*u+0.5*vp.*vp
   +0.5*wp.*wp).*wpp+f2);
dot=[ud; udd; vd; vdd; wd; wdd];
counter=counter+1;
if counter==2000*cn;
```

```
    t
    cn=cn+1;
end
```

Appendix D
Energy Loss Over One Cycle In Damped Case

The equations of motion are given by

$$0 = \rho A_o \ddot{u} - \left(EA_o \left(u' + \frac{1}{2} v'^2 \right) \right)' - p \tag{D.1}$$

$$\begin{aligned} 0 = {} & \left(\rho A_o + C_A \rho_f \pi r_o^2 \right) \ddot{v} - \left(EA_o \left(u' + \frac{1}{2} v'^2 \right) v' \right)' \\ & - \left(\rho I_o \ddot{v}' \right)' + \left(EI_o v'' \right)'' - C_D \rho_f r_o \left(\dot{u} v' - \dot{v} \right) \left| \dot{u} v' - \dot{v} \right| \\ & - C_A \rho_f \pi r_o^2 \ddot{u} v'. \end{aligned} \tag{D.2}$$

The potential energy of this system is given by

$$PE = \frac{1}{2} \int_0^L \left[EA_o \left(u' + \frac{1}{2} v'^2 \right)^2 + EI_o v''^2 \right] dX + \frac{1}{2} k v' (0,t)^2 , \tag{D.3}$$

and the kinetic energy is given by

$$KE = \frac{1}{2} \int_0^L \left[\rho A_o (\dot{u}^2 + \dot{v}^2) + \rho I_o \dot{v}'^2 \right] dX + \frac{1}{2} M_p \left[\dot{v}^2 (L,t) + \dot{u}^2 (L,t) \right] . \tag{D.4}$$

Then the total energy, $E = PE + KE$, is given by

$$\begin{aligned} E = {} & \frac{1}{2} \int_0^L \left[\rho A_o (\dot{u}^2 + \dot{v}^2) + \rho I_o \dot{v}'^2 + EA_o \left(u' + \frac{1}{2} v'^2 \right)^2 + EI_o v''^2 \right] dX \\ & + \frac{1}{2} M_p \left[\dot{v}^2 (L,t) + \dot{u}^2 (L,t) \right] + \frac{1}{2} k v' (0,t)^2 . \end{aligned} \tag{D.5}$$

The change in energy with time is given by

$$\begin{aligned} \frac{dE}{dt} = {} & \int_0^L \left[\rho A_o (\dot{u}\ddot{u} + \dot{v}\ddot{v}) + \rho I_o \dot{v}' \ddot{v}' \right. \\ & \left. + EA_o \left(u' + \frac{1}{2} v'^2 \right) \left(\dot{u}' + v' \dot{v}' \right) + EI_o v'' \dot{v}'' \right] dX \\ & + M_p \left[\dot{v} (L,t) \ddot{v} (L,t) + \dot{u} (L,t) \ddot{u} (L,t) \right] + k v' (0,t) \dot{v}' (0,t) . \end{aligned} \tag{D.6}$$

The terms, $\int_0^L \rho I_o \dot{v}' \ddot{v}' dX$, $\int_0^L EA_o \left(u' + \frac{1}{2}v'^2\right) v' \dot{v}' dX$, $\int_0^L EA_o \left(u' + \frac{1}{2}v'^2\right) \dot{u}' dX$, and $\int_0^L EI_o v'' \dot{v}'' dX$, are integrated by parts such that

$$\begin{aligned}\frac{dE}{dt} = &\int_0^L \left[\rho A_o(\dot{u}\ddot{u} + \dot{v}\ddot{v}) - (\rho I_o \ddot{v}')' \dot{v} - \left(EA_o\left(u' + \frac{1}{2}v'^2\right)\right)' \dot{u}\right. \\ &- \left(EA_o\left(u' + \frac{1}{2}v'^2\right)v'\right)' \dot{v} + (EI_o v'')'' \dot{v}\Big] dX \\ &+ \left(\rho I_o \ddot{v}' \dot{v} + EA_o\left(u' + \frac{1}{2}v'^2\right)\dot{u} + EA_o\left(u' + \frac{1}{2}v'^2\right)v'\dot{v}\right. \\ &+ \left.(EI_o v'')\dot{v}' - (EI_o v'')'\dot{v}\right)\Big|_0^L \\ &+ M_p\left[\dot{v}(L,t)\ddot{v}(L,t) + \dot{u}(L,t)\ddot{u}(L,t)\right] + kv'(0,t)\dot{v}'(0,t). \end{aligned} \tag{D.7}$$

The terms evaluated at the boundaries disappear due to boundary conditions. Therefore, we have

$$\begin{aligned}\frac{dE}{dt} = &\int_0^L \left\{\left[\rho A_o \ddot{u} - \left(EA_o\left(u' + \frac{1}{2}v'^2\right)\right)'\right]\dot{u}\right. \\ &+ \left.\left[\rho A_o \ddot{v} - (\rho I_o \ddot{v}')' - \left(EA_o\left(u' + \frac{1}{2}v'^2\right)v'\right)' + (EI_o v'')''\right]\dot{v}\right\} dX. \end{aligned} \tag{D.8}$$

From the equations of motion, we can write

$$\frac{dE}{dt} = \int_0^L \left\{C_D \rho_f r_o \left(\dot{u}v' - \dot{v}\right)\left|\dot{u}v' - \dot{v}\right| + C_A \rho_f \pi r_o^2 \left(\ddot{u}v' - \ddot{v}\right)\right\} \dot{v} dX. \tag{D.9}$$

The change in total energy between $t = \tau$ and τ_o is given by

$$\begin{aligned}&E(\tau) - E(\tau_o) \\ &= \int_0^L \left[\int_{\tau_o}^{\tau} \left\{C_D \rho_f r_o \left(\dot{u}v' - \dot{v}\right)\left|\dot{u}v' - \dot{v}\right| + C_A \rho_f \pi r_o^2 \left(\ddot{u}v' - \ddot{v}\right)\right\} \dot{v} dt\right] dX. \end{aligned} \tag{D.10}$$

Appendix E
Steady-State Response Due to Ocean Current

The equations of motion are given by

$$0 = \rho A_o \ddot{u} - \left(EA_o \left(u' + \frac{1}{2} v'^2 \right) \right)' - p \tag{E.1}$$

$$0 = \left(\rho A_o + C_A \rho_f \pi r_o^2 \right) \ddot{v} - \left(EA_o \left(u' + \frac{1}{2} v'^2 \right) v' \right)' - \left(\rho I_o \ddot{v}' \right)' + \left(EI_o v'' \right)''$$
$$- C_D \rho_f r_o \left(U + \dot{u} v' - \dot{v} \right) \left| U + \dot{u} v' - \dot{v} \right| - C_A \rho_f \pi r_o^2 \ddot{u} v'. \tag{E.2}$$

The steady-state response is obtained by setting the time derivatives equal to zero so that

$$- \left(EA_o \left(u' + \frac{1}{2} v'^2 \right) \right)' = p \tag{E.3}$$

$$- \left(EA_o \left(u' + \frac{1}{2} v'^2 \right) v' \right)' + \left(EI_o v'' \right)'' - C_D \rho_f r_o U^2 sign\left(U \right) = 0. \tag{E.4}$$

Substituting the first equation into the second, we obtain

$$pv' + v'' \int_0^X p dX + \left(EI_o v'' \right)'' = C_D \rho_f r_o U^2 sign\left(U \right). \tag{E.5}$$

In our case,

$$\int_0^X p dX = \left(\rho_f g A_f - \rho g A \right) X, \qquad \text{for } X < d$$
$$= \rho_f g A_f d - \rho g A X, \qquad \text{for } d < X < L. \tag{E.6}$$

Writing the spatial derivatives using finite difference equations, we can obtain the steady-state transverse displacement $v\left(X\right)$ numerically. The axial displacement u is then obtained using Equation E.3,

$$u = - \int_0^x \left[\frac{1}{EA_o} \int_0^x p dx + \frac{1}{2} v'^2 \right] dx. \tag{E.7}$$

The actual configuration of the beam is obtained by plotting $X + u\left(X\right)$ versus $v\left(X\right)$.

[13] G. Bhashyam and G. Prathap. The second frequency spectrum of Timoshenko beam. *Journal of Sound and Vibration*, 76:407–420, 1981.

[14] K. Billah. *A Study of Vortex Induced Vibration.* PhD thesis, Princeton University, 1989.

[15] L. Borgman. Ocean wave simulation for engineering design. *Journal of the Waterway and Harbors Division*, 95:557–583, 1969.

[16] W. Bottega. Dynamics and stability of support excited beam-columns with end mass. *Dynamics and Stability of Systems*, 1:201–215, 1986.

[17] S. Chakrabarti. *Hydrodynamics of Offshore Structures.* Computational Mechanics Publications, 1987.

[18] G. Cowper. The shear coefficient in Timoshenko's beam theory. *Journal of Applied Mechanics*, 88:335–340, 1966.

[19] R. Davies. The frequency of transverse vibration of a loaded fixed-free bar III. the effect of rotatory inertia of the bar. *Philosophical Magazine*, 23:563, 1937.

[20] S. de Groot. Quantitative assessment of the development of the offshore oil and gas industry in the North Sea. *ICES Journal of Marine Science*, 53:1045–1050, 1996.

[21] C. Dolph. On the Timoshenko theory of transverse beam vibrations. *Quarterly of Applied Mathematics*, 12:175–187, 1954.

[22] E. Dowell. Non-linear oscillator models in bluff body aeroelasticity. *Journal of Sound and Vibration*, 75(2):251–264, 1981.

[23] R. Haberman. *Elementary Applied Partial Differential Equations.* Prentice-Hall, Inc., 1987.

[24] S. Han and H. Benaroya. Nonlinear coupled transverse and axial vibration of a compliant structure 1: Formulation and free vibration. *Journal of Sound and Vibration*, 237(5):837–873, 2000.

[25] S. Han and H. Benaroya. Nonlinear coupled transverse and axial vibration of a compliant structure 2: Forced vibration. *Journal of Sound and Vibration*, 237(5):874–899, 2000.

[26] S. Han and H. Benaroya. Three dimensional vibration of a compliant tower. *Accepted to Journal of Sound and Vibration*, 2001. Accepted to Journal of Sound and Vibration.

[27] S. Han, H. Benaroya, and T. Wei. Dynamics of transversely vibrating beams using four engineering theories. *Journal of Sound and Vibration*, 225(5):935–988, 1999.

[28] G. Herrmann. Forced motions of Timoshenko beam theory. *Journal of Applied Mechanics, Tras. ASME*, 77:53–56, 1955.

[29] N. Hogben. Wave loads on structures. In *Behavior of Offshore Structures (BOSS)*, Oslo, Norway, 1976.

References

[1] B. Abbas and J. Thomas. The second frequency spectrum of Timoshenko beams. *Journal of Sound and Vibration*, 51:123–137, 1977.

[2] R. Adrezin, P. Bar-Avi, and H. Benaroya. Dynamic response of compliant offshore structures - review. *Journal of Aerospace Engineering*, 9(4):114–131, 1996.

[3] R. Adrezin and H. Benaroya. Non-linear stochastic dynamics of tension leg platforms. *Journal of Sound and Vibration*, 220(1):27–65, 1999.

[4] R. Adrezin and H. Benaroya. Response of a tension leg platform to stochastic wave forces. *Probabilistic Engineering Mechanics*, 14:3–17, 1999.

[5] S. Ahmad, N. Islam, and A. Ali. Wind-induced response of a tension leg platform. *Journal of Wind Engineering and Industrial Aerodynamics*, 72:225–240, 1997.

[6] R. Anderson. Flexural vibration of uniform beams according to the Timoshenko theory. *Journal of Applied Mechanics*, 75:504–510, 1953.

[7] G. Baker and J. Gollub. *Chaotic Dynamics, an Introduction.* Cambridge University Press, Cambridge, UK, 1996.

[8] P. Bar-Avi. *Dynamic Response of An Offshore Articulated Tower.* PhD thesis, Rutgers, the State University of New Jersey, May 1996.

[9] P. Bar-Avi and H. Benaroya. Planar motion of an articulated tower with an elastic apendage. *Journal of Sound and Vibration*, 198:27–50, 1996.

[10] P. Bar-Avi and H. Benaroya. *Nonlinear Dynamics of Compliant Offshore Structures.* Swets and Zeitlinger Publishers, Lisse, The Netherlands, 1997.

[11] A. Barr. Some notes on the resonance of Timoshenko beams and the effects of lateral inertia on flexural vibration. pages 448–458. Proceedings of the 9th International Congress of Applied Mechanics 7, 1956.

[12] H. Benaroya. *Mechanical Vibration.* Prentice Hall, Inc., 1998.

[30] T. Huang. The effect of rotatory inertia and of shear deformation on the frequency and normal mode equations of uniform beams with simple end conditions. *Journal of Applied Mechanics*, 28:579–584, 1961.

[31] D. Inman. *Engineering Vibration.* Prentice Hall, Inc., 1994.

[32] M. Isaacson. Wave and current forces on fixed offshore structures. *Canadian Journal of Civil Engineering*, 15:937–947, 1988.

[33] A. Jain. Nonlinear coupled response of offshore tension leg platforms to regular wave forces. *Ocean Engineering*, 24(7):577–592, 1997.

[34] R. Jain and C. Kirk. Dynamic response of a double articulated offshore loading structure to noncollinear waves and current. *Journal of Energy Resources Technology*, 103:41–47, 1981.

[35] A. Kareem and Y. Li. Response of tension leg platforms to wind, wave, and currents: A frequency domain approach. *Offshore Technology Conference*, 114:175–184, 1990.

[36] A. Kareem and Y. Li. Wind-excited surge response of tension-leg platform: Frequency domain approach. *Journal of Engineering Mechanics*, 119(1):161–173, 1993.

[37] E. Kruszewski. Effects of transverse shear and rotary inertia on the natural frequencies of a uniform beam. *National Advisory Committee for Aeronautics*, page TN 1909, 1949.

[38] H. Lamb. *Hydrodynamics.* Dover Publications, Inc., 1945.

[39] C. Lanczos. *The Variational Principles of Mechanics.* Dover Publications Inc., pg. 89, 1986.

[40] J. Leonard and R. Young. Coupled response of compliant offshore platforms. *Engineering Structures*, 7:74–84, 1985.

[41] M. Levinson. Further results of a new beam theory. *Journal of Sound and Vibration*, 77:440–444, 1981.

[42] M. Levinson. A new rectangular beam theory. *Journal of Sound and Vibration*, 74:81–87, 1981.

[43] M. Levinson and D. Cooke. On the two frequency spectra of Timoshenko beams. *Journal of Sound and Vibration*, 84:319–326, 1982.

[44] A. Love. *A Treatise on the Mathematical Theory of Elasticity.* Dover Publications, Inc., 1927.

[45] L. Meirovitch. *Analytical Methods in Vibrations.* Macmillian Publishing Co., Inc., 1967.

[46] L. Meirovitch. *Elements of Vibration Analysis.* McGraw-Hill Book Company, Inc., 1986.

[47] L. Meirovitch. *Principles and Techniques of Vibrations.* Prentice Hall, Inc., 1997.

[48] B. Mekha. Implications of tendon modeling on nonlinear response of TLP. *Journal of Structural Engineering*, 122(2):142–149, 1996.

[49] B. Miller. Wave slamming loads on horizontal circular elements of offshore structures. Technical Report RINA Paper No. 5, Journal of the Royal Institute of Naval Architecture, 1977.

[50] B. Miller. Wave slamming on offshore structures. Technical Report Report No. NMI-R81, National Maritime Institute, 1980.

[51] R. Mindlin and H. Deresiewicz. Timoshenko shear coefficient for flexural vibrations of beams. In *Proceedings of 2nd U.S. National Congress of Applied Mechanics*, pages 175–178, New York, 1954. ASME.

[52] N. Minorsky. *Nonlinear Oscillations.* Robert E. Krieger Publishing Company, Inc., 1962.

[53] J. Morgan and D. Malaeb. Dynamic analysis of tension leg platforms. In *Proceedings of the Second International Offshore Mechanics and Artic Engineering Symposium*, pages 31–37, 1983.

[54] J. Morison, M. O'Brien, J. Johnson, and S. Schaaf. The force exerted by surface waves on piles. *Petroleum Transactions, AIME*, 189:149–157, 1950.

[55] B. Muga and J. Wilson. *Dynamic Analysis of Ocean Structures.* Plenum Press, 1970.

[56] M. Mulk and J. Falzarano. Complete six-degrees-of-freedom nonlinear ship rolling motion. *Journal of Offshore Mechanics and Arctic Engineering*, 116:191–201, 1994.

[57] B. Munson, D. Young, and T. Okiishi. *Fundamentals of Fluid Mechanics.* John Wiley and Sons, Inc., 1994.

[58] B. Natvig and J. Pendered. Nonlinear motion response of floating structures to wave excitation. In *Proceedings of the Offshore Technology Conference*, 1977. OTC 2796.

[59] V. V. Novozhilov. *Foundations of the Nonlinear Theory of Elasticity.* Graylock Press, 1953.

[60] C. Oran. Effect of static offset on TLP modeling. *Journal of Engineering Mechanics*, 118(1):74–91, 1992.

[61] R. Panton. *Incompressible Flow.* John Wiley and Sons, Inc., 1996.

[62] M. Patel. *Dynamics of Offshore Structures.* Butterworths and Co. Ltd, 1989.

[63] E. Popov. *Engineering Mechanics of Solids.* Prentice-Hall, Inc., 1990.

[64] S. Rao. *Mechanical Vibrations.* Addison-Wesley Publishing Company, third edition, 1995.

[65] H. Reismann and P. Pawlik. *Elastokinetics.* West Publishing Co., 1974.

[66] S. Rice. *Mathematical Analysis of Random Noise.* Dover Publications, Inc., New York, 1954.

[67] T. Sarpkaya and M. Isaacson. *Mechanics of Wave Forces on Offshore Structures.* Van Nostrand Reinhold Company, 1981.

[68] I. Sokolnikoff. *Mathematical Theory of Elasticity.* McGraw-Hill Book Company, Inc., 1956.

[69] G. Spence and E. Seldin. Sonic resonances of a bar and compound torsion oscillator. *Journal of Applied Physics*, pages 3383–3389, 1970.

[70] N. Stephen. On the variation of Timoshenko's shear coefficient with frequency. *ASME Journal of Applied Mechanics*, 45:695–697, 1978.

[71] N. Stephen and M. Levinson. A second order beam theory. *Journal of Sound and Vibration*, 67:293–305, 1979.

[72] J. Strutt. *Theory of Sound.* Macmillan, London, 1877.

[73] H. Sverdrup and W. Munk. Wind, Sea, and Swell: Theory of Relations for Forecasting. *U.S. Navy Hydrographic Office, Publication No. 601*, 1947.

[74] K. Takahashi and Y. Konishi. Non-linear vibrations of cables in three dimensions, part I: Non-linear free vibrations. *Journal of Sound and Vibration*, 118(1):69–84, 1987.

[75] K. Takahashi and Y. Konishi. Non-linear vibrations of cables in three dimensions, part II: Out-of-plane vibrations under in-plain sinuoidally time-varying load. *Journal of Sound and Vibration*, 118(1):85–97, 1987.

[76] W. Thomson. *Theory of Vibration with Applications.* Prentice Hall, Inc., fourth edition, 1993.

[77] S. Timoshenko. On the correction for shear of the differential equation for transverse vibrations of bars of uniform cross-section. *Philosophical Magazine*, 41:744, 1921.

[78] S. Timoshenko. On the transverse vibration of bars of uniform cross-section. *Philosophical Magazine*, 43:125, 1922.

[79] S. Timoshenko. *History of Strength of Materials.* Dover Publications, Inc., 1953.

[80] R. Traill-Nash and A. Collar. The effects of shear flexibility and rotatory inertia on the bending vibrations of beams. *Quarterly Journal of Mechanics and Applied Mathematics*, 6:186–213, 1953.

[81] J. Wilson. *Dynamics of Offshore Structures.* John Wiley and Sons, Inc., 1984.

[82] A. Yigit and A. Christoforou. Coupled axial and transverse vibrations of oilwell drillstrings. *Journal of Sound and Vibration*, 195(4):617–627, 1996.

Index

Mechanics

SOLID MECHANICS AND ITS APPLICATIONS

Series Editor: G.M.L. Gladwell

Aims and Scope of the Series

The fundamental questions arising in mechanics are: *Why?*, *How?*, and *How much?* The aim of this series is to provide lucid accounts written by authoritative researchers giving vision and insight in answering these questions on the subject of mechanics as it relates to solids. The scope of the series covers the entire spectrum of solid mechanics. Thus it includes the foundation of mechanics; variational formulations; computational mechanics; statics, kinematics and dynamics of rigid and elastic bodies; vibrations of solids and structures; dynamical systems and chaos; the theories of elasticity, plasticity and viscoelasticity; composite materials; rods, beams, shells and membranes; structural control and stability; soils, rocks and geomechanics; fracture; tribology; experimental mechanics; biomechanics and machine design.

1. R.T. Haftka, Z. Gürdal and M.P. Kamat: *Elements of Structural Optimization.* 2nd rev.ed., 1990 ISBN 0-7923-0608-2
2. J.J. Kalker: *Three-Dimensional Elastic Bodies in Rolling Contact.* 1990 ISBN 0-7923-0712-7
3. P. Karasudhi: *Foundations of Solid Mechanics.* 1991 ISBN 0-7923-0772-0
4. *Not published*
5. *Not published.*
6. J.F. Doyle: *Static and Dynamic Analysis of Structures.* With an Emphasis on Mechanics and Computer Matrix Methods. 1991 ISBN 0-7923-1124-8; Pb 0-7923-1208-2
7. O.O. Ochoa and J.N. Reddy: *Finite Element Analysis of Composite Laminates.* ISBN 0-7923-1125-6
8. M.H. Aliabadi and D.P. Rooke: *Numerical Fracture Mechanics.* ISBN 0-7923-1175-2
9. J. Angeles and C.S. López-Cajún: *Optimization of Cam Mechanisms.* 1991 ISBN 0-7923-1355-0
10. D.E. Grierson, A. Franchi and P. Riva (eds.): *Progress in Structural Engineering.* 1991 ISBN 0-7923-1396-8
11. R.T. Haftka and Z. Gürdal: *Elements of Structural Optimization.* 3rd rev. and exp. ed. 1992 ISBN 0-7923-1504-9; Pb 0-7923-1505-7
12. J.R. Barber: *Elasticity.* 1992 ISBN 0-7923-1609-6; Pb 0-7923-1610-X
13. H.S. Tzou and G.L. Anderson (eds.): *Intelligent Structural Systems.* 1992 ISBN 0-7923-1920-6
14. E.E. Gdoutos: *Fracture Mechanics.* An Introduction. 1993 ISBN 0-7923-1932-X
15. J.P. Ward: *Solid Mechanics.* An Introduction. 1992 ISBN 0-7923-1949-4
16. M. Farshad: *Design and Analysis of Shell Structures.* 1992 ISBN 0-7923-1950-8
17. H.S. Tzou and T. Fukuda (eds.): *Precision Sensors, Actuators and Systems.* 1992 ISBN 0-7923-2015-8
18. J.R. Vinson: *The Behavior of Shells Composed of Isotropic and Composite Materials.* 1993 ISBN 0-7923-2113-8
19. H.S. Tzou: *Piezoelectric Shells.* Distributed Sensing and Control of Continua. 1993 ISBN 0-7923-2186-3
20. W. Schiehlen (ed.): *Advanced Multibody System Dynamics.* Simulation and Software Tools. 1993 ISBN 0-7923-2192-8
21. C.-W. Lee: *Vibration Analysis of Rotors.* 1993 ISBN 0-7923-2300-9
22. D.R. Smith: *An Introduction to Continuum Mechanics.* 1993 ISBN 0-7923-2454-4
23. G.M.L. Gladwell: *Inverse Problems in Scattering.* An Introduction. 1993 ISBN 0-7923-2478-1

Mechanics

SOLID MECHANICS AND ITS APPLICATIONS

Series Editor: G.M.L. Gladwell

24. G. Prathap: *The Finite Element Method in Structural Mechanics.* 1993 ISBN 0-7923-2492-7
25. J. Herskovits (ed.): *Advances in Structural Optimization.* 1995 ISBN 0-7923-2510-9
26. M.A. González-Palacios and J. Angeles: *Cam Synthesis.* 1993 ISBN 0-7923-2536-2
27. W.S. Hall: *The Boundary Element Method.* 1993 ISBN 0-7923-2580-X
28. J. Angeles, G. Hommel and P. Kovács (eds.): *Computational Kinematics.* 1993 ISBN 0-7923-2585-0
29. A. Curnier: *Computational Methods in Solid Mechanics.* 1994 ISBN 0-7923-2761-6
30. D.A. Hills and D. Nowell: *Mechanics of Fretting Fatigue.* 1994 ISBN 0-7923-2866-3
31. B. Tabarrok and F.P.J. Rimrott: *Variational Methods and Complementary Formulations in Dynamics.* 1994 ISBN 0-7923-2923-6
32. E.H. Dowell (ed.), E.F. Crawley, H.C. Curtiss Jr., D.A. Peters, R. H. Scanlan and F. Sisto: *A Modern Course in Aeroelasticity.* Third Revised and Enlarged Edition. 1995 ISBN 0-7923-2788-8; Pb: 0-7923-2789-6
33. A. Preumont: *Random Vibration and Spectral Analysis.* 1994 ISBN 0-7923-3036-6
34. J.N. Reddy (ed.): *Mechanics of Composite Materials.* Selected works of Nicholas J. Pagano. 1994 ISBN 0-7923-3041-2
35. A.P.S. Selvadurai (ed.): *Mechanics of Poroelastic Media.* 1996 ISBN 0-7923-3329-2
36. Z. Mróz, D. Weichert, S. Dorosz (eds.): *Inelastic Behaviour of Structures under Variable Loads.* 1995 ISBN 0-7923-3397-7
37. R. Pyrz (ed.): *IUTAM Symposium on Microstructure-Property Interactions in Composite Materials.* Proceedings of the IUTAM Symposium held in Aalborg, Denmark. 1995 ISBN 0-7923-3427-2
38. M.I. Friswell and J.E. Mottershead: *Finite Element Model Updating in Structural Dynamics.* 1995 ISBN 0-7923-3431-0
39. D.F. Parker and A.H. England (eds.): *IUTAM Symposium on Anisotropy, Inhomogeneity and Nonlinearity in Solid Mechanics.* Proceedings of the IUTAM Symposium held in Nottingham, U.K. 1995 ISBN 0-7923-3594-5
40. J.-P. Merlet and B. Ravani (eds.): *Computational Kinematics '95.* 1995 ISBN 0-7923-3673-9
41. L.P. Lebedev, I.I. Vorovich and G.M.L. Gladwell: *Functional Analysis.* Applications in Mechanics and Inverse Problems. 1996 ISBN 0-7923-3849-9
42. J. Menčik: *Mechanics of Components with Treated or Coated Surfaces.* 1996 ISBN 0-7923-3700-X
43. D. Bestle and W. Schiehlen (eds.): *IUTAM Symposium on Optimization of Mechanical Systems.* Proceedings of the IUTAM Symposium held in Stuttgart, Germany. 1996 ISBN 0-7923-3830-8
44. D.A. Hills, P.A. Kelly, D.N. Dai and A.M. Korsunsky: *Solution of Crack Problems.* The Distributed Dislocation Technique. 1996 ISBN 0-7923-3848-0
45. V.A. Squire, R.J. Hosking, A.D. Kerr and P.J. Langhorne: *Moving Loads on Ice Plates.* 1996 ISBN 0-7923-3953-3
46. A. Pineau and A. Zaoui (eds.): *IUTAM Symposium on Micromechanics of Plasticity and Damage of Multiphase Materials.* Proceedings of the IUTAM Symposium held in Sèvres, Paris, France. 1996 ISBN 0-7923-4188-0
47. A. Naess and S. Krenk (eds.): *IUTAM Symposium on Advances in Nonlinear Stochastic Mechanics.* Proceedings of the IUTAM Symposium held in Trondheim, Norway. 1996 ISBN 0-7923-4193-7
48. D. Ieşan and A. Scalia: *Thermoelastic Deformations.* 1996 ISBN 0-7923-4230-5

Mechanics

SOLID MECHANICS AND ITS APPLICATIONS

Series Editor: G.M.L. Gladwell

49. J.R. Willis (ed.): *IUTAM Symposium on Nonlinear Analysis of Fracture.* Proceedings of the IUTAM Symposium held in Cambridge, U.K. 1997 ISBN 0-7923-4378-6
50. A. Preumont: *Vibration Control of Active Structures.* An Introduction. 1997 ISBN 0-7923-4392-1
51. G.P. Cherepanov: *Methods of Fracture Mechanics: Solid Matter Physics.* 1997 ISBN 0-7923-4408-1
52. D.H. van Campen (ed.): *IUTAM Symposium on Interaction between Dynamics and Control in Advanced Mechanical Systems.* Proceedings of the IUTAM Symposium held in Eindhoven, The Netherlands. 1997 ISBN 0-7923-4429-4
53. N.A. Fleck and A.C.F. Cocks (eds.): *IUTAM Symposium on Mechanics of Granular and Porous Materials.* Proceedings of the IUTAM Symposium held in Cambridge, U.K. 1997 ISBN 0-7923-4553-3
54. J. Roorda and N.K. Srivastava (eds.): *Trends in Structural Mechanics.* Theory, Practice, Education. 1997 ISBN 0-7923-4603-3
55. Yu.A. Mitropolskii and N. Van Dao: *Applied Asymptotic Methods in Nonlinear Oscillations.* 1997 ISBN 0-7923-4605-X
56. C. Guedes Soares (ed.): *Probabilistic Methods for Structural Design.* 1997 ISBN 0-7923-4670-X
57. D. François, A. Pineau and A. Zaoui: *Mechanical Behaviour of Materials.* Volume I: Elasticity and Plasticity. 1998 ISBN 0-7923-4894-X
58. D. François, A. Pineau and A. Zaoui: *Mechanical Behaviour of Materials.* Volume II: Viscoplasticity, Damage, Fracture and Contact Mechanics. 1998 ISBN 0-7923-4895-8
59. L.T. Tenek and J. Argyris: *Finite Element Analysis for Composite Structures.* 1998 ISBN 0-7923-4899-0
60. Y.A. Bahei-El-Din and G.J. Dvorak (eds.): *IUTAM Symposium on Transformation Problems in Composite and Active Materials.* Proceedings of the IUTAM Symposium held in Cairo, Egypt. 1998 ISBN 0-7923-5122-3
61. I.G. Goryacheva: *Contact Mechanics in Tribology.* 1998 ISBN 0-7923-5257-2
62. O.T. Bruhns and E. Stein (eds.): *IUTAM Symposium on Micro- and Macrostructural Aspects of Thermoplasticity.* Proceedings of the IUTAM Symposium held in Bochum, Germany. 1999 ISBN 0-7923-5265-3
63. F.C. Moon: *IUTAM Symposium on New Applications of Nonlinear and Chaotic Dynamics in Mechanics.* Proceedings of the IUTAM Symposium held in Ithaca, NY, USA. 1998 ISBN 0-7923-5276-9
64. R. Wang: *IUTAM Symposium on Rheology of Bodies with Defects.* Proceedings of the IUTAM Symposium held in Beijing, China. 1999 ISBN 0-7923-5297-1
65. Yu.I. Dimitrienko: *Thermomechanics of Composites under High Temperatures.* 1999 ISBN 0-7923-4899-0
66. P. Argoul, M. Frémond and Q.S. Nguyen (eds.): *IUTAM Symposium on Variations of Domains and Free-Boundary Problems in Solid Mechanics.* Proceedings of the IUTAM Symposium held in Paris, France. 1999 ISBN 0-7923-5450-8
67. F.J. Fahy and W.G. Price (eds.): *IUTAM Symposium on Statistical Energy Analysis.* Proceedings of the IUTAM Symposium held in Southampton, U.K. 1999 ISBN 0-7923-5457-5
68. H.A. Mang and F.G. Rammerstorfer (eds.): *IUTAM Symposium on Discretization Methods in Structural Mechanics.* Proceedings of the IUTAM Symposium held in Vienna, Austria. 1999 ISBN 0-7923-5591-1

SOLID MECHANICS AND ITS APPLICATIONS

Series Editor: G.M.L. Gladwell

69. P. Pedersen and M.P. Bendsøe (eds.): *IUTAM Symposium on Synthesis in Bio Solid Mechanics.* Proceedings of the IUTAM Symposium held in Copenhagen, Denmark. 1999 ISBN 0-7923-5615-2
70. S.K. Agrawal and B.C. Fabien: *Optimization of Dynamic Systems.* 1999 ISBN 0-7923-5681-0
71. A. Carpinteri: *Nonlinear Crack Models for Nonmetallic Materials.* 1999 ISBN 0-7923-5750-7
72. F. Pfeifer (ed.): *IUTAM Symposium on Unilateral Multibody Contacts.* Proceedings of the IUTAM Symposium held in Munich, Germany. 1999 ISBN 0-7923-6030-3
73. E. Lavendelis and M. Zakrzhevsky (eds.): *IUTAM/IFToMM Symposium on Synthesis of Nonlinear Dynamical Systems.* Proceedings of the IUTAM/IFToMM Symposium held in Riga, Latvia. 2000 ISBN 0-7923-6106-7
74. J.-P. Merlet: *Parallel Robots.* 2000 ISBN 0-7923-6308-6
75. J.T. Pindera: *Techniques of Tomographic Isodyne Stress Analysis.* 2000 ISBN 0-7923-6388-4
76. G.A. Maugin, R. Drouot and F. Sidoroff (eds.): *Continuum Thermomechanics.* The Art and Science of Modelling Material Behaviour. 2000 ISBN 0-7923-6407-4
77. N. Van Dao and E.J. Kreuzer (eds.): *IUTAM Symposium on Recent Developments in Non-linear Oscillations of Mechanical Systems.* 2000 ISBN 0-7923-6470-8
78. S.D. Akbarov and A.N. Guz: *Mechanics of Curved Composites.* 2000 ISBN 0-7923-6477-5
79. M.B. Rubin: *Cosserat Theories: Shells, Rods and Points.* 2000 ISBN 0-7923-6489-9
80. S. Pellegrino and S.D. Guest (eds.): *IUTAM-IASS Symposium on Deployable Structures: Theory and Applications.* Proceedings of the IUTAM-IASS Symposium held in Cambridge, U.K., 6–9 September 1998. 2000 ISBN 0-7923-6516-X
81. A.D. Rosato and D.L. Blackmore (eds.): *IUTAM Symposium on Segregation in Granular Flows.* Proceedings of the IUTAM Symposium held in Cape May, NJ, U.S.A., June 5–10, 1999. 2000 ISBN 0-7923-6547-X
82. A. Lagarde (ed.): *IUTAM Symposium on Advanced Optical Methods and Applications in Solid Mechanics.* Proceedings of the IUTAM Symposium held in Futuroscope, Poitiers, France, August 31–September 4, 1998. 2000 ISBN 0-7923-6604-2
83. D. Weichert and G. Maier (eds.): *Inelastic Analysis of Structures under Variable Loads.* Theory and Engineering Applications. 2000 ISBN 0-7923-6645-X
84. T.-J. Chuang and J.W. Rudnicki (eds.): *Multiscale Deformation and Fracture in Materials and Structures.* The James R. Rice 60th Anniversary Volume. 2001 ISBN 0-7923-6718-9
85. S. Narayanan and R.N. Iyengar (eds.): *IUTAM Symposium on Nonlinearity and Stochastic Structural Dynamics.* Proceedings of the IUTAM Symposium held in Madras, Chennai, India, 4–8 January 1999 ISBN 0-7923-6733-2
86. S. Murakami and N. Ohno (eds.): *IUTAM Symposium on Creep in Structures.* Proceedings of the IUTAM Symposium held in Nagoya, Japan, 3-7 April 2000. 2001 ISBN 0-7923-6737-5
87. W. Ehlers (ed.): *IUTAM Symposium on Theoretical and Numerical Methods in Continuum Mechanics of Porous Materials.* Proceedings of the IUTAM Symposium held at the University of Stuttgart, Germany, September 5-10, 1999. 2001 ISBN 0-7923-6766-9
88. D. Durban, D. Givoli and J.G. Simmonds (eds.): *Advances in the Mechanis of Plates and Shells The Avinoam Libai Anniversary Volume.* 2001 ISBN 0-7923-6785-5
89. U. Gabbert and H.-S. Tzou (eds.): *IUTAM Symposium on Smart Structures and Structonic Systems.* Proceedings of the IUTAM Symposium held in Magdeburg, Germany, 26–29 September 2000. 2001 ISBN 0-7923-6968-8

SOLID MECHANICS AND ITS APPLICATIONS

Series Editor: G.M.L. Gladwell

90. Y. Ivanov, V. Cheshkov and M. Natova: *Polymer Composite Materials – Interface Phenomena & Processes*. 2001 ISBN 0-7923-7008-2
91. R.C. McPhedran, L.C. Botten and N.A. Nicorovici (eds.): *IUTAM Symposium on Mechanical and Electromagnetic Waves in Structured Media*. Proceedings of the IUTAM Symposium held in Sydney, NSW, Australia, 18-22 Januari 1999. 2001 ISBN 0-7923-7038-4
92. D.A. Sotiropoulos (ed.): *IUTAM Symposium on Mechanical Waves for Composite Structures Characterization*. Proceedings of the IUTAM Symposium held in Chania, Crete, Greece, June 14-17, 2000. 2001 ISBN 0-7923-7164-X
93. V.M. Alexandrov and D.A. Pozharskii: *Three-Dimensional Contact Problems*. 2001 ISBN 0-7923-7165-8
94. J.P. Dempsey and H.H. Shen (eds.): *IUTAM Symposium on Scaling Laws in Ice Mechanics and Ice Dynamics*. Proceedings of the IUTAM Symposium held in Fairbanks, Alaska, U.S.A., 13-16 June 2000. 2001 ISBN 1-4020-0171-1
95. U. Kirsch: *Design-Oriented Analysis of Structures*. A Unified Approach. 2002 ISBN 1-4020-0443-5
96. A. Preumont: *Vibration Control of Active Structures*. An Introduction (2^{nd} Edition). 2002 ISBN 1-4020-0496-6
97. B.L. Karihaloo (ed.): *IUTAM Symposium on Analytical and Computational Fracture Mechanics of Non-Homogeneous Materials*. Proceedings of the IUTAM Symposium held in Cardiff, U.K., 18-22 June 2001. 2002 ISBN 1-4020-0510-5
98. S.M. Han and H. Benaroya: *Nonlinear and Stochastic Dynamics of Compliant Offshore Structures*. 2002 ISBN 1-4020-0573-3

ICASE/LaRC Interdisciplinary Series in Science and Engineering

1. J. Buckmaster, T.L. Jackson and A. Kumar (eds.): *Combustion in High-Speed Flows.* 1994 ISBN 0-7923-2086-X
2. M.Y. Hussaini, T.B. Gatski and T.L. Jackson (eds.): *Transition, Turbulence and Combustion.* Volume I: Transition. 1994 ISBN 0-7923-3084-6; set 0-7923-3086-2
3. M.Y. Hussaini, T.B. Gatski and T.L. Jackson (eds.): *Transition, Turbulence and Combustion.* Volume II: Turbulence and Combustion. 1994 ISBN 0-7923-3085-4; set 0-7923-3086-2
4. D.E. Keyes, A. Sameh and V. Venkatakrishnan (eds): *Parallel Numerical Algorithms.* 1997 ISBN 0-7923-4282-8
5. T.G. Campbell, R.A. Nicolaides and M.D. Salas (eds.): *Computational Electromagnetics and Its Applications.* 1997 ISBN 0-7923-4733-1
6. V. Venkatakrishnan, M.D. Salas and S.R. Chakravarthy (eds.): *Barriers and Challenges in Computational Fluid Dynamics.* 1998 ISBN 0-7923-4855-9
7. M.D. Salas, J.N. Hefner and L. Sakell (eds.): *Modeling Complex Turbulent Flows.* 1999 ISBN 0-7923-5590-3

KLUWER ACADEMIC PUBLISHERS – DORDRECHT / BOSTON / LONDON